Jammed colloidal systems confined in drops and beads

Matteo Milani

THÈSE POUR OBTENIR LE GRADE DE DOCTEUR DE L'UNIVERSITÉ DE MONTPELLIER

En Physique

École doctorale Information Structure et Système

Unité de recherche Laboratoire Charles Coulomb

Jammed colloidal systems confined in drops and beads

Présentée par Matteo MILANI

Sous la direction de Laurence RAMOS
et Luca CIPELLETTI
Le 04 12 2023

Devant le jury composé de

Laurence RAMOS, Directrice de recherche, CNRS	Directrice de thèse
Luca CIPELLETTI, Professeur, Université de Montpellier	Co-directeur de thèse
Cécile COTTIN-BIZONNE, Directrice de recherche, CNRS	Présidente
Kevin ROGER, Charge de recherche, CNRS	Rapporteur
Ludovic PAUCHARD, Directeur de recherche, Université Paris-Saclay	Rapporteur
Emanuela DEL GADO, Professeur, Georgetown University	Examinatrice
Véronique TRAPPE, Professeur, Université de Fribourg	Examinatrice
Wilson C. K. POON, Professeur, University of Edinburgh	Examinateur

UNIVERSITÉ DE MONTPELLIER

Abstract

In this thesis, we investigate two kinds of jammed colloidal systems confined in millimetric spheres: beads of colloidal gels and drops of colloidal suspensions. We investigate these systems in three sets of experiments: beads of colloidal gel under uniaxial deformation, drying of beads of colloidal gel and drying drops of colloidal suspensions. Each of these experiments addresses a specific question. First, beads under uniaxial compression are investigated to obtain new insight on the yielding behaviour of colloidal gels. Indeed, the yielding transition of colloidal gels is commonly studied by shear rheology; thanks to an innovative experimental approach, we unveil new facets of yielding. Second, we study the drying of beads of gels to investigate the network restructuring due to the compression occurring during drying. We are interested in the spatial distribution of the network rearrangements, and their relevant lengths scales. Third, it is known that drying drops of colloidal suspensions undergo mechanical instabilities that change their shape, due to the evaporation-induced formation of a dense colloidal shell. Previous works proposed that this instability occurs when the particles in the shell aggregate forming a porous solid. However, no measurements could directly test this scenario and assess its generality with respect to changes in the drying rate and initial volume fraction of the colloidal particles.

To address these questions, we tackled several experimental challenges. To produce spherical beads of colloidal gels, we developed a new experimental protocol whose soundness has been demonstrated by checking that the structural and mechanical properties of the gel beads do not differ from those of bulk gels prepared according to conventional protocols. The stiffness and structure of the beads have been tuned by varying the colloidal volume fraction (VF). Moreover, for studying the drying of beads and drops, we developed a new Dynamic Light Scattering (DLS) setup suited to probe the microscopic dynamics with space- and time-resolution of spherical samples.

To impose a uniaxial compression the beads, we used a rheometer coupled with a camera, allowing for imaging the system while measuring its mechanical response. Beads prepared at high VF abruptly yielded in the linear regime breaking into pieces, while those prepared at low VF dissipated energy by deforming plastically, leading to a smooth yielding. These observations indicated a brittle-to-ductile transition (BDT), predicted theoretically but elusive in shear rheology experiments. Thus, our experimental approach opens a promising experimental avenue for further investigations of the BDT.

Beads of colloidal gel were dried on top of hydrophobic surfaces, minimizing the interactions between the substrate and the gel, leading to an isotropic drying. We investigated isotropic drying through three experimental techniques: DLS, X-ray scattering and uniax-

ial compression tests. DLS revealed that the stresses imposed by the drying on the surface of the bead are homogeneously propagated, thus inducing rearrangements in the whole volume. X-ray scattering indicated that drying gels rearrange in a hierarchical manner, restructuring first at large length scales and then at smaller length scales, down to few particles size. The drying of drops of colloidal suspension have been investigated with our new DLS setup. We measured the evolution of the thickness of the shell and the spatial dependence of the volume fraction of the colloids. We found that above a critical evaporation rate the drop undergoes successively two distinct shape instabilities: invagination and cracking. Interestingly, the permanent aggregation of nanoparticles accompanies only the second instability, while the first one results from a reversible glass transition within the shell, unreported so far. Based on our discovery, we proposed a unified state diagram that rationalizes the drying of colloidal suspensions.

Summary

Overture

In 1827, by using an optical microscope, the botanist Robert Brown noticed that grains of pollen suspended in water, instead of being steady in absence of any external perturbation, were randomly moving around. The observation of this phenomenon, which nowadays goes with the name of Brownian motion, represents one of very first works that opened our view on the colloidal world.

The establishment of colloidal science is associated with the first classification of a colloidal suspension, which dates back to 1845. Indeed, in that year, Francesco Selmi performed a rigorous investigation on different materials dispersed in water. Since he found that dispersions of silver chloride, sulfur, Prussian Blue, alumina and starch had the same properties, he decided to assign them to the same class named by him *'pseudosolutions'*.

However, the word *'colloid'* has been coined only 16 years later in 1861 by Thomas Graham. This term, which comes from Greek and means *'glue'*, was used to better identify the *'pseudosolutions'* studied by Francesco Selmi. Interestingly, Thomas Graham did not only coin the term colloid, but he also deduced the range of sizes of the colloidal particles that, to date, applies for colloidal particles. Indeed, the high viscosity of colloidal suspension led him to the conclusion that the particles were at least 1 nm in diameter. At the same time, by observing that the suspensions did not rapidly sediment, he deduced that the upper size should have been roughly 1 μm.

This specific range size makes colloids the bridge between the microscopic and macroscopic world. Thus, throughout history, scientists have used colloids to model and access information on the microscopic world. The increase in knowledge on colloids which has been achieved throughout the years is enormous, as compared to the understanding of Brown and Selmi when making their first observations. Here it seems the scientists have been able to unravel all the secrets concerning colloids. However, this is just an impression; indeed, the complexity of this world is impressive and the variety of behaviors that still require an explanation makes colloidal science still one of the broadest area of investigation in condensed matter physics.

The investigation present in this thesis represents one small piece of the huge puzzle that is the exploration of the colloidal domain. In particular, as the adjective *'jammed'* in the title suggests, we focus on colloidal systems characterized by a high density of colloids or colloidal aggregates. Intriguingly, due to the high packing of the colloids/colloidal aggregates of which they are composed, these jammed systems as a whole can be seen as solids with unique properties. In this thesis we focus on three kinds of jammed systems: gels, dense suspensions and glasses.

Moreover, the title contains a second clue regarding our investigation, which concerns the boundary conditions characterizing the jammed system under investigation. Indeed, *'confined in drops and beads'* indicates that we are interested in jammed systems bounded in millimetric spheres. Without anticipating here any of our results, the reader will see how a colloidal system confined in a drops (or beads) shows behavior dramatically different from the same system in the bulk. Very generally, this fact is extremely fascinating, since a colloid alone has a size which is ten orders of magnitude smaller than the drop in which it is confined. Indeed, to give an idea, the ratio between a colloid and the confining sphere is comparable to the ratio between our height and the diameter of the earth. However, although the confinement is negligible for a single colloid, the interactions between colloids lead to a rich and intriguing phenomenology, as we will illustrate in this thesis.

Chapter 1

State of the art & Objectives

1.1 Unified state diagram for colloidal systems

The purpose of this section is to give an unified view of the possible phases a colloidal system can assume. In particular we will present a unified phase diagram of colloidal systems, whose axes are three relevant parameter: the inter-particle potential, the volume fraction and the imposed external stress. We discuss the phase diagram by looking on one axis at a time: we first address the role of the inter-particles potential, then we focus on the role of the particles volume fraction and finally we will show how an imposed stress can alter the phase of a colloidal system.

1.1.1 Role of interparticle potential: Hard sphere and DLVO potentials

1.1.1.1 Hard sphere potential

Hard sphere interactions describes the impossibility of two particles to overlap in space. The hard sphere potential is formally defined as:

$$V(\mathbf{r}_1, \mathbf{r}_2) = \begin{cases} \infty, & \text{if } |\mathbf{r}_1 - \mathbf{r}_2| < d \\ 0, & \text{if } |\mathbf{r}_1 - \mathbf{r}_2| > d \end{cases} \tag{1.1}$$

where $\mathbf{r}_{1,2}$ are the position of the two particles and d their diameter. Thus, until they get in contact, two particles do not experience the presence of each other. Once in contact they both experience an infinite repulsive potential which prevents the inter penetration.

1.1.1.2 DLVO theory

One the most significant advancement in the area of colloidal science was achieved in 1940s with the formulation of the Derjaguin, Landau, Verwey, and Overbeek (DLVO) theory. DLVO provides a quantitative connection between the stability of a colloidal suspension and the interparticles interaction.

In a nutshell, DLVO theory explains the stability of a colloidal system in term of short-range van der Waals attractive forces and long-range electrostatic repulsion. Thus, in this theory, the local interaction potential between two particles whose surfaces are separated by a distance h reads as:

$$V(h) = V_a(h) + V_r(h) \tag{1.2}$$

where, $V_a(h)$ is the attractive van der Waals potential and $V_r(h)$ is the electrostatic repulsion. The attractive potential is obtained in the Derjaguin (or proximity) approximation where the colloids are approximates as planar object since they are separated by a distance h much smaller than their radii. Under this approximation, without going into the details of the derivation, the van der Waals potential reads:

$$V_a(h) = -\frac{H_{121}}{12\pi h^2} \tag{1.3}$$

where H_{121} is the Hamaker constant for a medium 1 separated by a liquid 2. The electrostatic repulsion, which is due the double layer structure of the free ions in the solvent, reads:

$$V_r(h) = \frac{64 k_B T c_0^* \Gamma_0^2}{\kappa} \exp(-\kappa h) \tag{1.4}$$

where c_0^* is the ion concentration, k_B the Boltzmann constant, $\Gamma_0 = \tanh Z\phi_0/4k_BT$ with Z the total charge on the colloid and ϕ_0 its potential at the surface. The quantity κ^{-1} is the Debye screening length and is determined by the electrolyte concentration in solution: low electrolyte concentration leads to large screening length (κ^{-1}), vice versa for high electrolyte concentration.

By inserting Eq. 1.3 and Eq. 1.4 into Eq. 1.2 we obtain:

$$\frac{V(h)}{A} = -\frac{H_{121}}{12\pi h^2} + \frac{64 k_B T c_0^* \Gamma_0^2}{\kappa} \exp(-\kappa h) \tag{1.5}$$

The DLVO potential of Eq. 1.5 is plotted as a function of the distance h between the surface of two particles in Fig. 1. We can see that for large Debye lengths the potential has a substantial energy barrier, which ensures the stability of the system. Contrary, for short Debye length the energy barrier is low or nonexistent and the system is unstable to aggregation.

This theory allows one to classify a colloidal system in two categories: repulsive stable colloids and unstable attractive colloids. However the inter-particle potential is not the only parameter which determines the state of the system. Indeed, as mentioned before, parameters such as the volume fraction ϕ of the colloids or the applied stress σ may affect the phase of the system and its properties.

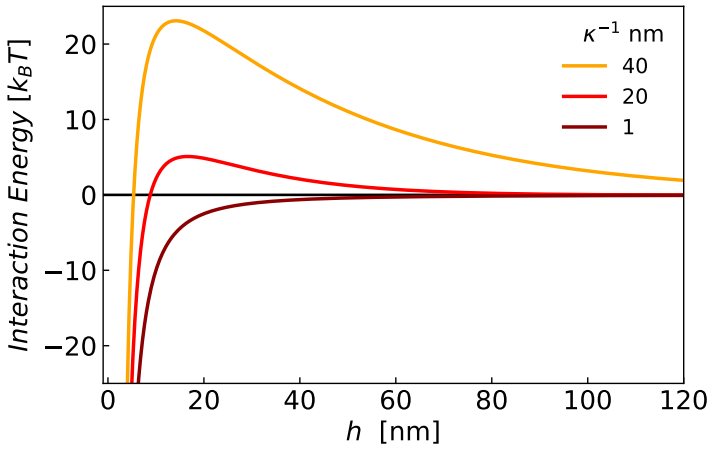

Figure 1: DLVO interaction energy with a colloid as a function of the distance with it core obtained expressed in k_bT units. Different colors correspond to different Debay length κ^{-1}.

1.1.2 Role of volume fraction and the glass transition

A key parameter determining the phase of a colloidal system is the particle volume fraction ϕ. One way to decouple the effects on the system of the volume fraction from the ones of inter-particle interactions is to use hard sphere systems. Indeed, as mentioned in the previous section, the hard sphere potential accounts only for the excluded volume experienced by a colloid due to the presence of the others.

A key work on the interplay between the equilibrium phase of a colloidal system and the volume fraction of the colloids has been done by Pusey and Van Megen in [Pusey and Van Megen (1986)]. The authors prepared suspensions of quasi hard sphere Poly(methyl methacrylate) (PMMA) particles of radius 304 ± 10 nm and relative polydispersity 0.05 at different ϕ and let them at rest for four days. As seen in Fig. 2, the authors found that the suspension had a different appearance according to the initial volume fraction. For the less concentrated sample (sample 2 with $\phi = 0.393$) no particular change has been observed over time and the colloids remained able to diffuse as in a liquid. For samples 3-4-5 a partial crystallization, as indicated by Bragg reflections, appears underneath a liquid phase. For samples 6-7-8 a crystalline phase spans the whole sample. Interestingly, samples 9-10, which correspond to the highest values of volume fractions ($\phi > 0.5$), did not fully crystallize. Indeed, a heterogeneous region is present underneath the crystalline one. Remarkably full crystallization was not reached even by waiting for several months. The authors suggested that the presence of this heterogeneous region was due to the increase of viscosity because of the high volume fraction. This fact led Pusey and Van Megen to define a glass phase for a purely hard sphere colloidal system occurring at $\phi \approx 0.58$.

A state diagram depicting the combined effects of particles volume fraction and the interpaticle potential (attractive interaction only) was proposed by Trappe and Sandkühler in [Trappe and Sandkühler (2004)], and is shown here in Fig. 3.

Figure 2: [Pusey and Van Megen (1986)]: Suspension of nearly hard sphere colloids 4 days after preparation. The volume fraction of colloids increases from left to right, from $\phi = 0.393$ to $\phi = 0.52$. The sample are illuminated from behind with bright light such to visualize the Bragg reflection for the crystalline phase. The cross section of the vial is 1 cnm $\times$ 1 cm.

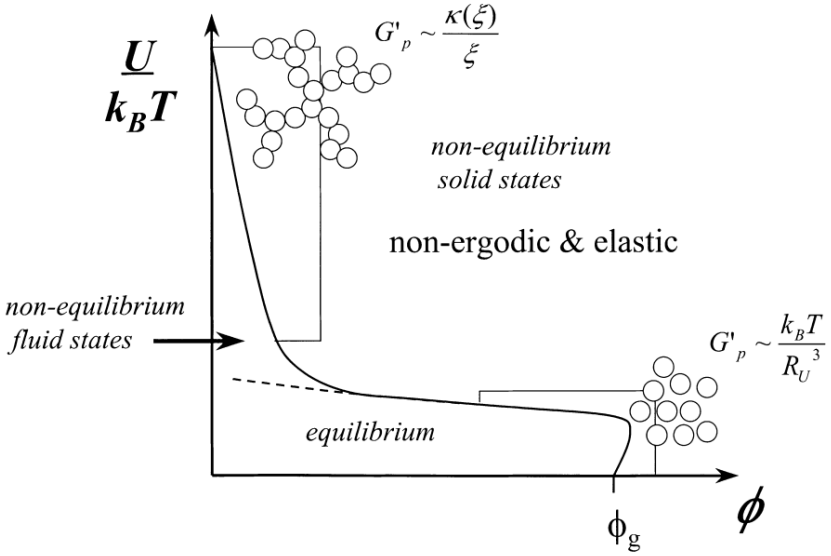

Figure 3: [Trappe and Sandkühler (2004)]: Schematic state diagram of colloidal particles with short range potential. The solid line represents the boundary between a fluid phase and a disordered solid phase.

When ϕ is close to 0 the system is diluted and by increasing U the system undergoes a liquid-to-solid transition due to particle aggregation. The system goes with the name of colloidal gel and will be further described in Sec. 1.2. On the contrary, when $U = 0$ the system is composed by hard sphere particles. So, as found by Pusey and Van Megen, when ϕ is increased the suspension acquires a solid-like behavior as the glass transition is approached. In the state diagram we also see a critical line obtained when both U and $\phi \neq 0$, delimiting an ergodic fluid phase to a non-ergodic and elastic fluid phase. In this context, the system is ergodic if all the colloids explore all the possible position in the space. Moreover, we also see that at low ϕ by increasing the strength of the attractive potential a dotted line separates equilibrium system from non equilibrium one. This indicates that, when the attraction is strong the system can not be in equilibrium even at low ϕ.

1.1.2.1 Glass transition in soft colloids

The state diagram proposed by Trappe and Sandkühler only deals with attractive particles. However, as shown before, colloids can strongly repulse each other due to electrostatic interactions, and even this kind of system can undergo a glass transition. Moreover, due to the long range electrostatic interaction, the system has a glass transition different from the one of hard sphere colloids. Since the glass transition of repulsive particles is of a great interest for this thesis, we analyze here some of its fundamental aspects.

An important investigation on this kind of system has been done by Philippe et al. in [Philippe et al. (2018)]. In this work the authors used charged stabilized silica nanoparticles with radius 23 nm , characterized by a long range electrostatic repulsion (the Debye length was estimated to be $\kappa^{-1} = 20$ nm).

Since probing the microscopic dynamics of the system, provides direct insights on the phase of colloidal system, the authors used dynamics light scattering (DLS) to characterize their system. In Fig. 4 we plot the $g_2 - 1$ intensity auto-correlation function measured by the authors for the system at a different colloidal volume fraction. The $g_2 - 1$ correlation function will be given in Sec. 2.1.2. As shown in Fig.4, the DLS correlation function of dilute suspension is well described by a simple exponential decay associated to the Brownian diffusion of the colloids. As the volume fraction of colloids φ increases, a two-step decay appears. A first decay, which goes with the name of β-relaxation, is associated to the particle motion within a cage formed by the neighbouring particles. The second decay, is termed α-relaxation and is associated to the cage-escape motion of the colloids, and it is responsible of the long time structural relaxation of the system. Upon increasing the concentration, the α-relaxation gets slower and slower until seemingly diverging at the glass transition. Indeed, as showed in Fig. 5a, from $\varphi = 0.3$ to $\varphi = 0.4$ the decay time abruptly increases by six orders of magnitude. By fitting the data with a critical like behavior ($\tau_\alpha = (\varphi_g - \varphi)^{-\gamma}$), the authors determined the critical value of the glass

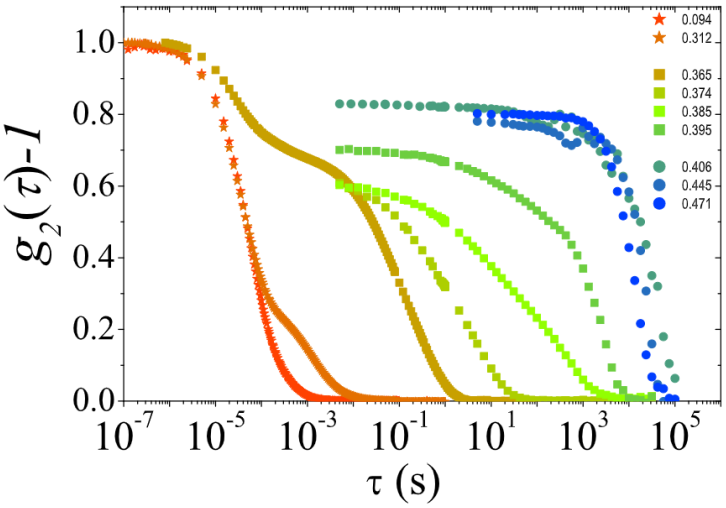

Figure 4: [Philippe et al. (2018)]: $g_2 - 1$ intensity auto-correlation functions measured by DLS for a Ludox suspension. As indicated in the legend, different colors correspond to different volume fractions

transition of this system to be $\varphi_g \approx 0.39$. Note that this value is much lower compare to $\phi_g \approx 0.58$ found for hard sphere colloids. Finally, for $\varphi > 0.4$ the authors found a plateau of τ_α, indicating that further increments of the volume fraction do not have an incidence on the microscopic dynamics of the system.

Interestingly, [Philippe et al. (2018)] analyzed in the same work two batches of PNIPAM microgels with hydrodynamic diameter of respectively $d_h = 353$ nm and $d_h = 268$ nm. Remarkably, by doing the same analysis done for the silica colloids, the authors found the same qualitative dependence of the α-relaxation on the volume fraction. Indeed, as shown in Fig. 5b by normalizing the volume fraction by the critical ϕ_g of the glass transition, and τ_α by the decay time of each system in the dilute regime they obtained a remarkable collapse of the data. Thus, the glass transition of hard colloids with a repulsive potential can be seen with the same regard of the glass transition of soft colloids. On this latter system, despite being less investigated than the hard sphere colloidal glass, some work have been done trying to elucidate several aspect of its glass transition, such as the influence of the softness of the particles on the critical volume fraction that leads the divergence of the viscosity, the change of the structure factor of the glass phase, the glassy dynamics etc. [Mattsson et al. (2009); Vlassopoulos and Cloitre (2014); Van Der Scheer et al. (2017); Gnan and Zaccarelli (2019); Philippe et al. (2018)].

1.1.3 Role of stress: yielding transition

So far we have investigated the effects of inter-particles potential and volume fraction on the state of a colloidal system. However, any imposed external stress σ may have a significant impact on a colloidal system. Indeed, it is sufficient to think about our daily

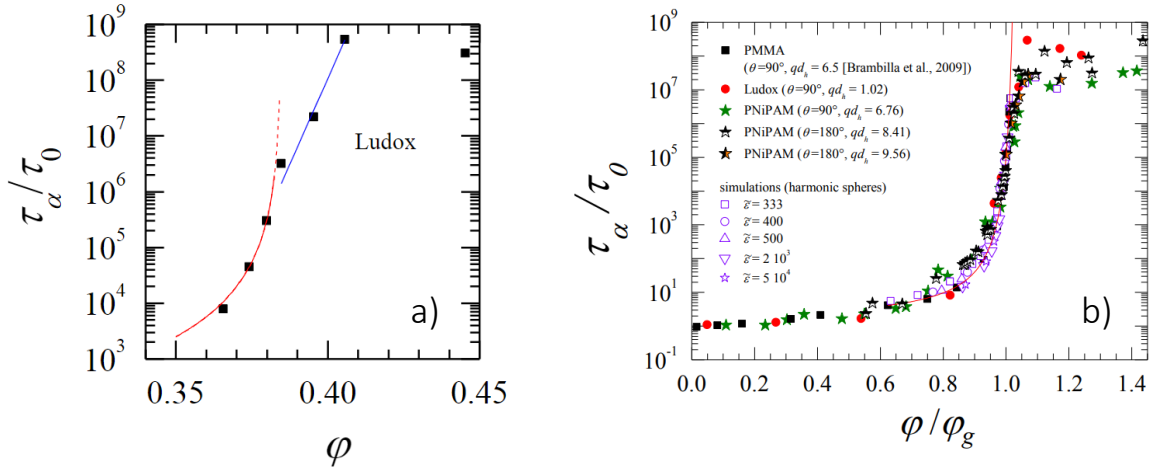

Figure 5: [Philippe et al. (2018)]: a) structural relaxation time τ_α normalized by the relaxation time in the dilute regime τ_0 as a function of the volume fraction for suspensions of Ludox particles. The red solid line represent a fit to the data of $\tau_\alpha/\tau_0 \sim (\varphi_g - \varphi)^{-\gamma}$. The blue line is a fit to the data of Arrhenius-like function ($\tau_\alpha/\tau_0 = \sim \exp(B\varphi)$). b) Rescaled relaxation time as a function of rescaled volume fraction. Different symbols correspond to different data: red filled circles represent Ludox particles, filled stars PNiPAM microgels, black squares are PMMA hard sphere data taken from the work of Brambilla et al. [Brambilla et al. (2009)], empty purple symbols are simulations of harmonic spheres.

life where soft material such as creams, jams, yogurts, ganache, etc. have a solid-like, elastic behavior, but when spread by hand/knife/spatula they flow as liquids. Such a behavior is encountered even in colloidal systems, where a solid-like phase sample can undergo a transition towards a fluid state via an imposed external stress. In soft matter the critical stress above which the system is fluidized goes with the name of yielding stress σ_y.

Considering the fluidification by yielding as an actual phase transition is a concept that has been introduced by Liu and Nagel in a pioneering communication [Liu and Nagel (1998)], where the authors proposed a possible state diagram for repulsive particles (see Fig. 6a). Note that the authors refer to the region at near the origin where the system is solid-like as *jammed* states, which is a broader definition than colloidal glass, since it includes non-Brownian particles as well. In the diagram a solid -to-liquid transition can be achieved by decreasing density (volume fraction), increasing the temperature (which is equivalent to decrease the inter-particle interaction) or by increasing the imposed load. The authors mentioned that the line in temperature-load axes (see Fig. 6a) is purely speculative and indicates that the yielding stress may vary for a colloidal system with thermal motion.

Interestingly, this type of state diagram has been extended to attractive particles in a later work by Trappe et al. [Trappe et al. (2001)]. Remarkably, the authors managed to reconstruct experimentally an unified state diagram describing the fluid-to-solid transition

of attractive particles as a function of three variables: the inter-particles potential U, the volume fraction of colloids ϕ and the applied stress σ. Such a state diagram is plotted in Fig. 6b. The authors found experimentally three critical-like functional forms that determines the boundaries between solid-like (jammed) systems ans liquid-like ones. The first critical relationship concerns the interplay between ϕ and U at the onset of gelation for PMMA colloids and carbon black particles : by playing with the particles interaction it is possible to turn a suspension of PMMA colloids into a gel. This transition is described by the critical behavior:

$$\phi_c = \phi_0 \exp\left(-U_c/\alpha k_B T\right) \tag{1.6}$$

where α is a coefficient of the order of one. Moreover, the authors found a critical like behavior for the viscosity η and the elastic modulus G_0. For a fixed U, $\eta = \eta_s(\phi_c - \phi)^{-\nu_\phi}$ and $G_0 = G_s(\phi - \phi_c)^{\nu_\phi}$. In other words they were able to obtain a jammed system by playing either with ϕ or with U. Finally, the third dimension of the phase diagram concerns the stress. In this case they found for polystyrene colloids, that it was possible to fludize a jammed system by increasing the stress. In particular the found that the yielding stress at which the system became fluid is well described by two critical-like relationships:

$$\sigma_y = \sigma_\phi(\phi - \phi_c)^{\mu_\phi} \tag{1.7}$$

and

$$\sigma_y = \sigma_U(U - U_c)^{\mu_U} \tag{1.8}$$

So, by using the functional forms of Eqs. 1.6,1.8, Trappe et al. found the critical lines of the phase diagram of Fig. 6. Lately an interesting paper by Aime et al. [Aime et al. (2023)], by employing an analogy with van der Waals phase diagram, proposed a unifying view on the yielding transition of soft colloids.

In this thesis, we will investigate both repulsive and attractive colloidal systems. On one hand, we investigated drying drops of suspensions of repulsive particles, whose volume fraction varied from low to high during the drying process, as we will briefly discuss in Sec. 1.3. On the other hand, we studied colloidal gels formed by strongly attractive colloidal particles at relatively low ϕ. These systems, which are briefly discussed in Sec. 1.2, correspond to the region labelled *'irreversible aggregation'* in Fig. 6.

1.2 Colloidal Gels

When salt is added to a charge-stabilized suspension, the electrostatic repulsive potential responsible for the stability of the system is screened. Short range van der Waals attractive interactions prevail, eventually leading to colloidal aggregation. The resulting

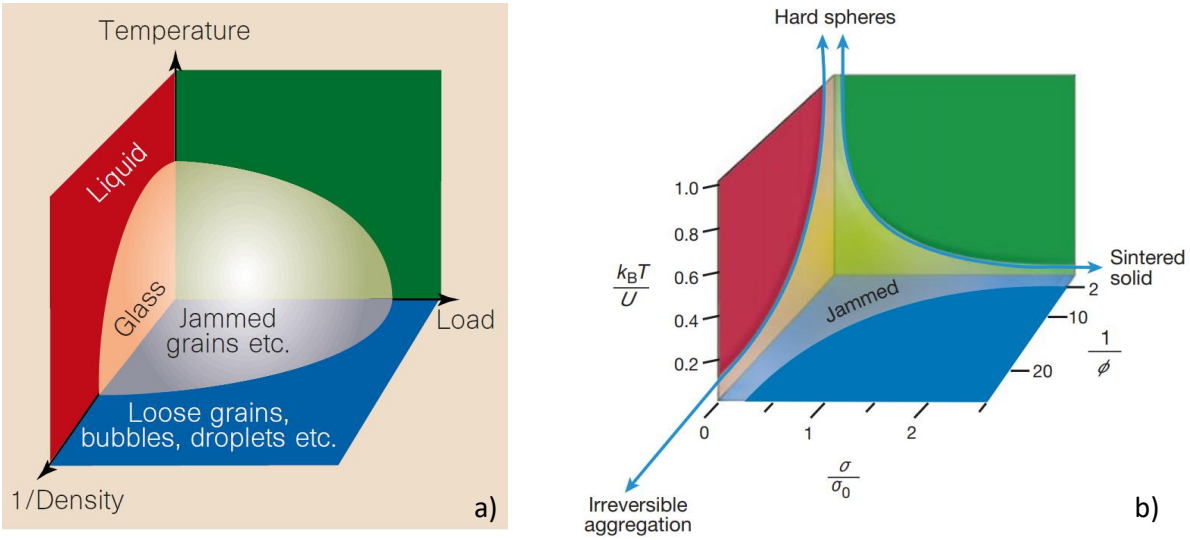

Figure 6: a) [Liu and Nagel (1998)] : Unified state diagram for repulsive particles. The authors indicated that the line in the temperature-load plane is purely speculative and suggests that the yield stress may vary with temperature due to thermal fluctuations. b) [Trappe et al. (2001)]: Unified state diagram for attractive particles. The authors indicates that the axes extend until $\phi < 0.5$ and $k_bT < 1$ to avoid the case of purely hard sphere particles and very high concentration where more complex behaviors with increasing σ may occur.

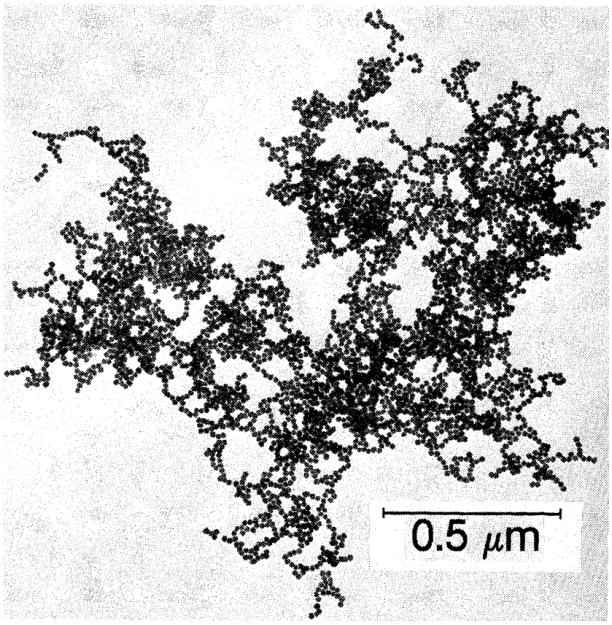

Figure 7: [Weitz and Oliveria (1984)]: Electron transmission microscopy (TEM) of a fractal cluster of gold colloids.

system, which has elastic properties despite being mainly composed by a liquid, goes with the name of colloidal gel.

1.2.1 General Properties

1.2.1.1 Structure

The first insights on the microscopic structure of a colloidal gel came from theoretical works done by [Witten Jr and Sander (1981); Meakin (1983)]. The authors predicted that the clusters composing the network were characterized by a fractal structure. The first experimental work able to unravel the fractal microscopic structure of colloidal aggregates was done by Weitz and Oliveira in [Weitz and Oliveria (1984)]. In this work the authors induced the aggregation of gold nanoparticles (diameter ≈ 14.5 nm) dispersed in water. By doing Transmission Electron Microscopy (TEM) the authors managed to take the image of a fractal cluster shown in Fig. 7. To illustrate the scale-invariant nature of the network, the authors measured the number of particles in the cluster N as a function of its linear dimension L. Remarkably, they found a power law relationship $N \sim L^D$, with $D = 1.75$ the fractal dimension of the cluster. The fractal dimension D tells how the mass scales with the volume. In an euclidean space with 3 dimension, the mass of a compact solid is proportional to the volume, thus $N \sim L^3$, implying $D = 3$. So, a fractal dimension $D = 1.75$ indicates that the aggregate has an extremely open structure.

Due to their multi-scale hierarchical network, one of the most efficient way of characterizing the structure of a colloidal gel formed by fractal clusters is by scattering techniques.

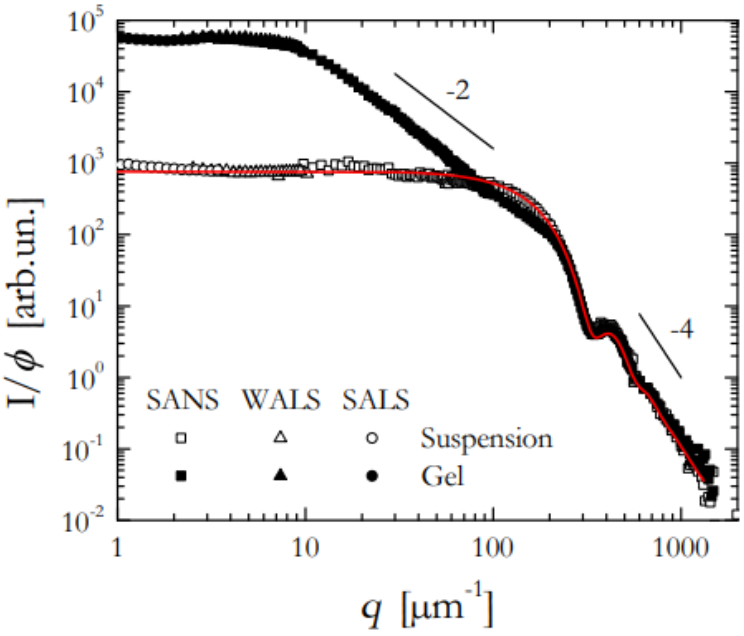

Figure 8: [Aime (2017)]: Scattering intensity profile of a colloidal gel (filled symbols) made with silica nanoparticles (Ludox TM-50, particle diameter 50 nm), prepared at volume fraction $\phi = 5\%$ and of a diluted suspension (empty symbols) of the same nanoparticles at concentration $\phi = 0.037\%$. As indicated in the legend different symbols represent different scattering techniques.

Indeed, scattering allows one to simultaneously probe a wide range of length scales. Figure 8 displays the normalized scattering intensity profile of a colloidal gel made by silica nanoparticles at volume fraction $\phi = 5\%$. In this particular case, Aime et al. ([Aime (2017)]) combined three techniques: Small Angle Neutron Scattering (SANS), Wide Angle Light Scattering (WALS) and Small Angle Light Scattering (SALS). In such a way the authors managed to probe the gel structure over four decades in scattering vector q. At the largest q ($200\ \mu m^{-1} < q < 1000\ \mu m^{-1}$), as we can see also from the overlap with the dilute system, one gets information about the single nanoparticle. At intermediate q ($10\ \mu m^{-1} < q < 200\ \mu m^{-1}$) we see a power law decrease of the scattering intensity with q: such a behavior reflects the fractal nature of the structure. Moreover, as indicated by Teixeira in [Teixeira (1988)] the exponent of the power law indicates the fractal dimension (in this case, as indicated by the figure $D = 2$). Finally at small q, the scattered intensity plateaus, indicating the homogeneity of the structure at large length scales. The scattering vector at which the scattered intensity crossover from the power law regime to constant value determines maximum size ζ of the clusters (in this case $\zeta = 2\pi/q_c \approx 630$ nm).

1.2.1.2 Aggregation mechanism

The structure of a colloidal gel depends on many parameters, which ultimately affect the aggregation mechanism of the solid structure. The purpose of this section is not to make a comprehensive description of the different aggregation mechanisms leading to a colloidal gel, but rather to provide some insight into the main processes. For the readers interested in a more detailed description we suggest the review by Lu and Weitz [Lu and Weitz (2013)]. Two main categories can be defined: for colloidal gels formed at high volume fraction and at low inter-particle attraction, the gels form via an arrested phase separation. By contrast, systems at low volume fraction and strong inter-particle attraction form gels by dynamic aggregation. In this case the colloidal particles diffusing in the fluid aggregate to form cluster. If the particles stick irreversibly upon contact, as in the case of Fig. 7, the clusters are fractal with low fractal dimension ($D \approx 1.7$): this particular kind of dynamic aggregation is termed of Diffusion Limited Cluster Aggregation (DLCA). By contrast, in the so called Reaction Limited Cluster Aggregation (RLCA) a small repulsive barrier is present between colloids, thus particles may require multiple attempts before sticking to each other. This behavior, leads to more compact clusters with higher fractal dimension, $D \geq 2$. In this thesis we form gels with relatively low volume fraction and strong attraction, thus the network formation is driven by dynamic aggregation. However, it is not possible to clearly distinguish between the DLCA and RLCA aggregation mechanism since we find a fractal dimension $D = 2$. However, as we will show in Fig. 45 of Chapter 4, for all the probed volume fractions the fractal properties of our gels do not change, thus allowing a direct comparison between samples.

1.2.1.3 Microscopic dynamics

The measurement of microscopic dynamics represents an extremely important task in the world of soft matter and for colloidal gels as well. Indeed, the motion at the nano-microscopic scale may reveal the intimate fundamental mechanisms ruling the macroscopic behavior of materials in phenomena such as elasticity, aging, failure and many others.

For example, Krall and Weitz [Krall and Weitz (1998)] manged to determine the elastic modulus of colloidal gels by measuring its microscopic dynamics. To do so, Krall and Weitz first used Dynamics Light Scattering (DLS) to measure the correlation function shown in Fig. 9a. Then, they fitted the data to the analytical function $f(q,t) = \exp\{q^2 < \Delta r_\zeta^2 > /6\}$, writing the mean square displacement $< \Delta r_\zeta^2 >$ in terms of the elastic properties of the clusters composing the gel. So, once fitted the data, they obtained the elastic properties of the fractal clusters from which they estimate the elastic modulus G_0 of the gel. Moreover, thank to this work, it is now commonly accepted that the origin of such fast dynamics is the collective, thermally activated vibrations of the clusters. Indeed, due to the interconnected nature of colloidal gels, the motion of each

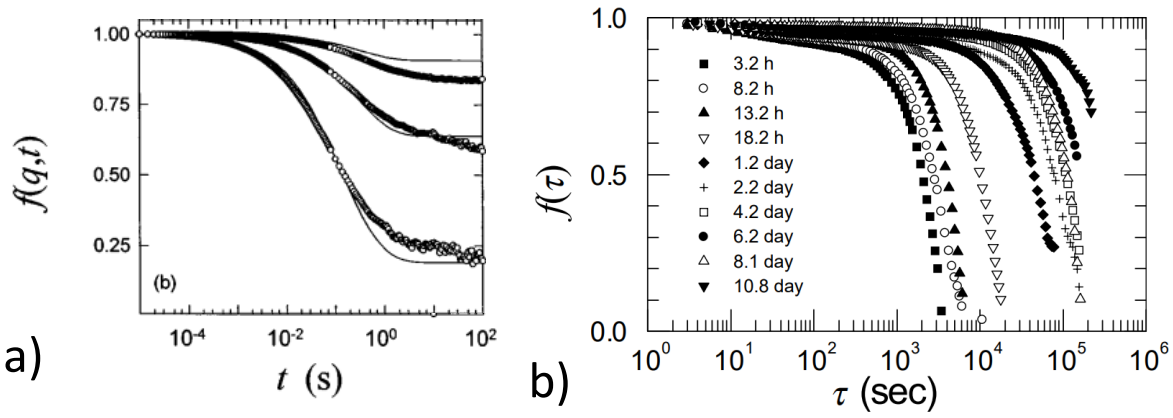

Figure 9: a) [Krall and Weitz (1998)]: DLS correlation functions of a polystyrene colloidal gel prepared at volume fraction $\phi = 0.15\%$, each curve correspond to a scattering angle, from top to bottom: q=4.1, 8.7, 16.7 μm^{-1} . b) [Cipelletti et al. (2000)]: Time evolution of the DLS correlation function of a polystyrene colloidal gel prepared at volume fraction $\phi = 0.048\%$; the scattering vector $q = 0.6756$ μm^{-1} is the same for all the curves.

portion of the gel is given by its own thermal fluctuations and the fluctuation of all larger segments present in the gel. Such a motion confers a q^2 dependence of the correlation function measured by DLS, thus allowing one to define an effective diffusion coefficient to describe such fast internal dynamics.

However, colloidal gels are not only characterized by the fast dynamics, as measured by Krall and Weitz. Indeed, slow internal dynamics are also present in colloidal gels. To measure the slow dynamics of a gel, [Cipelletti et al. (2000)] employed multi-speckle dynamic light scattering. It is important to know that, with multispeckle techniques it is possible to access dynamics much slower compared to traditional DLS (decay up to 10^5s, see Sec. 2.1.3 for a description of multispeckle techniques). Using multispeckle DLS, Cipelletti et al. managed to obtain the correlation functions of Fig. 9b. The complete loss of correlation indicates that on the scale of tens of thousands of seconds the rearrangements occur on length scales of the order of $2\pi/q \approx 10$ μm. Thus, slow dynamics are related to sample spanning network reorganization.

Moreover, the most striking difference between slow and fast dynamics is their time dependence. Indeed, while fast dynamics do not reflect any kind of sample aging, we clearly see from Fig. 9b that slow dynamics strongly evolve with time: the correlation function decays slower and slower with time. Moreover, contrary to fast dynamics, the relaxation time associated to these dynamics scales as q^{-1}, thus ruling out the possibility of a diffusive-like process for this kind of events. It rather suggests a ballistic-like process. Interestingly, the time-dependence of the microscopic dynamics is reflected also in their mechanical properties. Indeed, Manley et al. observed that the aging is not only manifested by a slow down of the microscopic dynamics, but also by an evolution of the shear storage modulus G, which becomes stiffer with time [Manley et al. (2005a)]. In this

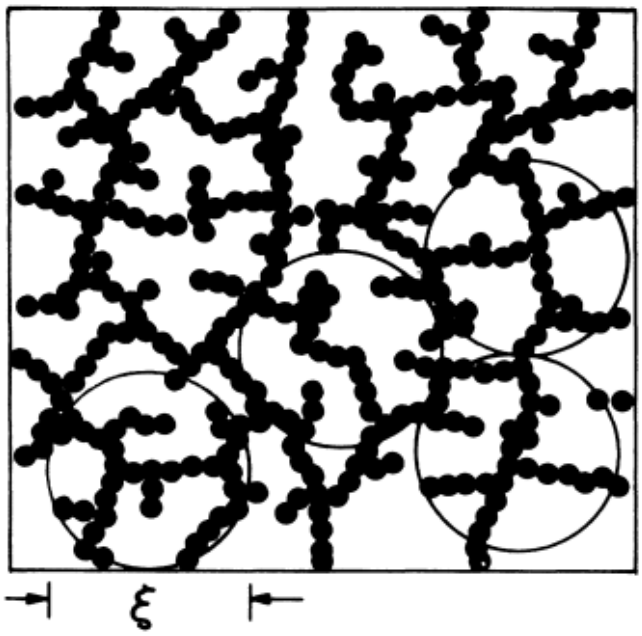

Figure 10: a) [Shih et al. (1990)]: Schematic representation of a colloidal gel, the circles indicates the cluster size ξ.

work, Manley et al. proved that the aging of the gel is given by the partial softness of polystyrene colloids. Indeed, with time, the colloids slightly compress reducing their core to core distance which reduces fluctuation and makes the bonds stiffer.

1.2.1.4 Linear rheology

In order to fully characterize the properties of colloidal gels, together with the microscopic investigation done by means of scattering experiments, macroscopic rheological measurements have been widely employed.

From the mechanical point of view, colloidal gels are characterized by both elasticity and viscosity. Indeed, despite being mainly composed by a fluid, the elastic character of colloidal gel dominates over the viscous one in the linear regime. Interestingly, the first studies on colloidal gels, done by Buscall et al. [Buscall et al. (1988)] and Sonntag and Russel [Sonntag and Russel (1986)], found a power law dependence of the elastic modulus G on the volume fraction of the gel ϕ: $G \sim \phi^{\alpha}$. This power law for relationship between G and ϕ has been rationalized by Shih et al. [Shih et al. (1990)].

In this work, the authors exploited the same scaling theory that was found about twenty years before by De Gennes in [De Gennes (1979)] for polymer gels. Shih et al. used the schematic view of the gel presented in Fig. 10, considering the gel network as a random close packing of fractal clusters of size ξ. In analogy with polymers ξ is the a correlation length of the system. For distances smaller than ξ the system is fractal, while on scales larger than ξ the system is homogeneous. Given the fractal structure of the

clusters, their size is directly proportional to the volume fraction:

$$\xi \sim \phi^{1/D-d} \tag{1.9}$$

where D is the fractal dimension and d the euclidean dimension, and their elastic constant reads as:

$$K_\xi \sim \frac{K_0}{\xi^{x+2}} \tag{1.10}$$

where K_0 is the elastic constant between two neighboring backbones and x is a number $1 < x < D$. For large cluster size the elastic constant between two neighboring backbones K_0 overcomes the elasticity of the cluster K_ξ; the authors refers to this case as strong link regime. On the contrary, when ξ is small, the internal elastic constant of a cluster is larger than K_0, thus the gel is in a weak link regime. Without going into the details, the authors found that, if the gel is in the strong link regime the macroscopic elastic modulus is:

$$G \sim \phi^{(d+x)/(d-D)} \tag{1.11}$$

while in the weak link regime:

$$G \sim \phi^{(d-2)/(d-D)} \tag{1.12}$$

Thus, in this model, the macroscopic elasticity of the gel depends on the fractal structure of the cluster and their size. To check their scaling model, Shih et al. performed shear bulk rheology measurements of colloidal gels made of alumina particles. Remarkably, they found for all the gels they probed a power law dependence of the elasticity on the volume fraction. Moreover, by finding a exponent ~ 4, and comparing with Eq. 1.11 and 1.12, they found that the system is in the strong link regime.

The success of this work helped to interpret the microscopic origin of the scaling law between the elastic properties of colloidal gel and the volume fraction. Over the years, several experiments tested the mechanical properties of different kind of colloidal gels finding a power law between G and ϕ. The exponents of the power low α are found to vary in a wide range, from 3 to 8 [Sonntag and Russel (1986); Buscall et al. (1988); Grant and Russel (1993); Yanez et al. (1996); Rueb and Zukoski (1997); Wyss et al. (2004); Manley et al. (2005a); Romer et al. (2014); Aime et al. (2018a)], thus questioning the simple scenario proposed by Shih et al., and more generally the possibility of finding a unifying scenario able to predict the mechanical properties of colloidal gels.

The current interest in finding a universal theory for interpreting the elastic properties of colloidal gels is testified by several recent works [Dagès et al. (2022); Bouthier and Gibaud (2023)] on the topic. In particular, a rationalization of the exponents found in the different experiments has been recently proposed by Bantawa et al. in [Bantawa et al. (2023)]. The authors based their model starting from the same gel structure proposed by Shih et al.: fractal objects (called blobs in their work) equally distributed in the space.

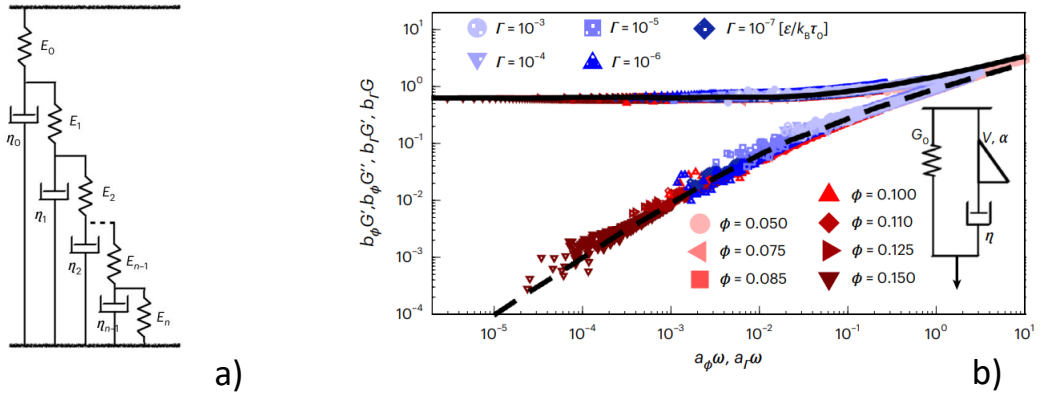

Figure 11: [Bantawa et al. (2023)] : a) The hierarchical ladder model used to obtain the master curve of panel b). b) Rescaled storage and loss moduli of fractal colloidal gels prepared at different volume fraction and gelation rate

However, Bantawa et al. proposed that the elasticity of the gel is arises from a hidden hierarchical organization of the fractal blobs which can be schematized as a recursive ladder model, shown in Fig. 11a. Remarkably, such a model allowed them to obtain a nice collapse of the mechanical properties of gels prepared at different volume fraction and gelation rate, Fig. 11b.

1.2.1.5 Yielding of colloidal gels

The yielding of colloidal gels is another extremely investigated topic. Indeed, due to their amorphous nature and their scaling with the volume fraction, they are representative to understand the failure of a huge variety of disordered solids. The techniques to investigate such a phenomenon are numerous, from macroscopic rheology to scattering and optical measurements. Providing a comprehensive review is beyond the scope of this section.To name just a few examples, Bonacci et al. observed with a microscope the behavior of small linear aggregates when bent with optical tweezers [Bonacci et al. (2022)]. On their side, Aime et al. developed a setup combining a shear cell with small angle DLS [Aime et al. (2016)] to investigate microscopic yielding precursors of colloidal gels [Aime et al. (2018b)]. Yielding of colloidal gels has been investigated also through simulations, in particular in the group of E. Del Gado [Colombo and Del Gado (2014); Bouzid and Del Gado (2018)]

The most popular approach to investigate yielding is by means of shear rheology. Thanks to this approach, several general features of the yielding of colloidal gel have been revealed, such as the scaling of the yielding strain γ_y and yielding stress σ_y with the volume fraction. Indeed, as for the elastic modulus, the yielding strain required to break the gel increases with the volume fraction following a power law relationship $\sigma_y \sim \varphi^\alpha$. Inversely, the yielding strain γ_y at which the colloidal gels yield is inversely proportional to the volume fraction.

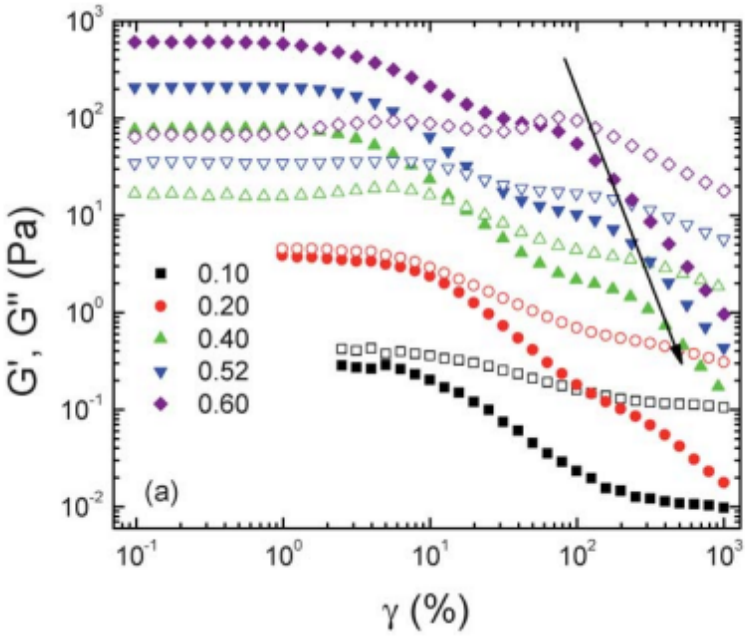

Figure 12: a) [Koumakis and Petekidis (2011)] Dynamics strain sweep at $\omega = 10$ rad/s for colloidal gels prepared at different volume fractions. Open symbols represent the storage modulus G' and empty symbols the loss modulus G''. The arrow is a guide for the eye indicating the shift of the second yielding strain with the volume fraction. The yielding strain is defined as the overshoot of G''.

Among all the works investigating the yielding under shear, Koumakis and Petekidis in [Koumakis and Petekidis (2011)] and Laurati et al. in [Laurati et al. (2011)] performed an accurate analysis by doing Large Amplitude Oscillatory Shear (LAOS) tests. LAOS consists in applying to the sample shear deformation γ at constant frequency of increasing amplitude. In such a way, the material is first perturbed in the linear regime and subsequently it experiences a deformation beyond linearity until eventually yielding. We report in Fig. 12 the characteristic results of a LAOS experiment on colloidal gels. At small deformation both the storage (G') and loss (G'') moduli are constant. Around typically $\gamma \approx 10\%$ G' and G'' start to decrease and at $\gamma \approx 100\%$ G'' becomes dominant due to a second larger drop of G' (G'' overshoot). As pointed out by the authors, this behavior indicates the the sample undergoes a double yielding event upon increasing γ . The first yielding has been associated with the onset of non-linearity due to the bond breaking of the gel network. The physical origin of the second yielding is more obscure; however the authors proposed that it is due to breaking events inside the clusters.

A new interesting rheological protocol to better interpret the G'' overshoot of soft materials under shear has been presented by Donley et al. [Donley et al. (2020)] . Thanks to their protocol, the authors managed to separate the solid-like response to the liquid-like for several systems undergoing yielding. Thus such a method could be exploited interpret the physical origin of this second yielding of colloidal gels described by Koumakis and

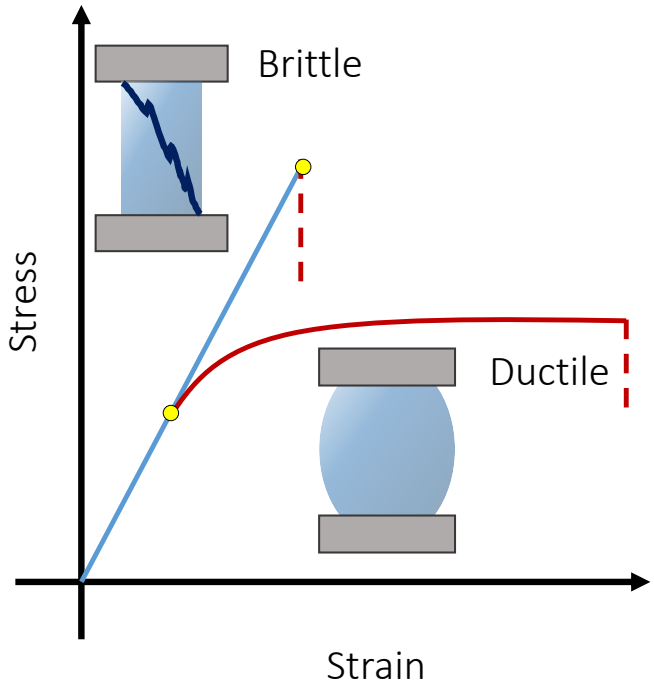

Figure 13: Schematic representation of the stress-strain curves for brittle and ductile behaviors under compression. The blue solid line indicates the linear regime, while the red line the non linear one. The yellow dots are guide lines for the eye at the transition between the two regions.

Petekidis.

Also relevant for this thesis is the investigation of the yielding of colloidal gels under compressive loads. For example, Miller et al., Green and Boger, Channell et al. rationalized the scaling of the yielding compressive stress with the volume fraction for a wide variety of aggregated suspensions [Miller et al. (1996); Green and Boger (1997); Channell et al. (2000)]. As for shear rheology, the authors found that the volume fraction and the yielding stress are related by a power law dependence: the higher ϕ the higher σ_y.

1.2.2 Brittle-to-ductile transition

1.2.2.1 Scientific Context

One objective of this thesis concerns the investigation of the brittle-to-ductile (BTD) transition in colloidal gels. The transition from a brittle to a ductile behavior is encountered in many fields of material science, e.g. for metals [Pineau et al. (2016)], rocks [Wong and Baud (2012)], polymers [Jang et al. (1984)], and many others.

Usually, when a material is compressed by using a 'universal testing machine' (UTM), the stress-strain curve is characterized by two regimes. At small strain, in the linear regime, the stress is proportional to the strain. At larger strain the stress-strain relationships deviates from linearity and becomes more complex. In the linear regime the

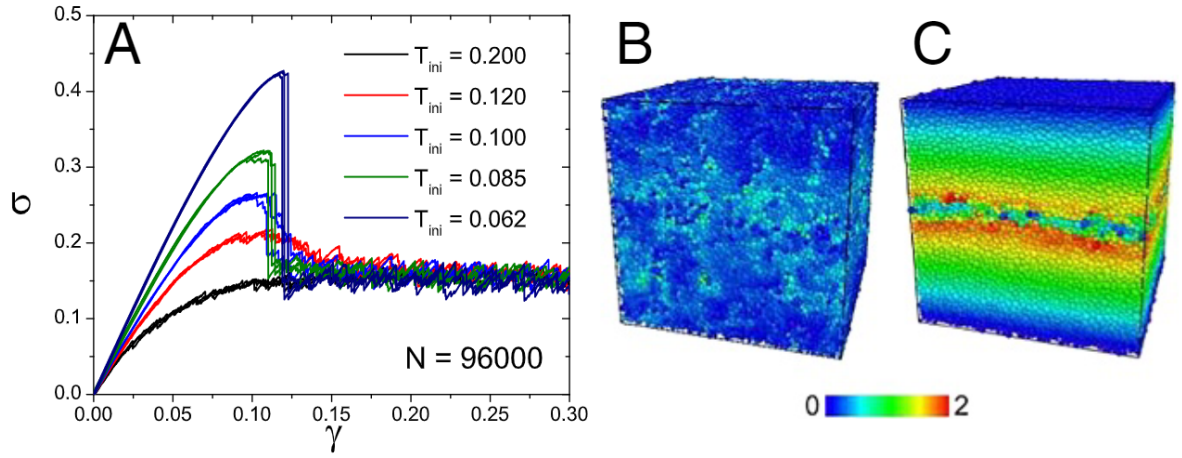

Figure 14: [Ozawa et al. (2018)]: a) Simulated stress strain curves for colloidal glasses formed via different preparation protocols. Low T_{ini} indicates slow (good) annealing, while high T_{ini} indicates fast (poor) annealing. b-c) 3D visualization of the non-affine displacement field at the onset of yielding for a poorly (B) and well (C) annealed colloidal glass, respectively.

deformation is purely elastic, while in the non-linear one the global response of the material is given by the complex interplay between a non-linear elastic response and irreversible plastic events. The difference between brittle and ductile materials is depicted in Fig. 13. A material is brittle when it suddenly yields before rearranging; thus, brittle materials fail within the linear regime. A ductile material instead, shows significant plastic events before failing; thus, its stress-strain curve is characterized by a wide non-linear regime. Moreover, the yielding may be a blend of two behaviors: according to the shape of the stress-strain, the yielding is then categorized as ductile-like or brittle-like. Besides the classification of the material based on their yielding behavior, the intimate reason which determines the kind of yielding behavior attracts a great research effort. Of particular interest is finding the key parameters which control a brittle-to-ductile transition in the yielding of materials.

In the last years, the brittle-to-ductile transition started to become a question of interest even in the framework of soft matter, especially jammed and glassy materials. In particular, many theoretical studies based on numerical simulations have been performed on jammed colloidal systems [Lu et al. (2021); Barlow et al. (2020); Richard et al. (2020); Nicolas et al. (2018); Baggioli et al. (2021); Singh et al. (2020)]. Among them, the work by Ozawa et al. gave an important insight on the problem [Ozawa et al. (2018)]. In this work, the authors investigated the yielding of glasses annealed according to different protocols, leading to samples with tunable heterogeneity (the faster the glass has been annealed, the more heterogeneous its structure). The stress-strain curves are shown in Fig. 14a for samples sheared at a constant quasi-static shear rate. Well annealed glass (in the legend labelled by $T_{ini} = 0.062$) show a marked stress overshoot when reaching the

yielding strain, typical of a brittle failure. As the annealing becomes poorer, the stress overshoot becomes less marked. Finally the poorly annealed glass ($T_{ini} = 0.2$) displays a smooth yielding, with the stress that plateaus after an initial growth.

Interestingly, the authors found that the macroscopic behavior of the curves is directly related to the microscopic non-affine displacements. In the poorly annealed glass the non-affine displacements span homogeneously the whole sample (Fig. 14b), in contrast with the well annealed glass in which a shear banding structure characterize the yielding at the microscopic level (Fig. 14c). This finding suggests that, by playing with the microscopic sample heterogeneity it is possible to tune the yielding of a glass.

1.2.2.2 Objectives

Despite these insightful theoretical works, a clear direct connection to experiments is still missing. Indeed, to the beast of our knowledge, no evidence of a brittle to ductile failure has been observed for soft material in shear rheology. This might be due to stress inhomogeneities at the sample plate interface or to the difficulty in reproducing a quasi-static shear deformation.

In this thesis, we propose a new experimental method to investigate the brittle-to-ductile transition of colloidal gels. To do so, we will use beads of colloidal gels, whose yielding is induced by imposing an uniaxial compression. This experimental configuration will allow us to perform experiments with a geometry closer to the UTM , as compared to shear rheology.

1.2.3 Drying of Colloidal Gel

1.2.3.1 Scientific Context

Besides shear or uniaxial compression tests, the drying of colloidal gels is another experimental realization of a mechanical perturbation imposed to a colloidal gel, see Chapter 8 of [Brinker and Scherer (2013)] for an exhaustive review.

The drying of amorphous porous materials formed through colloid aggregation is ubiquitous in nature and industry as well, including the food industry [Guiné (2018); van Vliet et al. (2009)], in personal care products [Xing et al. (2016)], clays [Augier et al. (2002)], ceramics [Omatete et al. (1991); Chiu and Cima (1993)] and concrete [Colina and Acker (2000)]. Due to its relevance in many applications, the drying of particulate material has been investigated since the early 30's [Sherwood (1930)]. At the macroscopic level, the drying of a colloidal gel is a two-step process: the first step, during which the gel dries at constant rate, is called the constant rate period (CRP). This period is followed by a second step named falling rate period (FRP), during which the gel does not shrink anymore but keeps loosing weight due to the water evaporation. The mechanism explaining the compaction of the structure is reported in Fig. 15a,b. As the water evaporates the

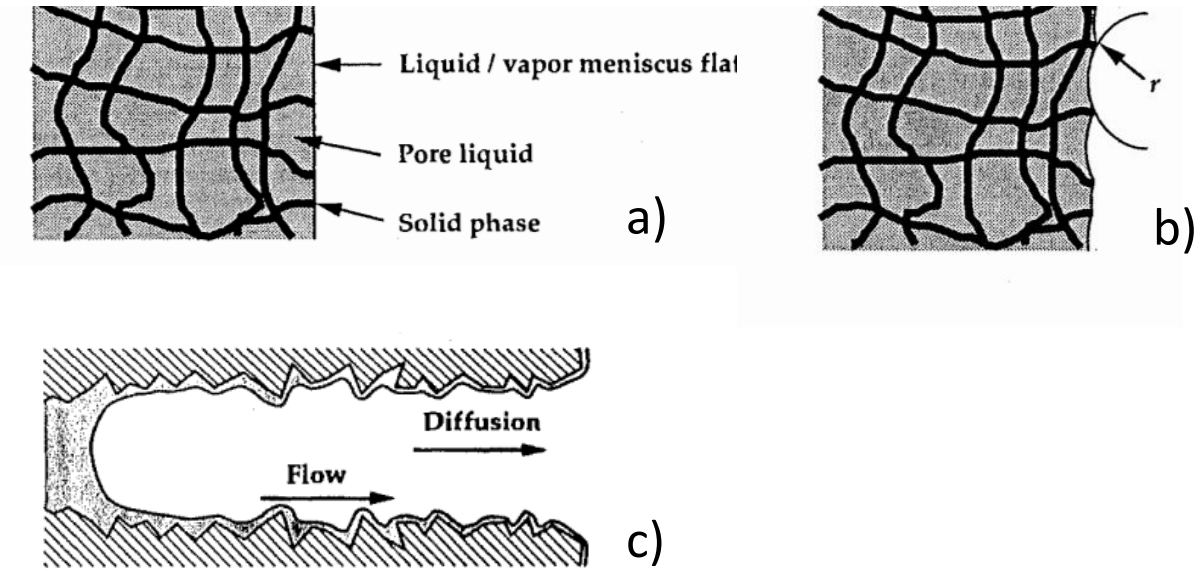

Figure 15: [Brinker and Scherer (2013)]: Schematic illustration of the drying process of a colloidal gel. a) Initially the liquid fills all the pores of the solid network and the gel and the liquid/vapor menisci are flat. b) In the CRP, menisci with curvature $1/r$ form, generating a Laplace pressure which compresses the solid network. c) In the FRP the pores of the structure are not completely filled by liquid and the water diffuses out forming capillary bridges.

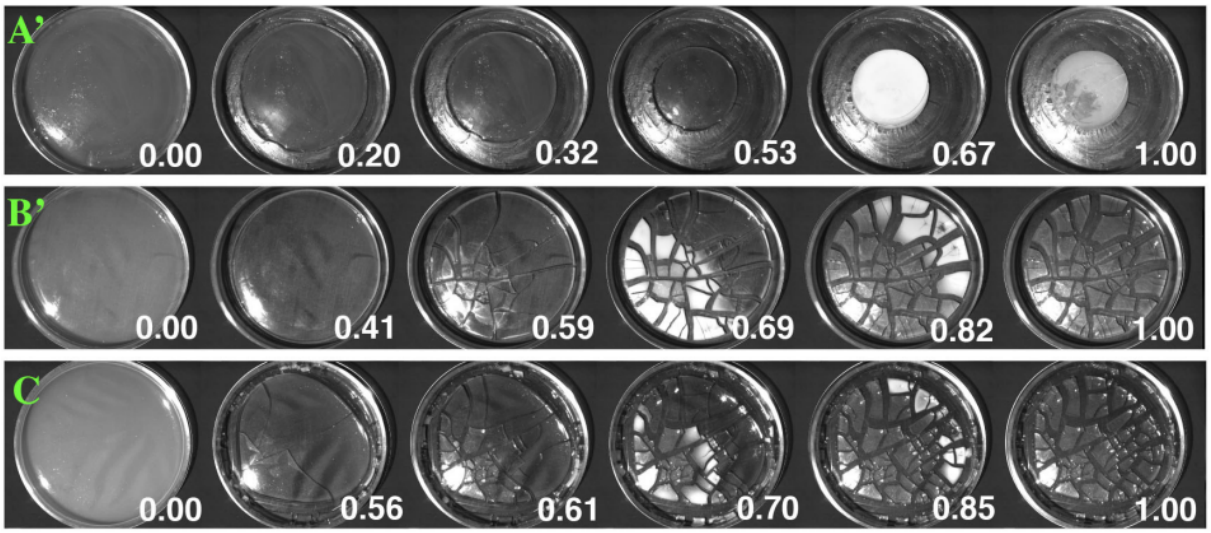

Figure 16: [Thiery et al. (2016)]: top view image sequence of a drying colloidal gel prepared in petri dishes with different surface coatings: A') non-adhering substrate, B') intermediate-adhering substrate, C') strongly adhering substrate. In the three panels the preparation volume fraction of the Ludox HS-40 suspension is $\varphi_p = 5\%$. The white numbers indicate the dimensionless drying time (0 no drying, 1 end of drying process).

pores/liquid menisci reach a finite radius of curvature, thus applying a Laplace pressure that compresses the gel network. This mechanisms holds until the solid network becomes stiff enough to balance the Laplace pressure: when a critical pressure is reached, the gel enters in the FRP regime and its solid structure does not evolve anymore. Figure 15c shows the evaporation in FRP: now the solvent flows through the network by exploiting capillary bridges and evaporates once reaching the exterior of the gel.

When the exterior of the gel shrinks faster than the core, tensile stresses arises leading to the failure of the gel. Indeed, drying often causes crack formation [Chiu and Cima (1993); Lakshmikantha et al. (2009); Goehring et al. (2010)], bending of the surface [Ogawa et al. (2020)] or delamination [Sarkar and Tirumkudulu (2011)]. Recent works done by Thiery et al. have deeply investigated the role of surface adhesion in the fate of the drying gel [Thiery et al. (2015, 2016)] using colloidal silica gels at a fixed preparation volume fraction $\varphi_p = 10\%$, into petri glass dishes. To vary the adhesion between the gels and the substrate, three different kind of petri dish have been used. High adhesion is obtained by using the non-treated glass. To lower the adhesion two kinds of coatings have been applied: a fluorinated grease (KRYTOX 205 from Dupont) lead to a very low adhesion of the gel, while intermediate adhesion properties have been achieved by coating with trichlorododecyl silane. Once the gel is formed, the drying is conducted at room temperature, $20 \pm 0.2°$ C, by imposing a constant uniaxial air-flux. The results of this experiment are shown in Fig. 16. When the adhesion between the sample and the wall is low the gel shrinks without macroscopic cracks, until becoming white at the onset of the FRP regime. By contrast, for intermediate/high adhesion with the surface, the drying

is characterized by many cracking events: the higher the adhesion the earlier the cracks appear. The cracking-free drying obtained with low surface adhesion is for us particularly interesting, since it allows one to reproduce a system which is undergoing an homogeneous compaction.

1.2.3.2 Objectives

Despite many work studied the drying of colloidal gel at a macroscopic level, experiments investigating this phenomenon at the microscopic scale are scarce. For this reason, a second goal of this thesis is the microscopic investigation of the structural rearrangements of the network of a colloidal gel due to the compression during the drying process. We aim at achieving an homogeneous drying in which the spurious effects given by the adhesion between the sample and the surface are minimized. To this end, we will use beads of colloidal gel and dry them on top of a hydrophobic surface. Once obtained a homogeneous isotropic drying, we shall investigate the compaction by using DLS, X-ray scattering and uniaxial compression to probe the phenomenon at a microscopic level.

1.3 Drying Drops of Colloidal Suspensions

In Sec. 1.1.2 of this chapter we have described how the colloidal volume fraction plays an important role on the state of a system comprising repulsive colloids. An extremely interesting situation where the packing of colloids rules the phenomenology of the system is the drying of a suspension of repulsive colloids, which we briefly review in this section.

1.3.0.1 State of the art

The general picture underlying the drying of a colloidal suspension is sketched in Fig. 17: when a drop of colloidal suspension dries, due to the loss of solvent, its surface recedes trapping colloids at the air-liquid interface. In turn, the colloids accumulation leads to the formation of a dense colloidal shell, which may eventually undergo mechanical instabilities, such as buckling [Tsapis et al. (2005); Bamboriya and Tirumkudulu (2023); Miglani and Basu (2015)], air invagination [Basu et al. (2016)], and cracking [Tsapis et al. (2005); Giorgiutti-Dauphiné and Pauchard (2014); Lyu et al. (2019)]. We report in Fig. 18 some examples of colloidal drops undergoing a shape instability during the drying process.

Not only is the drying of drops of colloidal suspension is an intriguing phenomena from the fundamental point of view, it is also involved in many industrial processes such as inkjet printing or spray drying. Moreover, the drying of colloidal suspensions is also relevant in many biological processes. For example, it has been observed in [Huynh et al.

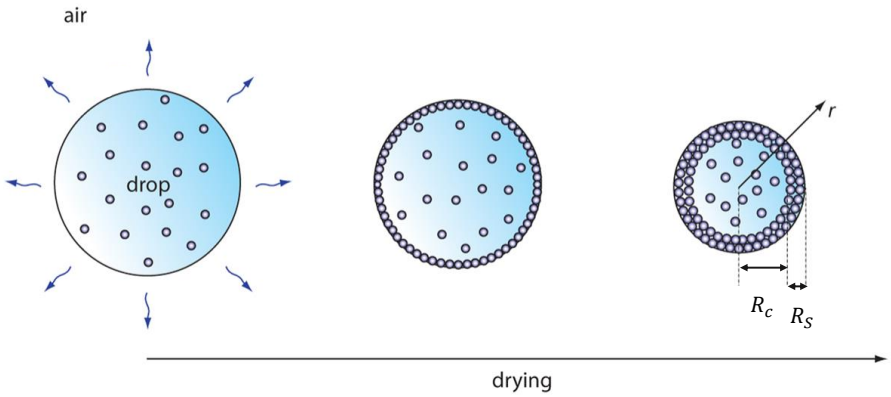

Figure 17: [Iskandar et al. (2002)]: representation of a drop of colloidal suspension during drying. The drop surface, which recedes due to the solvent loss, traps the colloids which form a shell that gets thicker with time.

(2022)] that the virus survival in aerosols occurs through the formation (during drying) of a semi-solid shell formed. Moreover, always in the biological field, a shape instability of a solid shell has been observed during the desiccation of blood drops [Iqbal et al. (2020); Brutin et al. (2011); Sobac and Brutin (2014, 2011)]. Another field of application concerns the production of powdered dairies. Indeed, drops of whey proteins dispersed in water undergo a peculiar shape instability during drying [Adhikari et al. (2007); Sadek et al. (2013); Schuck et al. (2016)]. Finally, the drying of colloidal suspensions is also widely used in the production of functional supraparticles for catalysis, photonics, or sensing applications [Liu et al. (2019); Kuncicky and Velev (2008); Marin et al. (2012); Sperling et al. (2014); Sekido et al. (2017)]

1.3.0.2 The Péclet Number

In the framework of evaporating drops, one defines the Péclet number, Pe, which compares the efficiency of advection to that of diffusion of the colloids. Low Pe implies that the colloids are free to diffuse and they remain homogeneously distributed over the whole volume of the drop during drying. By contrast, at high Pe advection dominates and the colloids are trapped at the liquid-air interface, leading to the formation of a shell.

In this framework, Pe is defined as $Pe = \tau_{\text{mix}}/\tau_{\text{ev}}$, where τ_{ev} is the evaporation time of drop and τ_{mix} is the characteristic mixing time. On one hand, τ_{ev}, as firstly proposed by Langmuir , is evaluated by extrapolating the small-t behavior of $R(t)^2$, with $R(t)$ representing the time-dependent radius of a drop with the same solvent but without colloids [Langmuir (1918)]. On the other hand, $\tau_{\text{mix}} = R_0^2/D$, where R_0 is the initial radius of the drop and D is the effective diffusion coefficient of the colloids.

It is important to notice that, when dealing with dilute suspensions D coincides with

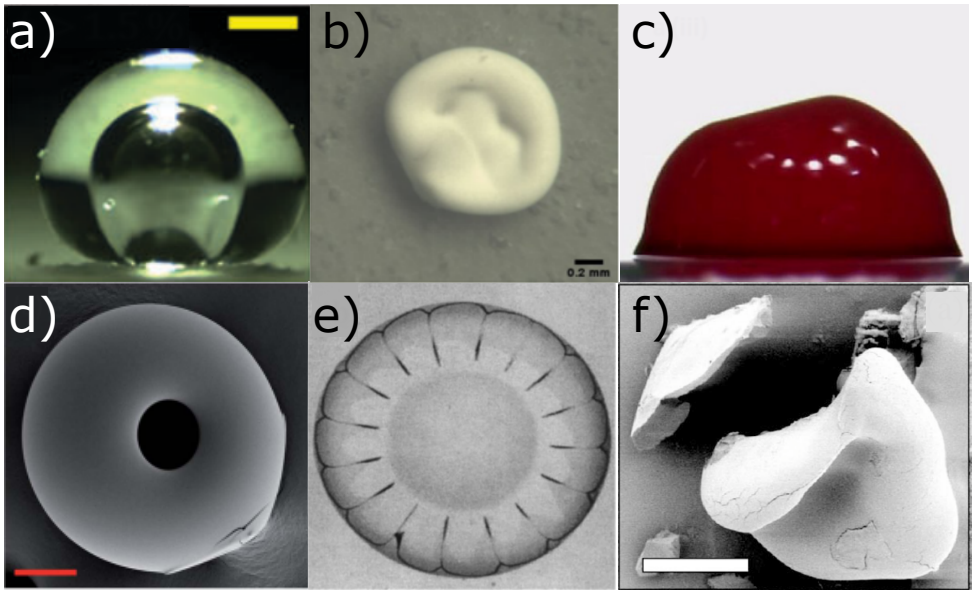

Figure 18: Images of colloidal drops that have undergone a shape instability while drying. a) [Basu et al. (2016)]: side view of a drop of 3μl of silica particles (radius $a = 25$ nm), initial volume fraction $\phi = 0.015$. The drop dried at 24°C and RH=45% on the top of a hydrophobic surface with initial contact angle $\theta_c = 106°$; the scale bar represents 0.5 mm. b) [Bamboriya and Tirumkudulu (2023)]: top view of a drop of 5μl of silica particles (radius $a = 3$ μm); the drop dried at $T = 160$°C on the top of a super-hydrophobic surface; the scale bar represents 0.2 mm. c) [Iqbal et al. (2020)]: optical image of a drop of 2μl of blood dried on the top of an hydrophobic surface at $T = 25$°C and RH=35%. d) [Miglani and Basu (2015)]: Scanning electron microscopy (SEM) top view of a drop with initial diameter 0.5 mm composing silica particles (radius $a = 25$ nm), the drop has dried on the top of a hot surface $T = 150$°C and RH=60%; the scale bar represents 50 μm. e) [Pauchard et al. (1999)]:top view of a drop with initial diameter 4mm composing silica nanoparticles (radius $a = 15$nm), the drop dried on the top of a hydrophobic surface with initial contact angle $\theta_c = 40°$. f) [Tsapis et al. (2005)]: SEM image of a drop with initial diameter 2.2 mm of polystyrene colloids (radius $a = 85$nm); the drop has dried on top of an hot surface, $T = 200$°C; the scale bar represents 10μm.

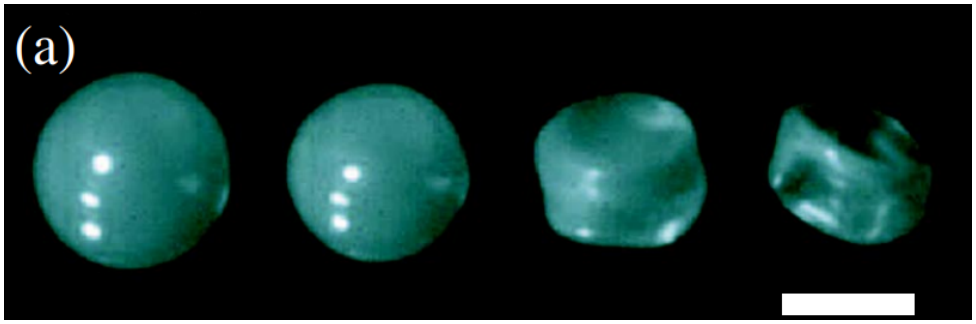

Figure 19: [Tsapis et al. (2005)]: time sequence of a drop of colloidal suspension during drying. The drop was suspended on a hot plate kept at 200°C. The initial particle volume fraction is $\phi = 4 \cdot 10^{-3}$, the nanoparticle radius $a = 85$ nm and the initial radius of the drop $R_i = 1.3$ mm. Adjacent snapshots are separated by 1.5 s. The scale bar represents 0.5 mm.

the single particle diffusion coefficient given by the Stokes Einstein equation, $D = \frac{k_b T}{6\pi\eta a}$. However, for concentrated system, due to particles interaction, the diffusion coefficient may be drastically smaller than that in the dilute regime [Philippe et al. (2018); Sobac et al. (2020)]. Thus, the high Pe regime may be reached by decreasing τ_{ev} by fastening the rate (increasing the temperature or lowering the relative humidity), or by reducing the particle mobility, by increasing the particle volume fraction or using larger particles.

1.3.0.3 Onset of Buckling in Drying Droplets of Colloidal Suspensions

The seminal work by Tsapis et al. explained for the first time the onset of buckling of drying colloidal drops in terms of the microscopic colloidal interactions [Tsapis et al. (2005)]. In this work, the authors used polystyrene spherical nanoparticles with two different diameters, 85 nm and 1000 nm. The nanoparticles were suspended in water at various volume fractions, from $\phi = 10^{-4}$ up to $\phi = 10^{-2}$. To induce a fast drying, the drops were levitated over a hot surface (200°C), using the Leidenfrost effect. In such experimental configurations, $Pe \sim 10^4$. During drying, the authors observed that the colloidal drops were first shrinking isotropically before undergoing a sudden buckling transition, see Fig. 19. Based on the general scenario of Fig 17, Tsapis et al. schematized the drop at the onset of buckling as a core-shell structure composed of a Brownian core where the local volume fraction is the same as the initial one and a dense shell. To estimate the thickness of the shell they measured the radius of the drop (only before the onset of buckling), and they extracted the thickness of the shell h through mass conservation:

$$\frac{h}{R} = 1 - \left[\frac{\phi_s - \phi_i (R_i/R)^3}{\phi_s - \phi_i}\right]^{1/3} \tag{1.13}$$

where R and R_i are the radius of the drop at the onset of bukling and at the beginning of drying, while ϕ_i and ϕ_s are the volume fraction of the core and of the shell respectively.

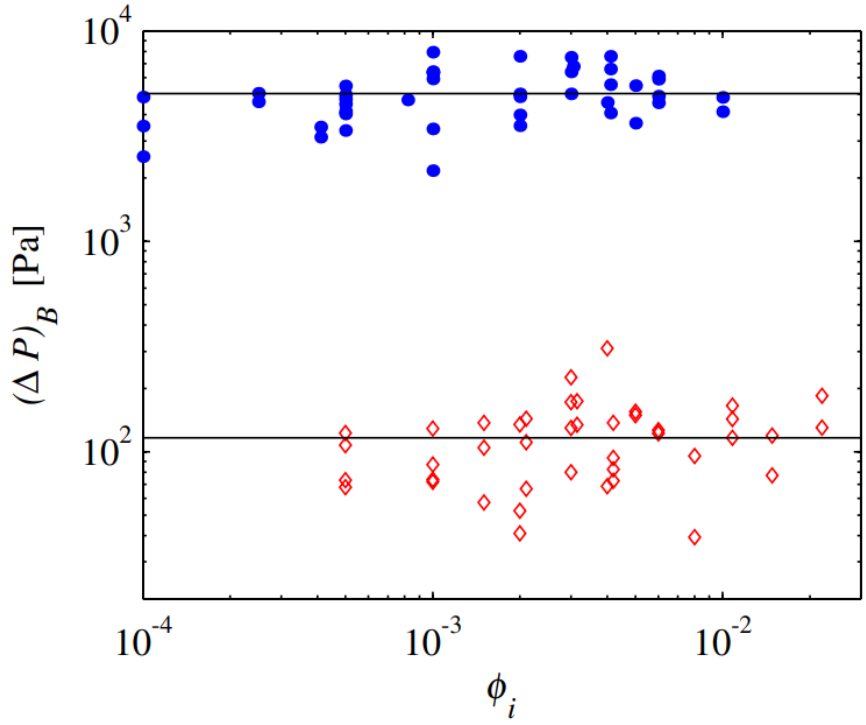

Figure 20: [Tsapis et al. (2005)]: pressure drop as a function of the initial volume fraction at the onset of buckling. Blue filled circles and red empty diamonds correspond to particles of radius $a = 85$ nm and $a = 1000$ nm, respectively.

Since they were not accessible experimentally, to solve the equation, the authors had to make assumptions concerning the values of ϕ_i and ϕ_s. The volume fraction in the core ϕ_i was assumed to be equal to the initial volume fraction in the drop, while the volume fraction in the shell was that of random close packing, e.g. $\phi_s = \phi_{\text{rcp}} \approx 0.64$ for spherical, monodisperse particles. Interestingly, Tsapis et al. managed to estimate the stress threshold necessary for the shell to buckle. To do so, they modeled the shell as a porous medium and, by using Darcy's law, they estimated the pressure difference ΔP required to drive fluid flow through the shell:

$$\Delta P = \frac{\eta h J}{k} \tag{1.14}$$

where η is the fluid viscosity, h the thickness of the shell, $J = -dR/dt$ the volumetric flux of fluid through the shell, and k the permeability of the shell. The permeability is modeled with the Carmen-Kozeny relation: $k = \frac{1}{45}\frac{(1-\phi_s)^3}{\phi_s^2}a^2$, where a is the particle size. Remarkably, as shown in Fig. 20, the authors found (for each particle size) that at the onset of buckling the pressure drop does not depend on the initial volume fraction in the drop, thus indicating the existence of a critical pressure ΔP_B at the onset of buckling. The authors suggested that the crossover between a viscous to an elastic behavior of the shell is driven by a critical stress. Moreover, they considered the capillary forces acting on

the particles at the air/liquid interface, $F = \pi a^2 \Delta P$, as being responsible for the particle aggregation. Accordingly, they calculated the magnitude of these capillary forces and they compared them with the maximum repulsive force between particles through [Jacob and Israelachvili (1992)]. Remarkably, they found that the capillary forces and the repulsive one had the same volume fraction dependence and the same order of magnitude. Thus, Tsapis et al. showed that the onset of buckling is initiated when capillary forces push the particles close enough to overcome the repulsive interactions leading to the irreversible particle aggregation due to van der Waals attraction. In this scenario, the shell is a porous solid formed by permanently aggregated colloids, and it buckles since it can not accommodate any change in volume. However, it is important to recall that the authors did not measure directly key microscopic quantities such as the thickness of the shell or its volume fraction.

This work has been widely recognized by the community, and many works investigating experimentally [Lintingre et al. (2015); Sugiyama et al. (2006); Marty and Tsapis (2008); Miglani and Basu (2015); Bamboriya and Tirumkudulu (2023)] and theoretically [Tirumkudulu (2018); Sobac et al. (2019)] different facets of the drying of colloidal suspension, interpreted their results based on this physical scenario.

1.3.0.4 Different experimental conditions

Despite being key in the framework of drying colloidal drops, the work done by Tsapis et al. did not explore many experimental conditions. Indeed, as presented in the previous section, the authors only considered drops characterized by a low initial volume fraction ($\phi_i < 2\%$) suspended on hot surfaces, drying at extremely high evaporation rates. However, over the years, researches have investigated the drying of drops of colloidal suspensions in many experimental configurations. As presented in a review by Sadek et al., the three main experimental configurations involved in this type of study are: levitating, free-flying and sessile drops [Sadek et al. (2015)]. The experiments concerning the levitating drops are performed either by using the Liedenfrost effect [Tsapis et al. (2005)] or by using acoustic levitation [Chen et al. (2022)]. The free flying technique, first used by Alexander and Judson King, consists of generating with a syringe a free-falling droplet in a controlled air stream [Alexander and Judson King (1985)]. However, despite the different geometry, parameters such as drying rate or initial volume fraction of the colloids are similar to those for levitating drops. By contrast, the sessile drop technique, which consists in drying a drop deposited on a super-hydrophobic/hydrophobic surface, has been privileged for studying drops drying at a slow rate and with high colloidal volume fraction.

For example, Basu et al. showed how the shape instability is influenced by the initial particle volume fraction and contact angle [Basu et al. (2016)] (see Fig. 21). In this work the authors used drops of silica particles (radius $a = 25$ nm) suspended in water in a

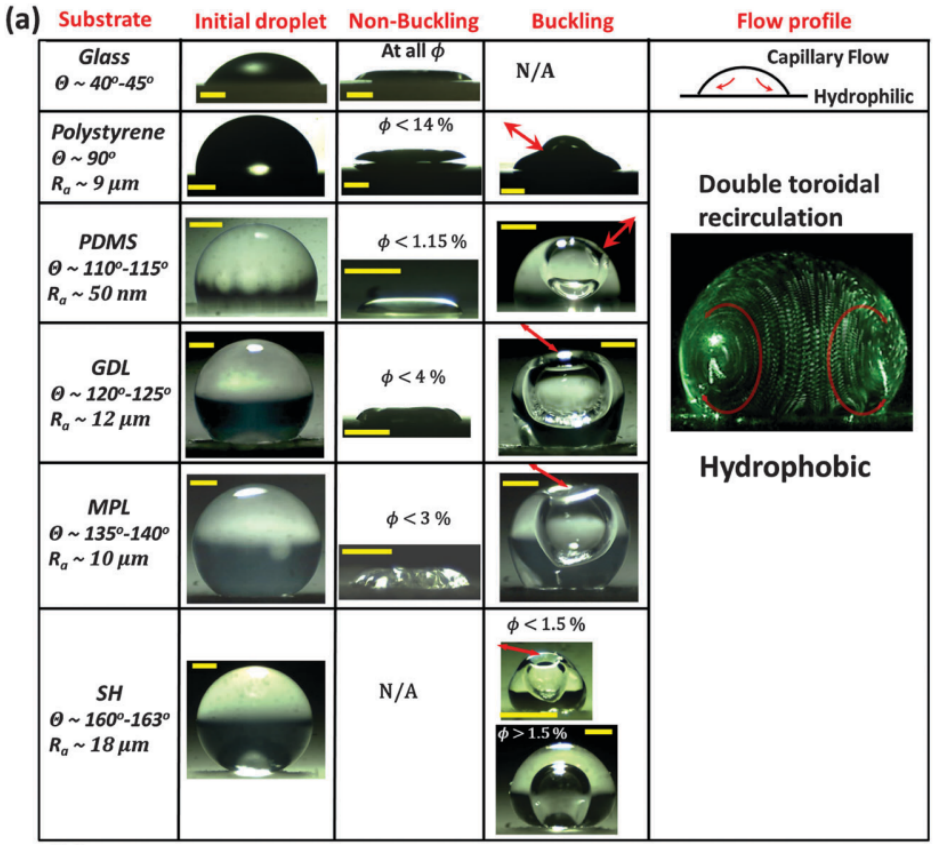

Figure 21: [Basu et al. (2016)]: Table of dried drops of colloidal suspensions in various experimental conditions. the colloids are silica nanoparticles (radius $a = 25$ nm). The authors changed the substrates and the initial solid volume fraction. The first colum indicates the substrate: PDMS, GDL, MPL and SH stand for polydimethylsiloxane, gas diffusion layer, micro porous layer and super-hydrophobic surface, respectively. The second column shows the drops just after deposition, the third column shows the shape for non-buckling drops, and the fourth column the buckled ones. The last column displays the flow profiles inside a drying drop.

broad range of volume fractions ($\phi = 0.0015 - 0.15$), drying them at ambient temperature, T =23°C. Similar experimental conditions were also used by Bansal et al. [Bansal et al. (2015)]. In both works, the authors stated that the buckling of the shell is initiated by particle aggregation due to capillary pressure. However, in these conditions, it is not straightforward that the physical scenario behind the shape instability as proposed by Tsapis et al. applies. For example, when lowering the drying rate by evaporating at room temperature, the time scales involved in the shell formation are orders of magnitude slower compared to timescales involved in drying on hot plates. Moreover, it is widely acknowledged that by increasing the solid volume fraction of colloidal suspensions one alters the visco-elastic properties of the systems [Chong et al. (1971); Koumakis et al. (2012); Guy et al. (2015)]. Finally, even the contact angle that the drop forms with the surface alters the shape instability of the shell. Indeed, it has been widely studied how the contact angle influences the internal flows of the drop, see [Gelderblom et al. (2022); Wilson and D'Ambrosio (2023)] for complete reviews.

These works point out the necessity of a wider investigation of the physical scenario underneath the buckling of the shell of drying colloidal drops.

1.3.0.5 Microscopic investigations

As mentioned in [Basu et al. (2016)], in the framework of the drying colloidal drops, one of the key challenges is measuring microscopic quantities such as the thickness of the shell, the volume fraction of colloids and their dynamics while the drop dries. To get these information, various experiments have been performed over the last years.

A first experiment that managed to measure the shell thickness during drying was reported by Sperling et al. [Sperling et al. (2016)]. In this work the authors used fluorescent confocal microscopy to track the shell formation during drying. As reported in Fig. 22, a drop of fumed silica dispersed in water was deposited on top of a glass slide. The fluorescent intensity was measured by vertically scanning a side of the drop. Thanks to this approach the authors managed to measure the thickness of the shell up to 18 min after the beginning of drying. However, they could not follow the entire evolution of the process: in particular the thickness of the shell at the onset of buckling remained unknown. Moreover, they could not estimate the volume fraction of particles in the shell. As a consequence, this work, despite its interest, could not provide a clear explanation of the shape instability of the shell.

Another approach consists in performing in situ X-ray scattering experiment on a drying colloidal drop which hangs on a narrow tip [Sen et al. (2014)]. In this case, the authors used a drop of 1 μl of ludox SM-30 suspension (silica particles with radius $a = 3$ nm suspended in water) measured at room temperature. Moreover, vary the Pe, the authors varied the volume fraction of the colloids ($\phi = 0.015$ or $\phi = 0.15$). As sketched in Fig. 23, the authors performed scans along the x axis during the drying. In this way they

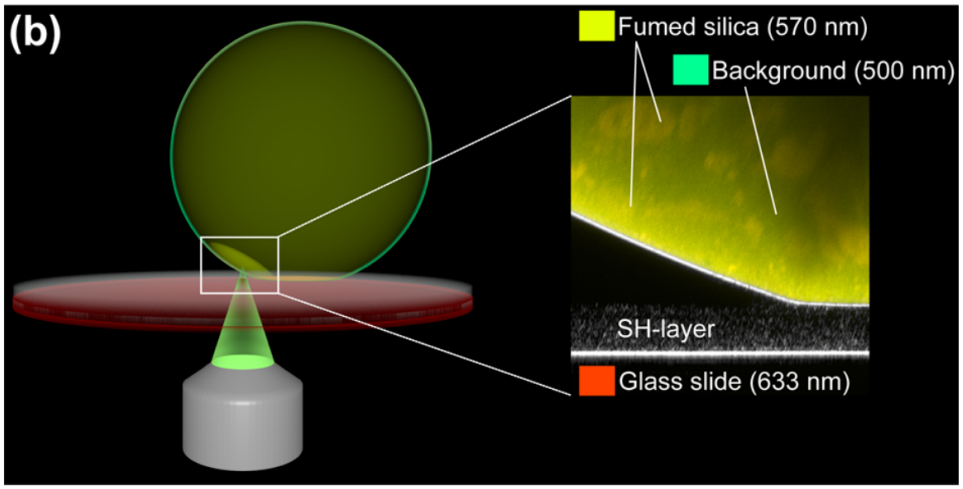

Figure 22: [Sperling et al. (2016)]: Illustration of a the experimental setup used to measure the shell thickness. On the right an overlay of confocal images. The colors correspond to the detected wavelengths: red (633 nm) for reflection and the two fluorescence channels for the background in green (500 nm) and the fumed silica particles in yellow (570 nm).

managed to measure the Porod invariant and made the comparison between the samples of the two volume fractions. We recall that the Porod invariant is a quantity independent of particle concentration and proportional to the molecular mass. Interestingly, as shown in Fig. 23b and c, [Sen et al. (2014)] found different profiles for the two volume fractions. Moreover, thanks to mathematical models, they managed to associate the Porod invariant profile of the drop with $\phi = 0.015$ at an isotropic particle distribution. By contrast, the Porod profile for the sample at $\phi = 0.15$ was related to an anisotropic particle distribution, indicating the formation of a shell. Similar results were also obtained by Bahadur et al. by using the same setup [Bahadur et al. (2015)]. However, due to the very nature of X-rays, even by doing a scan along the x axis, the structural information on the shell structure is always averaged over the z direction. As a consequence, with X-ray the authors could not obtain detailed information on the local shell thickness and colloidal volume fraction, thus preventing them to reach firm conclusions about the origin of the onset of the shape instability of drying colloidal drops.

1.3.0.6 Quasi-2D experiments

Arguably, the most insightful experiments regarding the shape instability in drying drops are the ones performed in a quasi-2D geometry. A classic example of a quasi-2D drop is sketched in Fig. 24a, where Boulogne et al. confined a drop in between two glass slides to observe the drying process with an optical microscope [Boulogne et al. (2013)]. Thanks to this setup, the authors imaged the drop over the entire drying process. As seen in Fig. 24b, quasi-2D drops follow qualitatively the same evolution as the 3D ones: they first shrink homogeneously, but eventually they undergo a shape instability. Moreover,

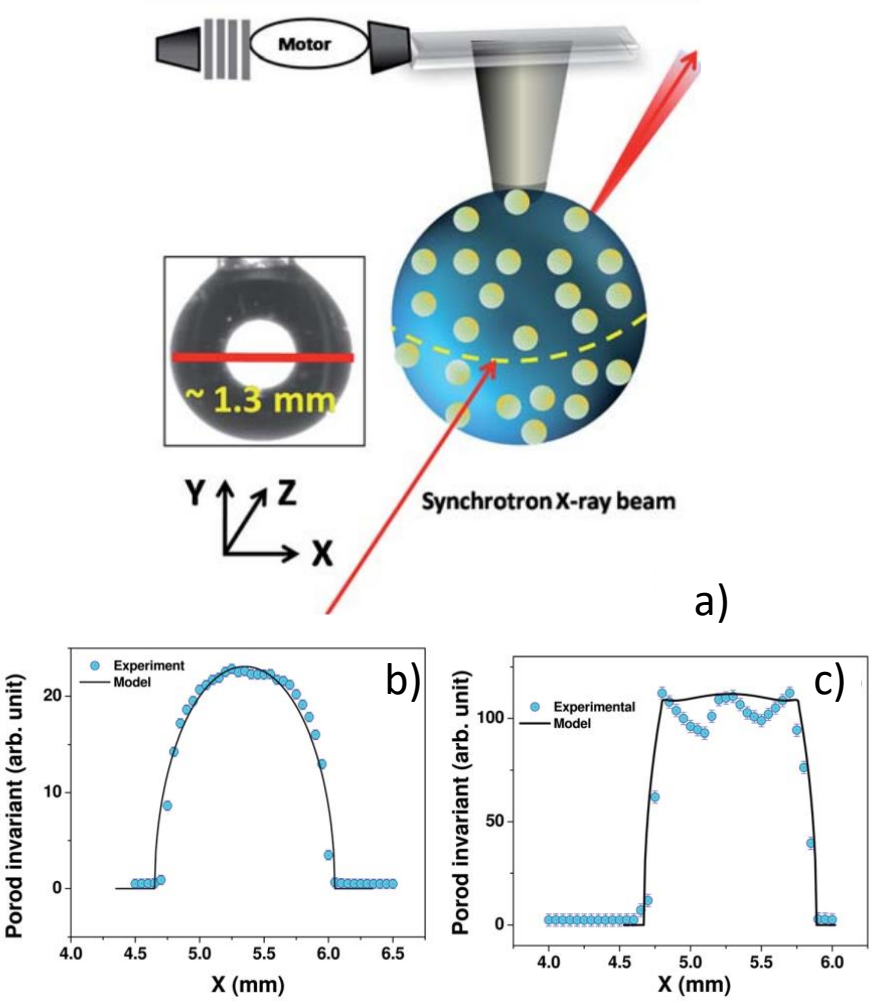

Figure 23: [Sen et al. (2014)]: a) Sketch of the experimental configuration: a thin Xray beam (beam size 32μm (H) x 23μm (V)) hits the drop of colloidal suspension in its equatorial plane. In the inset an optical image of a hanging droplet, the scale bar represents 1.3mm. b) Comparison between the experimental Porod invariant (blue circles) and the theoretical one (black solid line) for the isotropic case of a drop without a shell. c) Comparison between the experimental Porod invariant (blue circles) and the theoretical one (black solid line) for the anisotropic case of a drop with a solid shell.

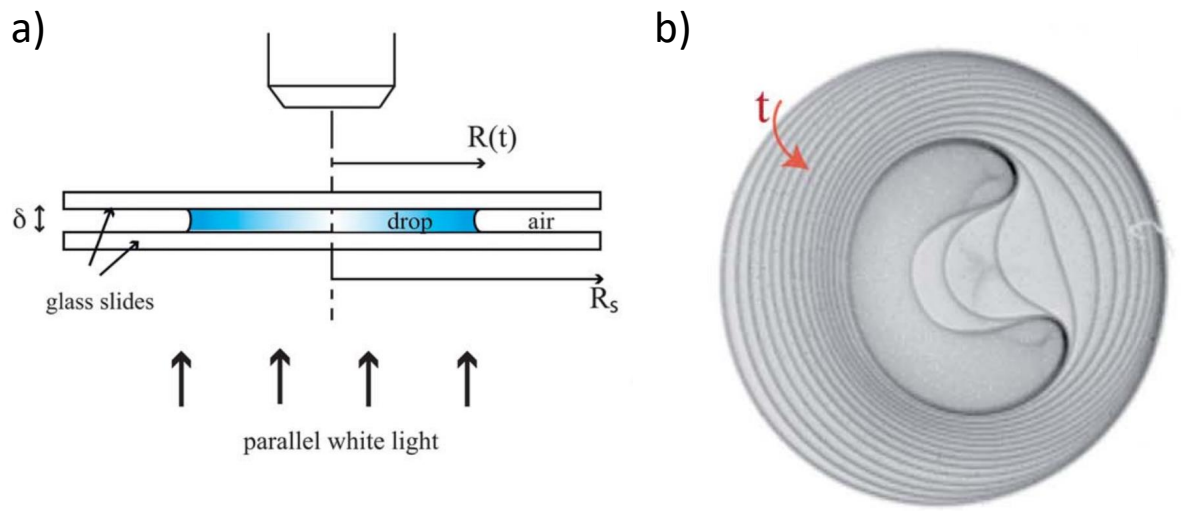

Figure 24: [Boulogne et al. (2013)]: a) Side view sketch of the experimental setup: a drop of solution, confined between two circular glass slides, dries while being illuminated by white light. An optical microscope is placed on the top of the glass slides. c) Superposition of images of the drop during the drying process. The rate of acquisition is 1 image/minute

thanks to the simpler geometry they managed to directly visualize and measure the shell thickness. The information on the shell thickness was used to rationalize the final shape of the drop. However, the authors didn't access experimentally the volume fraction of the suspension in the drop. Accordingly, they assumed the shell volume fraction to be $\phi_{\text{rcp}} \approx 0.64$, thus modelling the shell as a permanently aggregated porous solid.

An evolution of the quasi-2D geometry has been proposed by Bouchaudy and Salmon [Bouchaudy and Salmon (2019)]. A sketch of their setup is presented in Fig. 25a. Compared to the setup in [Boulogne et al. (2013)], Bouchaudy and Salmon coupled to the imaging system a micro-balance, which allowed them to measure the evolution of the mass during drying. Here silica nanoparticles of radius $a = 11$ nm dispersed in water at volume fraction $\phi = 0.24$ are used for the experiments. In addition, fluorescent tracers particles were added, allowing them to reconstruct the particles trajectory, as shown in Fig. 25b. Moreover, from the mass measurement coupled with the measurements of the area of the drop, the authors estimated the mechanical stresses present in the shell during the drying process, see Fig. 25c. Interestingly they found that the stresses build up in the drop much before the onset of buckling. This becomes particularly interesting when compared with the local volume fraction of colloids. Indeed, through Raman spectroscopy, the authors managed to measure the colloids concentration with space resolution, see Fig. 25d. Remarkably, they found that the volume fraction increases in the whole drop, reaching values lower than ϕ_{rcp} but higher than the critical value φ_c of the glass transition.

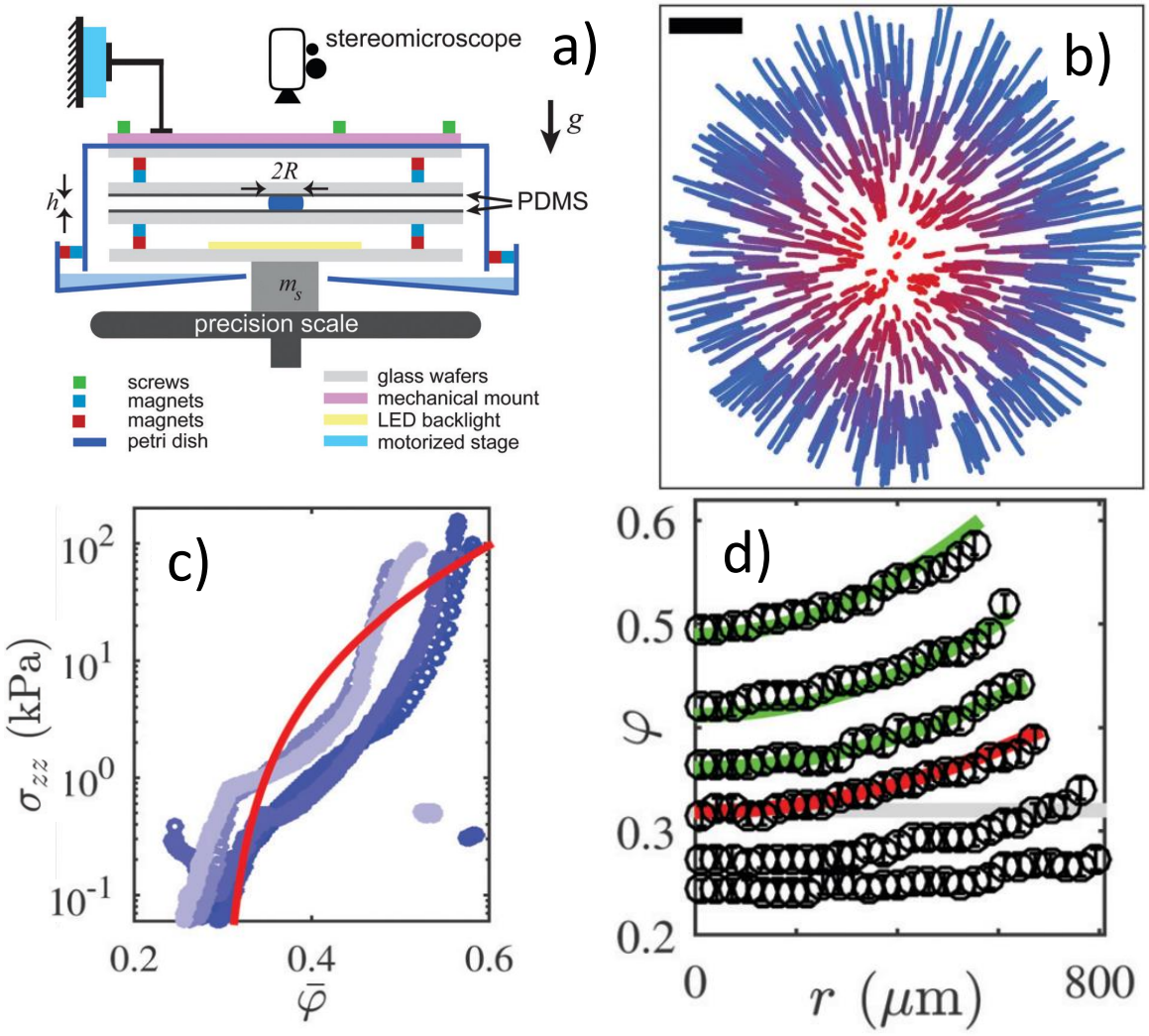

Figure 25: [Bouchaudy and Salmon (2019)]: a) Schematic side view of the setup used to measure the stresses induced by the drying of confined drops. The drop confined in between two PDMS slides which are kept at a fixed distance h while a balance measure the effective weight due to the build-up of stresses during the drying of the drop. b) Trajectories of the fluorescent particles before shape instability. The authors used a color code for the initial radial position of each tracer. The scale bar represents 100 μm. c) Normalized stress as a function of the average volume fraction. d) Time evolution of the volume fraction profiles: the different curves are obtained for $t = 0, 11, 23, 30, 37, 44$ min. The confinement height is $h = 250$ μm. The thick gray line represents the glass transition at $\varphi = 0.32$.

Indeed, as marked by the authors in Fig. 25d with the gray line, the volume fraction gets higher than the critical volume fraction of the glass transition for this system.

Moreover, from Fig. 25d we do not see a clear cut between a core and a shell, but a continuous growth of ϕ from the center of the drop to the periphery. This fact points out that considering the drop as a simple two-phase system composed of a dilute Brownian core and an aggregated shell does not capture the full complexity of the system. Interestingly, the authors stated explicitly in their conclusions, that their results question the general scenario of a shell made of closely packed colloids. Rather,the shell should be regarded as a soft solid in which mechanical stresses arise much before the macroscopic deformation.

Additional information on the drying of quasi 2D drops were given by [Sobac et al. (2020)]. In this work the authors used a Mach–Zehnder interferometer, shown in Fig. 26a, to investigate the phenomena. As for [Bouchaudy and Salmon (2019)], the authors found that the volume fraction is smaller than ϕ_{rcp} , but higher than the critical φ_c of the glass transition, see Fig. 26c. Remarkably, the authors also managed to get the microscopic dynamics of the system. As it is shown in Fig. 26b, the effective diffusivity changes with φ: after a first increase up to $\varphi \sim 0.26$, the effective diffusivity decreases for higher volume fraction due to the crowding of the colloids. Hence, having shown that the volume fraction increases towards the edges (see Fig. 26c), the authors proved that in the shell the dynamics are slower compared to the center.

Interestingly, some of these results are consistent with findings in a theoretical work for a 3D colloidal drop [Sobac et al. (2019)]. In this work, the authors modeled the drying of a spherical drop varying Pe in the range $Pe = 1-100$ by increasing the rate of evaporation. A key result of this work is the volume factor profiles obtained for the different Pe, shown in Fig. 27. Note that for their calculations the authors hypothesized that the shell, at the last stage of drying, has $\phi_{\text{rcp}} \approx 0.64$. Sobac et al. found that for the smallest $Pe = 1$, the evolution of the volume fraction is similar to that of Fig. 25d and Fig. 26c obtained for 2D drops: ϕ increases with time in the whole drop, being slightly higher at the edges. For intermediate $Pe = 10$, a gradient of volume fraction appears with time and, for the last time investigated, the volume fraction in the shell is more than 3 times larger than the one in the core. Finally, for the highest Pe (Pe=100), the system shows a sharp gradient between a core and a shell, with the volume fraction in the core that remains almost unaltered during the process. These finding are extremely interesting: indeed, not only they suggest that the results found for 2D evaporating drops may also apply for the 3D case, but they also show a link between slow and fast evaporating drops. Indeed, according to these results, by lowering the Peclet number, the drop goes from a core shell structure with a Brownian dilute core and an aggregated shell to a homogeneous drop that eventually becomes very concentrated as the drop dries.

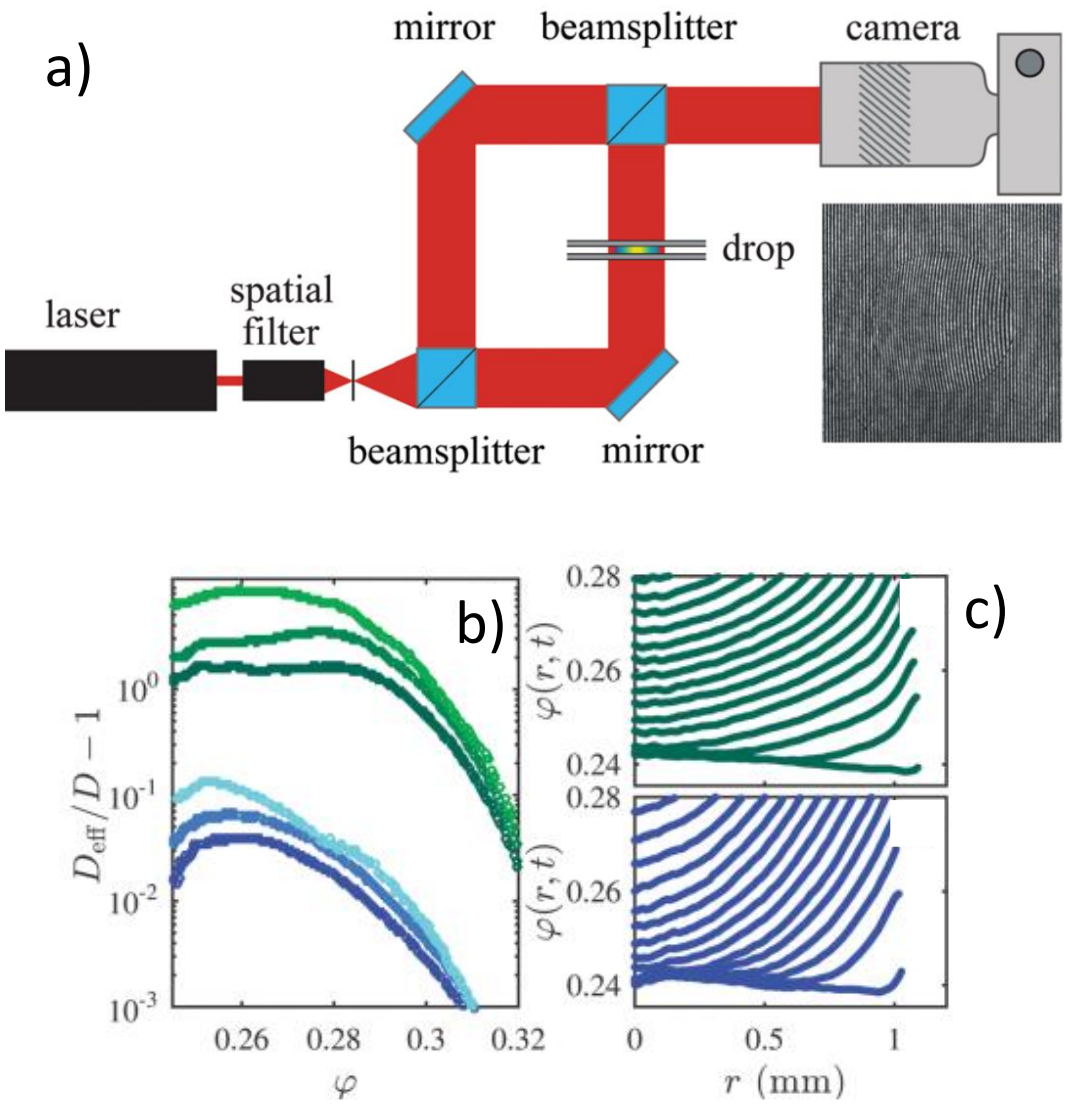

Figure 26: [Sobac et al. (2020)]: a) Sketch of the Mach–Zehnder interferometer setup: a laser is divided in two beams by a beam splitter, one of the two goes directly on a camera while the other passes trough a confined 2d drop that dries. The interference of the two beams forms the pattern on the right from which the microscopic diffusion coefficient of the colloids in the drop is measured. b) Reduced effective diffusivity obtained for two experiments: for both experiments the initial colloidal volume fraction is $\varphi_0 = 0.24$, but the experiments were performed with different confinement heights: $h = 150$ μm (blue) initial radius $R_0 = 1.04$ mm, $Pe = 5.3$ and $h = 300$ μm (green) which implies initial radius $R_0 = 1.11$ mm , $Pe = 5.8$. D_{eff} is computed from the gradient of the concentration profiles. c) volume fraction profiles $\varphi(r,t)$ for $h = 300$ μm (green) and $h = 150$ μm (blue).

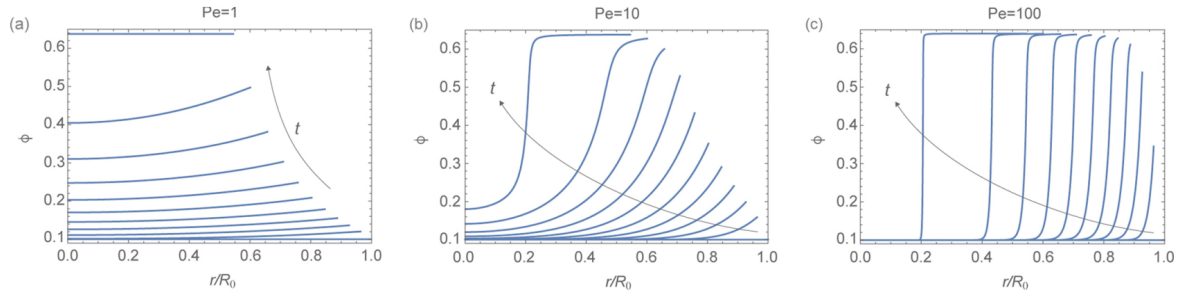

Figure 27: [Sobac et al. (2019)]: Time evolution of the particle volume fraction field inside a 3D drop, for different Péclet numbers: $Pe = 1$, $Pe = 10$, $Pe = 100$ from left to right.

1.3.1 Drying suspensions: our goals

This short review of the literature shows that many questions are still open, namely on the nature of the shell and the buckling of drying colloidal drops. This reason pushed us to investigate the drying of a 3D colloidal drop. In particular, by means of DLS, we wanted to get in-situ structural and dynamical information on the shell that forms during the drying. With such information our goal is to understand the link between the microscopic behavior of the drops and their macroscopic shape instability and to propose a unifying scenario depicting the shape instability of drying colloidal drops.

1.4 Structure of the thesis

This thesis is organized as follows:

- Chapter 2 is dedicated to the description of all the experimental techniques used in our experiments. In particular, Sec. 2.1 describes light scattering experiments: first, in Sec. 2.1.1 we describe the general principles behind static and dynamic light scattering. In Sec. 2.1.2 we then focus on the conventional DLS. In Sec. 2.1.3 we introduce a class of DLS experiments known as multispeckle techniques. In Sec. 2.1.4 we describe a specific multispeckle method application named Photon Correlation Imaging, which is of particular interest for this thesis.

  Section 2.2 is dedicated to X-ray scattering, focusing on the different information that can be gained from these experiments. In Sec. 2.2.4 we describe the X-ray setup we used for the experiments described in Chapter 6.

  In Sec. 2.3 we describe the basic principles and the instrumentation we exploit for the mechanical characterization of the samples. Of particular interest is Sec. 2.3.2, where we focus the attention on uniaxial compression which is widely used to obtain the results in Chapter 5 and 6.

  Sec. 2.4 details the drying protocol that we used in Chapters 6 and 7 to control the

relative humidity in our drying experiments and the preparation of the hydrophobic surface.

- Chapter 3 contains a paper describing the new DLS setup designed for probing microscopic dynamics with space and time resolution on samples with a spherical shape. Together with the technical description of the setup we also present the results of two experiments. The first concerns the measurement of the Brownian motion of a diluted suspension forming a millimetric-size drop and the second is the measurement of the microscopic dynamics of a polymer gel that swells in water. The aim of these experiments is to proof the working principle of our setup and show its versatility in measuring microscopic dynamics within a spherical drop.

- Chapter 4 describes the preparation and the characterization of beads of colloidal gel. Sec. 4.1 is entirely dedicated to the protocol for preparing such beads.

  Sec. 4.2 is devoted to the characterization of the microscopic dynamics, in particular, we exploit the setup described in Chapter 3 to identify the gelation time of the beads and verify that, the quiescent dynamics of the beads do not differ from the ones of bulk samples.

  Sec. 4.3 is dedicated to the analysis of the structure of colloidal gels. Firstly, we present the structures of a gel prepared in standard glass tube, as measured by X-ray scattering. Secondly, we check that the structure of our beads of gel is the same as the one of the gels prepared in bulk.

  Finally, in Sec. 4.4 we compare the mechanical properties of bulk colloidal gels and gel beads. To do so, we characterize the bulk gels by means of shear rheology, while we probe the beads through uniaxial compression.

- Chapter 5 deals with the yielding of beads colloidal gel under uniaxial compression. Firstly, in Sec. 5.1 visually introduce the problem by showing image sequences that characterize the yielding of beads of gel under uniaxial compression. Then in Sec. 5.2.1 we analize in detail the role of the volume fraction in the yielding of beads of colloidal gels, while in Sec. 5.2.2 we investigate the role of the rate of compression.

- Chapter 6 presents the results regarding the drying of beads of colloidal gels. For the case of reading, we first present the most relevant results in Sec. 6.2. Then we show in Sec. 6.4 additional results to support and enrich the scenario discussed in Sec. 6.2. The behavior of our colloidal gels is characterized using a combination of rheology, X-ray scattering and space- and time-resolved DLS.

- Chapter 7 contains the paper: *'A double rigidity transition rules the fate of drying colloidal drops'*. This work is dedicated to the investigation of drops of colloidal suspensions. In particular, by using the setup described in Chapter 3, we rationalize

the role of the microscopic dynamics in the shape instability of drying colloidal drops. Moreover, we propose a unified state diagram that rationalizes the evolution of drops of colloidal suspension during the drying process.

- Chapter 8 contains the perspectives and conclusions of the thesis. In Sec. 8.1 we summarize the main conclusions obtained in this thesis. In Sec. 8.2 we then present some perspectives and new research paths opened by the three main experiments described in Chapters 5,6,7.

Chapter 2

Experimental Methods

2.1 Light scattering

In a nutshell, all scattering experiments are composed by three elements: a sample, a source and a detector. The source, which can be light, X-rays, neutrons or electrons, is chosen according to the features of the sample the experimenter wants to investigate, and in turn the detector is selected according to the light source. In this thesis we use light scattering mainly to investigate dynamic properties of colloidal samples.

2.1.1 Principles of light scattering

In this Section and the following one, we follow [P.N. Pusey, Chapters 1 and 9 in Zemb and Lindner (2002)]. In light scattering (LS) experiments the source is a coherent beam of plane-wave monochromatic light:

$$E_{\mathrm{I}}(\mathbf{r},t) \equiv E_0 \exp\left[i\left(\mathbf{k}_i \cdot \mathbf{r} - \omega t\right)\right] \tag{2.1}$$

where E_0 is the amplitude of the electric field, ω the angular frequency, and $\mathbf{k}_i$ is the wave vector of magnitude $2\pi/\lambda$, where λ is the wave vector in the medium, related to the in-vacuo wave length λ_0 by $\lambda = \lambda_0/n$, with n the refractive index of the medium. Moreover, we consider the incident beam to be polarized, so that both the incident electric field and the scattered one may be treated as scalar quantities

To get an expression of the scattered intensity measured by the detector, we assume, here and in the following, that the so-called Rayleigh-Gans-Debye approximation applies. Such approximation implies that: (i) most photons pass through the sample without being scattered, (ii) a photon may be scattered only once, and (iii) the beam is not distorted by the sample [Zemb and Lindner (2002)]. Moreover we assume that the scattering is quasielastic, meaning that the beam does not exchange energy with the medium, leaving unaltered the magnitude of the out-coming wave-vector: $|\mathbf{k}_o| = |\mathbf{k}_i| = k = 2\pi/\lambda$.

To get an expression for the scattered wave $E_S(\mathbf{R},t)$ collected by a detector located in position $\mathbf{R}$ in the far field, corresponding to a scattering angle θ_S as shown in Fig. 28 , we

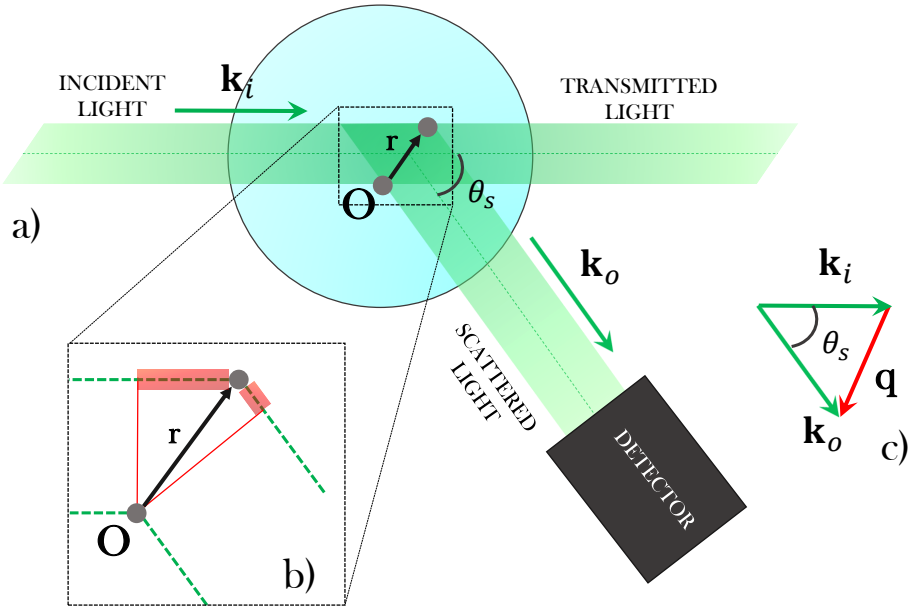

Figure 28: a) Schematic top view of a light scattering experiment: a laser beam illuminates the sample (light blue disk), with an incoming wave vector $\mathbf{k}_i$, and light scattered at a given scattering angle θ_s, and wave vector $\mathbf{k}_o$, is detected in the far field. b) Zoom in the scattering volume, showing two rays scattered by two elements in the sample (gray circles), one at position **O** and the other at position **r**. The red segments show the extra distance travelled by the ray scattered in point **r**. c) Geometric construction of the scattering vector **q**.

apply the Maxwell's equation propagating through a medium [Berne and Pecora (2000)]:

$$E_S(\mathbf{R},t) = -E_0 \frac{\exp[i(kR-\omega t)]}{R} \int_V \frac{k^2}{4\pi} \left[\frac{\varepsilon(\mathbf{r},t)-\varepsilon_0}{\varepsilon_0}\right] \exp(-i\mathbf{q}\cdot\mathbf{r})\mathrm{d}^3 r. \tag{2.2}$$

where $\varepsilon(\mathbf{r},t)$ is the dielectric constant of the medium at time t and position $\mathbf{r}$ with respect to the origin $\mathbf{O}$, ε_0 is the average dielectric constant of the medium, V is the scattering volume, defined as the region of intersection between the incident beam and the field of view of the detector, and $\mathbf{q}$ is the scattering vector defined as $\mathbf{q} = \mathbf{k}_o - \mathbf{k}_i$, which has modulus:

$$q = \frac{4\pi}{\lambda} \sin \frac{\theta_s}{2} \tag{2.3}$$

Equation 2.2 is composed by three terms. The first term is a prefactor with the features of the incident wave (Eq. 2.1). The second term is the propagation of a spherical wave. The third term is the spatial Fourier transform of the dielectric constant fluctuations. The term $\exp(-i\mathbf{q}\cdot\mathbf{r})$ in the integral of Eq. 2.2 accounts for the fact that the light scattered by an element in position $\mathbf{r}$ is shifted in phase compared to the light scattered by an element in $\mathbf{O}$, see Fig. 28b. It is worth to underline that, for a perfectly homogeneous material, the local dielectric constant $\varepsilon(\mathbf{r},t)$ is equal to ε_0 in every point at every time, implying that the scattered wave $E_S(\mathbf{R},t) = 0$. Equation 2.2shows that in light scattering, the physical origin of the scattering signal are local fluctuations of the dielectric constant. The first term in the integral can be written in a general way as:

$$\frac{k^2}{4\pi}\left[\frac{\varepsilon(\mathbf{r},t)-\varepsilon_0}{\varepsilon_0}\right] = \Delta\rho(\mathbf{r},t) \tag{2.4}$$

where the quantity $\Delta\rho(\mathbf{r},t)$ can be seen as a scattering length density. In such a way, as we will discuss in Sec. 2.2 with the appropriate identification, the same formalism applies to X-ray scattering, with an appropriate definition of $\Delta\rho(\mathbf{r},t)$.

In soft matter, it is particularly useful to extend Eq. 2.2 to the case of a sample composed of discrete scattering objects suspended in a liquid. The scattering objects could be polymer, micelles or colloids, in the form of a dilute suspension or possibly as a jammed material such as a glass or a gel. We consider N particles suspended in a scattering volume V. The positions of the center of mass of the j-th particle is described by the variable $\mathbf{R}_j(t)$, while r_j is the position of a volume element dV_j within the j-th particle, with respect to its center of mass. Regarding Eq. 2.2 we need now to sum all the different contributions coming from the different particles [Zemb and Lindner (2002)]:

$$\begin{aligned} E_S(\mathbf{R},t) = &- E_0 \frac{\exp[i(kR-\omega t)]}{R} \\ &\times \sum_j \left\{ \int_{V_j} \Delta\rho(\mathbf{r}_j,t) \exp\left(-i\mathbf{q}\cdot\mathbf{r}_j\right) \mathrm{d}^3 r_j \right\} \exp\left[-i\mathbf{q}\cdot\mathbf{R}_j(t)\right] \end{aligned} \tag{2.5}$$

where we define the term in brackets as the scattering length of particle j:

$$b_j(\mathbf{q},t) = \int_{V_j} \Delta\rho\left(\mathbf{r}_j,t\right) \exp\left(-i\mathbf{q}\cdot\mathbf{r}_j\right) \mathrm{d}^3 r_j \tag{2.6}$$

This quantity, which is the spatial Fourier transform of the scattering length density, describes the distribution of scattering material within each particle. In such a way, Eq. 2.5 reduces to:

$$E_S(\mathbf{R},t) = -E_0 \frac{\exp[i(kR-\omega t)]}{R} \sum_{j=1}^{N} b_j(\mathbf{q},t) \exp\left[-i\mathbf{q}\cdot\mathbf{R}_j(t)\right] \tag{2.7}$$

For a sample containing discrete scattering particles, the total scattered electric field is due to the interference of the spherical waves coming from the individual particles. The phase and amplitude of these waves depends on the scattering length $b_j(\mathbf{q},t)$ and the phase factor $\exp\left[-i\mathbf{q}\cdot\mathbf{R}_j(t)\right]$, which depends on the instantaneous position of the particle. From now on we will express the scattered field E_S as a function of the scattering vector $\mathbf{q}$ instead of the position $\mathbf{R}$ of the detector. These two quantities are equivalent since $\mathbf{R}$ is in the direction of $\mathbf{k}_o$ and the scattering vector is related to $\mathbf{k}_o$ by $\mathbf{q} = \mathbf{k}_o - \mathbf{k}_i$.

Moreover, in scattering experiments the physical quantity that is measured is not the electric scattered field $E_S(\mathbf{q},t)$, but rather the scattered intensity $I(\mathbf{q})$ seen at a scattering vector $\mathbf{q}$. Since $I(\mathbf{q},t) = |E_S(\mathbf{q},t)|^2$ the intensity is:

$$I(\mathbf{q},t) = \frac{E_0^2}{R^2} \sum_{j=1}^{N}\sum_{k=1}^{N} b_j(\mathbf{q},t) b_k^*(\mathbf{q},t) \exp\left\{-i\mathbf{q}\cdot\left[\mathbf{R}_j(t) - \mathbf{R}_k(t)\right]\right\}. \tag{2.8}$$

where the $b_k^*(\mathbf{q},t)$ is the complex conjugate of the scattering length $b_j(\mathbf{q},t)$.

2.1.2 Conventional dynamic light scattering

When a sample containing discrete scattering objects, such as the colloidal suspension depicted in Fig. 29, is illuminated by a laser, it forms onto a detector in the far field, a granular pattern. Each bright spot of this diffraction pattern is called speckle. In dynamic light scattering (DLS), the time fluctuation of speckles are exploited to gain insight on the microscopic dynamics of the sample. As an illustration of how to get the microscopic dynamics of the system from the speckle fluctuations, we discuss the case of a dilute suspension of spherical particles undergoing Brownian motion.

2.1.2.1 Derivation of the intensity correlation function

For identical spherical particles, the amplitude of scattered field $b_j(\mathbf{q},t)$ of Eq. 2.7 are the same for all particles at any time. Moreover, since in DLS we are only interested in time averaged normalized quantities, we can omit all the amplitude prefactors of Eq. 2.7 and

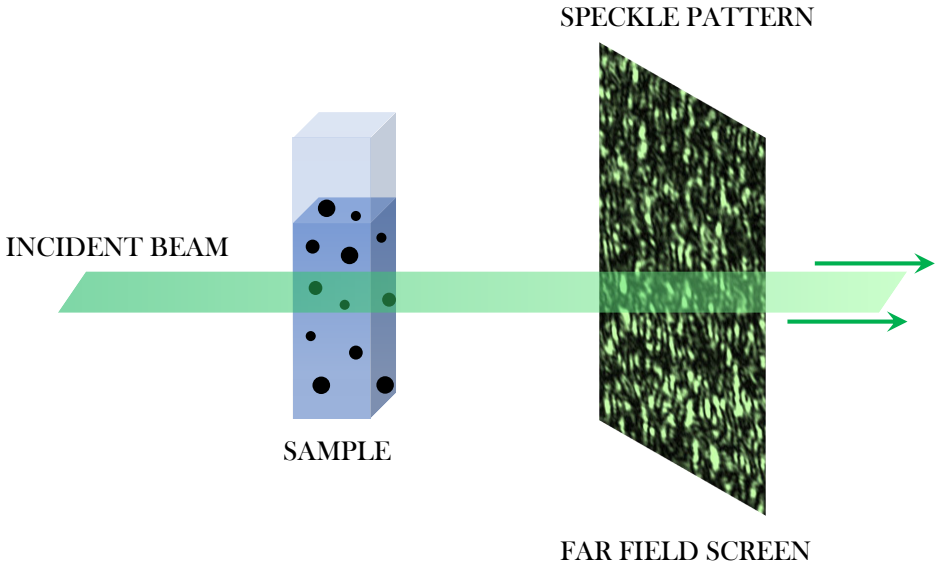

Figure 29: Scheme of the speckle pattern formed on a screen in far field by a colloidal suspension illuminated by a laser light.

write the electric field as:

$$E_S(\mathbf{q},t) \propto \sum_{j=1}^{N} \exp\left[-i\mathbf{q}\cdot\mathbf{R}_j(t)\right] \tag{2.9}$$

Written in this way, the scattered electric field is simply proportional the sum of all the phase shifts associated with each particle position. Moreover, if we assume that the particles are randomly distributed within the sample, the phases $\mathbf{q}\cdot\mathbf{R}_j(t)$ are randomly distributed between 0 and 2π. Consequently, $E_S(\mathbf{q},t)$ can be seen as a two-dimensional random walk, whose average value $\langle E_S(\mathbf{q},t)\rangle$ is null. Since the particles are moving, if at instant t the particles positions are described by the set of variables $[\mathbf{R}_j(t)]$ at an instant $t+\tau$ the particles position will be described by $[\mathbf{R}_j(t+\tau)]$, leading to a change in the scattered field. For small time differences the electric field remains basically unaltered; however, for time changes over which the phase changes by a factor 2π or more the fields $E_S(\mathbf{q},t)$ and $E_S(\mathbf{q},t+\tau)$ are completely uncorrelated. To quantify the loss of correlation in time of the scattered field, we calculate the time average:

$$\langle E_S(\mathbf{q},0)E_S^*(\mathbf{q},\tau)\rangle = N\left\langle \exp\left[-i\mathbf{q}\cdot\Big(\mathbf{R}(0)-\mathbf{R}(\tau)\Big)\right]\right\rangle \tag{2.10}$$

Starting from Eq. 2.8, we now calculate the time-averaged scattered intensity:

$$\langle I(\mathbf{q},t)\rangle = \left\langle \sum_{j=1}^{N}\sum_{k=1}^{N} \exp\left[-i\mathbf{q}\cdot\Big(\mathbf{R}_j(t)-\mathbf{R}_k(t)\Big)\right]\right\rangle = N \tag{2.11}$$

We notice that $\langle E_S(\mathbf{q},t)\rangle = 0$ and $\langle I(\mathbf{q},t)\rangle = N$ are well known results for a two-dimensional random walk. By normalizing Eq. 2.10 by the average scattered intensity (Eq. 2.11) we define the field time correlation function $g_1(q,\tau)$ as:

$$g_1(q,\tau) = \frac{\langle E_S(\mathbf{q},0)E_S^*(\mathbf{q},\tau)\rangle}{\langle I(\mathbf{q},t)\rangle} = \Big\langle \exp\Big[-i\mathbf{q}\cdot\Big(\mathbf{R}(0)-\mathbf{R}(\tau)\Big)\Big]\Big\rangle \tag{2.12}$$

However, as written before, detectors are sensitive to the scattered intensity. Consequently, in DLS we are interested in the correlations between the scattered intensities at times 0 and τ: $\langle I(\boldsymbol{q},0)I(\boldsymbol{q},\tau)\rangle$. Without going into the mathematical details, which can be found in [Zemb and Lindner (2002)], we quote the final results from the unormalized intensity time autocorrelation function:

$$\begin{aligned}
&\langle I(\boldsymbol{q},0)I(\boldsymbol{q},\tau)\rangle \\
&\quad\sim \sum_j 1 \sum_l 1 + \sum_j \langle \exp\{-i\boldsymbol{q}\cdot[\boldsymbol{R}_j(0)-\boldsymbol{R}_j(\tau)]\}\rangle \sum_k \langle \exp\{i\boldsymbol{q}\cdot[\boldsymbol{R}_k(0)-\boldsymbol{R}_k(\tau)]\}\rangle \\
&\quad= N^2 + N^2|\langle \exp\{-i\boldsymbol{q}\cdot[\boldsymbol{R}(0)-\boldsymbol{R}(\tau)]\}\rangle|^2.
\end{aligned} \tag{2.13}$$

whose normalization by the average scattered intensity is the intensity correlation function $g_2(q,\tau)$:

$$g_2(q,\tau) = \frac{\langle I(\mathbf{q},0)I(\mathbf{q},\tau)\rangle}{\langle I(\mathbf{q})\rangle^2} \tag{2.14}$$

Equations. 2.11, 2.12, 2.10 2.14 and 2.13 establish relation between $g_1(q,\tau)$ and $g_2(q,\tau)$, which is called Siegert relation:

$$g_2(q,\tau) - 1 = \Big[g_1(q,\tau)\Big]^2 \tag{2.15}$$

Note that Eq. 2.15 applies to any fluid system in which the range of spatial correlations is much smaller than the linear dimension of the scattering volume.

2.1.2.2 Intensity correlation function for Brownian particles

For monodisperse Brownian particles we can obtain an analytical expression for $g_1(q,\tau)$. Indeed, the displacement of the particles follow a Gaussian probability distribution. The distribution $P\Big[\Delta\mathbf{R}(\tau)\Big]$ of the displacements $\Delta\mathbf{R}(\tau) = \mathbf{R}(0) - \mathbf{R}(\tau)$ of Eq. 2.12 reads:

$$P\Big[\Delta\mathbf{R}(\tau)\Big] = \left[\frac{3}{2\pi\left\langle\Delta\mathbf{R}^2(\tau)\right\rangle}\right]^{\frac{3}{2}} \exp\left[-\frac{3\Delta\mathbf{R}^2(\tau)}{2\left\langle\Delta\mathbf{R}^2(\tau)\right\rangle}\right] \tag{2.16}$$

where the mean square displacement during a time interval τ reads:

$$\left\langle\Delta\mathbf{R}^2(\tau)\right\rangle = 6D_0\tau \tag{2.17}$$

Here D_0 is the diffusion coefficient given by the Stokes-Einstein equation:

$$D_0 = \frac{k_b T}{6\pi\nu a} \tag{2.18}$$

where k_b is the Boltzmann constant, T the temperature, ν the viscosity of the solvent and a the radius of the spherical particles. Inserting Eq. 2.16 into Eq. 2.12 we obtain:

$$g_1(q,\tau) = \exp\left[-\frac{q^2}{6}\left\langle \Delta\mathbf{R}^2(\tau)\right\rangle\right] = e^{-q^2 D_0 \tau} = e^{-\tau/\tau_D} \tag{2.19}$$

where we have defined the decay time $\tau_D = \frac{1}{q^2 D_0}$, which is the characteristic time over which the correlation decreases by a factor $1/e$. Using the Siegert relation (Eq. 2.15) we obtain the analytical expression for the intensity correlation function:

$$g_2(q,\tau) - 1 = e^{-2\tau/\tau_D} \tag{2.20}$$

More generally, and in the context of this thesis, we re-write $g_2 - 1$ by inserting a fractional power law into the exponential function:

$$g_2(\tau) - 1 = e^{-2\left(\frac{\tau}{\tau_E}\right)^{\beta}} \tag{2.21}$$

The exponent β depends on the sample type and dynamics. As mentioned before, for Brownian diffusion of monodisperse particles $\beta = 1$, while for sample exhibiting a broad distribution of relaxation times, like in the case of polydisperse suspension, $\beta \leq 1$ (stretched exponential) [Zemb and Lindner (2002)]. Moreover, for many jammed materials [Cipelletti et al. (2003)] $g_2 - 1$ assumes the form of a compressed exponential ($\beta \geq 1$). The average relaxation time is

$$\tau_D = \int_0^\infty e^{-2\left(\frac{\tau}{\tau_E}\right)^{\beta}} \mathrm{d}\tau = \frac{\tau_E}{2^{1/\beta}\cdot\beta}\Gamma(\frac{1}{\beta}) \tag{2.22}$$

which reduces to the characteristic decay time used in Eq. 2.19 for $\beta = 1$.

2.1.2.3 Standard DLS Setup

In Fig. 30 we sketch a standard DLS setup. The sample is placed in a bath (usually toluene) to index match the glass of the cylindrical vial in which the sample is kept and to better control temperature. A laser light illuminates the sample and the scattered light is collected by the detector, which is mounted on the arm of a goniometer in order to easily change the scattering vector $\mathbf{q}$. Some optics are used to select the scattering volume. A standard configuration includes a lens which images with magnification the center of the sample onto a pinhole. In this way the scattering volume is only the center

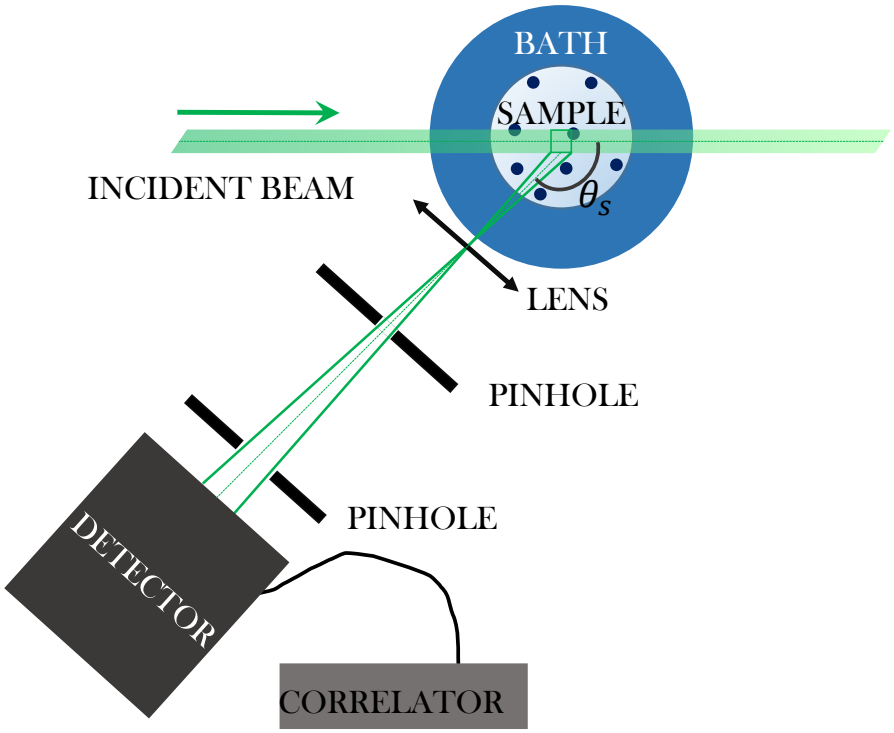

Figure 30: Scheme of a conventional DLS setup: The green laser beam illuminates the sample which is hold in a bath to index match the index of refraction of the cylindrical glass vial containing the sample. The detector is placed at scattering angle θ_s the scattering vector $\mathbf{q}$. On the detection branch, the combination of a lens and a first pinhole selects the scattering volume in the center of the sample. A second pinhole in front of the detector defines a small solid angle centered around the direction defined by θ_s, within which the scattered light is collected. The signal is then analysed by a dedicated hardware correlator.

of the sample, avoiding the stray light that might eventually come from the vial walls. A second pinhole is placed in front of the detector, such as to collect only light scattered within a small solid angle, usually corresponding one speckle. The detector is usually a photo-multiplier tube or a avalanche photodiode.

Nowadays many commercial DLS setup are available. In this work, we have performed some standard DLS measurements with the particle size analyser Litesizer by Anton Paar®. This instrument allows one to measure the $g_2 - 1$ correlation function at three different angles: $15°, 90°, 175°$.

2.1.3 Multispeckle techniques

Operationally DLS works on the assumption that the time average of the scattered electric field (Eq. 2.12) coincides with the ensemble average. Such an assumption applies when the sample is ergodic, that is when the particles explore a significant fraction of possible configurations during the experimental acquisition. This assumption is easily fulfilled in dilute suspension since the relaxation time hardly exceeds 10^{-2} s. However, in soft matter there is a wide class of materials whose relaxation dynamics largely exceeds thousands of seconds. In this case relying on time average to obtain the ensemble average of Eq. 2.12 becomes unfeasible, since one typically need to acquire data for a time that is at least two orders of magnitude longer that the characteristic decay of the sample. To solve this problem, two methods have been proposed: a first one, introduced by [Xue et al. (1992)] consists of displacing the sample such as to probe the dynamics of different speckles. The second method was first proposed by [Pusey and Van Megen (1989)] and is based on the fact that the ensemble average can be reconstructed from the intensity correlation function g_I^{run} of a single run and the ensemble-averaged static intensity: g_I^{run} is measured for a single position together with its averaged scattered intensity I^{run}; the sample is then rotated such as to collect the ensemble averaged scattered intensity I^{en}. The correct intensity correlation function is obtained from g_I^{run} and the ratio I^{en}/I^{run} [Pusey and Van Megen (1989)].

Nowadays, the most efficient way of measuring slow relaxation dynamics is through multispeckle methods. In a nutshell, this family of techniques takes advantage of multi-elements detectors such as those of CCD or CMOS cameras to measure the time fluctuation of several speckles at the same time [Cipelletti et al. (2016)]. Indeed, when illuminated by the speckle pattern, the pixels of the camera are basically a large number of detectors, collecting a large number of independent speckles. In such a way, the local dynamics of the sample are quantified by a two-time degree of correlation [Duri et al. (2005)]:

$$c_I(t,\tau) = A\frac{\langle I_p(t)I_p(t+\tau)\rangle_x}{\langle I_p(t)\rangle_x\langle I_p(t+\tau)\rangle_x} - 1 \tag{2.23}$$

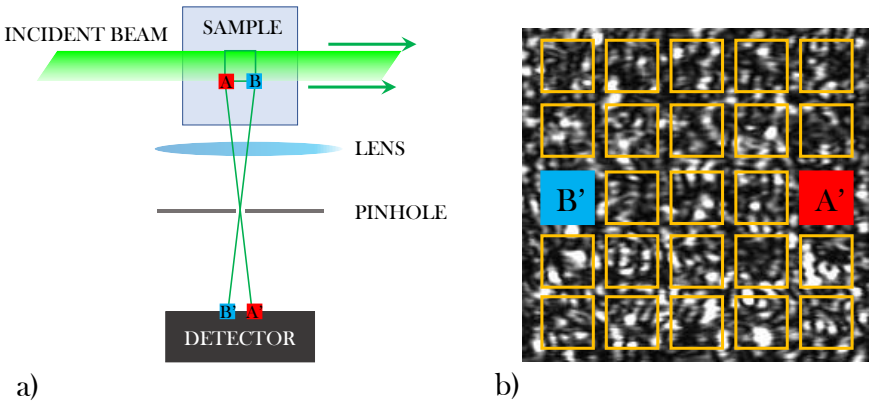

Figure 31: Scheme of a conventional PCI setup: a) A green laser beam illuminates the sample, which scatters light. The combination fof the lens and a pinhole selects a scattering vector **q** at which the image is formed on the camera. The points A and B and the respective images A' and B' underline the imaging properties of PCI. b) Multispeckle image formed on the screen of the camera, divided in ROIs (yellow squares), whose size usually ranges from 15 to 50 μm, from which space-resolved microscopic dynamics are extracted with a space-resolution.

with τ the time delay between images, $I_p(t)$ the intensity of the p-th pixel of the ROI at time t, and $\langle ... \rangle_x$ a spacial average over all pixels of the camera. By averaging $c_I(t, \tau, x)$ over a suitable time interval we obtain the intensity correlation function $g_2(\tau) - 1$ of Eq. 2.14. It is worth to notice that, contrary to conventional DLS, by obtaining the intensity correlation function from 2.23, since $c_I(t, \tau)$ is obtained from an enable average, it is not required anymore the hypothesis of ergodicity of the sample. Another advantage of these techniques is that, in addition to the average dynamics, the $c_I(t, \tau)$ provides a time-resolution of the system dynamics. Indeed, thanks to the pixel average, the $c_I(t, \tau, x)$ is a robust quantity from which it is possible to appreciate the time evolution of the sample, such as aging of colloidal gel or spatial heterogeneities in rearranging foams [Cipelletti et al. (2000); Sessoms et al. (2010)]. Depending on the collection optics, the average $\langle ... \rangle_x$ in Eq. 2.23 may correspond to an average over slightly different q vectors (far field configurations), or over small regions in the sample (imaging configuration). In the next section we discuss the alter case.

2.1.4 Photon Correlation Imaging

Among the different multispeckle techniques, Photon Correlation Imaging (PCI) allows one to measure the microscopic dynamics of a sample by analysing simultaneously multiple speckles [Duri et al. (2009)]. As sketched in Fig. 31a, a PCI setup involves using a lens and a pinhole to form an image of the sample while using light scattered at a well defined angle: a pinhole is set in the focal plane of an image-forming lens such that only the light scattered a fixed **q** illuminates the detector. The combination of these two optical

elements makes PCI an hybrid between a scattering technique and standard imaging: indeed, each position on the detector corresponds to a position in the sample, as in conventional imaging. Operationally, as shown in Fig. 31b, an image is divided into Regions Of Interest (ROIs) whose size is chosen so that each ROI contains at least about 100 speckles, which provides an acceptable statistical noise [Duri et al. (2005)]. From each ROI the c_I correlation function is obtained:

$$c_I(t,\tau,x) = A\left(\frac{\langle I_p(t)I_p(t+\tau)\rangle_{\mathrm{ROI}}}{\langle I_p(t)\rangle_{\mathrm{ROI}}\langle I_p(t+\tau)\rangle_{\mathrm{ROI}}} - 1\right) \tag{2.24}$$

where the intensity is averaged on all pixels in an ROI centered in x. Equation 2.24 shows that the degree of correlation c_I obtained by PCI quantifies the microscopic dynamics with both temporal and spatial resolution, due to the dependence on both t and x. This feature makes PCI a suitable technique for measuring spatially heterogeneous dynamics such as gel, glasses and dense suspensions [Duri et al. (2009); Maccarrone et al. (2010)].

In this thesis, as we will show in detail in Chapter 3, we have designed a PCI setup suited to measure microscopic dynamics for spherical samples.

2.2 X-ray scattering

A X-ray is a high-energy electromagnetic radiation. When sent against a sample, X-ray photons are scattered by the electrons of the medium. In this thesis we use X-rays scattering mainly to investigate the static structural properties of our samples.

2.2.1 Density of scattering

In order to exploit the expression of the scattered intensity (Eq. 2.8), which has been developed for light scattering above, we follow [P.N. Pusey, Chapters 1 and 9 in Zemb and Lindner (2002)] to rewrite the expression of the density of scatterers, (Eq. 2.4), in the case of X-rays. When an X-rays beam hits a sample the photons are scattered by the electrons of the sample. The scattering by a single electron is described by the scattering length $b_0^X = 2.8 \cdot 10^{-15}$ m [Zemb and Lindner (2002)]. For an atom containing n electrons the scattering length associated to the atom is $b_j^X = nb_0^X$. Thus, for a suspension of particles in a solvent Eq. 2.4 becomes:

$$\Delta\rho(\mathbf{r},t) = \frac{1}{\Delta V}\sum_j \left[b_j^{X,P} - \frac{v_p}{v_l}b_j^{X,L}\right] \tag{2.25}$$

where $b_j^{X,P}$ and $b_j^{X,L}$ are the scattering length of the molecules composing the particles and the solvent respectively.

2.2.2 Form Factor

The structural properties of a system are extracted from the average scattered intensity of Eq. 2.8 . If we consider a dilute system of non interacting Brownian particles, the time averaged scattered intensity becomes:

$$\begin{aligned}\langle I(\boldsymbol{q})\rangle &\propto \left\langle \sum_j \sum_k b_j(q) b_k^*(q) \exp\Big[-i\mathbf{q}\cdot(\mathbf{R}_j - \mathbf{R}_k)\Big]\right\rangle \\ &= \sum_j \langle |b_j(q)|^2\rangle + \sum_{j\neq} \sum_k \langle b_j(q)\exp(-i\mathbf{q}\cdot\mathbf{R}_j)\rangle\langle b_k^*(q)\exp(i\mathbf{q}\cdot\mathbf{R}_k)\rangle \\ &= \sum_j \langle |b_j(q)|^2\rangle\end{aligned} \tag{2.26}$$

where the double sum term $\sum_{j\neq}\sum_k ... = 0$ because for dilute, non-interacting particles the particles positions are uncorrelated. As a consequence, for a dilute system, the average intensity yields a direct measurements of the average scattering length, which in turn depends on the shape, size and composition of the particles, averaged over all possible orientations and the particle distribution. The average intensity scattered by N identical particles is then:

$$\langle I(\boldsymbol{q})\rangle = N\langle |b(q)|^2\rangle = N\langle |b(0)|^2\rangle P(q) \tag{2.27}$$

where we have defined the form factor $P(q)$ as $\frac{\langle |b(q)|^2\rangle}{\langle |b(0)|^2\rangle}$ such that $P(q)\to 1$ as $q\to 0$. In the case of homogeneous spherical particles of radius a, Eq. 2.6 becomes:

$$b(\mathbf{q}) = \Delta\rho \int_{\text{sphere}} \exp\left(-i\mathbf{q}\cdot\mathbf{r}\right) \mathrm{d}^3 r = \left[\Delta\rho \frac{4}{3}\pi a^3 \frac{3}{qa} J_1(qa)\right] \tag{2.28}$$

where J_1 is the Bessel function of the first kind. Since $(3/qa)J_1(qa)\to 1$ as $qa\to 0$, the form factor of a sphere is:

$$P(q) = \left[\frac{3}{(qa)^3}(\sin qa - qa\cos qa)\right]^2 \tag{2.29}$$

In the case the spherical particles are polydisperse the form factor is convoluted with the distribution function of the particle size.

2.2.3 Structure Factor

In case of an interacting system each particle position is affected by the positions of the others, so the second equality in solving Eq. 2.26 does not hold anymore. For spherical

homogeneous spheres Eq. 2.8 becomes:

$$\langle I(\boldsymbol{q})\rangle = \langle |b(q)|^2\rangle \Big\langle \sum_j \sum_k \exp\Big[-i\mathbf{q}\cdot(\mathbf{R}_j - \mathbf{R}_k)\Big]\Big\rangle = N\langle |b(0)|^2\rangle P(q)S(q) \tag{2.30}$$

Equation 2.30 shows that the scattered intensity is the product of the form factor of N uncorrelated particles and of the structure factor $S(q)$, with:

$$S(q) = \frac{1}{N}\sum_j \sum_k \langle \exp\Big[-i\mathbf{q}\cdot(\mathbf{R}_j - \mathbf{R}_k)\Big]\rangle \tag{2.31}$$

which accounts for the modification of the signal due to correlations between the particles positions.

2.2.4 X-ray sources

In this these we use two different sources of X-ray for probing the structure of our gels, whose preparation is detailed in Chapter 4. To probe the structure of colloidal gels prepared in capillaries we use X-ray photons produced by the beam line Swing of the Synchrotron Soleil. To probe the structure of beads of colloidal gel, we use a X-ray apparatus GeniX^{3D} of the Laboratoire Charles Coulomb (L2C) of Montpellier.The GeniX^{3D} device from Xenocs® consists of a micro-focused X-ray tube coupled with a parabolic multilayer monochromator mirror. It delivers a beam (flux: 20 Mphotons/s) of parallel X-rays (divergence: 0.5 mrad) that are monochromatic (wavelength: λ=1.5418 Å). The beam diameter is 0.6 mm. We work in a transmission configuration where the X-ray beam passes through the sample. The scattered signal measured using a 2D hybrid pixel detector called Pilatus (from Dectris®). The detector has 3490·600 pixels with pixel size of 172×172 μm^2, and is placed at a distance of 1.9 m from the sample. The accessible q ranges from $q = 7\cdot 10^{-2}$ nm^{-1} to 2 nm^{-1}.

2.3 Rheology

In a first approximation we can divide all materials in three different categories: gas, liquids and solids. However, it is sufficient to look at our daily life to understand that this classification is an oversimplification. Indeed, most of the materials show a complex so-called viscoelastic behavior, which depends on the way they are perturbed and on the timescales of observation. Rheology, from the Greek rhéō = 'flow' + logia = 'study of', is the branch of science that investigates the response of materials to mechanical forces and deformations.

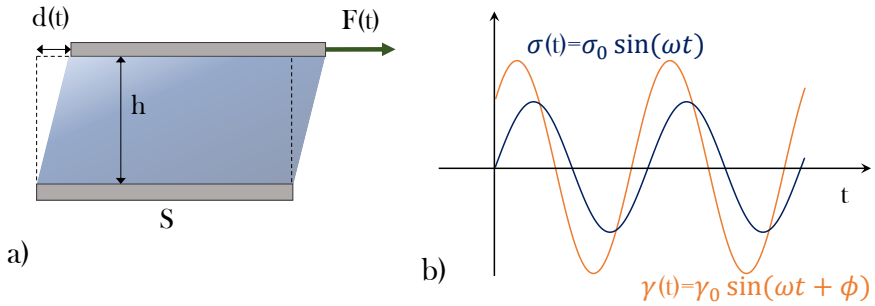

Figure 32: a) Sketch of a shear rheology experiment. The sample is confined between two parallel plates of surface S and separated by a gap h. A force $F(t)$ is applied on the upper plate induces the displacement $d(t)$. Dotted lines represent the sample before being deformed. The shear stress is defined as $\sigma(t) = \frac{F(t)}{S}$, while the shear strain is defined as the ratio between the deformation and the sample thickness $\gamma(t) = \frac{d(t)}{h}$. b) Plot of a typical response of a viscoelastic material: when a shear sinusoidal stress ($\sigma(t) = \sigma_0 \cos \omega t$) is applied to the material the strain presents a non null phase $\phi \neq \frac{\pi}{2}$. The amplitude response is characterized by the elastic G' modulus and the out of phase the viscous modulus G''.

2.3.1 Shear Rheology

When a stress $\overline{\overline{\sigma}}$ is applied to an object, the object undergoes a relative change in dimension and angles, which is described by a tensorial strain $\overline{\overline{\gamma}}$. For a generic geometry both $\overline{\overline{\sigma}}$ and $\overline{\overline{\gamma}}$ depend on the position in the sample $\mathbf{x}$, making the relation between the two quantities a complex tensorial equation. However, in specific case stress and strain are space-independent: One of this specific case is simple shear, where two opposite faces of a parallelepipedic element that are displaced by a force $F(t)$, see Fig. 32a. In this geometry, it is possible, by measuring the applied force and the resulting deformation $d(t)$, to obtain the time-dependent stress $\sigma(t) = \frac{F(t)}{S}$ and strain $\gamma(t) = \frac{d(t)}{h}$, where S and h are, respectively, the surface and the height of the sample.

Force and displacement are imposed and measured by complex instruments called rheometers. Rhometers can control either stress or strain, meaning that they can impose a deformation and measure the stress or impose a stress and measure the resulting strain. As an example, we consider an imposed sinusoidal stress $\sigma(t) = \sigma_0 \cos \omega t$ as the one depicted in Fig. 32b. A pure elastic solid would respond according to the Hooke's law: $\sigma(t) = G_0 \gamma(t)$, where the proportionality constant G_0 is the elastic modulus of the material. As a consequence, the strain would be an in-phase oscillation $\gamma(t) = \gamma_0 \cos \omega t$. Contrary, a pure viscous liquid would show an out-of-phase response $\gamma(t) = \gamma_0 \sin \omega t$. Indeed, for a Newtonian fluid the stress is proportional to the strain rate $\dot{\gamma} = \frac{d\gamma}{dt}$: $\sigma(t) = \eta \dot{\gamma}(t)$, with η the viscosity of the fluid.

However, as depicted in Fig. 32b, a material could exhibit a viscoelastic behavior, char-

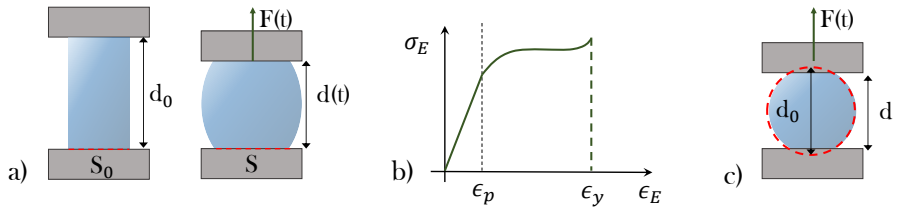

Figure 33: a) Sketch of a cylindrical sample under uniaxial compression. Upon compression the sample exerts a normal force on the plates while changing its shape and contact area S. b) Engineering stress σ_E as a function of the engineering strain as defined in Eq. 2.32. The sample undergoes three regimes: a linear regime where the deformation is elastic; beyond a strain ϵ_p the curve deviates from the linear regime with the sample showing irreversible plastic deformations and a yielding where the sample fails at a critical strain ϵ_y. c) Sketch of an uniaxial for a spherical sample with initial diameter d_0. The force exercised by the sample upon compression is described by the Hertz model of Eq. 2.34.

acterized by a strain with a phase between 0 and $\frac{\pi}{2}$. To describe a viscoelastic response, it is convenient to introduce the complex modulus $G^*(\omega)$. In the small deformation regime, to a given harmonic stress oscillating at a frequency ω, $\sigma(t) = \sigma_0 e^{i\omega t}$, is associated an harmonic perturbation oscillating at the same frequency $\gamma(t) = \gamma_0 e^{i\omega t}$. The strain related to the stress through the complex modulus $G^*(\omega)$: $\sigma(t) = G^*(\omega)\gamma(t)$ [Macosko (1994)]. The real part of the complex modulus G', is called elastic or storage modulus, and describes the elastic response of the material. The imaginary part G'', which is called viscous or loss modulus, represents the viscous character of the material. Effectively, linear shear rheology consists of imposing a small harmonic perturbation recording the amplitude and phase response from which the two moduli G' and G'' are extracted. In this thesis shear rheology is performed with the rheometer *MCR 502* by Anton Paar® in a plane plane geometry, for standard characterization of the colloidal gels.

2.3.2 Uniaxial compression

2.3.2.1 General principles

Despite being the most used geometry in rheology, shearing does not represent the only way to probe materials properties. Among the others, uniaxial compression constitutes one of the most used alternatives, especially for characterizing the failure of materials. In this geometry, as sketched in Fig. 33a, the sample of initial height d_0 is compressed between two plates and the normal force $F(t)$ that the sample exerts to the plate is measured. However, due to the variation of the contact area between the plate and the sample, it is not straightforward to obtain the stress $\sigma(t)$ from the measured force $F(t)$.

Moreover, contrary to shear, the strain γ depends on the position $\mathbf{x}$ within the sample. For this reason two quantities have been introduced in order to describe the problem in simple terms; the engineering stress $\sigma_E(t)$:

$$\sigma_E(t) = \frac{F(t)}{S_0} \tag{2.32}$$

and the engineering strain $\epsilon_E(t)$:

$$\epsilon_E(t) = \frac{d_0 - d}{d_0} \tag{2.33}$$

where S_0 and h_0 are, respectively the initial surface and height of the sample, and d the distance between the two plates. Thanks to these quantities it is possible to draw the distinctive stress strain curve, represented Fig. 33b, which schematically characterizes the common behaviour of a material under compression. Three regimes may be observed. In the first regime the stress increases linearly with the strain. This characterizes elastic deformations. Such regime interrupts at a critical strain ϵ_p, beyond which the sample may shows irreversible plastic deformations. Finally the stress drops due to the material failure at a yielding strain ϵ_y [Johnson and Johnson (1987)].

2.3.2.2 Data analysis

In this thesis we characterize, through uniaxial compression, the mechanical properties of beads of gel with spherical shape, (see Chapter 7 for the details of the preparation). As sketched in Fig. 33c, when a spherical object is compressed, as for the cylindrical one, it deforms while exerting a normal force on the upper plate. However, for a spherical contact, in the limit of small deformation and assuming a pure elastic response of the sample, the Hertz contact model applies [Johnson (1982)]. According to this model the force exhibits a power law dependence with the distance:

$$F = \frac{4}{3} E^* \left(\frac{d_0}{2}\right)^{1/2} d_c^{3/2} \tag{2.34}$$

where $\frac{d_0}{2}$ is the radius of the spherical sample, d_c is the indentation depth defined as $d_c = d_0 - d$, where d is the distance between the two plates, and E^* is defined as:

$$E^* = \left(\frac{1 - \nu_s^2}{E_s} + \frac{1 - \nu_p^2}{E_p}\right)^{-1} \tag{2.35}$$

where E_s and E_p are the Young's modulus , and ν_s and ν_p the Poisson ratio of the sample and the plate respectively. In case of a hard plate compressing a much softer material

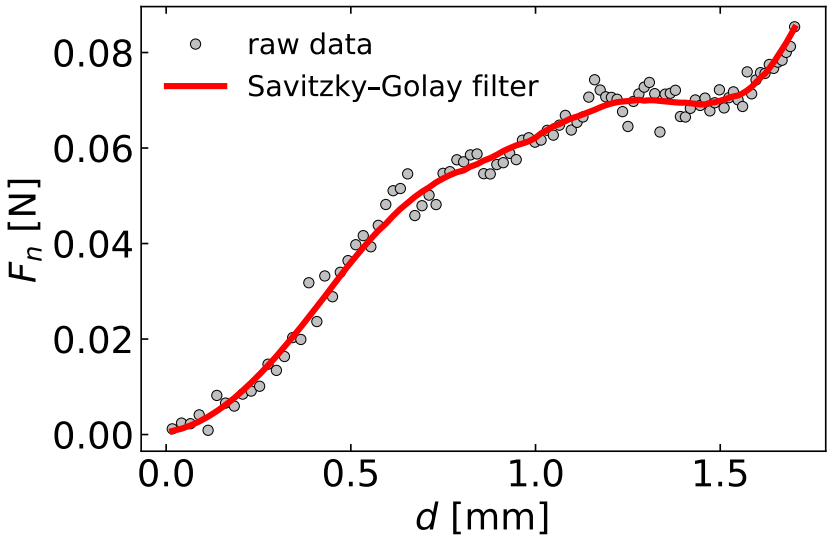

Figure 34: Normal force as a function of the indentation depth d_c (see text definition) for a bead of gel prepared at $\varphi = 3\%$. Gray circles are the raw data, the red solid line is the interpolation obtained by smoothing the data with Savitzky–Golay filter. The number of interpolated point is here 47.

$E_s << E_p$, hence Eq. 2.35 reduces to:

$$E^* = \left(\frac{1-\nu_s^2}{E_s}\right)^{-1} \tag{2.36}$$

Moreover, for homogeneous isotropic materials simple relation exists between the Young's modulus and the shear storage modulus G':

$$E = 2G'(1+\nu_s) \tag{2.37}$$

In view of characterizing the failure of beads of gel, it is key to find an efficient way of comparing material characterized by much different Young moduli. To do so we normalize the engineering stress of Eq. 2.32 by E^* to obtain the adimensional engineering stress, which reads as:

$$\tilde{\sigma}_E = \frac{F}{E^* \cdot S_0} \tag{2.38}$$

Due to the sensitivity of the rheometer, for soft beads (made with volume fraction $\varphi \leq 5\%$) the normal force data are very noisy. To get the results show in Chapter 5 we apply a Savitzky–Golay filter to smooth the data [Savitzky and Golay (1964)]. We vary the number of interpolated point according to the noisiness of the data and check for the consistency between the interpolated data and the original one. An example of this treatment is shown in Fig. 34, where we compare between the raw data and the interpolated ones, for the normal force as a function of the indentation depth for a gel bead prepared at $\varphi = 3\%$.

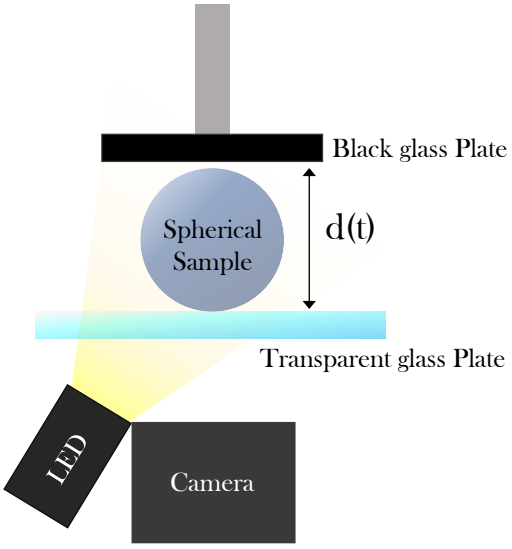

Figure 35: Sketch of the experimental setup used for uniaxial compression test: the spherical sample is compressed between two plates. The top plate compresses the gel by moving downward. The lower plate is made of glass allowing one to put the camera and a LED underneath the setup to image the sample during compression.

2.3.2.3 Experimental setup

In this thesis uniaxial compression experiments are performed with the rheometer *MCR 502* by Anton Paar®. As shown in Fig. 35, the spherical beads are compressed at a fixed rate between the two plates of the rheometer: the bottom one, which is made by a transparent glass, is fixed while the top one, made of black glass, moves downward allowing the contact with the sample and the normal force exerted on the plate is recorded. All the experimental parameters used in the experiments are reported in appendix B. Using a transparent glass plate allows one to couple an imaging system to the rheometer. We use a *acA2000 340km* camera by Basler® underneath the lower plate, and next to it we place a LED light, LIUCWHA from Thorlabs®, to illuminate the sample.

2.4 Drying protocols

Drying is a mass transfer process consisting of the removal of water or another solvent by evaporation. To study the drying of different water-based samples it is key to control the drying rate. To do so, we establish a protocol for drying our samples in a controlled manner.

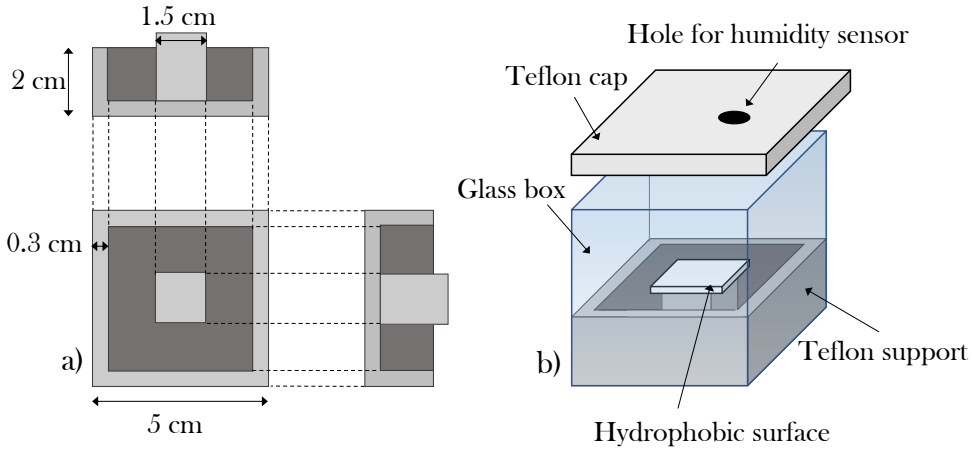

Figure 36: a) Orthogonal projections of the Teflon support. b) Sketch of the drying chamber for DLS measurements: the Teflon support is placed in the bottom of a glass box. The spherical sample sits on a hydrophobic surface placed on the top of the pillar which raises the sample above the support edges. The saturated salt solution used to control the RH fills the bottom of the support. The box is closed with a cap which has been perforated to insert the humidity sensor.

2.4.1 Design of the chamber

To perform our drying experiments, we designed an ad hoc support, sketched in Fig. 36a, which consists in an hollow parallelepiped with a pillar in its center. To control the relative humidity, as detailed in Sec. 2.4.2, a saturated salt solution is placed around the pillar, such that its level is lower than the support edges. For drying beads of gel or drop of suspension, we put on the top of the pillar an hydrophobic surface, whose preparation is detailed in Sec. 2.4.3, see Fig. 36b. The support and the surface are then placed in an optical box by Hellma® whose internal size matches the one of the support. The use of such a box allows one to perform DLS experiments. The box is closed by a Teflon cap, on which a hole is drilled in order to insert the humidity sensor.

2.4.2 Relative humidity control

The main parameter that governs the rate of drying is the relative humidity (RH). RH depends on temperature. For this reason the drying experiments described in Chapters 3, 7 and 6 are performed at (22 ± 1)°C. To control the relative humidity, we fill the bottom of the sample chamber (a cubic glass box of side 5 cm, see Sec. 2.4.1) with different chemicals or saturated salt solutions. We vary RH in the range 20% to 94%, thereby imposing different evaporation rates to our water-based samples. The values are reported in Table 2.1. The typical amount of humidity-controlling material is 15 cm^3, and the cell volume is 125 cm^3. RH is measured with a humidity sensor (SENISOR SEK-SensorBridge®). For a given relative humidity and temperature, a drop of a fixed volume dries completely in a evaporation time τ_{ev}. For drops of 30 μL, τ_{ev} is evaluated by extrapolating the short

	RH [%]	τ_{ev} [min]
H_2O	94	732
KCl	85	694
NaCl	75	476
K_2CO_3	43	248
$MgCl_2$	33	186
A.S.	20	112

Table 2.1: List of chemicals used to control the relative humidity, the corresponding time for evaporation, τ_{ev}. The salts are used as saturated water solutions. A.S. is a commercial silica xerogel.

time behaviour of $R(t)^2$, with $R(t)$ the time-dependent drop radius and $t = 0$ the time at which evaporation starts. We measure that τ_{ev} ranges between 112 and 732 min.

2.4.3 Hydrophobic surface

To produce the hydrophobic surface onto which the drop or bead sits, a water/ethanol solution (50% − 50%) of trimethoxy-(octadecyl)-silane (20 mg/mL) is deposited on a glass slide and heated in an oven (1 h ramp from 30°C to 70°C, and then 12 h at 70°C). The contact angle of the drop (30 − 40 μL) on the surface, as measured by imaging, is approximately 120°. In Chapter 7 to perform few additional experiments at different contact angle, a glass surface is treated with Sigmacote® from Sigma Aldrich. The contact angle of the drop on the surface, as measured by imaging, is approximately 60°. Finally, to test a third kind of contact conditions for which the contact with a substrate is reduced as much as possible, we build a support formed by three human hairs that intersect forming a suspended triangle, over which we deposit a drop with a maximum volume of 10 μL.

Chapter 3

Dynamic light scattering from a sphere

Space-resolved DLS within a millimetric drop: from Brownian diffusion to the swelling of hydrogel beads.

Matteo Milani, Ty Phou, Guillame Prevot, Laurence Ramos,* and Luca Cipelletti†
Laboratoire Charles Coulomb (L2C),
Université Montpellier, CNRS, Montpellier, France

(Dated: December 11, 2023)

We present a novel dynamic light scattering setup to probe the microscopic dynamics with time- and space-resolution resolution within millimeter-sized spherical samples. By using an ad-hoc optical layout, we tackle the challenges raised by refraction effects due to the unconventional shape of the samples. We demonstrate the setup by investigating the dynamics of two soft matter systems confined in spherical drops: a suspension of Brownian colloids and hydrogel beads made of a polymer gel undergoing swelling. For the suspension, we find that the dynamics measured at different positions in the drop, and hence different scattering angles, are in excellent agreement with those obtained for the same sample in a conventional light scattering setup. For the beads of polymer gel, we find that the microscopic dynamics exhibit a space dependence that strongly varies with time elapsed since the beginning of swelling. Initially, the periphery of the bead exhibits dynamics much faster than the core, indicative of non-uniform swelling. As the swelling proceeds, the dynamics slow down and become more spatially homogeneous. By comparing the experimental results to numerical and analytical calculations for the dynamics of a homogeneous, purely elastic sphere undergoing swelling, we establish that the mean square displacement of the gel strands deviates from the affine motion associated to the macroscopic deformation, displaying fast non-affine, ballistic relaxations.

I. INTRODUCTION

In Soft Matter probing the microscopic dynamics of a sample represents one of they key challenges in order to address many fundamental question regarding its behavior. Among many techniques, dynamic light scattering (DLS) is an ideal experimental tool for probing the dynamics without perturbing the system. Along the years,

Among the different techniques that exploits DLS principles, Photon Correlation Imaging (PCI) represents the ideal technique to probe microscopic dynamics with time- and space-resolution [1]. The peculiarity of PCI is combining standard imaging and light scattering techniques. Indeed, as in conventional imaging, each position on the detector corresponds to a position in the sample. However the images are formed by light that has been scattered at a specific scattering vector $\mathbf{q}$, typical of DLS experiments. An advantage of PCI is its easy realization: indeed, as show in detail in [1], it is sufficient to illuminate the sample with a monochromatic laser and collected the scattered light with a camera and ad-hoc optical layout composed only by a lens and a pinhole. For its very nature, PCI have been develop for studying samples confined in glass holders such cylindrical vials, rectangular scattering cells [1], plates of rheometers with glass plates rheometers [2] and even shear cells [3].

However, in Soft Matter many samples comes with the shape of drops or beads. One example are drops of colloidal suspensions, which are widely involved in fundamental studies [4–7], biological field in problem such as drying of casein [8], virus survival [9], or blood desiccation [10] and even in the design of functional supraparticles [11, 12]. On other example of extremely common spherical samples are hydrogel beads. They are widespread and their applications go from food science [13, 14] to adsorption of dyes [15] acids [16] and metals [17] and drug delivery [18]. Confining these spherical samples into a glass containers such to probe their microscopic dynamics, would probably affect the overall phenomenology. Indeed, the behaviors of a drop- or bead-like samples are often intimately related to their very shape and/or to the absence of interactions with the sample container. For instance, polymeric hydrogels exhibit a wide variety of behaviors such as syneresis [19], shrinkage during gelation [20], swelling [21–23] when they are in a bad-like shape, but not shown when constrained to the walls of a container. An other example where they spherical shape and the interaction of the substrate play a key role regards the drying of drops colloidal suspension as indicated in [5, 24].

Moreover, we have recently used the setup to measure the microscopic dynamics of drying colloidal drops, revealing unprecedented information regarding the shape instability incurred by the sample [25].

Unfortunately, to the best of our knowledge, a DLS setup able to probe microscopic dynamics directly on millimetric spherical samples does not yet exists. Here, we propose to fill this gap by developing a new DLS setup suited for measuring microscopic dynamics with time- and space-resolution within spherical samples. To do so, we will exploit the working principle of PCI coupled with an ad-hoc optical layout. We will demonstrate the potentiality of the setup with two experiments. First, by measuring the dynamics of Brownian particles confined

* laurence.ramos@umontpellier.fr
† luca.cipelletti@umontpellier.fr

in a millimetric drop, we will check the unavoidable entanglement between between the position and the scattering vector raised by the spherical shape of the sample. Second, we will use the setup to investigate the swelling of a bead of polymeric hydrogels. Due to the implications in several applications, the swelling of polymer gels has been largely investigated both from an experimental [21, 22, 26] and computational point of view [23, 27]. Here, by using our setup, we discover unprecedented information regarding the microscopic motion of the gel network which can be incorporated in future models of computational mechanics.

II. PHOTON CORRELATION IMAGING SETUP

A. Optical layout

Figure 1a shows schematically the light scattering setup, specifically designed to probe with space and time-resolution the microscopic dynamics within millimeter-sized spherical samples. Due to the small radius of curvature of the sample, whenever the refractive index of the solvent in the drop, n, is different from that of the surrounding medium, refraction effects considerably complicate the definition of the scattering angle. We minimize these complications by illuminating the sample with a thin beam impinging perpendicularly to the drop surface, such that the incoming beam is not refracted, and by collecting light exiting the sample along a single, well-defined direction.

The light source is a single-mode continuous wave laser (Verdi V-2 by Coherent) operating at an in-vacuo wavelength $\lambda_0 = 532.5$ nm with a maximum power of 2 W. A first lens (L_1 in Fig. 1a, with diameter 65 mm and focal length 64 mm), collimates the beam down to a beam waist $w = 59.5 \pm 0.1$ μm, much smaller than the typical drop radius (see Sec. II D for the measurement of w). Thus, the scattering volume is a thin cylinder centered around a drop diameter, along the x axis direction. To achieve spatial resolution, the scattered light is not collected in the far field, as in conventional scattering, but rather by forming an image of the scattering volume on the detector of a CMOS camera, using lens L2 (diameter 40 mm, focal length 82 mm). To insure that only light propagating along the direction of the y axis is collected by the camera, we place a slit and a diaphragm in the back focal plane of L2, which reject scattered light propagating at angles larger than $\theta_{yz} = 1.65$ deg and $\theta_{yx} = 0.55$ deg with respect to the y axis, in the (y, z) and (x, y) planes, respectively. Note that the drop and the surrounding medium are contained in a cubic sample chamber with walls perpendicular to the x and y directions, so as to avoid refraction effects at the chamber-air interfaces. Finally, by taking the image of a ruler placed at the sample position, we determine the system magnification to be $M = 2.11 \pm 0.02$. The combination of the illumination and collection optical layout described above allows for associating a well defined scattering angle θ_s, and thus a well defined magnitude of the scattering vector $q = 4\pi n \lambda_0^{-1} \sin(\theta_s/2)$, to each point within the scattering volume, as we will detail in Sec II B.

Depending on the sample dynamics, we use either a fast camera (Phantom Miro M310, e.g. for the Brownian dynamics described in Sec. III) or a conventional camera (acA2000 340km by Basler, e.g. for the polymer gel of Sec. IV). The fast camera is run at 19000 fps, for a typical run duration of 60 ms. The size of the acquired images is 896 pixels $\times$184 pixels, and the pixel size is 20×20 μm^2. By contrast, to measure slow dynamics, e.g. the dynamics of a polymer gel, we use a CMOS a camera (acA2000 340km by Basler). In this case the collected images have a full frame size of 2048 pixels $\times$1088 pixels and a pixel size of 5.5 μm. To allow for faster image acquisition, we typically acquire only a fraction of the full frame, selecting a region of interest of 2048 pixels $\times$512 pixels. Here the acquisition is taken using the variable delay scheme of Ref. [28], with shortest delay 1 s.

B. Refraction effects

Due to its spherical shape, the sample itself acts as an optical component of the setup. As shown in the inset of Fig. 1a, the scattered light propagating towards the detector is refracted at the interface between the sample and the external medium, whenever the index of refraction of the surrounding medium is different from that of the sample. As a consequence, each ray is associated with a particular scattering angle θ_s, such that there is an intrinsic coupling between position and scattering vector $\mathbf{q} = \mathbf{k}_o - \mathbf{k}_i$, where $\mathbf{k}_i$ is the wave vector of the incident beam and $\mathbf{k}_o$ that of the scattered light.

We now determine the components and magnitude of $\mathbf{q}$ as a function of the coordinates (x_P, y_P, z_P) of a point P at the intersection between a scattered ray collected by the camera and the drop surface, where we take the drop center as the origin of a Cartesian reference frame. The incident wave vector is $\mathbf{k}_i = 2\pi n \lambda_0 \hat{e}_x$, with $\hat{e}_x$ the unit vector along the x axis. Thanks to the combination of the slit and diaphragm, only scattered light propagating along $\hat{e}_y$ after leaving the drop contributes to the image formed on the camera detector. The propagation direction of the scattered light within the drop, $\hat{k}_o = \mathbf{k}_o/k_o$, is found by imposing Snell's law at the drop-surrounding medium interface. By introducing the unit vector pointing at P, $\hat{r}_P = (x_P\hat{e}_x + y_P\hat{e}_y + z_P\hat{e}_z)/\sqrt{x_p^2 + y_P^2 + z_P^2}$, after some tedious but straightforward calculations, one finds

$$\hat{k}_o = a\hat{r}_P + b\hat{e}_y \,, \tag{1}$$

with a and b two prefactors that depend on the position of P and the refractive index mismatch between the drop and the surrounding medium, and whose expression is given in Eqs. A8 of Appendix A. Once $\mathbf{k}_o$ is determined,

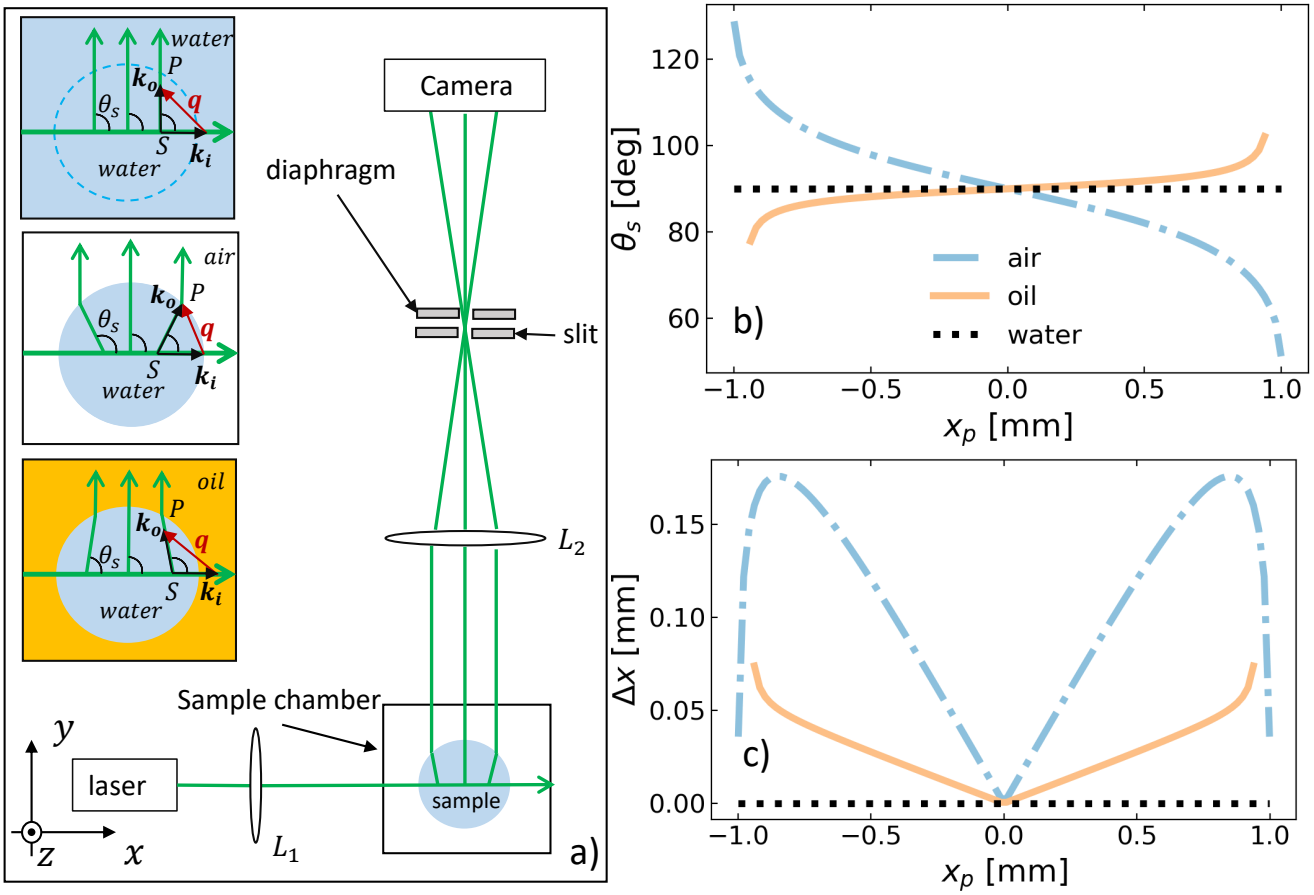

FIG. 1. (a) Scheme of the dynamic light scattering setup optimized for spherical, millimiter-sized samples. The incoming laser beam propagates along the x axis and is mildly focused by the lens L_1 in the middle of the sample. The lens L_2 forms an image of the scattering volume on the sensor of a CMOS camera. By combining a vertical slit, parallel to the z direction, and a diaphragm, we ensure that the image is formed by scattered light exiting the drop along the y direction, to within acceptance angles of 0.55 deg and 1.65 deg in the (x, y) and (y, z) planes, respectively. The sample is placed in a cubic glass box of side 4 cm. Insets: Schematic top view of the relevant optical rays for a water-based spherical sample surrounded by water, air and oil, respectively. Due to refraction, in general the scattering angle θ_s for light exiting the drop along the y direction depends on the x coordinate of the scatterer. (b) Scattering angle θ_s as a function of x_p, the x coordinate of the point P on the bead surface shown in the insets of a). Data for a bead of radius 1 mm surrounded by air, oil or water, as shown by the labels. (c) Absolute difference Δx between x_S, the abscissa of the point S from which a scattering ray originates, and x_P, as a function of x_P. The curves refer to the case of a bead of 1 mm radius surrounded by air, oil or water, see legend in b).

the scattering vector and the scattering angle are calculated according to

$$\mathbf{q} = \mathbf{k}_o - \mathbf{k}_i \,, \tag{2}$$

$$\theta_s = \arccos(\hat{k}_o \cdot \hat{e}_x) \,, \tag{3}$$

where we have used $\hat{k}_i = \hat{e}_x$. Figure 1b shows the scattering angle θ_s as a function of x_P, for a water-based sample (refractive index of the solvent in a one-millimeter, water-based drop ($n = 1.33$) in air ($n_{air} = 1$), or surrounded by the oil used for the experiments of Sec. III, $n_{oil} = 1.403$. Note that the trend is opposite for air or oil as a surrounding medium, and that the deviations with respect to $\theta_s = 90$, the scattering angle for a ray originating from the center of the drop, can be as large as 30 deg for a water-in-air drop. The corresponding scattering vectors have magnitude $14\mu\text{m}^{-1} \leq q \leq 28\mu\text{m}^{-1}$, with $q \approx 22\mu\text{m}^{-1}$ for $\theta_s = 90°$. Since DLS techniques are sensitive to relative displacements of the order of $1/q$, our setup is sensitive to motion on length scales of the order of a few tens of nanometers.

Another consequence of refraction at the drop surface is the fact that the coordinate x_P where a scattered ray intersects the drop surface differs from the coordinate x_S along the scattering volume from which that scattered light originates, see also Fig. 4b. Note that x_P is directly obtained from the position on the image collected by the CMOS camera, but the desired, physically relevant quan-

tity is the position in the sample, i.e. x_S. Assuming for simplicity that the incident beam is infinitely thin, i.e. that the scattering originates from a point S on the x axis, and using $\mathbf{OS} = \mathbf{OP} - \mathbf{SP}$, one finds

$$x_S = x_P + \frac{\hat{k}_{ox}}{|1 - \hat{k}_{ox}|} \sqrt{y_P^2 + z_P^2}\,, \tag{4}$$

with $\hat{k}_{ox} = \hat{k}_o \cdot \hat{e}_x$. Figure 1c shows $\Delta x = |x_S - x_P|$, as a function of x_P: deviations as large as 15% may be observed for a water drop in air. In the following, we systematically use the coordinate x_S when showing space-dependent data.

C. Quantifying the dynamics: multispeckle intensity correlation functions

To quantify the sample dynamics we take a time series of images of the speckle pattern imaged onto the CMOS detector. Each image is divided into several Regions of Interest (ROIs), typically rectangles of dimensions (30×100) pixels^2, corresponding to about (70×260) μm^2 in the sample. The size of the ROIs is chosen so that each ROI contains around 100 speckles, which provides an acceptable statistical noise [29], while keeping the ROI size small enough to obtain about 10 ROIs over the bead diameter. The local dynamics within a given ROI is quantified by a two-time degree of correlation [30]:

$$c_I(t, \tau, x) = \alpha \frac{\langle I_p(t) I_p(t+\tau)\rangle_x}{\langle I_p(t)\rangle_x \langle I_p(t+\tau)\rangle_x} - 1 \tag{5}$$

with x the position along the diameter of the sample, τ the delay between images, $I_p(t)$ the intensity of the p-th pixel of the ROI at time t, and $\langle\cdots\rangle_x$ an average over all pixels within a ROI centred around x. The multiplicative factor α is chosen such that the intensity correlation function $g_2(\tau, x)-1$, obtained by averaging $c_I(t, \tau, x)$ over a suitable time interval, tends to one for $\tau \to 0$.

For a dilute suspension of identical spheres of radius a undergoing Brownian motion, the intensity correlation function is a simple exponential decay:

$$g_2(\tau) - 1 = \exp(-2q^2 D_0 \tau) = \exp\left(-2\frac{\tau}{\tau_D}\right) \tag{6}$$

where D_0 is the diffusion coefficient given by the Stokes-Einstein relation: $D_0 = \frac{k_B T}{6\pi\eta a}$, with k_B Boltzmann's constant, T the temperature, and η the solvent viscosity. More generally, $g_2 - 1$ may be conveniently expressed by a stretched or compressed exponential:

$$g_2(\tau) - 1 = \exp\left[-2\left(\frac{\tau}{\tau_E}\right)^{\beta}\right] \tag{7}$$

The exponent β depends on the sample type and dynamics. For Brownian diffusion of monodisperse particles $\beta = 1$, while for a sample exhibiting a broad distribution of relaxation times, e.g. a polydisperse suspension or a supercooled colloidal fluid, $\beta \leq 1$ (stretched exponential) [31]. By contrast, compressed exponential decays, $\beta \geq 1$, are typically measured for dynamics associated to the stress relaxation of jammed materials [32]. The average relaxation time of a stretched or compressed exponential decay may be defined as

$$\tau_D = \int_0^\infty \exp\left[-2\left(\frac{\tau}{\tau_E}\right)^{\beta}\right] \mathrm{d}\tau = \frac{\tau_E}{\beta 2^{1/\beta}} \Gamma\left(\frac{1}{\beta}\right)\,, \tag{8}$$

with $\Gamma(x)$ the Gamma function, which coincides with the decay time τ_D in Eq. 6 for a simple exponential, $\beta = 1$.

D. Setup characterization

As an essential step before any further measurements, we characterize our setup concerning two points that are important for the interpretation of the data presented in the following: the size of the scattering volume and the mechanical stability of the apparatus.

Dynamic light scattering is sensitive to the relative motion of the scatterers within the scattering volume, V_S. In most cases, detailed knowledge of the geometry of the scattering volume is not necessary, e.g. for the Brownian particles of Sec. III, whose relative displacement is independent of V_S. However, there are situations where the dynamics do depend on the size and shape of V_S, e.g. for the beads of polymer gels of Sec. IV undergoing a swelling strain ϵ, where the relative motion between portions of the gel separated by a distance L scales as ϵL. In our setup, the scattering volume is a thin "cylinder" centered around the x axis. More precisely, the incoming beam cross section has a Gaussian profile, characterized by the beam waist w, the distance from the x axis over which the incident intensity decays by a factor e^{-2} [33]. In order to measure w precisely, we replace the sample by a frosted glass positioned perpendicularly to the incoming beam, at $x = 0$. We place a lens with focal length $f = 40$ mm on the x axis, right after the ground glass, and use a CMOS camera placed in the focal plane of the lens to take an image of the speckle pattern generated by the ground glass. Under these conditions, the speckle size is directly related to w through the spatial auto-correlation function of the speckle pattern, $C_I(\Delta x, \Delta y) = \langle I(x_c, y_c) I(x_c + \Delta x, y_c + \Delta y)\rangle$, with $I(x_c, y_c)$ the intensity measured at position (x_c, y_c) on the detector. Indeed, for a sample illuminated by a Gaussian beam with beam waist w and wavelength λ, the space-varying part of the auto-correlation function measured at small angles reads [33]:

$$C_I(\Delta x, \Delta y) \propto \exp\left[-\frac{\pi^2 w^2}{2f^2\lambda^2}(\Delta x^2 + \Delta y^2)\right]\,. \tag{9}$$

By fitting Eq. 9 to the measured $C_I(\Delta x, \Delta y)$, we find $w = 59.5 \pm 0.1$ μm.

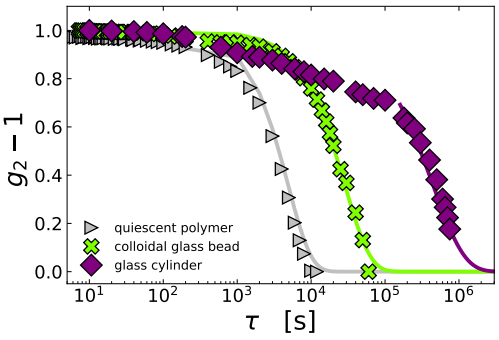

FIG. 2. Intensity correlation functions for a glass cylinder (purple diamonds), a colloidal glass bead (green crosses) and a quiescent bead of polymer gel (light gray triangles). Solid lines are a fit of the slow decay to Eq. 7. For the final decay of $g_2 - 1$ for the glass cylinder, $\tau_E = 434803$ s and $\beta = 1$, for the colloidal glass $\tau_E = 28036$ s and $\beta = 1.24$, and for the polymer gel $\tau_E = 2649$ s and $\beta = 1.37$.

Mechanical stability is another important issue, since DLS is sensitive to displacements down to a few nanometers and the peculiar geometry of our samples makes it difficult to immobilize them as firmly as for a standard cuvette. Furthermore, samples like the gels of Sec. IV may have relaxation times as long as several tens of seconds, making the requirement on mechanical stability quite stringent. We first probe the overall stability of the apparatus for a tightly fixed sample. We use a cylindrical piece of glass (1 cm diameter and 7 cm height) firmly held by a clamp. The glass contains frozen impurities that scatter sufficiently for $g_2 - 1$ to be measurable. We plot in Fig. 2 the correlation function for a ROI in the center of the cylindrical sample, measured during an experiment lasting ten days we obtain a decay time $\tau_D = 217401$ s (2.3 days), which demonstrates the excellent overall mechanical stability of the apparatus.

We then repeat stability tests for a sample configuration similar to that in experiments on spherical, water-based samples. The green crosses in Fig. 2 show $g_2 - 1$ for a bead of colloidal glass, prepared by depositing 10μL of an aqueous suspension of commercial silica nanoparticles (Ludox TM-50 from Sigma Aldrich) on a hydrophobic surface immersed in silicon oil (47 V 100, VWR chemicals). The oil has a small miscibility with water; thus, water in the suspension slowly diffuses into the oil, decreasing the drop radius from 3.94 mm to 3.31 mm. Accordingly, the particle volume fraction grows from an initial value $\varphi_i = 0.31$ to $\varphi_f = 0.52$, well within the glassy regime for this sample [34]. Since there may still be some ultra-slow relaxations in the bead of colloidal glass, the decay time obtained from a fit to the data, $\tau_D = 14956$ s, provides a lower bound for the slowest dynamics that can be reliably measured on a drop sample. The compressing exponent $\beta = 1.24$ is indicative of dynamics stemming from the relaxation of internal stresses, as reported for the same system studied in the bulk [34] and for other jammed or glassy soft materials[35–37].

Finally, the grey triangles in Fig. 2 show the $g_2 - 1$ function for a quiescent bead of the polymer gel investigated in Sec. IV. In this case, the surrounding medium is water-saturated oil, to prevent any changes of the drop size. The measured dynamics are thus due to the spontaneous relaxation of the gel, and are expected to be slower than the driven dynamics during swelling. We find $\beta = 1.37$, larger than one, as expected for the slow, spontaneous dynamics of a gel. The relaxation time is $\tau_D = 1460$ s, faster than that of the colloidal glass. This proves that the quiescent dynamics of the polymer gel reported here, as well as the faster dynamics during swelling discussed in Sec. IV, are not affected by any artifact due to mechanical instabilities.

III. BROWNIAN PARTICLES IN A DROP

We first test our setup on a drop of a diluted suspension of Brownian particles, whose dynamics are well known and can be easily measured in a conventional DLS setup, for comparison. By running experiments that last a fraction of a second, we insure that the drop radius does not change during the measurements, regardless of the surrounding medium. Thus, the dynamics are due solely to Brownian diffusion and should be isotropic and spatially homogeneous. However, as discussed in Sec. II B, the relaxation time of $g_2 - 1$ is still expected to depend on the position of the ROI for which the intensity correlation function is calculated, due to refraction effects that lead to a spatial dependence of the scattering angle, see Fig. 1b. In the following, we shall demonstrate that $g_2 - 1$ is fully consistent with data obtained for the same sample using a conventional setup. Moreover, we will show that the space dependence of the intensity correlation function is fully accounted for by the x-dependence of the scattering vector $\mathbf{q}$ stemming from refraction effects.

A. Materials

The Brownian sample is a suspension of polystyrene particles from Microparticles GmbH (diameter $2a = 105$ nm), at a concentration 4×10^{-3} % w/v. The solvent is a 80/20 w/w water/glycerol mixture, with refractive index $n = 1.3585$ [38], viscosity $\eta = 2.3 \cdot 10^{-3}$ Pa s, and density $\rho = 1048$ kg m^{-3} that nearly matches that of the particles [39]. A suspension drop of volume 30 μL (radius $R_0 = 1.9$ mm) is gently deposited on a hydrophobic surface (contact angle 120 deg). To prepare the hydrophobic surface, we deposit on a microscope glass slide a 50/50 v/v water/ethanol solution of trimethoxy-(octadecyl)-silane (20 mg/mL). The glass slide is then heated in an oven, raising linearly the temperature T from 30°C to 70°C in 1 h, followed by 12 h at constant $T = 70$°C. To test refractive effects with opposite trends, we use either air ($n_m = 1$) or silicon oil (47 V 100 from VWR

chemicals, $n_m = 1.403$) as the surrounding medium. The setup has no temperature control, the room temperature is controlled and measured to be $T = 22.0 \pm 0.1°\mathrm{C}$, where the quoted uncertainty is that of the temperature probe. Sequences of speckle images lasting 60 ms are acquired using a fast camera, see Sec. II A, and processed to calculate $g_2 - 1$.

B. Experimental results

We plot in Fig. 3a the intensity correlation functions for a drop in air. Data are acquired for different ROIs, centered around different positions x_S along a drop diameter. The correlation functions are very well fitted with a simple exponential decay as theoretically expected for monodisperse Brownian particles (Eq. 6). We find that the decay time of the correlation function, τ_D, increases from 7.9 to 16.2 ms as x_S grows. This trend is consistent with what expected from the variation of the scattering vector $\mathbf{q}$ associated with the position of the ROIs for $n > n_m$. The opposite case $n < n_m$ is illustrated by the data in Fig. 3b, acquired for a drop immersed in oil. In this case, the relationship between θ_s and x_S has an opposite trend, see Fig. 3c, leading to a faster decay for smaller x_S. Moreover, since the refractive index mismatch between oil and water is smaller than for air and water, the variation of the scattering angle, and hence of q, is smaller for the drop in oil than for the same drop in air. This explains the smaller variation of $g_2 - 1$ with ROI position for the drop in oil, compare Figs. 3a and b. These observations are summarized in Fig. 3c, which shows the relaxation time τ_D along the drop diameter for both surrounding media. To quantitatively check the relationship between position x_S and q, we plot in Fig. 3d, $1/\tau_D$ as a function of q^2 for the data acquired with the drop in air and in oil, where q is calculated from the position of each ROI as explained in Sec. II B and Appendix A. We find that the two sets of data nicely collapse on the theoretical curve $1/\tau_D = D_0 q^2$, with D_0 the diffusion coefficient measured independently on the same suspension, but in the bulk, using a commercial DLS apparatus with a standard cuvette. These results confirm that the setup and data analysis presented here allow for reliably measuring the microscopic dynamics in millimeter-size drops.

IV. SWELLING OF A POLYMER GEL

In this section we investigate a bead of a water-based polyacrylamide gel that is initially partially dried and then is swollen by immersing it in water. As for the Brownian suspension, we use sequences of speckles images to measure the microscopic dynamics. However, some caution is required when analyzing $g_2 - 1$ functions taken during swelling. Due to the imaging geometry, the speckle pattern associated to a given portion of the gel moves away from the center of the bead as the gel swells. This drift motion would result in a spurious fast decay of $g_2 - 1$. To avoid this artifact, we use the drift correction scheme of Ref. [40], where the intensity correlation function is calculated in a moving reference frame that compensates for the drift. A second, more subtle effect concerns the nature of the displacements within the gel. The microscopic dynamics are due to the strain field generated during swelling, which in turn may be decomposed in a component associated to the expansion of a perfectly elastic and homogeneous spherical body, and additional displacements stemming from spatial heterogeneity in the elastic response of the gel or strain-induced rearrangements [3, 41]. The latter component is often the one of greater interest. Unfortunately, the geometry of our experiments does not allow one to disentangle the two components. In order to gauge the relative importance of each component, we first derive in Sec. IV A a theoretical expression for the intensity correlation function during the expansion or contraction at a macroscopic strain rate $\dot{\varepsilon}$ of an ideal, perfectly elastic and homogeneous spherical body. We then describe the preparation protocol for the gel beads in Sec. IV B and compare the experimental $g_2 - 1$ functions to those for the ideal case in Sec. IV C. Our results will be briefly discussed and compared to other studies of swelling polymer beads in Sec. IV C.

A. Theory: intensity correlation function for the expansion or compression of a purely elastic homogeneous sphere

We discuss here the case of a perfectly elastic and homogeneous sphere surrounded by a medium with arbitrary refractive index and undergoing expansion or contraction. We shall derive a general expression for the decay of $g_2 - 1$ in response to a strain increment (or decrement) $\Delta\varepsilon = \Delta R/R$, with ΔR the change of the sphere's radius. This general expression will be used in numerical calculations; a simpler analytical expression valid under some approximations will also be introduced.

Operationally, the intensity correlation function is calculated pixel by pixel, see Eq. 5. Any given pixel of the CMOS detector corresponds to a small portion of the sphere surface centered around the point P from which the scattered light emerges from the sphere, see Fig. 4. The normalized intensity correlation function can be written as an integral over the contributions of all scatterers in the scattering volume V_P associated to point P [31]:

$$g_2(\mathbf{P}, \Delta\varepsilon) - 1 \propto \left| \int_{V_P} e^{-i\mathbf{q}\cdot\Delta\mathbf{u}(\mathbf{x},\Delta\varepsilon)} I(\mathbf{x},\mathbf{q}) \mathrm{d}^3\mathbf{x} \right|^2 , \quad (10)$$

where $\mathbf{q}$ is the scattering vector determined as shown in Sec. II B, $I(\mathbf{x}, \mathbf{q})$ is the scattered intensity originating from a point at position $\mathbf{x} = x\hat{e}_x + y\hat{e}_y + z\hat{e}_z$ and $\Delta\mathbf{u}(\mathbf{x}, \Delta\varepsilon)$ is the displacement field generated by the

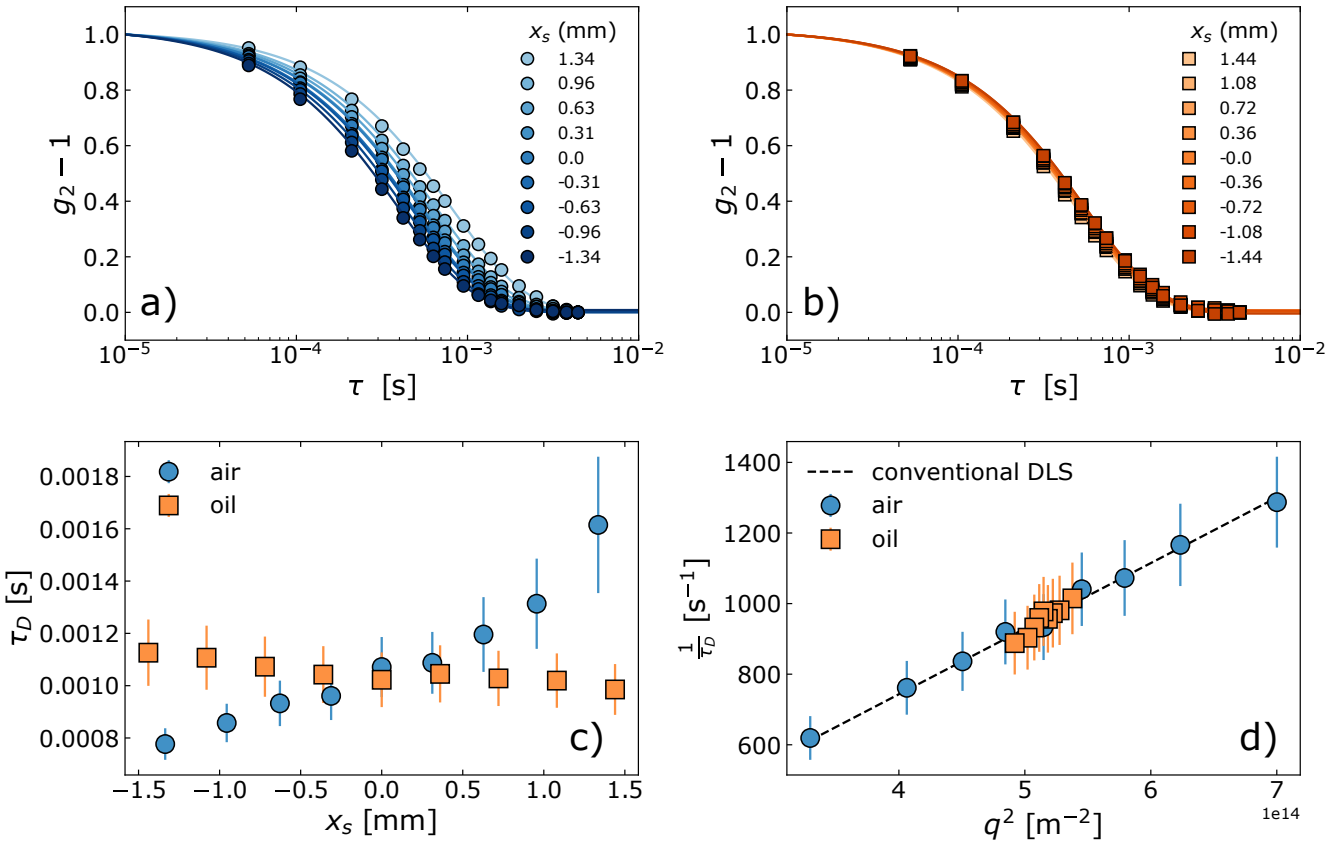

FIG. 3. Intensity correlation functions for a drop of diluted suspension of Brownian particles surrounded by air (a) and oil (b), respectively. Symbols are experimental data and solid lines are fits to the data with a single exponential decay, Eq. 6. (c) Decay time of $g_2 - 1$ as a function of position inside the drop, with $x_S = 0$ the center of the drop. (d) Inverse of the decay time of $g_2 - 1$ as a function of q^2. The dotted line shows $1/\tau_D = D_0 q^2$, as predicted for dilute particles undergoing Brownian diffusion, with the diffusion coefficient D_0 independently measured by conventional dynamic light scattering at $\theta_S = 90$ deg on the same suspension, but contained in a standard DLS cuvette. In c) and d), error bars are estimated from the covariance matrix of the fit.

strain increment $\Delta\varepsilon$. Note that in writing Eq. 10 we have dropped inessential prefactors, keeping in mind that the final expression for the correlation function has to be normalized such that $g_2 - 1 \to 1$ for $\Delta\varepsilon \to 0$.

In our setup, the pixel size corresponds roughly to the speckle size, and both are $<< R$. Given that the intensity value does not change significantly within a speckle [33], the integral in Eq. 10 may be simplified by recognising that I and $\Delta\mathbf{u}$ depend essentially only on position along the segment PT. Thus, the 3D integration over V_P may by replaced by a one-dimensional integration over the scalar $l \in [0, 1]$ that parametrizes the position along PT:

$$\mathbf{x}(l) = l(\mathbf{OP} - \mathbf{OT}) + \mathbf{OT}\,, \tag{11}$$

with $\mathbf{x}(0) = \mathbf{OT}$ and $\mathbf{x}(1) = \mathbf{OP}$ (see Appendix B for expressions of the coordinates of P and T). Furthermore, we note that the scattered intensity $I(\mathbf{x}, \mathbf{q})$ is proportional to $I_0(\mathbf{x})$, the $\mathbf{x}$-dependent intensity of the incident beam. The proportionality factor accounts for the q dependence of the scattered light; in this context, this proportionality factor is unimportant, since it may be included in the normalization of $g_2 - 1$. Given that the incident beam has a Gaussian profile and dropping again inessential prefactors, one has

$$I_0[\mathbf{x}(l)] \propto \exp\left\{-\frac{2\left[y(l)^2 + z(l)^2\right]}{w_0^2}\right\}. \tag{12}$$

In writing Eq. 12, we have used the fact that the incoming beam is mildly focused, such that the Rayleigh range is comparable to the drop diameter and the cross section w of the beam is nearly constant and equal to the beam waist w_0. With these assumptions, Eq. 10 simplifies to

$$g_2(\mathbf{P}, \Delta\varepsilon) - 1 \propto \left| \int_0^1 e^{-i\mathbf{q}\cdot\Delta\mathbf{u}[\mathbf{x}(l),\Delta\varepsilon]} \exp\left\{-\frac{2\left[y(l)^2 + z(l)^2\right]}{w_0^2}\right\} \mathrm{d}l \right|^2 . \tag{13}$$

The displacement field for the compression or expan-

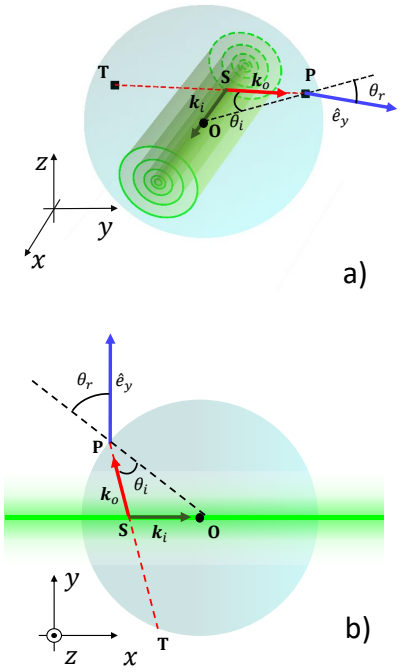

FIG. 4. a): 3D view of the scattering from a water-based sample surrounded by air. The green concentric cylinders represent the incoming laser, which has a Gaussian radial profile. Scattered light emerging in P is issued by all points lying on the segment PT (red dotted line), which is colinear with the scattered light wave vector $\mathbf{k}_o$. The blue line shows the propagation direction of the scattered light travelling outside the sphere along the $\hat{e}_y$ direction, before being imaged on the camera sensor by the collection optics (not shown). The black dashed line shows the perpendicular to the drop surface through point P. b): Top view of a).

sion of a homogeneous, purely elastic sphere reads [42]

$$\begin{cases} \Delta\mathbf{u}(\mathbf{x},\Delta\varepsilon) = \left[C_1(\Delta\varepsilon)r + \frac{C_2(\Delta\varepsilon)}{r}\right]\hat{r}\,, r \geq r_c \\ \Delta\mathbf{u}(\mathbf{x},\Delta\varepsilon) = 0\,, r < r_c \end{cases} \tag{14}$$

with $r = |\mathbf{x}|$, $\hat{r} = \mathbf{x}/r$, r_c the radius of an incompressible core, and C_1, C_2 two constants such that

$$\begin{cases} C_1 = -\frac{C_2}{r_c^3} \\ C_2 = R_i\Delta\varepsilon\left(-\frac{R_i}{r_c^3} + \frac{1}{R_i^2}\right) \end{cases} \tag{15}$$

where R_i is the initial radius of the sphere. Mathematically, r_c is introduced to avoid the divergence of $\Delta\mathbf{u}$ at the sphere center; physically, is accounts for the fact that the continuum medium description of Eq. 14 must break down at the structural length scale of the gel. In practice, we expect r_c to be of the order of the monomer size or the mesh size at most; we checked that varying r_c in the range 10^{-9}—10^{-5} m, $\Delta\mathbf{u}$ and hence $g_2 - 1$ do not vary appreciably.

Equation 13, together with the expressions for the displacement field, Eqs. 14-15, may be solved numerically to obtain the decay of $g_2 - 1$ as a function of the strain increment $\Delta\varepsilon$ or, assuming a constant expansion or contraction rate $\dot{\varepsilon}$, for increasing time lags $\tau = \Delta\varepsilon/\dot{\varepsilon}$. Note that $g_2 - 1$ is insensitive to the sign of $\Delta\varepsilon$, i.e. the same correlation function is recovered for compression or expansion, provided that $|\Delta\varepsilon|$ is the same.

Equation 13 holds quite generally and may be used to compute $g_2 - 1$ for various kinds of dynamics, using the suitable expression for $\Delta\mathbf{u}$. For the case of expansion or contraction discussed here, we show in Appendix B that an approximated analytical solution can be found for Eq. 13, provided that one uses a simplified expression for the displacement field, dropping the $1/r$ term in Eq. 15 and assuming

$$\Delta\mathbf{u}(\mathbf{x},\Delta\varepsilon) = \mathbf{x}\Delta\varepsilon\,. \tag{16}$$

Under this hypothesis, we show in Appendix B that the correlation function decays as a Gaussian function:

$$g_2(\tau) - 1 = \exp\left[-2\left(\frac{\tau}{\tau_E}\right)^2\right], \tag{17}$$

where the relaxation time τ_E depends on the position of point P, the strain rate $\dot{\varepsilon}$, the scattering vector $\mathbf{q}$ and the beam waist w_0, see Eq. B9.

The triangles in Fig. 5a show an example of the intensity correlation function $g_2(\mathbf{P},\tau)-1$ obtained numerically using the laser beam parameters of our setup, for a point $\mathbf{P} = (0.001, 0.9999, 0.001)$ mm on a sphere with $R = 1$ mm, refractive index $n = 1.33$, and surrounded by water, $n_m = 1.33$. The strain increment varies in the range $10^{-4} \leq \Delta\varepsilon \leq 6.3 \times 10^{-3}$ and $g_2 - 1$ is plotted as a function of time delay τ, assuming expansion or contraction at a constant rate $\dot{\varepsilon} = 5 \times 10^{-4}$ s^{-1}. The continuous line shows a fit to the the numerical data with Eq. 7, yielding $\tau_E = 6.15$ s and $\beta = 2$. The dotted line shows the approximated analytical solution, Eq. 17, where the relaxation time τ_E has been calculated based on the same parameters as for the numerical calculations, using Eq. B9. We find that the approximated analytical form is indistinguishable from both the numerical calculation and its fit, indicating that for the typical experimental parameters of our measurements the simplified expression of the displacement field, Eq. 16, is in excellent agreement with the full expression.

Finally, to demonstrate the impact on $g_2 - 1$ of the refractive index mismatch between the gel bead and the surrounding medium, we show in Fig. 5b the decay time τ_D obtained from the numerical $g_2 - 1$ as a function of the position in the bead, for different surrounding media: air, water and oil. In the center of the bead ($x_S = 0$), we obtain the same decay time independently of n_m, as expected since in this position the scattering angle, and hence q, does not depend on n_m, see Fig. 1b. For $x_S \neq 0$, τ_D depends in general on the refractive index mismatch. For $n_m = n = 1.33$, which is the case of hydrogel beads

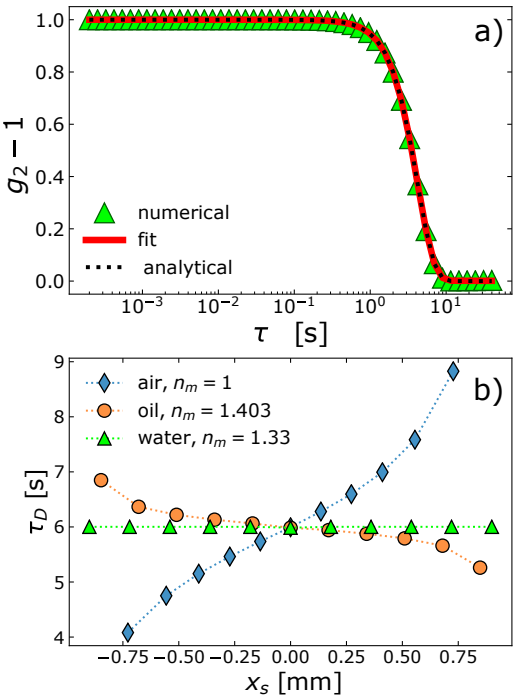

FIG. 5. a) Symbols: intensity correlation function calculated numerically for a water-based spherical bead of gel in water undergoing contraction or expansion at a fixed strain rate, see text for details. The red solid line is a fit to the data using Eq. 7, yielding $\tau_E = 6.15$ s and $\beta = 2$. The black dotted line is $g_2 - 1$ obtained via the analytical approximation of Eq. 17. b) Decay time τ_D as a function of position obtained from the numerical $g_2 - 1$, for different surrounding media, as indicated by the lablel.

immersed in water (green triangles in Fig. 5b), τ_D is independent of position. By contrast, for a sample surrounded by air, $n_m = 1$, the decay time varies by more than a factor of two along the bead diameter, reflecting the change in q. For a sphere surrounded by oil, $n_m = 1.403$, a reverse trend of $\tau_D(x_S)$ is seen (compare the blue diamonds and the orange circles), since $n_m - n$ has an opposite sign compared to the case of a bead in air. Note also that the variation of τ_D is smaller, since the refractive index mismatch is lesser.

B. Experiments: Materials

Polyacrylamide gels are prepared by copolymerization of acrylamide (46.03 g/L) as a monomer and methylenebisacrylamide (0.373 g/L) as a co-monomer in the presence of tetramethylenediamine (0.6 g/L) and sodium persulfate (0.93 g/L) as initiators in water. All chemicals are quickly mixed together and a 30 μL drop of the solution is injected in an Eppendorf tube, filled with poly(methylhydrosiloxane) oil, where polymerization occurs. The oil has been previously saturated with nitrogen, since polymerization is inhibited by oxygen. The oil mass density is nearly equal to that of water (1006 kgkg m^{-3} g/mL at 25 °C), such that gravity effects are negligible and the drop has a spherical shape, due to surface tension. Changing the relative amounts of the monomer and co-monomer allows one to tune the gel mechanical properties; the beads used here have an elastic modulus $G_0 = 700$ Pa [43]. The mesh size of the gel, defined as the average distance between two crosslinks and obtained from mechanical measurements, is $\zeta \approx (k_B T/G_0)^{\frac{1}{3}} \approx 20$ nm.

The gel bead is first shrunk by letting it dry in air for about 1 hour. During this phase, the bead rests on a super-hydrophobic substrate prepared as described in Sec. III A and placed in the sample chamber left open, resulting in a $\sim 14\%$ decrease of the bead radius. The sample chamber, an optical glass box of size $5 \times 5 \times 5$ cm^3, is then filled with water, initiating swelling and defining the experiment time $t = 0$. All measurements are performed in a room where $T = 22.0 \pm 0.1$°C. In order to keep illuminating the bead in its equatorial plane all along the swelling process, the bead is translated upwards using a micrometric vertical translation stage in between the acquisition of series of speckle images.

C. Experimental results

We first show in Fig. 6 the microscopic relaxation time measured during the last 14 minutes of the drying phase that precedes the swelling experiment. Remarkably, we find that τ_D is in very good agreement with both the spatial trend and the magnitude predicted for the microscopic relaxation time for a purely elastic sphere undergoing isotropic contraction. In the following, for the sake of simplicity, we shall refer to the radial displacement field associated with the contraction or expansion of such a homogeneous, purely elastic sphere as to the "affine dynamics", and shall term "non-affine dynamics" any microscopic displacements that may add up to the affine component. Note that, although strictly speaking the strain field for an expanding or contracting sphere is not purely affine due to the $1/r$ term in the r.h.s. of Eq. 14, in practice in our experiments this term is negligible, justifying this terminology. The data in Fig. 6 thus demonstrate that the microscopic dynamics during the late stages of drying are essentially purely affine, with a local strain rate that is identical to the macroscopic one regardless of x_S. This suggests that any radial gradients in solvent content that may have developed in the initial stages of drying have relaxed by the time the swelling experiment starts.

Figure 7 describes the gel behavior during the swelling phase. The time evolution of the radius of the gel bead as obtained from the speckle images is shown in Fig. 7a. At $t = 0$ the bead radius is $R_0 = 2.08$ mm; as the gel absorbs water and swells, R grows reaching $R_\mathrm{f} = 2.63$ mm at the end of the experiment, corresponding to a maximum engineering strain $\varepsilon_\mathrm{sw} = (R_\mathrm{f} - R_0)/R_0 = 28\%$.

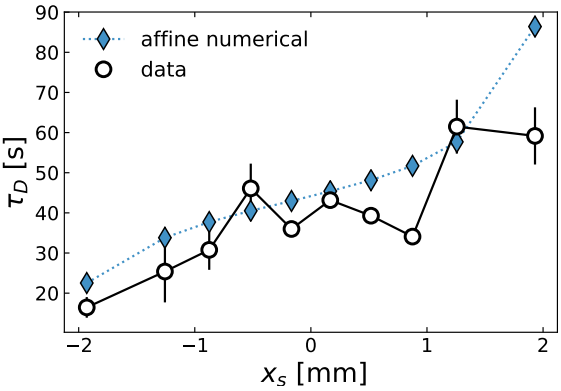

FIG. 6. Decay time τ_D as a function of position for a bead of polymer gel drying at a rate $\dot{\epsilon} = 4.3 \times 10^{-5}$ s^{-1}. Empty circles are experimental data, blue diamonds are numerical results obtained using Eqs. 13-15 for a homogeneous, purely elastic sphere undergoing compression at the same rate as in the experiments.

During swelling, the radius growth can be very well fitted by $R(t) = R_0 + Ct^{\gamma}$, with R_0 fixed to $= 2.08$ mm and $C = 0.076 \pm 0.022$ mm min$^{-\gamma}$ and $\gamma = 0.35 \pm 0.06$ fitting parameters. The sublinear growth of R is similar to that reported by Bertrand *et al.* [23] for the swelling of commercial polyacrylamide hydrogel beads, with an exponent closer to the theoretical predictions of Ref. [23]($\gamma = 0.38$), rather than the experimental observations therein ($\gamma = 0.45$). The macroscopic swelling rate $\dot{\varepsilon} = R(t)^{-1}\mathrm{d}R/\mathrm{d}t$ obtained from the fit to $R(t)$ is shown as a red line in the inset of Fig. 7a: it is essentially indistinguishable from a power law decay $\dot{\varepsilon} \propto t^{-0.69}$ and is in very good agreement with the swelling ratio obtained at selected t by measuring the increment of R over a time interval Δt directly from the speckle images, using $\Delta t \approx 3.5$ min for the first two points and $\Delta t \approx 14$ min for $t \geq 15$ min.

To gain insight on the swelling phenomenon at the microscopic level, we inspect correlation functions measured at various t and positions in the gel. Since the hydrogel is immersed in water, the solvent refractive index is the same of that of the surrounding medium, $n = n_m$. Thus, there are no refractive effects: regardless of x_S, the dynamics are probed at the same scattering vector $\mathbf{q}$, corresponding to a typical length scale $1/q \approx 45$ nm, comparable to a few mesh sizes. In Figure. 7b we plot the intensity correlation functions for a region in the center of the bead, $x_S = 0$, and various t. During swelling, the correlations functions decay much faster than for a quiescent gel, compare the colored symbols to the grey right triangles. This indicates that, due to the interconnected structure of the gel, stresses due to swelling generate strain fields and microscopic rearrangements throughout the whole network, even at the beginning of the experiment, where swelling presumably is occurs preferentially at the gel periphery. Over the duration of experiment (6 hours), the dynamics slow down by more than one order of magnitude, mirroring the decrease of the macroscopic expansion rate $\dot{\varepsilon}$ shown in the inset of Fig. 7a. We quantify the microscopic dynamics by fitting $g_2 - 1$ to a stretched exponential function, Eq. 7, expressing the microscopic decay time as τ_D, calculated using Eq. 8. We find that the decay time τ_D increases with time by an order of magnitude, ranging from 4.44 s to 47.34 s at $t = 360$ min. Concomitantly, the stretching exponent evolves from $\beta \approx 1$ in the early stages of swelling to $\beta \approx 1.5$ for $t \geq 90$ min (inset of Fig. 7b).

We find that the microscopic dynamics have a non-trivial spatio-temporal dependence. Figure 7c displays the characteristic relaxation time τ_D at different times during the swelling process, as a function of position x_S along the bead diameter. The slowing down of the microscopic dynamics as the gel swells, observed in the center of the bead, is seen at all x_S. However, at the beginning of the swelling process the microscopic dynamics clearly depend on position: τ_D is roughly two times smaller near the bead edges as compared to in the center. This space dependence becomes weaker with time, and eventually vanishes: nearly uniform microscopic dynamics are recovered 180 min from the beginning of the experiment.

As discussed at the beginning of Sec. IV, our setup does not allow one to separately measure the dynamics along the radial direction and perpendicularly to it, which makes it difficult to directly asses the relative importance of affine and non-affine dynamics. The data shown in Figs. 8b,c, however, already point to deviations from affinity: indeed, we recall that for affine dynamics $\beta = 2$ as opposed to $\beta \lesssim 1.5$ as measured here, and that for $n = n_m$ τ_D should be independent of position (see the triangles in Fig. 5b), which is not the case in our experiments, at least in the initial stages of swelling, see Fig. 8c. To further investigate deviations from affinity, we compare τ_D as obtained in the swelling experiment to the theoretical relaxation time for purely affine dynamics, which we calculate using Eqs. 13-15 with $\Delta\varepsilon = \tau\dot{\varepsilon}$, where $\dot{\varepsilon}$ is the experimental macroscopic strain rate. Figure 8d compares the theoretical relaxation time of affine dynamics (line) to the experimental relaxation time $< \tau_D >$, obtained by averaging over space τ_D. The experimental dynamics are up to a factor of ten faster than the theoretical prediction. Furthermore, for affine motion τ_D is inversely proportional to $\dot{\varepsilon}$, see Fig. 7d and Eq. B9, while the experimental $< \tau_D >$ clearly deviates from such a $\dot{\varepsilon}^{-1}$ dependence.

These discrepancies indicate that additional non-affine relaxations occur during the swelling process. In order to quantify non-affine dynamics, we assume that the affine and non-affine contributions to $g_2 - 1$ are uncorrelated. Accordingly, the intensity correlation function may be factorized:

$$g_2(\Delta\varepsilon, \mathbf{q}) - 1 = \left[g_2^{aff}(\Delta\varepsilon, \mathbf{q}) - 1\right] \left[g_2^{n.a.}(\Delta\varepsilon, \mathbf{q}) - 1\right] , \tag{18}$$

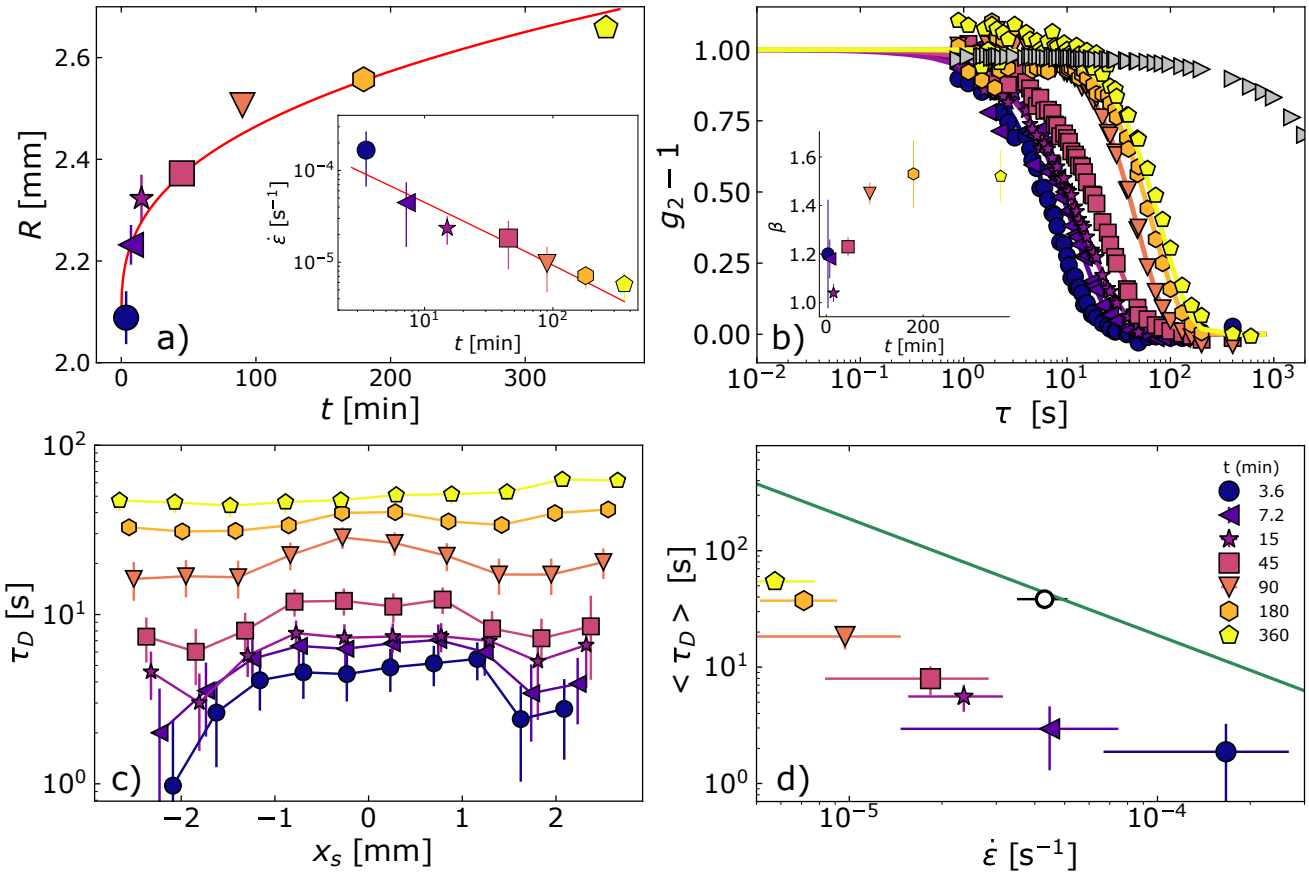

FIG. 7. (a) Radius of a swelling polyacrylamide gel bead as function of time. The line is a power law fit to the increment of R, see the text for details. Inset: strain rate as a function of time, measured directly from the speckle images (symbols) or by differentiating the power law fit of the main panel (line). Error bars represent the uncertainty of the gel boundary as measured from the speckle images. (b) Intensity correlation functions measured during the swelling of the bead, for a ROI located at the center of the bead, $x_S = 0$. The solid lines are fits with Eq. 7, yielding $\tau_D = 4.44$, 6.52, 7.25, 12.04, 27.94, 39.86, 47.34 s and $\beta = 1.20$, 1.18, 1.04, 1.23, 1.45, 1.53, 1.52 for the t values shown by the labels in panel d). The grey right triangles show $g_2 - 1$ for a gel where swelling is prevented, see Sec. II D (same data as in Fig. 2). Inset: time dependence of the stretching exponent β. (c) Decay time τ_D as a function of position x_S along the bead diameter, same symbols and colors as in b) and d). (d) Decay time τ_D averaged over position x_S, as a function of strain rate $\dot{\varepsilon}$. Error bars on $< \tau_D >$ are the standard deviation of the data shown, for each t, in c). The green line is the decay time expected for the expansion of a purely elastic, homogeneous sphere, as obtained by fitting correlation functions calculated numerically by inserting the experimental $\dot{\varepsilon}$ in Eq. 13. The empty circle is $< \tau_D >$ for the shrinking gel measured during drying, obtained form the data of Fig. 6.

where the superscripts aff and $n.a.$ indicate affine and non-affine contributions, respectively. By dividing the experimental $g_2 - 1$ by the affine correlation function $g_2^{aff}(\Delta\varepsilon, \mathbf{q}) - 1$ obtained numerically using the macroscopic strain rate $\dot{\varepsilon}$, we obtain the non-affine correlation function. Figure 8a shows an example for $\dot{\varepsilon} = 5.74 \times 10^{-6}$ s^{-1}, the strain rate for which the experimental and theoretical decay times are closest and thus the difference between $g_2^{n.a.} - 1$ and the experimental correlation function are the largest. Even in this case, the experimental correlation function is very close to its non-affine contribution, reflecting the fact that non-affine dynamics dominate the relaxation of $g_2 - 1$, as already inferred from Fig. 8d.

A thorough interpretation of the non-affine dynamics would require collecting data at different q vectors, which would allow one, e.g., to unambiguously distinguish between diffusive and ballistic dynamics. Unfortunately, this is not possible with our setup, due to the limitations imposed by the spherical shape of the gel beads. To make progress, we assume that, for any given $\Delta\varepsilon$ (or, equivalently, any τ), the probability distribution of the non-affine displacements is Gaussian. This hypothesis is motivated by previous work on polyacrylamide gels seeded with ∼micron-sized tracer particles and submitted to a shear strain [41]. The particle displacements where found to have both an affine and a non-affine component, the latter being distributed according to a Gaussian function. Under this assumption, the intensity correlation function depends on the (non-affine) particle mean

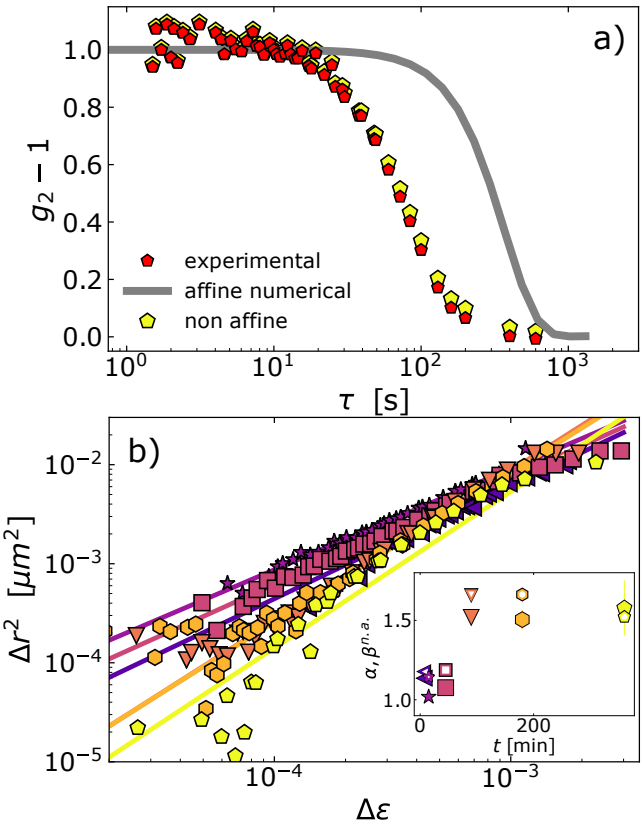

FIG. 8. (a) Intensity correlation functions for a polymer gels swelling at rate $\dot{\varepsilon} = 5.73 \times 10^{-6}$ s^{-1}. Gray solid line: theoretical intensity correlation function for purely affine dynamics; small red symbols: experimental $g_2 - 1$ for $x_S = 0$; large yellow symbols: corresponding intensity correlation function for the non-affine displacements only, calculated using Eq. 18. (b) Non-affine mean square displacement Δr^2 obtained via Eq. 19 as a function of the strain increment $\Delta\varepsilon$ during swelling. The solid lines are power law fits, $\Delta r^2 \propto \Delta\varepsilon^{\alpha}$, the exponent α is shown in the inset (solid symbols), together with $\beta^{n.a.}$ (open symbols), the stretching exponent obtained by fitting $g_2^{n.a.} - 1$ with a stretched exponential. In both the main plot and the inset the symbols are as in Fig. 7.

square displacement $\Delta r^2(\Delta\varepsilon)$ as

$$g_2^{n.a.}(\Delta\varepsilon, \mathbf{q}) - 1 = \exp\left[-2(\Delta r^2 q^2)/3\right] , \qquad (19)$$

a result easily obtained from standard dynamic light scattering theory [44, 45] by replacing the usual time delay τ by $\Delta\varepsilon = \tau\dot{\varepsilon}$.

We show in the double-logarithmic plot of Fig. 8b the non-affine mean square displacement $\Delta r^2(\Delta\varepsilon)$ for $x_S = 0$, obtained from Eq. 19 using $g_2^{n.a.} - 1$ calculated according to Eq. 18 (data for $t = 3.6$ min are omitted because they are too noisy). The lines are power law fits to the data, yielding an exponent α, whose t dependence is shown by the solid symbols in the inset. In the initial stages of swelling, $\alpha \approx 1$, indicative of diffusive dynamics, consistent with the shape of $g_2^{n.a.} - 1$, for which a fit with Eq. 7 yields an exponent $\beta^{n.a.}$ close to one, as expected for a diffusive process [44, 45] (see the open symbols in the inset of Fig. 8b). However, for $t \geq 90$ min, both α and $\beta^{n.a.}$ significantly deviate from unity, approaching or even exceeding a value of 1. These values are not compatible with diffusive dynamics. Rather, $\beta \approx 1.5$ has been reported for the ballistic dynamics attributed to the strain field resulting from the relaxation of internal stresses in a variety of amorphous systems. In this case, the probability distribution of the particle displacements at fixed τ (corresponding to fixed $\Delta\varepsilon$ in our case) is described by a Levy law, with a power-law decaying wing $\sim \Delta r^{-(\beta+1)}$ at large Δr [32]. This non-Gaussian distribution is incompatible with the assumptions underlying Eq. 19, which was used to calculate the mean squared displacements shown in Fig. 8b. Accordingly, one should be cautious in commenting the value of the exponent α for the latest stages of swelling. However, it is worth pointing out that $\alpha > 1$ indicates supradiffusive behavior, thus confirming that in the late stages of swelling the microscopic dynamics are non-diffusive.

Finally, we can relate the mean square displacement related to the non affine motion, to the macroscopic imposed strain $\Delta\varepsilon$, which is defined as $\Delta\varepsilon = \tau\dot{\varepsilon}$. In Fig. 8b we plot the mean square displacement Δr^2 as a function of the incremental strain $\Delta\varepsilon^2$. Remarkably, we find a linear growth of the mean square displacement with the square of the imposed displacement $\Delta r^2 \sim \Delta\varepsilon^2$, which is the analogous of ballistic dynamics in the time domain. So, while at the macroscopic scale, the expansion of the bead is sub-diffusive (the growth scales as $t^{0.35}$), the local microscopic motion of the gel network, at the scale of the mesh size, is dominated by ballistic non affine displacements. This behavior reflects the elastic response of an heterogeneous medium to an external strain. Indeed, the same ballistic-like of the microscopic mean square displacements has been found for polymer gels under shear [41] and many other jammed systems such as colloidal gels and glasses [3, 46–48] and polymer glass [49].

This finding is particularly intriguing: at the macroscopic scale, the behavior of the bead is sub-diffusive (the bead growth scales as $t^{0.35}$) during swelling), whereas the local motion of the gel , at the scale of the mesh size, is dominated by ballistic non affine displacements.

V. CONCLUSIONS

We have presented a new dynamic light scattering apparatus specifically designed for probing soft matter systems within a millimetric drop. By combining Photon Correlation Imaging [1], the use of a thin incident beam, and a carefully designed collection optics, we have addressed the challenges posed by the small radius of curvature of the sample-surrounding medium interface, which acts as an additional refractive element. The setup allows for measuring the dynamics coarse-grained over regions of interest that typically correspond to sections of

the incident beam of length 250-500 μm. For the central ROI, the scattering angle is 90 deg; the scattering angle associated to the other ROIs depend on the refractive index contrast between the sample and the surrounding medium; typical deviations from 90 deg are up to ± 30 deg. Thus, the length scales probed by the setup are of the order of a few tens of nm. Given the sample geometry, spatial resolution requires the scattered light to be collected from the side: it would be impossible to significantly extend the range of accessible q vectors, e.g. to smaller angles, while retaining PCI capabilities. The accessible time scales are dictated by the use of a CMOS detector: using a fast camera, the smallest delay time can be of the order of 10^{-4} s or shorter. On the other hand, the setup is sufficiently stable to probe relaxation process as slow as several thousands of seconds. Finally, the multispeckle method used to calculate $g_2 - 1$ drastically reduces the averaging time, such that time-varying dynamics, e.g. during gelation, drying or swelling, can be thoroughly characterized.

Measurements on a drop of non-evaporating, diluted Brownian suspension, for which spatially homogenous dynamics are expected, showed instead a variation of the DLS relaxation time according to position within the drop. This effect, however, was fully accounted for by considering the x_S dependence of the scattering vector: we have shown that data for the suspension drop are in excellent quantitative agreement with measurements on the same sample but using a conventional cuvette and a commercial DLS apparatus.

After validating the setup on the Brownian system, we demonstrated some of its capabilities by studying the swelling of a polymer gel upon re-hydration. We found an asymmetry between shrinking and swelling. Thanks to the comparison with a theoretical and numerical analysis of DLS from a homogeneous elastic sphere under strain, we showed that during shrinking the dynamics are affine. Quite remarkably, this implies that the same deformation field holds on length scales ranging from the macroscopic drop radius down to a few tens of nm. By contrast, during swelling the microscopic dynamics are up to one order of magnitude faster than those inferred from the macroscopic affine strain field, presumably reflecting the extra degree of freedom available to the chains as their local configurations become less constrained during swelling. As in previous works [**?**], we found that swelling is spatially heterogeneous, starting from the gel periphery and propagating inwardly as time proceeds. Our space-resolved measurements of the dynamics, unavailable in previous works, point however to a scenario more complex than expected: at the microscopic level, rearrangements and chain displacements are not limited to the swelling shell, but also occur in the core, albeit at a slower rate.

Overall, the results presented here demonstrate the potentiality of the setup for investigating microscopic dynamics in millimeter-sized spherical samples. A key feature is the possibility of collecting data with both temporal and spatial resolution, making the apparatus an ideal tool for understanding the rich phenomenology occurring in a wide range of applications and phenomena, from the drying of drops of colloidal or biological suspensions, aggregation phenomena e.g. in the production of suprparticles for industrial applications, to polymer drops degradation or gel syneresis and swelling.

ACKNOWLEDGMENTS

We thank J. Barbat for help in designing and building the sample environment, C. Kindelberger for help in measuring the setup stability, and C. Ligoure and P. Olmsted for enlightening discussions. We acknowledge financial support from the French Agence Nationale de la Recherche (ANR) (Grant No. ANR-19-CE06-0030-02, BOGUS). LC gratefully acknowledges support from the Institut Universitaire de France.

Appendix A: Calculation of the scattering vector

With reference to Fig. 4b, we calculate the scattering vector q for a ray emerging from the drop in $P = (x_P, y_P, z_P)$ and propagating along the y axis. With no loss of generality, we shall assume that the camera is placed in the $y > 0$ half-space and that the scattering angle θ_s, the angle of incidence θ_i and the angle of refraction θ_r are taken to be non-negative, implying $0 \leq \theta_s \leq \pi$, $0 \leq \theta_i \leq \pi/2$, $0 \leq \theta_r \leq \pi/2$. The unit vector associated with P is

$$\hat{r}_P = \frac{x_P \hat{e}_x + y_P \hat{e}_y + z_P \hat{e}_z}{\sqrt{x_P^2 + y_P^2 + z_P^2}}\,, \tag{A1}$$

which also defines the outgoing normal to the drop surface in P. The angle of refraction satisfies

$$\cos\theta_r = \hat{e}_y \cdot \hat{r}_P \equiv A\,. \tag{A2}$$

The angles of refraction and of incidence are thus given by

$$\theta_r = \arccos A\,, \tag{A3}$$

$$\theta_i = \arcsin\left(\frac{n_m}{n}\sin\theta_r\right)\,, \tag{A4}$$

where in writing Eq. A4 we have used Snell's law, with n and n_m the refractive indices of the drop and of the surrounding medium, respectively.

For the special case $n = n_m$, the scattering angle is $\theta_s = \pi/2$ for all x_P. Similarly, $\theta_s = \pi/2$ for $x_P = 0$ and arbitrary n, n_m. For these cases, $\hat{k}_o = \hat{e}_y$, with $\hat{k}_o$ the unit vector along the direction of the scattered light in the drop. It is then straightforward to calculate $\mathbf{q}$ using Eq. 2. For all the other cases, it is convenient to express

$\hat{k}_o$ as a linear combination of the two unit vectors $\hat{r}_P$ and $\hat{e}_y$:

$$\hat{k}_o = a\hat{r}_P + b\hat{e}_y\,, \tag{A5}$$

with a and b two coefficients to be determined. Figure 4b shows that

$$\begin{aligned} \hat{k}_o \cdot \hat{r}_P &= \cos\theta_i \\ \hat{k}_o \cdot \hat{e}_y &= \cos(\theta_r - \theta_i)\,. \end{aligned} \tag{A6}$$

By inserting Eqs. A2 and A5 into Eqs. A6, one has

$$\begin{aligned} a + bA &= \cos\theta_i \\ aA + b &= \cos(\theta_r - \theta_i)\,. \end{aligned} \tag{A7}$$

For the ease of writing, we define $B = \cos\theta_i$ and $C = \cos(\theta_r - \theta_i)$ and solve Eqs. A7 for a and b, finding

$$\begin{aligned} a &= \frac{B - AC}{1 - A^2} \\ b &= \frac{C - AB}{1 - A^2}\,. \end{aligned} \tag{A8}$$

Equations A8, together with $\mathbf{k}_o = 2\pi n\lambda^{-1}\hat{k}_o$ and Eqs. A1 and A5 allow for calculating the scattering vector for scattered light being imaged on the camera detector after emerging from the drop in x_P and having propagated along the y direction, for the general case $\hat{k}_o \neq \hat{e}_y$.

Appendix B: Determination of analytical $g_2 - 1$

We aim at calculating an analytical expression of the intensity correlation function $g_2 - 1$ for the light scattered by a contracting or expanding sphere and emerging in point P, as shown in Fig. 4. We assume in the following that the strain field within the sphere is that of an ideal solid, i.e. we calculate only the contribution to $g_2 - 1$ due to affine displacements. As shown in Fig. 4, light emerging in P is scattered by all points on the PT segment. In our experiments, the incident beam is Gaussian, with a thin cross section (beam waist $w_0 \approx 60$ μm), much smaller than the drop radius R. Thus, most of the scattered light originates from a small portion of PT centered around point S on the x axis. However, to ease the calculation, it is convenient to consider the whole segment PT. Since $w_0 << R$, refraction effects on the incoming beam may be neglected, since they are only relevant for the portions of the incoming beam far from the x axis, whose intensity is vanishingly small. We thus assume that the incident beam within the drop propagates along the $\hat{e}_x$ direction, regardless of the distance from the x axis. This insures that light scattered by any point along PT has the same wave vector $\mathbf{k}_o$ and thus the same scattering vector $\mathbf{q}$.

We start by determining the coordinates of P and T. Experimentally, $g_2 - 1$ is calculated for all pixels belonging to a ROI, i.e. for a set of pixels identified by x_P and z_P, the coordinates of P in the (x, z) plane, which are obtained directly from the CMOS image. Since P lies on the surface of the drop, one has

$$\mathbf{OP} = x_P\hat{e}_x + \sqrt{R^2 - (x_P^2 + z_P)^2}\hat{e}_y + z_P\hat{e}_z\,. \tag{B1}$$

The coordinates of point T are found by imposing that PT is colinear with $\hat{k}_o$ and that T lies on the drop surface, in the $y < 0$ half-space (see Fig. 4). One finds

$$\mathbf{OT} = \mathbf{OP} + \left(2\mathbf{OP}\cdot\hat{k}_o\right)\hat{k}_o\,. \tag{B2}$$

Equation B2, together with Eq. B1 and the expression of $\hat{k}_o$ provided in Appendix A fully determines the coordinates of$T$ for any experimentally chosen (x_P, z_P).

To find an analytical expression for $g_2 - 1$, we need to write the scattered intensity I originating from an arbitrary point $\mathbf{x}$ along PT as a function of the parameter l, see Eq. 12. Using Eqs. 11-12 and the coordinates of P and T given above, one finds

$$I(\mathbf{x}) \propto \exp\Big\{-(Dl^2 + El + F)/(w_0^2/2)\Big\} \tag{B3}$$

where

$$\begin{aligned} D &= (y_T - y_P)^2 + (z_T - z_P)^2 \\ E &= 2z_T(y_T - y_P) + 2y_T(z_T - z_P) \\ F &= y_T^2 + z_T^2\,, \end{aligned} \tag{B4}$$

and where we have omitted all unnecessary prefactors. Finally, we need an expression for the the displacement field $\Delta\mathbf{u}(\mathbf{x}, \Delta\varepsilon)$ in $\mathbf{x}$ corresponding to a change of macroscopic strain $\Delta\varepsilon$. We use a simplified version of Eq. 14, where we drop the second term in the r.h.s., which is typically negligible, finding

$$\Delta\mathbf{u}[\mathbf{x}(l), \Delta\varepsilon] = l\Delta\varepsilon(\mathbf{OT} - \mathbf{OP}) + \Delta\varepsilon\mathbf{OT}\,. \tag{B5}$$

The projection of the displacement onto the scattering vector is then

$$\Delta\mathbf{u}\cdot\mathbf{q} = l\Delta\varepsilon\left[\mathbf{q}\cdot(\mathbf{OT} - \mathbf{OP})\right] + \Delta\varepsilon\big(\mathbf{q}\cdot\mathbf{OT}\big) = \tilde{q}l + K \tag{B6}$$

where we have introduced the strain-dependent generalized wave vector $\tilde{q} = \Delta\varepsilon\left[\mathbf{q}\cdot(\mathbf{OT} - \mathbf{OP})\right]$ and defined $K = \Delta\varepsilon\big(\mathbf{q}\cdot\mathbf{OT}\big)$. By inserting Eqs. B3 and B6 into Eq. 13 and omitting temporarily any normalization factor, we obtain:

$$g_2 - 1 \propto \left|\int_0^1 e^{-i\tilde{q}l}\exp\left\{-(Dl^2 + El + F)/(w_0^2/2)\right\}\mathrm{d}l\right|^2 \tag{B7}$$

which, by extending to $\pm\infty$ the integration limits with no significant change since the integrand is vanishingly small out of $[0, 1]$, is the Fourier transform of a generalized Gaussian function. This Fourier transform has an analytical solution [50]:

$$g_2 - 1 = e^{-2\frac{(w_0^2/2)\tilde{q}}{4D}}\,, \tag{B8}$$

where we have used the correct normalization. Note that in the above expression $g_2 - 1$ depends on $\Delta\varepsilon$ through $\tilde{q}$. Over a time laps short enough for the strain rate $\dot{\varepsilon}$ to be considered constant, one has $\Delta\varepsilon = \tau\dot{\varepsilon}$. Under these conditions, Eq. B8 is of the form of Eq. 7 of the main text with $\beta = 2$ and

$$\tau_E = \frac{2\sqrt{2}\sqrt{(y_T - y_P)^2 + (z_T - z_P)^2}}{\dot{\varepsilon}\,[\mathbf{q}\cdot(\mathbf{OT} - \mathbf{OP})]\,w_0}\,. \qquad \text{(B9)}$$

[1] A. Duri, D. A. Sessoms, V. Trappe, and L. Cipelletti, Resolving long-range spatial correlations in jammed colloidal systems using photon correlation imaging, Physical review letters **102**, 085702 (2009).

[2] A.-M. Philippe, Coupling space-resolved dynamic light scattering and rheometry to investigate heterogeneous flow and nonaffine dynamics in glassy and jammed soft matter, Physical Review Applied **11**, 034073 (2019).

[3] S. Aime, L. Ramos, and L. Cipelletti, Microscopic dynamics and failure precursors of a gel under mechanical load, Proceedings of the National Academy of Sciences **115**, 3587 (2018).

[4] N. Tsapis, E. R. Dufresne, S. S. Sinha, C. S. Riera, J. W. Hutchinson, L. Mahadevan, and D. A. Weitz, Onset of buckling in drying droplets of colloidal suspensions, Physical review letters **94**, 018302 (2005).

[5] S. Basu, L. Bansal, and A. Miglani, Towards universal buckling dynamics in nanocolloidal sessile droplets: the effect of hydrophilic to superhydrophobic substrates and evaporation modes, Soft Matter **12**, 4896 (2016).

[6] F. Boulogne, F. Giorgiutti-Dauphiné, and L. Pauchard, The buckling and invagination process during consolidation of colloidal droplets, Soft Matter **9**, 750 (2013).

[7] O. P. Bamboriya and M. S. Tirumkudulu, Universality in the buckling behavior of drying suspension drops, Soft Matter **19**, 2605 (2023).

[8] C. Sadek, P. Schuck, Y. Fallourd, N. Pradeau, C. Le Floch-Fouéré, and R. Jeantet, Drying of a single droplet to investigate process–structure–function relationships: a review, Dairy Science & Technology **95**, 771 (2015).

[9] E. Huynh, A. Olinger, D. Woolley, R. K. Kohli, J. M. Choczynski, J. F. Davies, K. Lin, L. C. Marr, and R. D. Davis, Evidence for a semisolid phase state of aerosols and droplets relevant to the airborne and surface survival of pathogens, Proceedings of the National Academy of Sciences **119**, e2109750119 (2022).

[10] D. Brutin, B. Sobac, B. Loquet, and J. Sampol, Pattern formation in drying drops of blood, Journal of fluid mechanics **667**, 85 (2011).

[11] W. Liu, M. Kappl, and H.-J. Butt, Tuning the porosity of supraparticles, ACS nano **13**, 13949 (2019).

[12] S. Wooh, H. Huesmann, M. N. Tahir, M. Paven, K. Wichmann, D. Vollmer, W. Tremel, P. Papadopoulos, and H.-J. Butt, Synthesis of Mesoporous Supraparticles on Superamphiphobic Surfaces, Advanced Materials **27**, 7338 (2015).

[13] M. N. Saqib, B. Khaled, F. Liu, and F. Zhong, Hydrogel beads for designing future foods: structure, mechanisms, application, and challenges, Food Hydrocolloids for Health , 100073 (2022).

[14] P. Patel and P. Thareja, Hydrogels differentiated by length scales: A review of biopolymer-based hydrogel preparation methods, characterization techniques, and targeted applications, European Polymer Journal **163**, 110935 (2022).

[15] S. Chatterjee, M. W. Lee, and S. H. Woo, Adsorption of congo red by chitosan hydrogel beads impregnated with carbon nanotubes, Bioresource technology **101**, 1800 (2010).

[16] W. Yan and R. Bai, Adsorption of lead and humic acid on chitosan hydrogel beads, Water Research **39**, 688 (2005).

[17] N. Li and R. Bai, Copper adsorption on chitosan–cellulose hydrogel beads: behaviors and mechanisms, Separation and purification technology **42**, 237 (2005).

[18] S. K. Jain, A. Jain, Y. Gupta, and M. Ahirwar, Design and development of hydrogel beads for targeted drug delivery to the colon, Aaps Pharmscitech **8**, E34 (2007).

[19] N. M. Velings and M. M. Mestdagh, Physico-chemical properties of alginate gel beads, Polymer Gels and Networks **3**, 311 (1995).

[20] D. Lin, A. L. Kelly, V. Maidannyk, and S. Miao, Effect of concentrations of alginate, soy protein isolate and sunflower oil on water loss, shrinkage, elastic and structural properties of alginate-based emulsion gel beads during gelation, Food Hydrocolloids **108**, 105998 (2020).

[21] T. Tanaka and D. J. Fillmore, Kinetics of swelling of gels, The Journal of Chemical Physics **70**, 1214 (1979).

[22] W. Barros, E. N. de Azevedo, and M. Engelsberg, Surface pattern formation in a swelling gel, Soft Matter **8**, 8511 (2012).

[23] T. Bertrand, J. Peixinho, S. Mukhopadhyay, and C. W. MacMinn, Dynamics of swelling and drying in a spherical gel, Physical Review Applied **6**, 064010 (2016).

[24] J. Y. Kim, K. Cho, S.-a. Ryu, S. Y. Kim, and B. M. Weon, Crack formation and prevention in colloidal drops, Scientific reports **5**, 13166 (2015).

[25] M. Milani, T. Phou, C. Ligoure, L. Cipelletti, and L. Ramos, A double rigidity transition rules the fate of drying colloidal drops, Soft Matter **19**, 6968 (2023).

[26] S. K. Patel, F. Rodriguez, and C. Cohen, Mechanical and swelling properties of polyacrylamide gel spheres, Polymer **30**, 2198 (1989).

[27] W. Hong, X. Zhao, J. Zhou, and Z. Suo, A theory of coupled diffusion and large deformation in polymeric gels, Journal of the Mechanics and Physics of Solids **56**, 1779 (2008).

[28] A. Philippe, S. Aime, V. Roger, R. Jelinek, G. Prevot, L. Berthier, and L. Cipelletti, An efficient scheme for sampling fast dynamics at a low average data acquisition rate, Journal of Physics: Condensed Matter **28**, 075201 (2016).

[29] S. Maccarrone, G. Brambilla, O. Pravaz, A. Duri, M. Ciccotti, J.-M. Fromental, E. Pashkovski, A. Lips, D. Sessoms, V. Trappe, *et al.*, Ultra-long range correlations of the dynamics of jammed soft matter, Soft Matter **6**, 5514 (2010).

[30] L. Cipelletti, H. Bissig, V. Trappe, P. Ballesta, and S. Mazoyer, Time-resolved correlation: a new tool for studying temporally heterogeneous dynamics, Journal of

Physics: Condensed Matter **15**, S257 (2002).
[31] P. Linder and T. Zemb, Neutrons, x-rays and light: scattering methods applied to soft condensed matter, Delta Series-Elsevier, Netherlands (2002).
[32] L. Cipelletti, L. Ramos, S. Manley, E. Pitard, D. A. Weitz, E. E. Pashkovski, and M. Johansson, Universal non-diffusive slow dynamics in aging soft matter, Faraday discussions **123**, 237 (2003).
[33] J. W. Goodman, *Speckle phenomena in optics: theory and applications* (Roberts and Company Publishers, 2007).
[34] A.-M. Philippe, D. Truzzolillo, J. Galvan-Myoshi, P. Dieudonné-George, V. Trappe, L. Berthier, and L. Cipelletti, Glass transition of soft colloids, Physical Review E **97**, 040601 (2018).
[35] A. Duri and L. Cipelletti, Length scale dependence of dynamical heterogeneity in a colloidal fractal gel, Europhysics Letters **76**, 972 (2006).
[36] L. Ramos and L. Cipelletti, Ultraslow dynamics and stress relaxation in the aging of a soft glassy system, Physical review letters **87**, 245503 (2001).
[37] J. Gabriel, T. Blochowicz, and B. Stühn, Compressed exponential decays in correlation experiments: The influence of temperature gradients and convection, The Journal of chemical physics **142** (2015).
[38] L. Hoyt, New table of the refractive index of pure glycerol at 20 c, Industrial & Engineering Chemistry **26**, 329 (1934).
[39] J. B. Segur and H. E. Oberstar, Viscosity of glycerol and its aqueous solutions, Industrial & Engineering Chemistry **43**, 2117 (1951).
[40] L. Cipelletti, G. Brambilla, S. Maccarrone, and S. Caroff, Simultaneous measurement of the microscopic dynamics and the mesoscopic displacement field in soft systems by speckle imaging, Optics Express **21**, 22353 (2013).
[41] A. Basu, Q. Wen, X. Mao, T. Lubensky, P. A. Janmey, and A. Yodh, Nonaffine displacements in flexible polymer networks, Macromolecules **44**, 1671 (2011).
[42] A. F. Bower, *Applied mechanics of solids* (CRC press, 2009).
[43] S. Arora, J.-M. Fromental, S. Mora, T. Phou, L. Ramos, and C. Ligoure, Impact of beads and drops on a repellent solid surface: a unified description, Physical Review Letters **120**, 148003 (2018).
[44] B. J. Berne and R. Pecora, *Dynamic light scattering: with applications to chemistry, biology, and physics* (Courier Corporation, 2000).
[45] P. Pusey, Dynamic light scattering, in *Neutron, X-rays and Light. Scattering Methods Applied to Soft Condensed Matter* (Zemb, Thomas and Lindner, Peter, North Holland, 2002) elsevier ed.
[46] R. Besseling, E. R. Weeks, A. Schofield, and W. Poon, Three-dimensional imaging of colloidal glasses under steady shear, Physical review letters **99**, 028301 (2007).
[47] M. Laurati, K. J. Mutch, N. Koumakis, J. Zausch, C. P. Amann, A. B. Schofield, G. Petekidis, J. F. Brady, J. Horbach, M. Fuchs, *et al.*, Transient dynamics in dense colloidal suspensions under shear: Shear rate dependence, Journal of Physics: Condensed Matter **24**, 464104 (2012).
[48] F. Varnik, Structural relaxation and rheological response of a driven amorphous system, The Journal of chemical physics **125**, 164514 (2006).
[49] H.-N. Lee, K. Paeng, S. F. Swallen, and M. Ediger, Direct measurement of molecular mobility in actively deformed polymer glasses, Science **323**, 231 (2009).
[50] H. Bateman, *Tables of Integral Transforms [Volumes I & II]*, edited by A. Erdélyi, Vol. I & II (McGraw-Hill Book Company, New York, 1954).
[51] *Neutron, X-rays and Light. Scattering Methods Applied to Soft Condensed Matter*, elsevier ed. (Zemb, Thomas and Lindner, Peter, North Holland, 2002).
[52] D. Larobina, A. Pommella, A.-M. Philippe, M. Y. Nagazi, and L. Cipelletti, Enhanced microscopic dynamics in mucus gels under a mechanical load in the linear viscoelastic regime, Proceedings of the National Academy of Sciences **118**, e2103995118 (2021).
[53] M. Engelsberg and W. Barros Jr, Free-evolution kinetics in a high-swelling polymeric hydrogel, Physical Review E **88**, 062602 (2013).

Chapter 4

Preparation & Characterization of Beads of Colloidal Gel

4.1 Gel preparation

In this section we present the protocol used to prepare our samples. We first present the method followed to produce colloidal gels in standard containers (capillaries, NMR tubes or rheometer tools). We then focus on how, starting from the same protocol, to prepare beads of colloidal gel. Finally we briefly discuss the experimental difficulties encountered in the preparation.

4.1.1 Standard preparation in a closed container

Here we describe the standard procedure to prepare colloidal gels in a capillary or in the plate-plate geometry of the rheometer. We use a commercial, charge stabilized, colloidal suspension Ludox SM-30, from Sigma Aldrich®. The colloidal particles are suspended in water. They have nominal diameter $2a = 6$ nm. The particles aggregation is triggered by destabilizing the suspension through an urea-urease reaction [Wyss et al. (2004)]. To do so we add to the suspension a solution of urea such that, in the mixture, the concentration of urea is 1 M. We also add the enzyme Urease (U 5378) from Canavalia ensiformis, from Sigma Aldrich®, at a fixed concentration (m_e =30 U/ml). The enzymatic reaction of urea in water reads:

$$CO(NH_2)_2 + 2H_2O \rightleftharpoons NH_4^+ + NH_3 + HCO_3^- \tag{4.1}$$

where $CO(NH_2)_2$ is urea, H_2O is water, NH_3 is ammonia, NH_4^+ is ammonia ion, and HCO_3^- is bicarbonate. The reaction produces ions, inducing a screening of the electrostatic repulsive interaction between the colloidal particles. Their interaction is then governed by the short-range van der Waals attraction, which leads to colloidal aggregation. The aggregates grow in time until forming a solid network which spans the entire volume. To prepare gels at different prescribed volume fractions we need first to determine the volume fraction φ_B of the mother batch. To do so we first measure the mass

fraction ω_{B}. By evaporating an aliquot of the suspension and weighting the dry mass we find $\omega_{\mathrm{B}} = 0.300$. Then, knowing the density of the suspension $\rho_{\mathrm{Ludox}} = 1.22$ g/cm^3, as given by the supplier, and the density of amorphous silica particles $\rho_{\mathrm{P}} = 2.19$, we solve the system of equations:

$$\varphi_{\mathrm{B}} = \omega_{\mathrm{B}} \frac{\rho_{\mathrm{S}}}{\rho_{\mathrm{P}}} \tag{4.2}$$

$$\rho_{\mathrm{Ludox}} = (1 - \varphi_{\mathrm{B}})\rho_{\mathrm{S}} + \varphi_{\mathrm{B}}\rho_{\mathrm{P}} \tag{4.3}$$

from which we get the volume fraction of the batch $\varphi_{\mathrm{B}} = 0.146$ and the density of the solvent $\rho_{\mathrm{S}} = 1.07$. This density id close to the expected one (the solvent is mainly water, whose density is $\rho_{\mathrm{H_2O}} = 0.997$ at 22°)

As mentioned before, to prepare our colloidal gels we target a volume fraction φ, which is obtained by diluting the initial Ludox suspension with two water-based solutions: one containing urea and one containing the enzyme. The target volume fraction is then obtained adding the two water-based solutions to the mother batch:

$$\varphi = \frac{\varphi_B V_L}{V_L + V_{\mathrm{S}}} \tag{4.4}$$

The volume V_{S} is the sum of the volume of urea solution V_U and of enzyme solution V_e. The two volumes are found by solving the system:

$$\begin{cases} V_{\mathrm{S}} = V_e + V_U \\ V_U = \frac{C_{\mathrm{U_f}}}{C_{\mathrm{U_i}}}\Big(V_{\mathrm{S}} + V_L \cdot (1 - \varphi_{\mathrm{B}})\Big) \end{cases} \tag{4.5}$$

The final concentration of urea is kept constant in all experiments at $C_{\mathrm{U_f}} = 1$M. The initial concentration $C_{\mathrm{U_i}}$ varies according to the sample up to a maximum of 7.4M. In this thesis we vary φ from 1% up to 10%. Knowing that the enzyme has concentration 1unit/mg, we take a mass of the enzyme powder such that, as mentioned before, its concentration in the final mixture is 30 units/ml. The gelation occurs depending on φ between 30 min and 3h after having mixed the two solutions with the colloidal suspension.

We also prepare some gels with $\varphi > 10\%$. Do do so we concentrated the Ludox mother batch with a centrifuge and, as we did for the mother batch, we measure the mass fraction. From the mass fraction and the solvent density that we obtained before we estimate the volume fraction of the concentrated solution $\varphi_{\mathrm{c}} = 22\%$. Using this concentrated Ludox suspension we manage to produce colloidal gels with prescribed volume fraction up to 15%.

A standard way of characterizing the gelation is by means of shear rheology: as shown in Fig. 37a we follow the evolution of the elastic and loss moduli over time. Shortly after having prepared the gel, the two moduli are low, with the viscous modulus G'' larger than elastic modulus G'. At a time $t \approx 1500$s an abrupt increase of the two moduli is measured

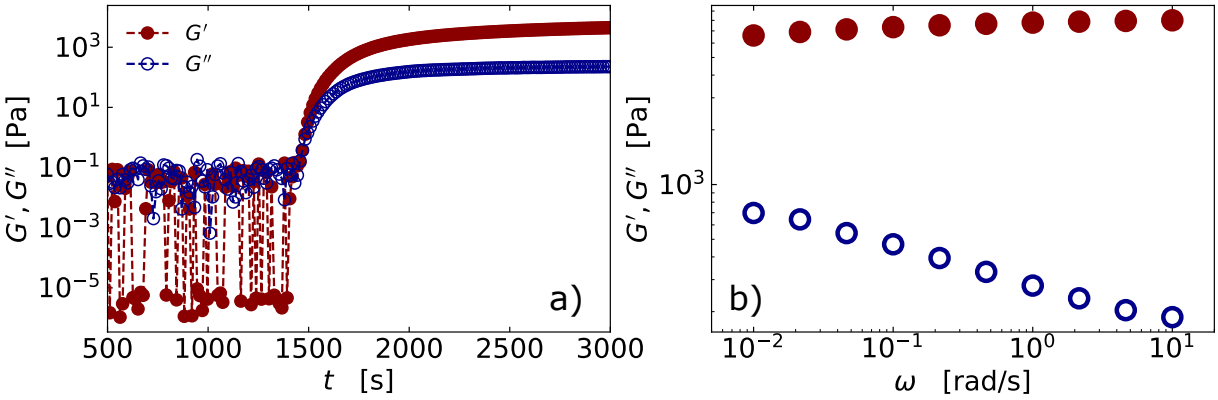

Figure 37: a) Time evolution of the elastic (red filled circles) and loss (blue empty circles) moduli for a gel prepared at $\varphi = 3\%$. Initially, G' and G'' are low and fluctuate, with $G'' > G'$ indicating that the suspension is a liquid. At time $t_g \approx 1500$s the two moduli increase abruptly, with $G' > G''$ indicating that the sample has undergone a liquid-gel transition. b) Elastic and loss modulus as a function of the oscillatory frequency ω extracted from a frequency sweep at imposed strain $\gamma = 0.1$

and G' becomes larger than G''. The crossover time is defined as the gelation time t_g. After gelation the moduli increase with time until $t \approx 3000$ s when they plateau. After roughly 12h, we perform a frequency sweep to measure the two moduli as a function of frequency. As shown in Fig. 37b, the elastic modulus is essentially constant over three decades in frequency, while G'' slightly decreases with increasing frequency. We define the shear modulus G_0 as the average of G' over the range of frequencies we probed, typically ranging from 10^-2 to 10 rad/s.

4.1.2 Beads of colloidal gel

To prepare beads of colloidal gel we start by following the protocol detailed in the previous section. However, as soon as all the chemicals are mixed, we pipette 40 μl of the solution and deposit a liquid drop (radius $\sim$ 2mm) onto a hydrophobic surface, which is immersed in a silicon oil bath (47 V 100 from VWR chemicals). The oil has density lower than that of the suspension so that the drop remains still on the surface. Moreover, we saturate with water the silicon oil such that no water diffusion occurs during the gelation process and as long as the bead remains immersed in oil. Once the gel is formed we let it age in oil for at least 24h. A sketch of the gelation process is shown in Fig. 39. Most of the measurements are performed with beads in air. In that case, before the measurement, we remove the bead from the oil bath and rinse it carefully with cyclohexane to remove all traces of silicon oil. Fig. 38 displays an image of a bead of colloidal gel prepared following the protocol described here.

Figure 38: Image of a colloidal bead of gel on the top of a glassy slide prepared at volume fraction $\varphi = 10\%$. The scale bar is the same for all images

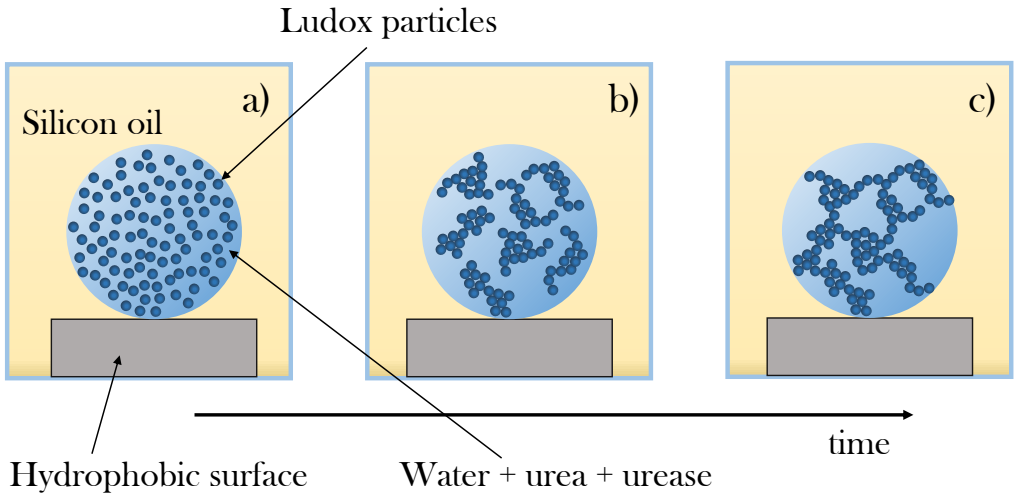

Figure 39: Sketch of the gelation of a bead of colloidal gel. a) a drop of colloidal suspension is deposited into the oil bath onto a hydrophobic surface. b) Clusters grow in size with time. c) a solid network spans the whole volume.

4.1.3 Experimental problems

During the experiments we encountered two problems related to the urea-urease reaction involved in the preparation of colloidal gels. The first one is the inhibition of the reaction when the solution gets in contact with the metallic plates of the rheometer. To overcome this problem we used glass plates for the shear rheology experiments. The other issue is related to the inhibition of the reaction when the solution is exposed to air. Indeed, behind the simple equilibrium reaction written above (Eq. 4.1) many sub-reactions, which involve the production of volatile molecules, are hidden. As a consequence, when a drop of suspension is surrounded by air, due to the large surface of exchange, such volatile molecules evaporate inhibiting the reaction and thus preventing the gel to form. So, surrounding the drops by oil, together with all the advantages explained in Sec. 4.1.2, is an efficient way to avoid the problem related to exchanges with air.

4.2 Gelation & quiescent dynamics

In this section we compare, the main properties of beads and conventional colloidal gels. By means of Dynamic Light Scattering, X-ray scattering and mechanical test we check that gelation time, spontaneous dynamics and elasticity are not altered by the size and shape of the gel or by the preparation method of beads of gel.

With the setup described in Chapter 3 we measure the microscopic dynamics of the colloidal suspension before, during and after gelation. In this experiment the sample is a drop immersed in oil. In Fig. 40 we plot a characteristic image of a bead of gel illuminated by a laser light. The laser produces the bright speckle pattern in the equatorial plane of the bead. Such a pattern, as explained in Sec. 2.1.4 of Chapter 2, is divided into several regions of interest (ROIs) to measure the microscopic dynamics with space resolution.

We first probe the gelation process of the beads. Fig. 41a shows the $c_I(\tau, t)$ correlation function calculated for several delay times τ in [5 ms - 5000 s] for the ROI in the center of the bead. Time 0 is defined as the time at which we start measuring the dynamics. Usually, since the laser requires to be aligned before running the experiment, the measurement starts roughly 1-2 min after the drop has been deposited on the substrate.

At the beginning (t=0), $c_I(\tau, t)$ is ≈ 0 for all the delay times τ. This fact indicates that, at short times, the sample is constituted by small aggregates which move by thermal fluctuations. At time $t_g = 2000$ s, c_I increases abruptly for $\tau > 200$ s. The increase in the correlation reflects the abrupt slowing down of the dynamics, which is due to the percolation of the gel clusters [Carpineti and Giglio (1993)] into a system spanning network. t_g is identified as gelation time. Thanks to the space-resolution with which

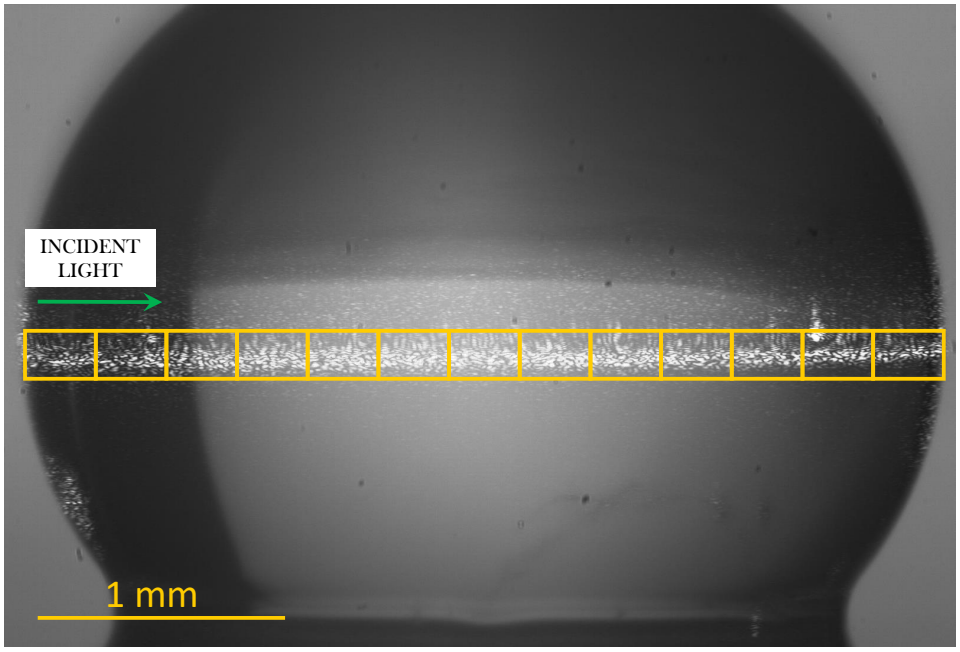

Figure 40: bead of colloidal gel surrounded by air and illuminated by a laser in its equatorial plane. The laser produces a typical speckle pattern. The yellow rectangles divides the speckle pattern in 13 regions for which intensity correlation functions are measured as described in the text. The green arrow indicates the propagation direction of the laser. Scale-bar is 1mm.

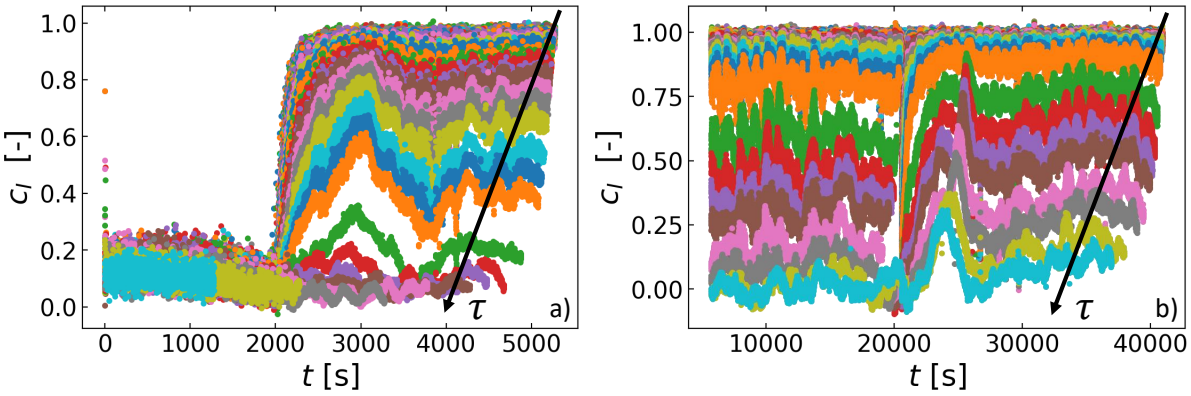

Figure 41: Plots of the c_I correlation functions as a function of time t. Each color corresponds to a delay time τ for which the correlation has been calculated. a) c_I for a colloidal sample prepared at $\varphi = 1\%$. At the beginning of the experiment the value of correlation is close to zero for all delay times. The c_I abruptly increases at $t_g = 2000$ s, reflecting the slowing down of the dynamics due to the percolation of the gel network. After gelation the value of the correlation increases for roughly 1000 s before reaching a nearly stationary regime with large fluctuations. In this plot τ ranges from $5 \cdot 10^{-3}$ s to 5000 s. b) c_I correlation function for the same gel in a time interval from 5279 s to 40000 s. During this time interval of time ($\sim$ 11 h) the correlation remains constant except at 20000 s when a major fluctuation is observed. In this plot τ ranges from $5 \cdot 10^{-3}$ s to 30000 s.

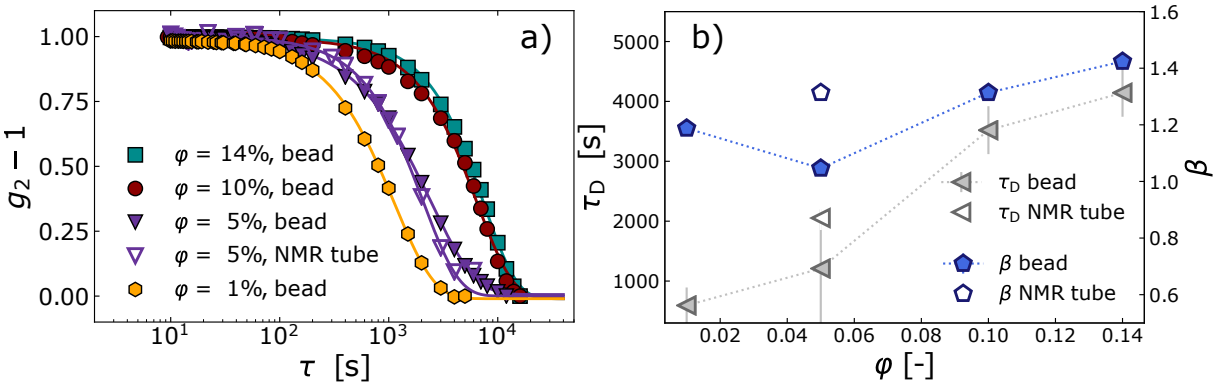

Figure 42: a) Intensity correlation function for beads of gel prepared at different volume fractions φ. Filled symbols correspond to beads of colloidal gel, while empty triangles are data for a gel prepared in a NMR tube. Solid lines are fits of Eq. 2.20 to the data. b) Decay time τ_D (left axis) and β (right axis) coefficient of the fits to the curves in a) as a function of the volume fraction. Gray triangles correspond to τ_D while blue pentagons represent β. Filled symbols correspond to beads of gel while empty ones correspond to a gel the gel prepared in a NMR tube.

the setup measures the dynamics, we check the gelation in homogeneous in the bead by finding the same gelation time $t_g = 2000 \pm 10$s.

After gelation the dynamics of the gel keep evolving rapidly up to $t \approx 3000$ s due to rearrangements of the network. This rapid evolution coincide with the large variation of the macroscopic mechanical properties shown in Fig. 37.

As shown in Fig. 41b we follow the evolution of the dynamics for about 11h. for t >3000 s c_I fluctuates around a constant value over time. apparently,they do not show the typical aging of gel network [Cipelletti et al. (2000); Manley et al. (2005a)], although this may be due to the relatively short observation window. At 20000s an abrupt drop of c_I is observed for all delays τ. This feature is associated to a major network reorganization occurring in the sample. Such temporally heterogeneous dynamics have been previously observed for same kind of samples with time-resolved light scattering experiments [Cipelletti et al. (2002), Duri and Cipelletti (2006)].

Once the c_I correlation function does not significantly evolve anymore we obtain the intensity correlation function $g_2(\tau)-1$ by averaging the c_I over a time interval over which it is roughly constant. For example, for the data shown in Fig. 41b, the average is performed for t in the interval [9000 s -15000 s]. In Fig. 42a we plot the intensity correlation functions obtained for beads of gels prepared at different volume fractions ($\varphi = 1, 5, 10, 15\%$). In the same plot, we also show the $g_2(\tau) - 1$ for a gel prepared at $\varphi = 5\%$ in an NMR tube, calculated at a time $t = 2000\text{s} + t_g$. We find that, the correlation functions for the same volume fraction nicely overlap for the two preparations (bead and NMR). Note that for both beads and NMR the ROI used for the analysis is located at the center of the sample. As a consequence, as explained in detail in Chapter 3, the q vector with which the dynamics are probe is the same for the two geometries.

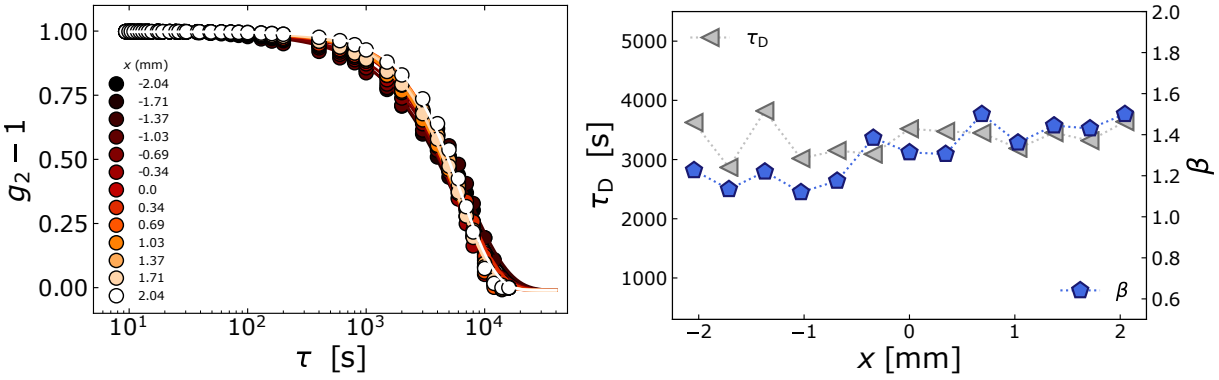

Figure 43: a) Intensity correlation function for beads of gel prepared at volume fraction $\varphi = 10\%$ for different positions along the bead diameter. Filled symbols are the experimental data while solid lines are a fits of Eq. 2.20 to the data. b) Decay time τ_D and β coefficient of the curves shown in a) as a function of the volume fraction. Gray triangles correspond to τ_D while blue pentagons represent β.

By fitting the intensity correlation function to Eq. 2.20 we extract the spontaneous decay time τ_D and the stretching coefficient β of the quiescent gels. As shown in Fig. 42b, we obtain for all samples a slow decay which varies from 900 to 4000 s as φ increases. This slow dynamics have been associated to intermittent rearrangements of the solid network [Duri and Cipelletti (2006)], since this kind of physical gel is not at thermal equilibrium. Moreover, as also previously observed for these gels [Cipelletti et al. (2000)], the dynamics of the quiescent gels depend on the volume fraction: the higher φ the higher τ_D. A similar dependence of the spontaneous decay time with the volume fraction has been observed in the past for similar kind of colloidal gels [Cipelletti et al. (2000)]. In Fig. 42b, we also see that the samples show a β exponent which depends weakly on φ, ranging from 1.1 to 1.5. Such a compressed decay of the $g_2(\tau) - 1$ is typical for this kind of gels [Duri and Cipelletti (2006), Aime et al. (2018a)].

Finally, we find that the dynamics of the quiescent samples are homogeneous in the whole gel, as checked by measuring the intensity correlation function along the bead radius. As mentioned in Chapter 3, the spherical shape of the sample and the index refraction mismatch change the q vector along the bead radius. However, being the bead immersed in oil, the index refraction mismatch is small, thus the q remains constant to within 4% and so does the probed length scale. We plot in Fig. 43a the intensity correlation functions for a gel prepared at $\varphi = 10\%$ measured at different positions along the bead diameter. The curves nicely overlap, suggesting an uniform dynamics. As we did for the different volume fractions, by fitting the data to Eq. 2.20 we obtain the decay time τ_D and the coefficient β. These two quantities are plotted in Fig. 43b as a function of the position. Interestingly, the decay time is constant for all positions along the radius, fluctuating around $\tau_D = 3355 \pm 20$s. The coefficient β slightly increases with position, always ranging from 1.1 up to 1.5.

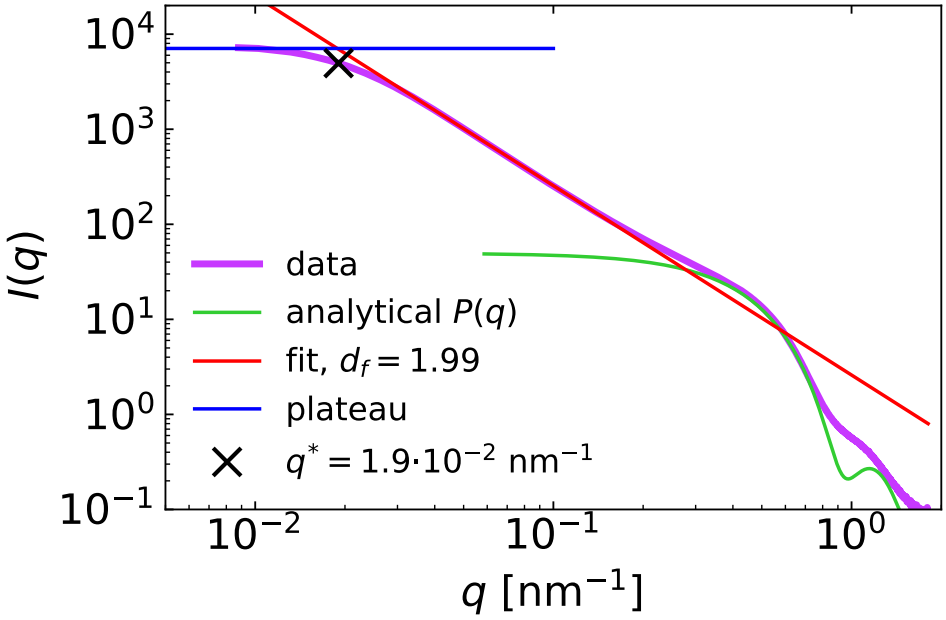

Figure 44: X-ray Scattered intensity as a function of the scattering vector as obtained in a Synchrotron experiment for a sample prepared at $\varphi = 3\%$. The violet line are the raw data from which the structural information of the gel are extracted. The green line is the analytical form factor $P(q)$ of Eq. 2.29 convoluted with a Gaussian from which the radius of the particles ($2a = 5.5$nm) and polydispersity ($\sigma = 0.55$) are extracted. The red curve is a fit of the data to $\sim \ q^{-d_f}$ from which the fractal dimension $d_f = 1.99$ is obtained. The blue horizontal curve is a line indicating the value at which the intensity plateaus, signalling the large-scale homogeneity of the gel. The black cross represents the characteristic cluster size ζ of the gel. It is obtained as the abscissa of the interception between by the power law regime (red line) and the plateau regime (blue line).

4.3 Structural information

In this section we compare, the main properties of beads and conventional colloidal gels. By means of Dynamic Light Scattering, X-ray scattering and mechanical test we check that gelation time, spontaneous dynamics and elasticity are not altered by the size and shape of the gel or by the preparation method of beads of gel.

We first probe by X-ray scattering the structure of colloidal gels prepared in capillaries (diameter 1.5 mm). Data are collected at Synchrotron Soleil (from Swing line). In Fig. 44 we show a typical plot of the scattered intensity as a function of the scattering vector q for a gel with volume fraction $\varphi = 3\%$. From this plot several structural information can be extracted. Firstly, from the region at high q ($q > 0.5$ nm^{-1}), which corresponds to the smallest length scales, we extract the information regarding the individual colloidal particles composing the gel. The scattered intensity is here proportional to the form factor of the particles. In this region we fit the intensity to the form factor of a sphere (Eq. 2.29)

φ [%]	q nm^{-1}
1	0.02-0.1
2	0.03-0.1
3	0.035-0.1
4	0.05-0.1
5	0.06-0.1
6	0.08-0.1
7	0.08-0.1
8	0.08-0.1
9	0.08-0.1
10	0.08-0.1

Table 4.1: Intermediate q range from which the fractal dimension d_f is obtained by fitting the data to $\sim\ q^{-d_f}$.

convoluted with a Gaussian to account for polydispersity. From the fit parameters we obtain the colloidal particles average diameter $2a = 5.5$ nm and the polydispersity, defined as the relative standard deviation $\sigma = 0.55$, in good agreement with the data provided by the producer and measured in other works [Sen et al. (2012)].

At intermediate q, the scattered intensity shows a power law decay with the scattering vector, $I \sim q^{-d_f}$. For colloidal gels, this indicates that in this q range the solid network is fractal (fractal dimension d_f), and the mass scales with the radius as $M \sim R^{-d_f}$ [Weitz and Oliveria (1984)]. A fit of the data yields $d_f = 1.99$. This value is in good agreement to what has been found in previous works for similar kind of colloidal gels [Weitz and Oliveria (1984), Cipelletti et al. (2000), Krall and Weitz (1998), Gisler et al. (1999), Aime et al. (2018a)]. The range in which the fractal dimension is fitted, changes with the volume fraction and is detailed in Table 4.1. Note that for high volume fractions ($\varphi \geq 5\%$), the q range over which the fractal dimension is defined is very limited, spanning not even an order of magnitude. The curve eventually plateaus at q smaller than a characteristic q^*, indicating that the gel structure is homogeneous above a characteristic length scale of the order of $2\pi/q^*$, which defines the characteristic cluster size ζ. As shown in Fig. 44, we identify q^* as the crossover between the plateau and the power law regimes. In the case of the gel shown in Fig. 44, we find $\zeta = 330$ nm.

We study the evolution of the gel structure as a function of the volume fraction. In Fig. 45a we plot the scattering intensity for φ ranging from 1% to 10%. At high q ($q > 10^{-1}$ nm^{-1}) the scattered intensity increases with the volume fraction. Indeed, as shown analytically Eq. 2.30, the scattered intensity is directly proportional to the number of scatterers in the scattering volume.

Accordingly, to compare the data at different volume fraction, we normalize $I(q)$ by

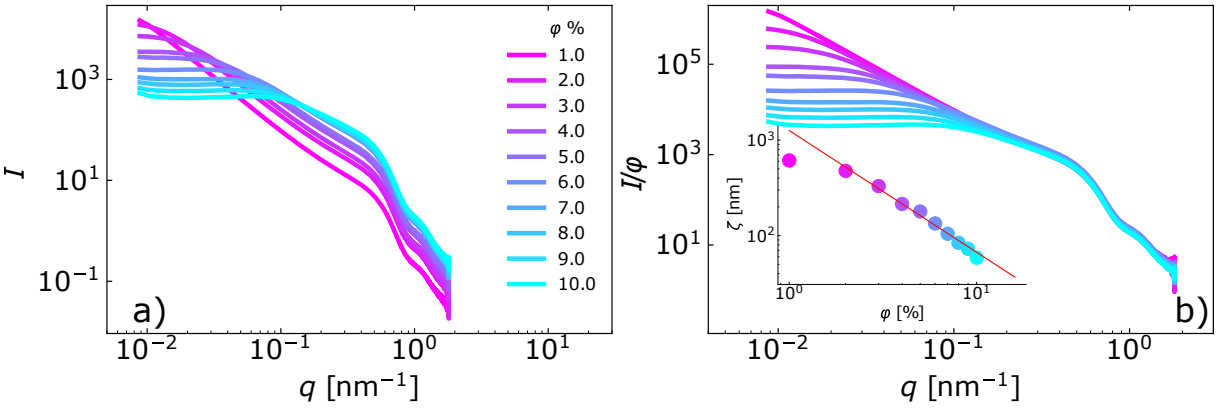

Figure 45: a) Scattered intensity as a function of scattering vector for gels prepared at different volume fractions. At high q the curves are proportional to φ. b) Scattered intensity normalized by the volume fraction: the curve nicely overlap for high q, while they differ at small q: the plateau of intensity shifts towards large q for increasing volume fraction. The shows the variation of the cluster size ζ with the volume fraction φ. The red lines is a fit of the data to a power law function $\sim \varphi^{-\alpha}$, which return $\alpha = 1.25$.

the corresponding φ. As expected, since at high q one probes the signal of individual particles ($S(q) = 1$), the curves nicely overlap for $q > 3 \cdot 10^{-2}$ nm^{-1}, see Fig. 45b.

Contrary to the overlapping at high q, the curves deviate from each other at low q. In particular the value of q^* decreases when increasing the volume fraction, indicating that by increasing φ the cluster size ζ decreases. In the inset of Fig. 45b we plot the cluster size as a function of φ. More quantitatively, we find that ζ goes from ≈ 620 nm $\varphi = 1\%$ to ≈ 60 nm for $\varphi = 10\%$. Moreover, ζ scales with φ following a power law $\zeta \sim \varphi^{-\alpha}$. By fitting the data to $\sim \varphi^{-\alpha}$ we obtain $\alpha = 1.25$, which is compatible to what found in literature. Indeed, for this kind of colloidal gel it has been found a power law dependence of the cluster size to volume fraction with an exponent $\alpha \sim 1$ [Krall and Weitz (1998); Manley et al. (2005b); Cipelletti et al. (2000)]. Note that, for gels with $\varphi \geq 5\%$ the gel comprises cluster composed by a few tens of particles.

Finally, we compare the structure of our beads of colloidal gel to that of the gels prepared in a capillary. As mentioned in Chapter 2, the structure of beads of colloidal gel is measured using the Laboratoire Charles Coulomb (L2C) X-rays apparatus (GeniX^{3D}). Doing X-ray on spherical samples introduces an additional difficulty. Indeed, it is not possible to precisely identify the scattering volume which is responsible of the signal. Moreover, changing the setup also changes the absolute scattered intensity. As a consequence, dividing the measured scattered intensities by the volume fraction does not yield an overlap of the data at high q, as the one obtained in Fig. 45 for samples in capillaries. For this reason, to compare the scattered intensities for beads prepared at different volume fractions, we divide by an arbitrary value the scattered intensity so as to overlap $I(q)$ in the high q regime ($q > 3 \cdot 10^{-1}$ nm^{-1}). This normalization is justified by overlap of U/φ obtained in Fig. 45b, which proves that for $q > 3 \cdot 10^{-1}$ nm^{-1} the curves only reflect

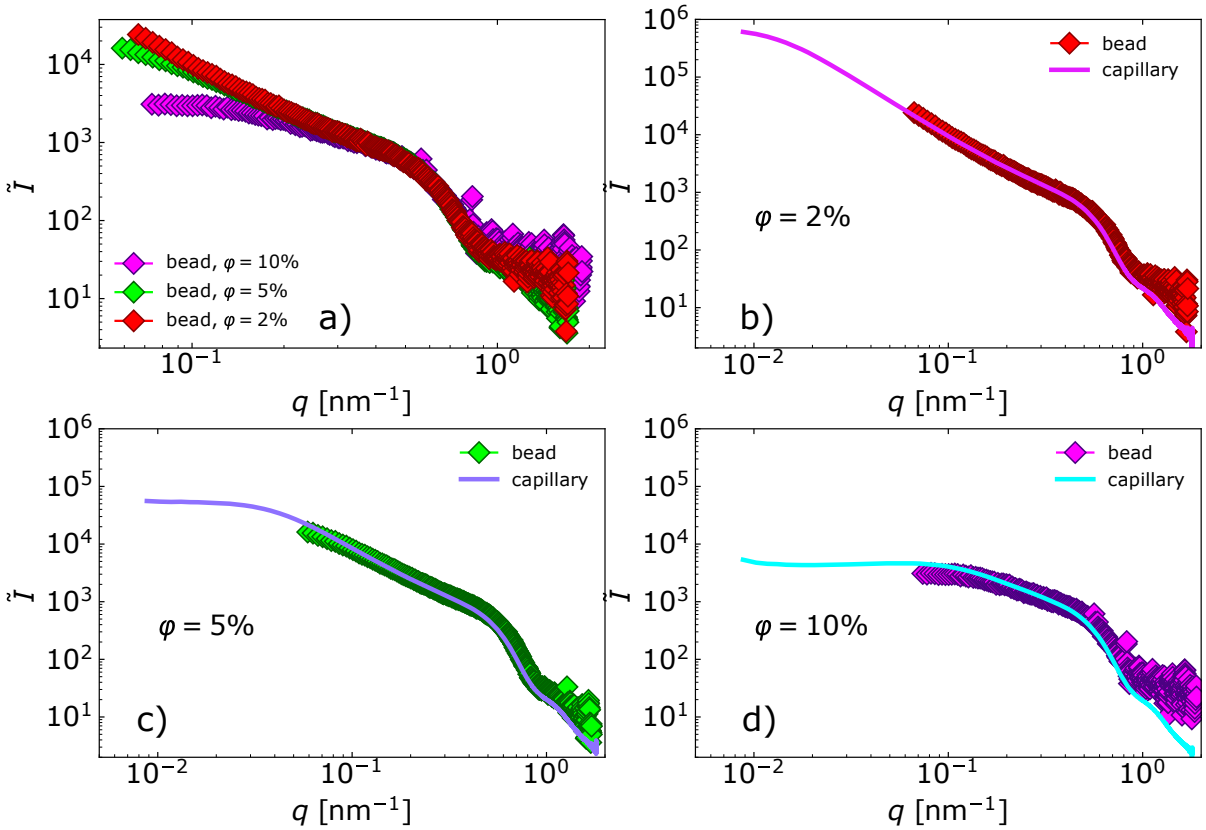

Figure 46: a) Normalized scattered intensity as a function of scattering vector for beads of colloidal gel prepared at different volume fractions: red $\varphi = 2\%$, green $\varphi = 5\%$, violet $\varphi = 10\%$. b-d) Comparison of the normalized scattered intensity between a bead of gel (diamonds) and a gel prepared in a capillary (solid lines). The different range of q vector with which the spectra are measured is due to the different experimental apparatus.

the feature of the individual particles.

We plot in Fig. 46a the normalized scattered intensity $\tilde{I}(q)$ for three beads of gel prepared at $\varphi = 2\%$, 5% and 10%. The curves evolve with φ as it was for the gels prepared in the capillary. Moreover, to compare the structure of gel beads and gels formed in a capillary, we plot in Fig. 46b, c and d the normalized scattered intensity obtained for the two sample geometries for $\varphi = 2\%$, 5% and 10% respectively. The good overlap between the curves over the q range accessible in the two experiments confirms that our preparation method does not alter the structure of the gels.

4.4 Mechanical properties

In this section we investigate the mechanical properties of the beads of colloidal gel. Firstly, we check, by comparing Young Modulus of the beads with the elastic modulus in bulk, if the preparation methods alters the mechanical properties of the beads of colloidal gels. Secondly we investigate the irreversible character of beads of colloidal gel when an uniaxial compression is imposed. To do so we impose cycles of loading/unloading and we observe how the response of the material changes at each cycle. For a clear interpretation of the data, we compare the results with beads of polymer gels, which show a purely elastic behavior.

4.4.1 Young Modulus

In order to check if the preparation methods affect the mechanical properties of the gels, we compare the mechanical properties of the beads of gel with those of gels with the same composition but prepared directly in the gap between the two glass plates of a rheometer. To do so, we measure the Young modulus E of the beads of gel under compression in the rheometer, and the shear elastic modulus G_0 of a gel prepared in situ in the rheometer. We recall that E and G_0 are related to each other via Eq. 2.37 which we have used with a Poisson ratio $\nu = 0.5$.

To measure the shear modulus G_0 we perform a frequency sweep at a constant shear strain $\gamma = 0.1\%$ in a plate-plate geometry once the gel has aged for 12h. Figure 47 shows the frequency dependence of the elastic modulus for several gels with different volume fractions φ in the range 1-10%. We find that the elastic modulus is nearly constant over the three decades of frequency investigated (from 0.01 to 10 rad/s). We define the modulus G_0 by averaging G' over the whole frequency range. We find that G_0 strongly increases with φ from $G_0 = 146 \pm 1$ Pa for $\varphi = 1\%$ to $G_0 = 194832 \pm 1200$ Pa for $\varphi = 10\%$.

As discussed in Sec. 2.3.2 of Chapter 2, the Young modulus of a bead of gel can be

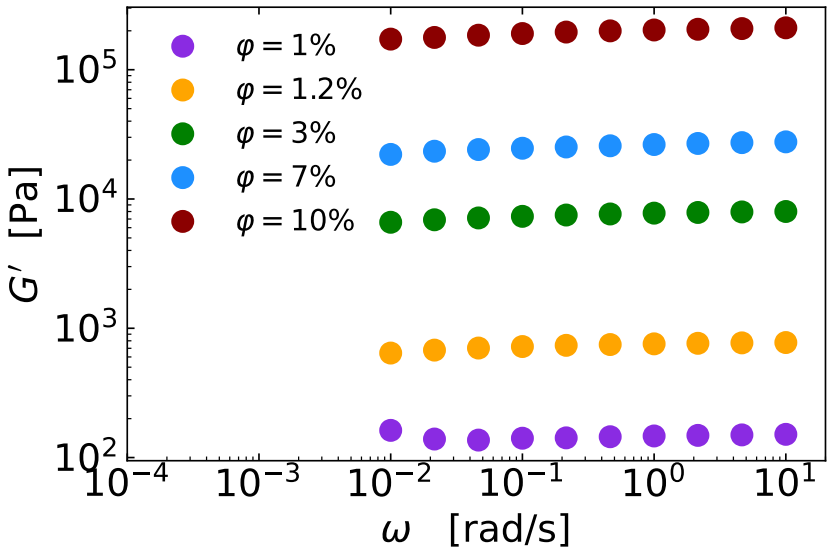

Figure 47: Elastic modulus G' as a function of the oscillatory frequency ω obtained in a frequency sweep experiment for colloidal gels prepared at different volume fractions as indicated in the legend. The imposed strain is $\gamma = 0.1\%$.

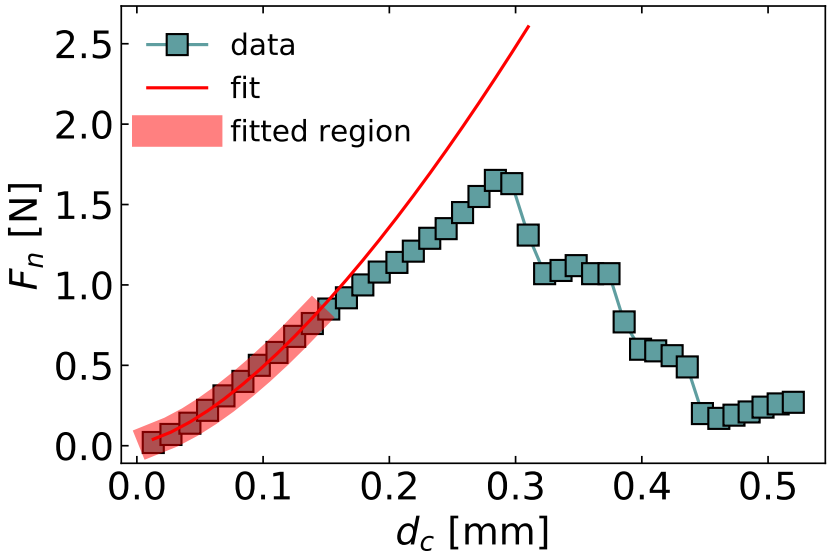

Figure 48: Normal force as a function of the indentation depth d_c (see text definition) for a bead of gel prepared at $\varphi = 10\%$. Blue squares are the experimental data, the red solid line is the fit to Eq. 2.34, the red shade indicates the range of the data that have been used for the fit.

obtained by compression. By measuring the force as a function of deformation we probe the mechanical properties of the beads. In Fig. 48 we plot the normal force F_n as a function of indentation depth d_c while being compressed.

As the indentation depth increases, the normal force increases monotonically up to $d_c = 0.3$ mm, when F_n drops abruptly, indicating the failure of the gel. As shown in Fig. 48, by fitting the data at small deformation to Eq. 2.34, we extract the Young modulus of the gel. Since, the Young modulus and the shear modulus are related through Eq. 2.37, by assuming a Poisson ratio $\nu = 0.5$, we can calculate the shear modulus of the gel and compare it to the shear modulus G_0 obtained for gel formed in the rheometer. Remarkably, the data obtained with the two methods nicely overlap over the whole range of φ explored, confirming that neither the custom preparation protocol nor the spherical shape of the gel alter the bulk mechanical properties of the gel. Moreover, we find a power law dependence $G_0 \sim \varphi^{\alpha}$, which is in agreement to that previously found in the literature for this kind of colloidal gels [Manley et al. (2005a), Aime et al. (2018a), Grant and Russel (1993), Rueb and Zukoski (1997), Shih et al. (1990)]. Best fit yields $\alpha = 2.9 \pm 0.2$. This value is slightly lower compared to what has been found previously when the exponent ranges usually from 3 to 4.5 [Krall and Weitz (1998), Gisler et al. (1999), Aime et al. (2018a), Grant and Russel (1993), Rueb and Zukoski (1997), Shih et al. (1990)]. The reason lies in the fact that, as explained before, gels with $\varphi \geq 5\%$ do not have a fractal structure. So, by fitting only the data with $\varphi < 5\%$ we obtain $\alpha = 3.6 \pm 0.2$ which is compatible to what has been found in the past. Moreover, from the exponent α we can estimate the backbone fractal dimension d_b of the backbones. Indeed, supposing a string link behaviour [Shih et al. (1990)], $\alpha = (3+d_b)/(3-d_f)$. by using d_f obtained from X-ray scattering and $\alpha = 3.6$ we get $d_b = 0.96$.

4.4.2 Multiple loads

It has been shown by [Aime et al. (2018a)] that for small strain deformations, the colloidal gels have a linear elastic regime where the deformation is purely reversible. However, when a bead of gel is compressed by uniaxial compression, even by small indentation depth, it may deform in a reversible or irreversible manner. Differentiating between the two behaviors is extremely important, especially for the energy consideration we do in Sec. 5.2.1 and Sec. 5.2.2.

To check if we observe a linear regime, we apply to a bead of gel prepared at $\varphi = 10\%$ a series of loading/unloading, making sure that the applied strain does not overcome the $\epsilon = 7\%$. We chose such a value of strain since, as we will show in the next section, it is much smaller that the yielding strain of the bead ($\epsilon_y = 14\%$). Moreover, to check that this behaviour is not an artefact of the experimental protocol, a change in stiffness due to evaporation (see Chapter 6), the sticking of the bead to the plates or a translation of

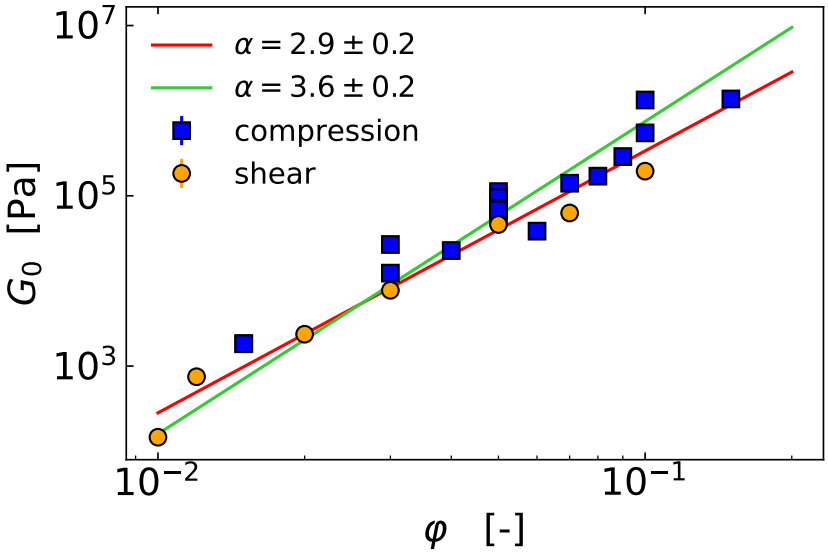

Figure 49: Shear modulus G_0 as a function of the volume fraction φ. Green circles correspond to the shear modulus G_0 directly measured by shear rheology, while blue squares correspond to the Young modulus obtained from compression of beads of gel which have been converted into G_0 using Eq. 2.37. The red solid line is a fit of the whole set of data to power law, with an exponent $\alpha = 2.9 \pm 0.2$. The green solid line is a fit of data with $\varphi < 5\%$ to power law, with an exponent $\alpha = 3.6 \pm 0.2$.

the bead; we apply the same multi-load protocol to a bead of polyacrylamide gel, which preparation is detailed in Chapter 3.

We plot the results of this test in Fig. 50. Interestingly, in Fig. 50a we see that for a bead of colloidal gel the contact point decreases at each cycle, indicating that the bead deforms at each load in the direction of the compression. Contrary, the contact of the polyacrylamide gel remains constant, indicating that the deformation is reversible. By translating the force-indentation curves by the contact point we obtain Fig. 50b and Fig. 50c for the bead of polyacrylamide gel and for the bead of colloidal gel. Interestingly, for the bead of polyacrylamide gel (Fig. 50b) we find that the force indentation curves perfectly overlap at each load, as aspect for a purely elastic sample. Thus confirming the constant value of the contact point. Contrary, for the bead of colloidal gel (Fig. 50c) we see that the force changes at every load, in particular we appreciate the biggest change between the first and the second load. The different behaviors of the two kind of beads indicates that, the compression induces in the bead of colloidal gel plastic irreversible rearrangements. Moreover, to get an insight to the changes of the Young Modulus of the bead of colloidal gel, we fit the force indentation curves to the Hertz contact model. The results are plotted in Fig. 50d: as it is possible to see, the Young Modulus increases at each load indicating a stiffening of the gel at each compression.

We further investigate the irreversible character of the compression by studying the energy dissipated by the bead of colloidal gel during the compression. For doing so, we

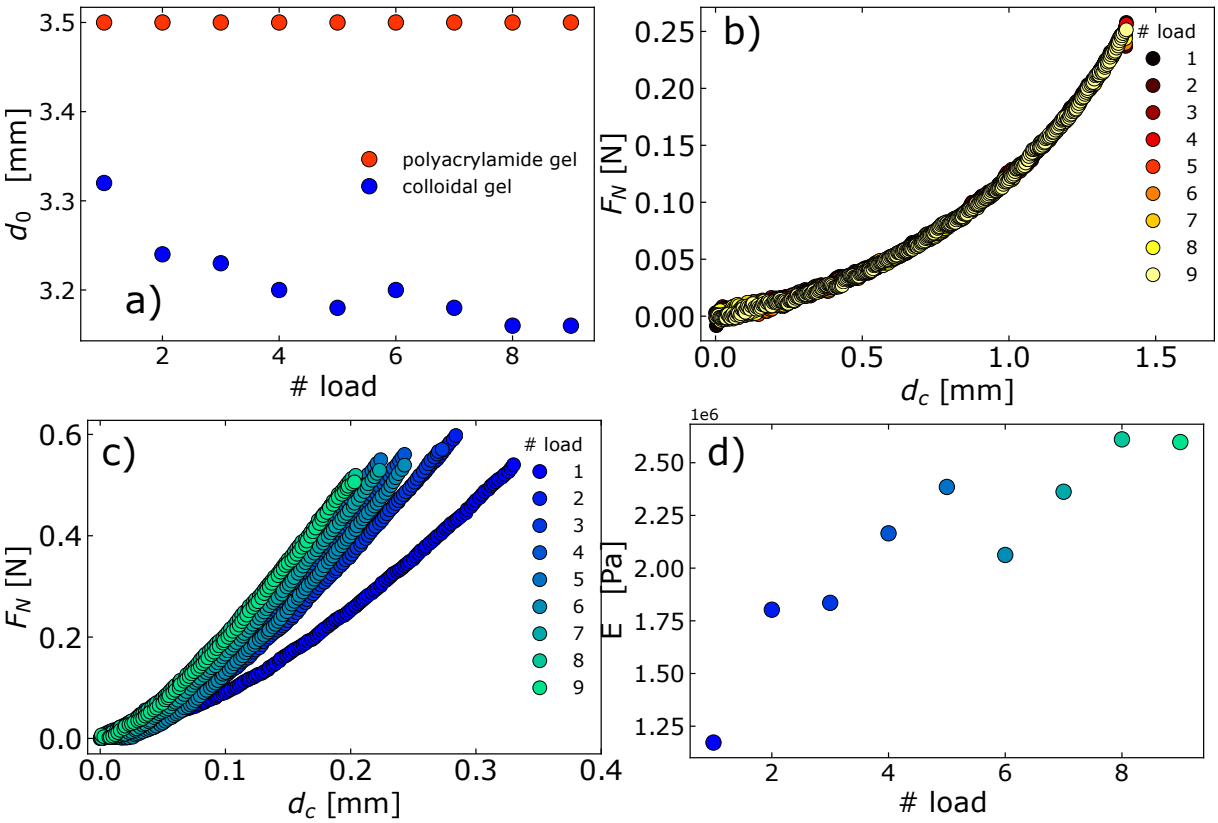

Figure 50: a) Contact point as a function of the number of load: blue symbols represent a bead of polyacrylamide gel while blue symbols represent a bead of colloidal gel. b) Normal force as a function of the indentation depth d_c (see text definition) for a bead of polyacrylamide gel, different colors correspond to a different load. c) Same plot as in b) but for a bead of colloidal gel . prepared at $\varphi = 10\%$. d) Young modulus as a function of the number of load for a bead of colloidal gel . prepared at $\varphi = 10\%$. Different colors correspond to a different load.

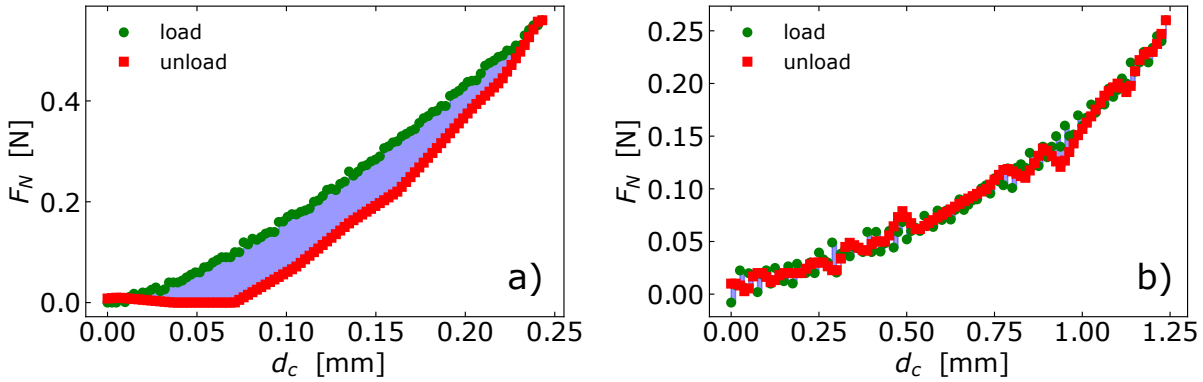

Figure 51: a) Normal force as a function of the indentation depth d_c for a bead of gel prepared at $\varphi = 10\%$. The green circles represent the loading, while the red squares the unloading. The blue area between the two curves represents the energy dissipated by the system. b) Same plot as in a) but for a polyacrylamide gel.

measure the loading and unloading force as a function of the distance at each load, and we calculate the area underneath them: the dissipated energy E_D is the difference between the two curves. We plot in Fig. 51a an example of the dissipated energy obtained from the force distance curves for a bead of colloidal gel prepared at $\varphi = 10\%$. Interestingly, we find that $E_D \neq 0$ at each cycle, confirming that a bead of colloidal gel dissipates energy when compressed. Moreover, as done before, we repeat the same operation for a bead of polyacrylamide gel. Fig. 51b shows that in this case the load and unload curves overlap and as a consequence $E_D \approx 0$. Thus, the bead of polymer gel do not dissipate energy.

4.5 Conclusions

Using DLS, X-ray scattering and rheology, we have proven that the gelation, spontaneous dynamics, structure and mechanical properties are the same for gels prepared in tubes, between glass plates of the rheometer or for beads. Hence, neither the protocol to produce gel beads nor the manipulation required to transfer the beads from the production glassware to the various characterization setups alter the key features of the colloidal gels studied in this thesis.

Indeed, in shear rheology these gels have a elastic linear regime. Contrary, under uniaxial compression, even in the small deformation regime, the beads of colloidal gels undergo irreversible plastic rearrangements. Note that this fact might see in contradiction with the fact that we used Hertz contact model to fit our data in order to extract the Young modulus of the beads of gel. Indeed, Hertz contact model applies for small deformation of perfectly elastic bodies. In our case despite respecting the small deformation regime over which we fit our data to obtain the Young modulus, we do not fully respect the elasticity condition. However, by finding that the Young modulus obtained by Hertz model correspond to the shear modulus via Eq. 2.37 (see Fig. 49), we prove that in the

small deformation regime the plasticity is small and negligible when obtaining the Young modulus.

Finally, by imposing cycles of loading/unloading and measuring the mechanical response of the samples, we found that the response of the beads of colloidal gel to an uniaxial compression is characterized by plastic events. Indeed, while beads of polyacrylamide have a purely elastic response to the cycles of compression, when the beads of colloidal gel are compressed they change their shape, leading to an increase of the Young modulus. Moreover, we found that at each loading/unloading cycle, the force-distance curves of a beads of colloidal gel are characterized by an hysteresis, which also clearly indicates that the system is dissipating energy.

Chapter 5

Colloidal Gels Under Extreme Deformation

5.1 Imaging the Failure

In this section we investigate the macroscopic behavior of beads of colloidal gel under uniaxial deformation. Firstly we look at general differences between a soft and a tough bead during the whole compression process. Secondly, we focus the onset of cracking, compare beads prepared at different volume fractions.

To impose to a bead of gel an uniaxial compression, we deposit the bead on the lower plate of the rheometer (which is fixed), and we compress it by the lowering the upper plate at a constant rate. We recall that, since d is the distance between the two plates, the rate of compression is defined as $\dot{\epsilon} = \frac{\partial d}{\partial t} \cdot \frac{1}{d}$. To get a general idea on the macroscopic behavior of the beads of gel during compression, we take images from underneath using the camera mounted below the transparent lower plate (see in Sec. 2.3.2.3 for a detailed description).

Figure 52 displays a soft bead of gel prepared at $\varphi = 3\%$, which is compressed at a constant rate $\dot{\epsilon} = 10^{-1}$ s^{-1}. In the first frame (Fig. 52a) the bead is already in contact with the plate. At $t = 1.32$ s (Fig. 52b), it is possible to appreciate the onset of a crack, which develops until spanning through the whole bead diameter (Fig. 52c). By analyzing the movie it is possible to obtain a rough estimation of the propagation speed of the crack: $v_c = d_c/\Delta t$, where d_c is the distance traveled by the crack in between two frames taken at an interval Δt. In the case of Fig. 52a-c $v_c \approx 1.5 \cdot 10^{-3}$ m/s. As the indentation depth increases other cracks develop in the sample (Fig. 52d). Moreover, at time $t = 16.5$ s (Fig. 52f) we can appreciate that the sample is composed by two regions: an opaque central region with an irregular shape which is the gel, surrounded by a transparent region with more regular shape, which is the water that has been expelled by the solid network. The scenario get more clear at $t = 16.5$ (Fig. 52g): indeed as underlined by the dotted green line, the sample is divided in two distinct regions: a central region with the smashed bead still composed by the solid silica network and water and a second region where mainly

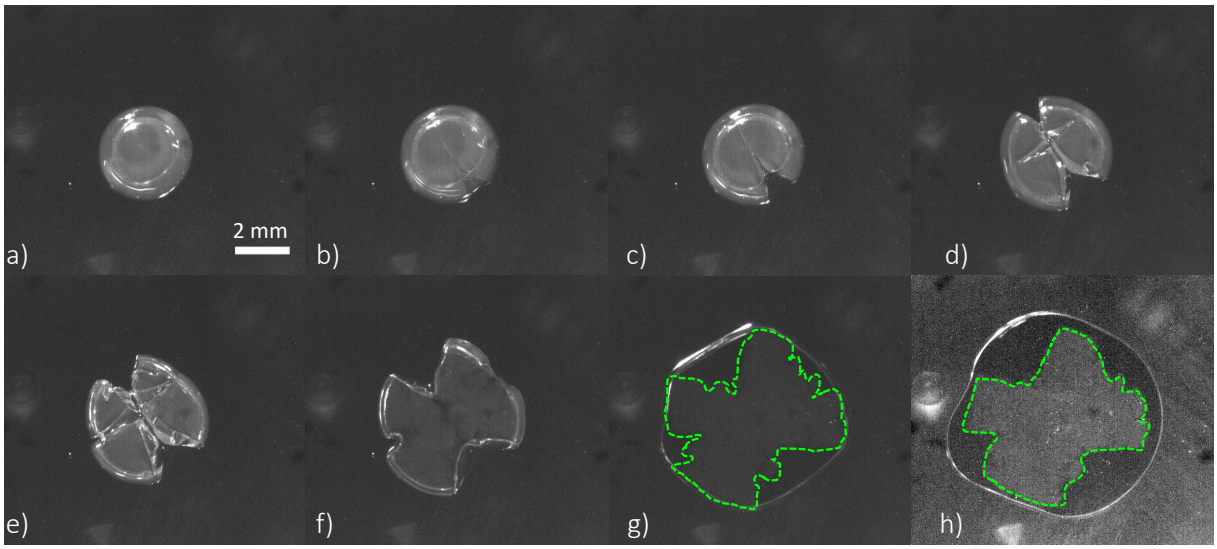

Figure 52: Time laps of a bead of gel prepared at $\varphi = 3\%$ under uniaxial compression, the rate is $\dot{\epsilon} = 10^{-1}\text{s}^{-1}$. The images are taken respectively at a) $t = 0$ s, b) $t = 1.32$ s, c) $t = 1.98$ s, d) $t = 4.62$ s, e) $t = 7.92$ s, f) $t = 16.50$ s, g) $t = 23.10$ s, h) $t = 36.30$ s. The dotted green lines separate the sample in two regions of different opacity, corresponding to a gel (white central region) and a liquid phase (dark region). In panel h) the contrast has been modified to better visualize the two regions. The scale bar is the same for all images.

the water that has flown out is present. Note that in this second region some colloidal aggregates might be present in the liquid phase; however, due to the transparency of the liquid, their size is small and their concentration low. In Fig. 52g-h this division becomes even more evident (in Fig. 52h we have increased the contrast in order to better visualize the separation between the two regions).

A different scenario is observed in Fig. 53 where a tough bead, prepared at $\phi = 10\%$, is compressed also at rate $\dot{\epsilon} = 10^{-1}$ s^{-1}. In this case we see that, contrary to the slow crack propagation observed for the soft bead, the tough bead, from being intact at time $t = 21.6$ s, abruptly breaks in several pieces (Fig. 53c). In this case it is not possible to estimate the speed propagation of the crack. However, since the bead entirely fragments over two consecutive frames taken at time interval $\Delta t = 600$ ms(Fig. 53c-d) it is safe to assume that the speed propagation is higher than $v_c > 5 \cdot 10^{-3}$ m/s. At time $t = 22.2$ s (Fig. 53e), we see that some pieces of the gel are ejected outside the plates of the rheometer. The pieces of the bead that are not ejected keep being compressed by the plates, and they fragment in smaller pieces (Fig. 53f-h). Only in the last frame of the movie (Fig. 53h) we can appreciate some water that has flown out of the sample. However, contrary to the case of the soft gel, it is not possible to clearly draw a line dividing a region with only water and another one with the gel.

In Figure 54 we focus on the macroscopic aspect of the failure at its onset. Interestingly, the first failure of soft and stiff beads is very different even in its macroscopic aspect. In

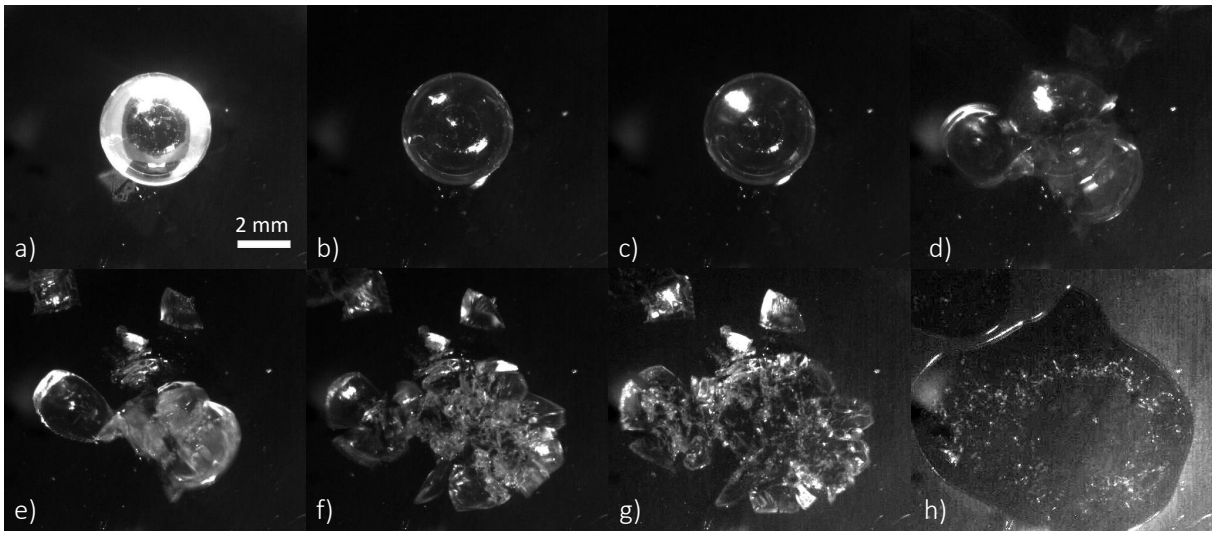

Figure 53: Time laps of a bead of gel prepared at $\varphi = 10\%$ under uniaxial compression, the rate is $\dot{\epsilon} = 10^{-1}\text{s}^{-1}$. The images are taken respectively at a) $t = 0$ s, b) $t = 19.0$ s, c) $t = 21.0$ s, d) $t = 21.6$ s, e) $t = 22.2$ s, f) $t = 24.6$ s, g) $t = 25.6$ s, h) $t = 54.3$ s. In panel b) the bead looks darker since the upper plate of the rheometer become closer ot the bead thus decreasing the light illuminating the bead. In panel h) the contrast has been modified to better visualize the two regions. The scale bar is the same for all images.

Figure 54 we plot two snapshots, taken at an interval of roughly 700 ms, of soft beads ($\varphi = 1.5\%$, 3%) showing the beads just before and right after the failure. We see that for the gel at $\varphi = 1.5\%$, 3% (in Fig. 54a-b and Fig. 54c-d respectively) the failure of soft beads is characterized by one crack. In the images the cracks do not have fully developed after 660 ms. By contrast, the failure of tough beads ($\varphi = 10\%$, 15%) is much more abrupt and fast (see Fig. 54g-j). Indeed, in the frame taken 600 ms after the failure the beads are already broken in several small pieces and, as mentioned before, the pieces are ejected far apart from each other. The bead prepared at $\varphi = 5\%$ (in Fig. 54e-f) displays an intermediate behavior. Indeed, in the time interval of 700 ms, three cracks which joins in the center of the bead. However, these pieces are not ejected from the plates as for the tougher beads.

In the next section we analyze the mechanical data acquired by the rheometer.

5.2 Yielding in Uniaxial Compression

In this section we investigate the mechanical response of beads under uniaxial deformation. Firstly, we investigate the behavior for beads prepared at different volume fractions. Secondly, we check the role of the rate of compression.

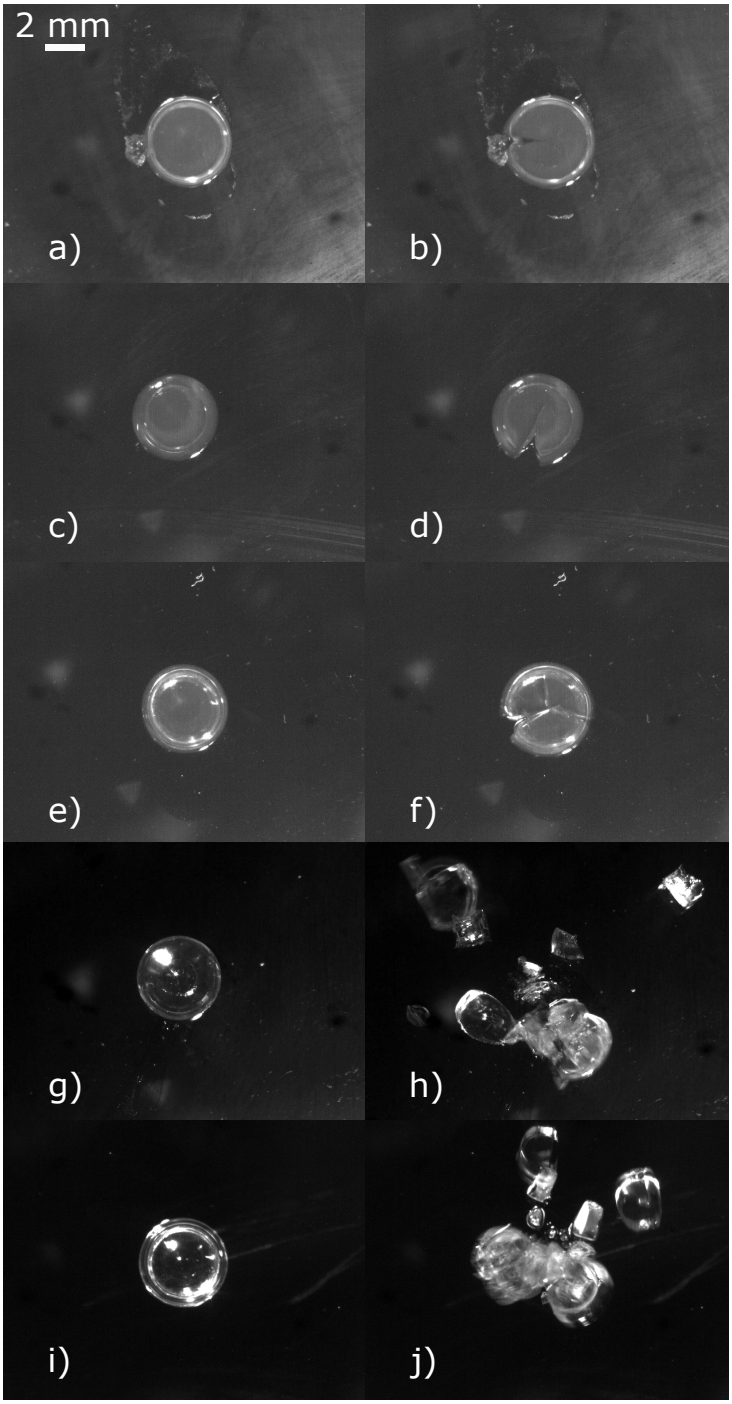

Figure 54: Failure of soft beads of colloidal gel. a-f) Images taken just before and just after the rupture of a gel prepared at different volume fractions. Images on the left are taken just before the the failure, while the images on the right are taken right after the failure of the gel. a-b) bead of gel prepared at $\varphi = 1.5\%$, the time delay between images is $\Delta t = 700$ ms. c-d) Bead of gel prepared at $\varphi = 3\%$, the time delay between images is $\Delta t = 660$ ms. e-f) Bead of gel prepared at $\varphi = 5\%$, the time delay between images is $\Delta t = 660$ ms. g-h) Bead of gel prepared at $\varphi = 10\%$, the time delay between images is $\Delta t = 600$ ms. i-h) Bead of gel prepared at $\varphi = 15\%$, the time delay between images is $\Delta t = 460$ ms. The scale bar is the same for all images.

5.2.1 Volume fraction dependence

In Figure 55 we plot the normal force F_n as a function of the indentation distance d_c for several beads of colloidal gel, whose volume fraction ranges from $\varphi = 1.5\%$ to $\varphi = 15\%$. From the small linear regime we quantify the stiffness of the gel by fitting the data to the Hertz model (Eq. 2.34, see Chapter 2). Data are fitted up to an indentation strain $\epsilon = d_c/d_0 = 5\%$. By performing a cumulant fit, we check that the results do not vary significantly for small variation of the fitted region. For each bead, we extract the generalized Young modulus E^* defined as $E^* = \left(\frac{1-\nu_s^2}{E_s}\right)^{-1}$ in Eq. 2.36, where E is the young modulus and ν the Poisson ratio of the bead. We plot E^* as a function of φ in Fig. 55f. As already described in the previous chapter (Fig. 49), we find that E^* increases monotonically with the volume fraction following a power law relationship $E^* \sim \varphi^\alpha$, with $\alpha = 2.9 \pm 0.2$.

However, for large deformations, the shape of the curves drastically change with φ. Indeed, for $\varphi = 1.5\%$ the force increases for the whole duration of the experiment. Note that in Fig. 55a we plot the data until $d_c = 1.25$ mm since for larger indentation depths the force increases sharply due to the small gap between the two plates. For $\varphi = 3\%$, the force increases until it plateaus at $d_c = 0.85$ mm ($\epsilon = 0.408$). For gels prepared at higher volume fraction ($\varphi = 10\%$ and $\varphi = 15\%$) the force increases with d_c until abruptly decreasing $d_c = 0.47$ mm ($\epsilon = 0.145$) and $d_c = 0.44$ mm ($\epsilon = 0.138$) for $\varphi = 10\%$ and $\varphi = 15\%$ respectively. Eventually in both cases the normal force drops to 0. This fact reflects what has been observed with the imaging. Indeed, we have seen (Fig. 53) that the failure of stiff beads is accompanied by a fragmentation of the bead is several pieces that are ejected away. The fact that the pieces are ejected implies a loss of connectivity between the bead and the rheometer plates, which leads to $F_n = 0$. The bead prepared at $\varphi = 5\%$ represents an intermediate case between stiff beads and soft ones. Indeed, it also shows a decrease of the force at $d_c = 0.6$ mm ($\epsilon = 0.180$). However the decrease of the force is much less abrupt compared to the higher volume fraction and never drops to 0.

To compare the data for beads prepared at different φ, we calculate the adimensional engineering stress $\tilde{\sigma}_E$, which has been defined as $\tilde{\sigma}_E = \frac{F_n}{E^* \cdot S_0}$ (Eq. 2.38, see Chapter 2), where S_0 is the nominal contact area, which reads as $S_0 = \pi\left(\frac{d_0}{2}\right)^2$. In Fig. 56 we plot $\tilde{\sigma}_E$ as a function of the engineering strain $\epsilon = \frac{d_0 - d}{d_0}$. The curves nicely overlap at small strain ($\epsilon \leq 0.10$). This fact indicates that, in the small deformation regime, the Hertz model entirely depicts the physics of the system. Contrary, the curves are qualitatively different at large deformation. Indeed, gels prepared at high volume fraction undergo a brittle failure, characterized by an abrupt stress drop. Contrary, gels prepared at low volume fractions show a ductile-like behavior, deforming continuously and displaying a large plateau or a small and gentle decrease of the stress.

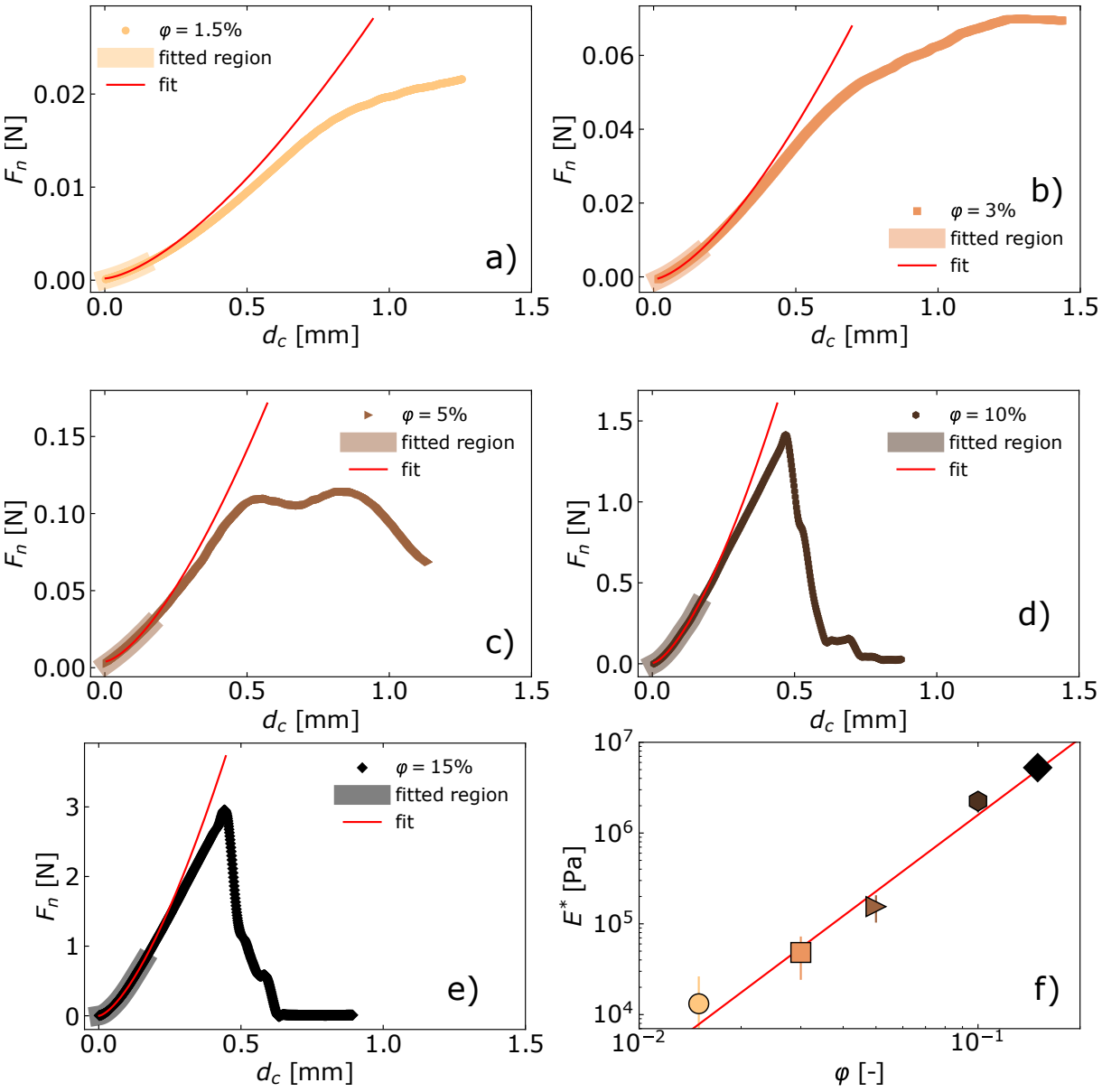

Figure 55: Normal force as a function of the indentation depth d_c (see text definition) for beads of gel prepared at volume fraction: a) $\varphi = 1.5\%$, b) $\varphi = 3\%$, c) $\varphi = 5\%$, d) $\varphi = 10\%$, e) $\varphi = 15\%$. Symbols represent the experimental data, the red solid line is the fit to the Hertz contact model (Eq. 2.34), the shaded area indicates the range of the data that have been used for the fit. The beads are compressed at constant rate $\dot{\epsilon} = 0.1$ s^{-1}. f) Generalized Young modulus obtained from the fit as a function of the volume fraction. The red solid line is a fit of the whole set of data to power law, with an exponent $\alpha = 2.9 \pm 0.2$.

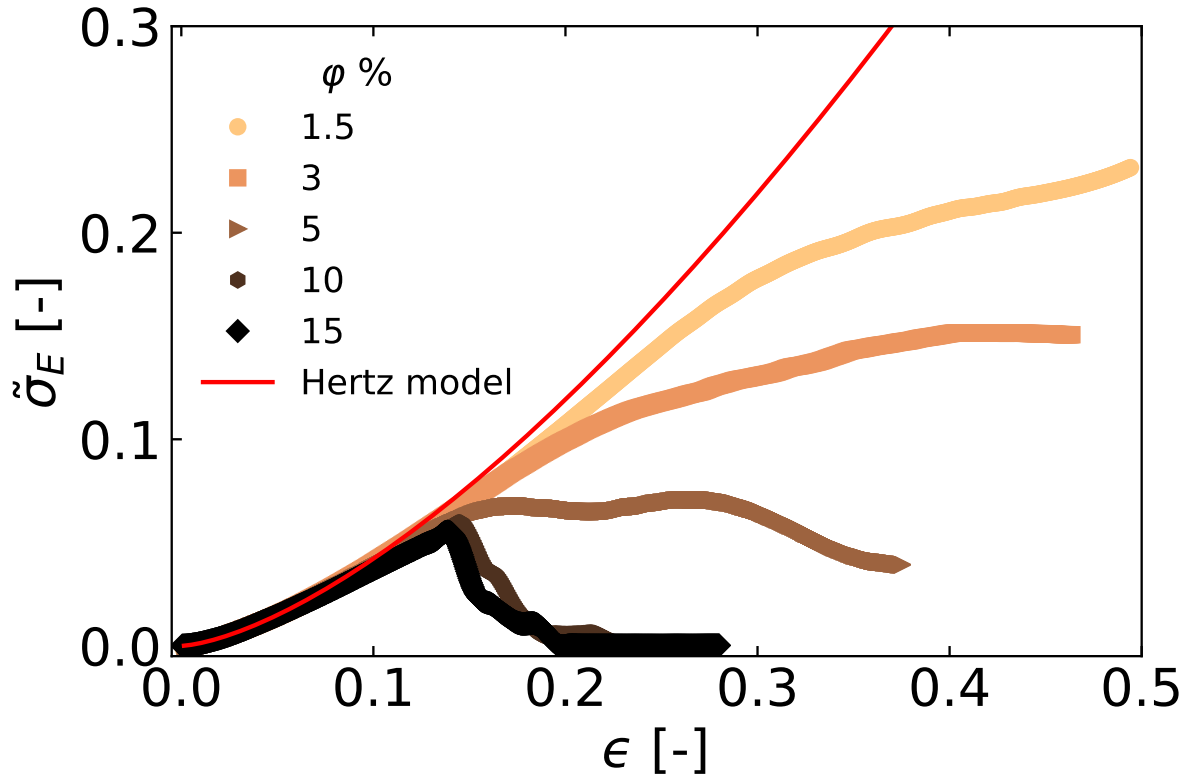

Figure 56: Adimensional engineering stress as a function of the indentation strain. Solid symbols correspond to experimental data of beads of colloidal gel prepared at different volume fractions. The red solid line represents the Hertz contact model.

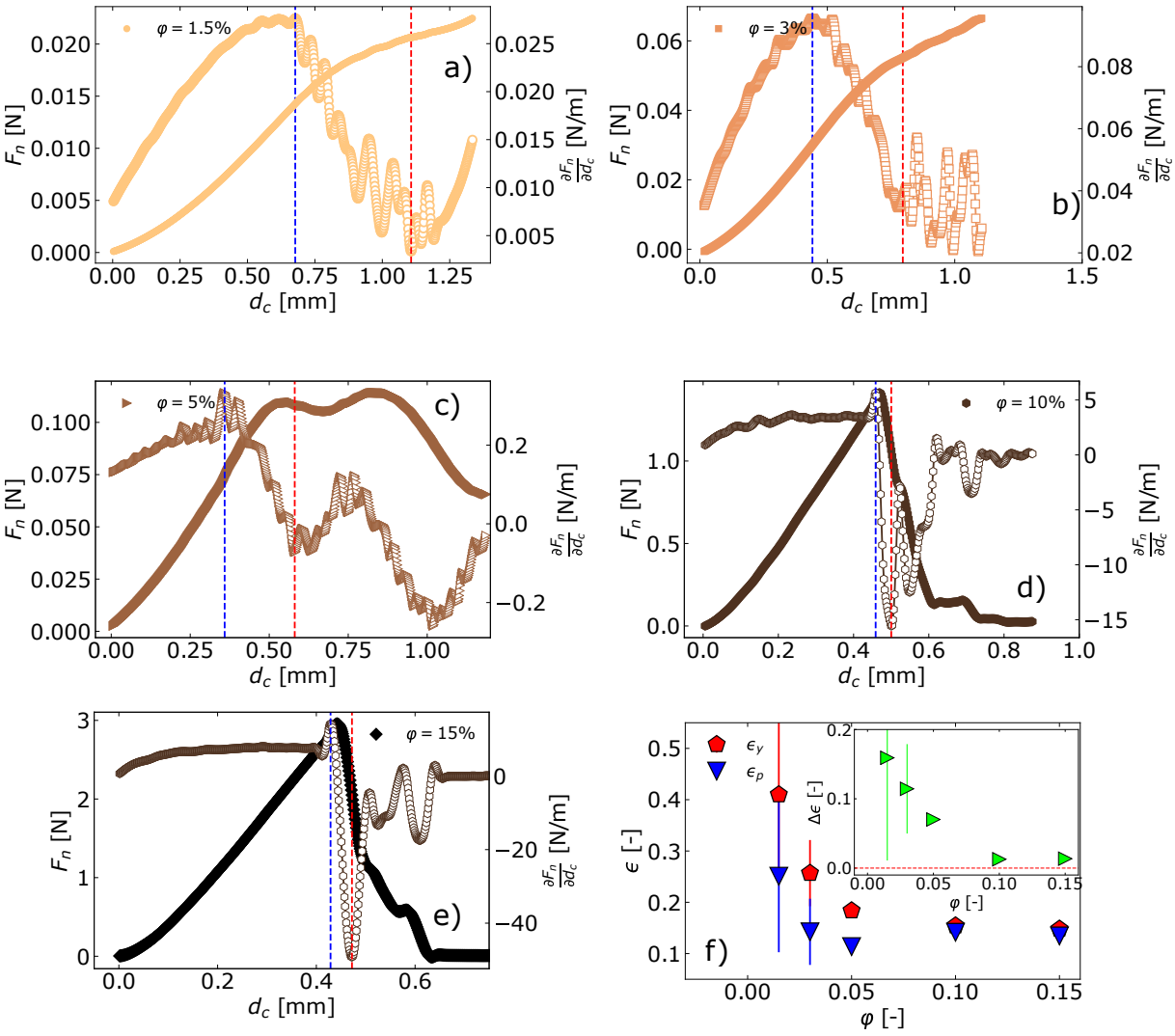

Figure 57: Normal force (filled symbols on the left axes) and derivative of the normal force (empty symbols on the right axes) as a function of the indentation depth for beads of gel prepared at different volume fractions: a) $\varphi = 1.5\%$, b) $\varphi = 3\%$, c) $\varphi = 5\%$, d) $\varphi = 10\%$, e) $\varphi = 15\%$. Blue and red dashed lines indicate the plasticity strain ϵ_p and the yielding strain ϵ_y, respectively. f) Plasticity and yielding strain as a function of the volume fraction. (Inset) Difference between yielding and plasticity strain as a function of the volume fraction

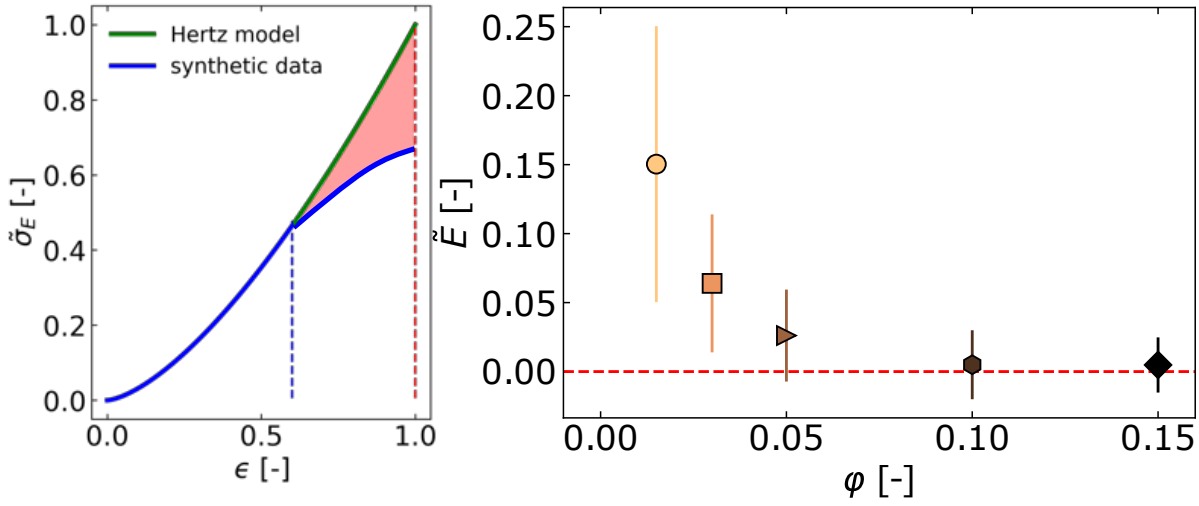

Figure 58: a) Sketch of the energy dissipated by the sample: the green line represents the response of a pure elastic body (following the Hertz contact model) in normalized units, while the blue line is a schematic representation of the data. The reduced dissipated energy is the integral between the two curves. b) Reduced energy $\tilde{E}$ (see Eq. 5.1) as a function of the volume fraction.

To further characterize the failure of the beads, we compute the first derivative of the force with respect to the indentation distance $\partial F_n/\partial d_c$, which is plotted as a function of the indentation depth d_c in Fig. 57. Then, by finding the first maximum and the consecutive minimum of $\partial F_n/\partial d_c$, we easily identify the positions of the inflection points of the force. One one hand, the position of the first maximum identifies the indentation depth d_p at which the force stops growing as the Hertz model, thus identifying the end of the elastic regime. We define the corresponding strain plasticity as $\epsilon_p = d_p/d_0$. On the other hand, the position of the first minimum of $\partial F_n/\partial d_c$ identifies the yielding indentation depth d_y. We define the yielding strain as $\epsilon_y = d_y/d_0$. Both ϵ_p and ϵ_y decrease as the volume fraction increases, see Fig. 57f. Moreover, the difference $\Delta\epsilon$ between ϵ_p and ϵ_y decreases as well for increasing φ, see inset of Fig. 57f. This fact is particularly interesting since indicates that beads prepared at high volume fraction ($\varphi = 10, 15\%$) fail basically in the linear regime. In contrast with beads prepared at low volume fraction ($\varphi = 1.5, 3\%$), which, before yielding, display a region in which they undergo plastic rearrangements.

Finally, we quantify the adimensional dissipated energy before yielding. To do so we define the reduced energy $\tilde{E}$ as:

$$\tilde{E} = \tilde{E}_{p.e.b.} - \tilde{E}_s \tag{5.1}$$

where $\tilde{E}_s$ is the total energy of the sample before yielding, and $\tilde{E}_{p.e.b.}$ is the elastic energy that a perfect elastic body with the same E^* would have stored if compressed by the same amount. $\tilde{E}_s$ is defined as

$$\tilde{E}_s = \int_{\epsilon_p}^{\epsilon_y} \tilde{\sigma}_E \delta\epsilon \tag{5.2}$$

and

$$\tilde{E}_{p.e.b.} = \int_{\epsilon_p}^{\epsilon_y} \frac{4}{3}\epsilon^{3/2}\delta\epsilon \tag{5.3}$$

A sketch to visualize $\tilde{E}$ is plotted in Fig. 58a. In both integrals the lower integration limit is the plasticity strain ϵ_p while the upper integration limit is the yielding strain ϵ_y. We plot in Fig. 58b $\tilde{E}$ as a function of the volume fraction. Interestingly, we find that the higher the volume fraction the lower is $\tilde{E}$. So, the different way of failing of the materials is also affected by the energy dissipation: beads that dissipate energy during the compression display a smooth failure. Contrarily, when a stiff beads undergo compression, the energy is mainly stored and it released at the failure $\tilde{E} \approx 0$.

All these results are obtained for a single compression rate $\dot{\epsilon} = 10^{-1}$ s^{-1}. To check whether or not our findings strictly depend on the strain rate we used, we show in the next section the results gathered at different $\dot{\epsilon}$.

5.2.2 Rate Dependence

5.2.2.1 Hertz contact model for small deformation

To understand the role of the compression rate we perform, for each volume fraction, several experiments in which we vary the compression rate by four orders of magnitude, in the range $\dot{\epsilon} \in [10^{-3}, 1]$ s^{-1}. Figures 59a-c display in log-log scales the adimensional engineering stress as a function of the strain of compression for different $\dot{\epsilon}$ for beads prepared at different volume fraction, $\varphi = 1.5\%$, $\varphi = 5\%$ and $\varphi = 10\%$ in panel a, b, c respectively. Interestingly, for each φ, the data taken at different $\dot{\epsilon}$ collapse together, indicating that the Hertz contact model applies independently of the rate. The differences between the curves at small strain are due to the noise given by the low value of the force for small strains. Moreover, in Fig. 59d we plot the generalized Young Modulus as a function of the rate for all volume fraction. We find that E^* is constant in the range of compression rate we have explored, thus indicating that the mechanical properties in the small regime do not depend on the rate.

5.2.2.2 Failure at large deformation

To understand the role of the compression rate on the failure of the gel. We plot in Fig. 60 the normalized engineering strain as a function of the compression strain for different compression rates. The four plots display the same qualitative trend: at small strain all curves overlaps following the Hertz contact model, while for deviating from it at large strain. Moreover, for all rates we observe that stiff gels ($\varphi = 10, 15\%$) suddenly deviate from the Hertz behavior with an abrupt decrease of the force, while softer gels ($\varphi = 1, 3\%$) display a smoother deviation from the Hertz model. The bead of gel prepared at $\varphi = 5\%$ represents the crossover between the two behaviors. Note that, the plot for

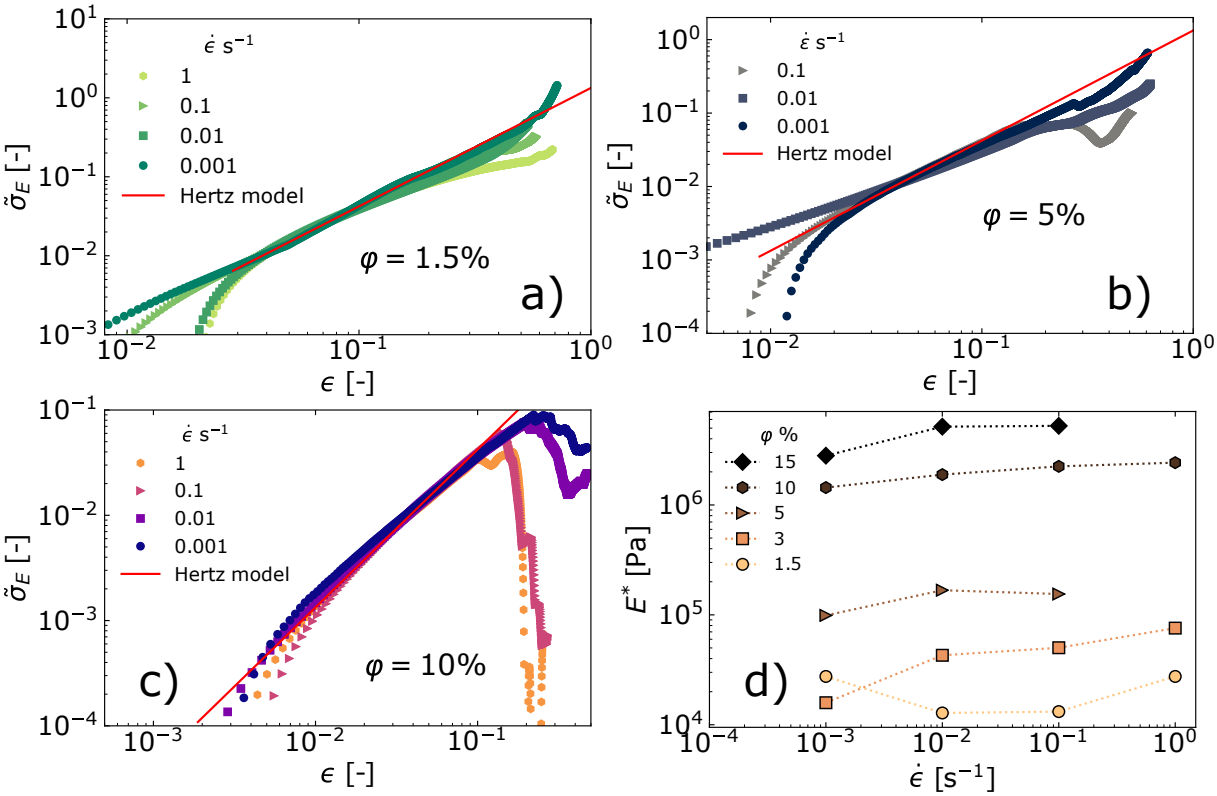

Figure 59: a-c) Log-log plots of the adimansional engineering stress as a function of the compression strain for beads compressed at different compression rates. Different panels represent different preparation volume fraction: a) $\varphi = 1.5\%$, b) $\varphi = 5\%$, c) $\varphi = 10\%$. d) Generalized Young modulus as a function of the rate of compression: different symbols represent different volume fraction, dotted line are guides for the eye.

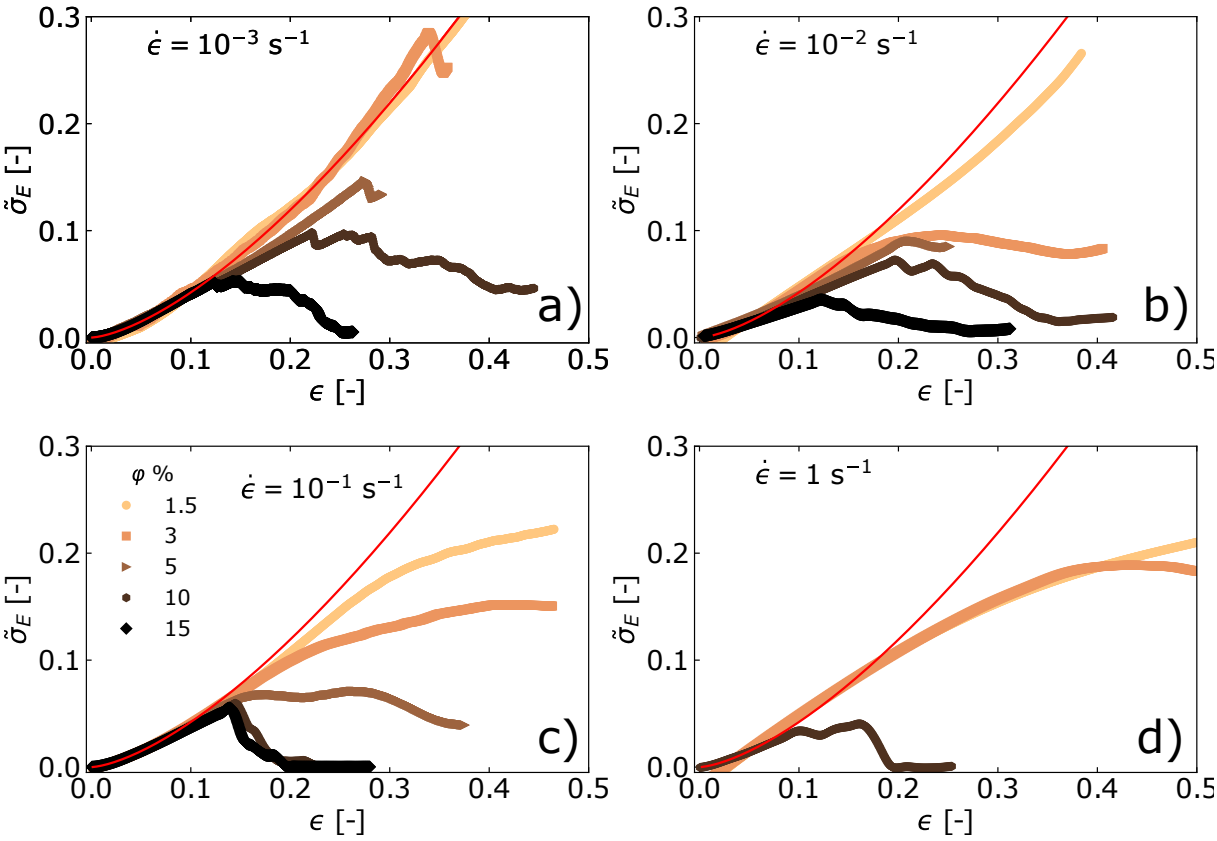

Figure 60: Adimensional engineering stress as a function of the strain for beads of colloidal gel prepared at different volume fractions. Different panels correspond to different rates of compression a) $\dot{\epsilon} = 10^{-3}$ s^{-1}, b) $\dot{\epsilon} = 10^{-2}$ s^{-1}, c) $\dot{\epsilon} = 10^{-1}$ s^{-1}, d) $\dot{\epsilon} = 1$ s^{-1}

$\dot{\epsilon} = 1\ s^{-1}$ (Fig. 60d) is the one that differ the most from the others. We believe this is due to the poor sampling of the data acquisition. Indeed, when compressing at high rates, the maximum number of points per second which the rheometer allows one to take limits us in taking a satisfying sampling.

Moreover, we plot the plasticity strain ϵ_p, the yielding strain ϵ_y and the adimansional dissipated energy $\tilde{E}$ as a function of the volume fraction φ for each compression rate $\dot{\epsilon}$ in Fig. 61a, b, c respectively. Overall, for all rates, ϵ_p, ϵ_y and $\tilde{E}$ decreases with increasing volume fraction; thus indicating that in the rate does not play a major role. To enhance the dependence of the compression rate, we re-plot data ϵ_p, ϵ_y and $\tilde{E}$ as a function of $\dot{\epsilon}$ for each volume fraction in Fig. 61d, e, f respectively. In these plots a clear dependence of these quantities on $\dot{\epsilon}$ does not emerge.

5.3 Discussion

In this section we summarize the results obtained from the experiment on uniaxial compression. Firstly, we focus on some experimental issues. Secondly, we focus on the shape of the stress strain curve, making a connection with the brittle-to-ductile transition observed in the literature. Thirdly, we make a comparison with shear rheology, showing the differences between the two geometries to underline novelty introduced by using the uniaxial compression. Finally we focus on the open questions of this work.

5.3.1 Experimental issues

Firstly, the spherical shape of the beads itself makes difficult the interpretation of the phenomenon. Indeed, in a previous work based on molecular dynamics simulation [Akl et al. (2023)], it has been shown that the failure of glassy spheres composed of nanoparticles is governed by local stress distribution. For this reason describing the failure of the beads only with global quantities such as ϵ_p, ϵ_y and $\tilde{E}$ may be reductive. Indeed, a full characterization of the strain and stress fields would have been extremely insightful for the description of the yielding in such a geometry.

Secondly, despite having checked that $\dot{\epsilon}$ does not alter the mechanical properties in the small deformation regime, the exact role of the compression rate needs to be further investigated. Indeed, a clear scenario unraveling the role in the failure of the rate of compression is still missing. Two of the main challenges in solving this task are: 1) that a complex system such as a colloidal gel is characterized by several characteristic relaxation time, which are related to network rearrangements (occurring at different length scale) and to the flow of water out of the residual structure; 2) the interaction between the plates

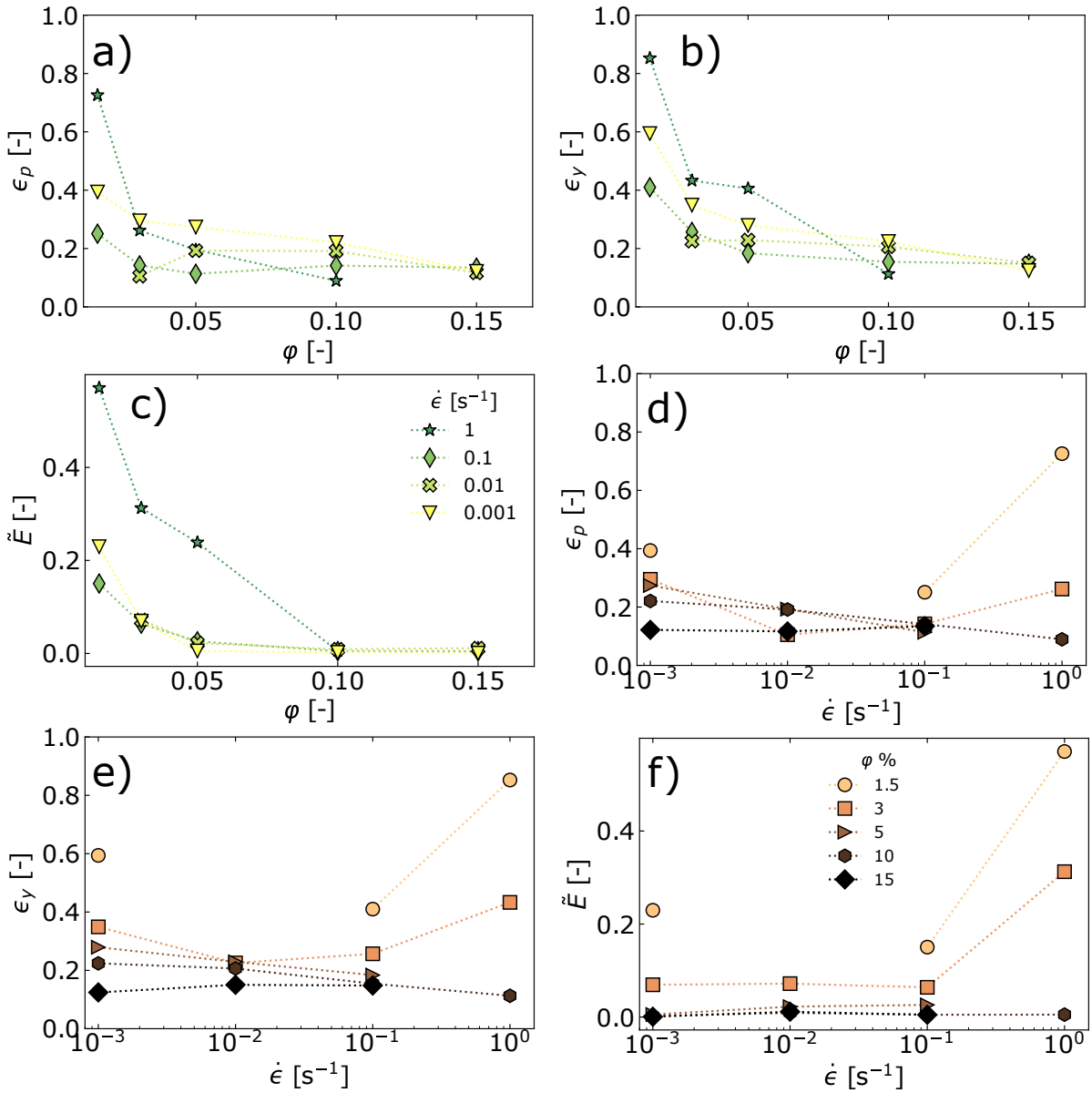

Figure 61: a) Plasticity strain as a function of the volume fraction for different compression rates. b) Yielding strain as a function of the volume fraction for different compression rates. c) Reduced energy $\tilde{E}$ (see Eq. 5.1) of the volume fraction for different compression rates. d) Plasticity strain as a function of the compression rate for different volume fractions. e) Yielding strain as a function of the compression rate for different volume fractions. f) Reduced energy as a function of the compression rate for different volume fractions. Dotted line are guides for the eye.

of the rheometer and the bead, which changes the contact area during the indentation.

Thirdly, the imaging of the beads under the compression needs to be improved, since so far it has only provided us a qualitatively view on the failure of the beads. In first instance the introduction of a fast camera would allow us to get a better visualization of the propagation of the cracks. Then a synchronization between the camera and the rheometer will allow us to get a one to one correspondence between the macroscopic aspect of the bead and the force measured by the rheometer.

5.3.2 Brittle-to-ductile failure

The most important result achieved in this chapter concerns the emergence of the brittle-to-ductile transition in the yielding of beads of colloidal gels under uniaxial compression. First, the stress-strain curves shown Fig. 56, display the typical features characterizing the stress-strain curves of a brittle-to-ductile transition (see description in Chapter 1): the stress of beads prepared at high volume fraction drops abruptly at yielding, while the stress of soft beads smoothly change shape at ϵ_y. Second, the difference $\Delta\epsilon = \epsilon_y - \epsilon_p$ between the yielding and plasticity strain (inset in Fig. 57f), well quantifies the fact that tough beads (high volume fraction) yield almost in the linear regime, while soft beads (low volume fraction) are characterized by a plasticity region before yielding. Third, while the adimensional dissipated is approximately 0 for tough beads, $\tilde{E}$ assume a finite value for soft beads. These aspects raised by the analysis on mechanical data are also encountered in the macroscopic aspect of yielding: indeed, tough beads fail abruptly by fragmenting into several pieces, while the failure of soft beads is smooth, accompanied by one or few cracks which slowly propagates through the sample. Finally we proved that our results do not strictly depend on the rate at which the gels are compressed.

One possible explanation of such a dependence on the volume fraction may be the influence of φ on the homogeneity of the systems. Indeed, the scattering intensity profiles in Fig. 45 show that colloidal gels prepared at high volume fraction have a smaller cluster size compared to gels prepared at low φ. Since the cluster size also represent the threshold length scale above which the sample is homogeneous, high volume fraction implies homogeneity at smaller length scales, while low volume fraction implies homogeneity at large length scales. Interestingly, a similar microscopic scenario behind the brittle-to-ductile transition have been proposed in [Ozawa et al. (2018)]. In this work, the authors studied with numerical calculations the failure of a glass under shear. They found that the ductile-to-brittle transition was driven by the heterogeneity of the sample: the heterogeneous samples broke in a ductile manner, while homogeneous one were displaying a brittle failure.

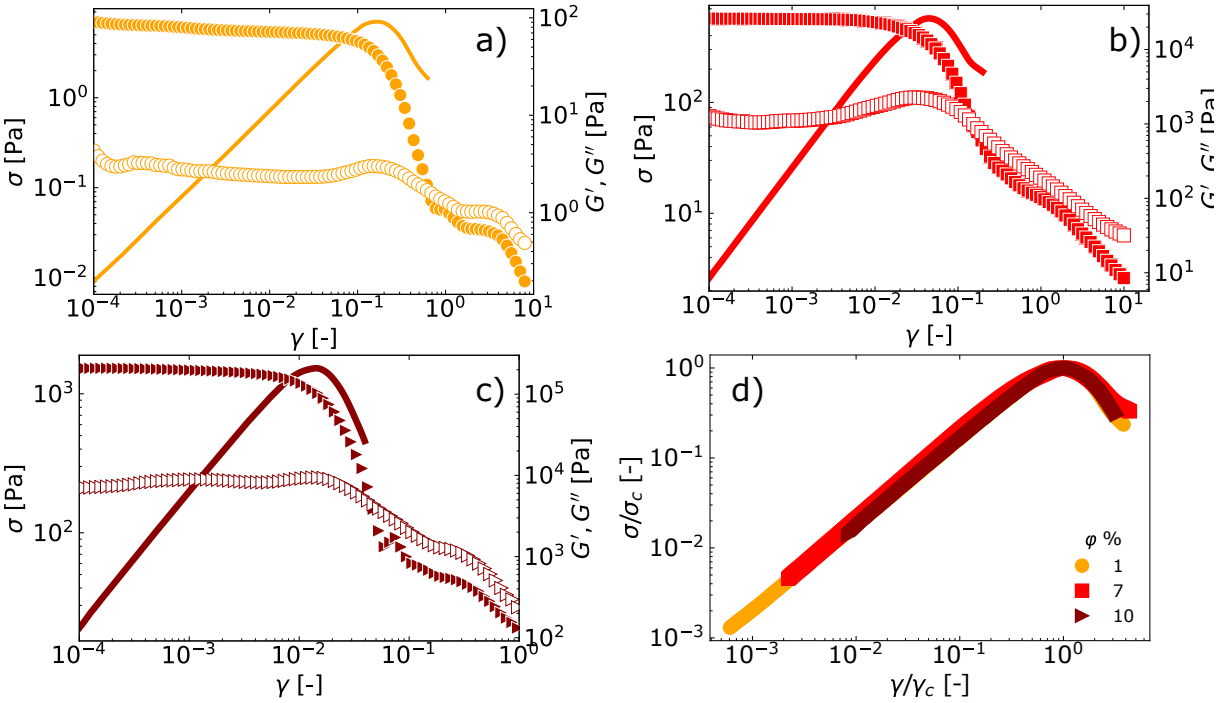

Figure 62: LAOS test on colloidal gels prepared at different volume fractions $\varphi = 1\%, 7\%, 10\%$ for panels a), b), c) respectively. On the left axes is represented the stress as a function of the shear strain, while on the right axes the storage and loss moduli are plotted as a function of the shear strains. Data are acquired in shear at $\omega = 1$ [rad/s] for gels prepared in between the two plates of the rheometers.

5.3.3 Failure in Shear Rheology

It is also extremely interesting to compare the yielding in uniaxial compression and in shear. We are particularly interested in this comparison since, to the best of our knowledge, a brittle-to-ductile transition has not been observed so far in the yielding of this kind of gels under shear. In Fig. 62 we plot the results of Large Amplitude Oscillatory Shear (LAOS) test we performed on colloidal gels prepared between the plates of the rheometer. After a first linear regime, in which G' and G'' are constant, at intermediate amplitudes ($1\% < \gamma < 20\%$) a drop of the elastic modulus is observed, which is accompanied by a peak in stress. Such a peak is associated with a critical strain γ_c which depends on the volume fraction, ranging from $\gamma_c = 18\%$ for $\varphi = 1\%$ to $\gamma_c = 1.5\%$ for $\varphi = 10\%$. This first yielding strain has been associated with the onset of non-linearity due to the bond breaking of the gel network [Koumakis and Petekidis (2011)]. After the first yielding the loss modulus becomes higher than the storage one, indicating the fluidification of the samples. At large amplitudes ($\gamma > 20\%$) the samples show a second peak in G'' indicating a second yielding process. The physical origin of this second yielding is more obscure; previous works associate it to cluster breaking and rotation [Koumakis and Petekidis (2011); Hoekstra et al. (2003)]. Finally, we rescale the curves: the strain is divided by the yielding strain γ_y, and the stress σ by its maximum value σ_c. Interestingly, we

find a nice overlap between all data, displaying no significant differences between samples prepared at low or high volume fractions. This overlap points out that all gels fail in the same qualitative way when sheared above the yielding strain. Such a result is intriguing since such a behavior is not observe in uniaxial compression. Indeed, while in Fig. 62d we obtain a nice overlap between the normalized stress and strain, in Fig. 56 the curves strongly deviate at large strain.

5.3.4 Open questions

This new experimental method opens several questions. Firstly, a clear explanation unraveling the role of the volume fraction into the brittle-to-ductile transition still needs to be found. Indeed, the consideration based on sample heterogeneities (see Sec. 5.3.2) remains an hypothesis to be further investigated and verified.

To better understand the yielding, we tried to compare the speed of propagation of the cracks with the speed of sound in the media. We found that the speed propagation turns out to be much lower than the speed of propagation of the transverse waves of sound in the media. Indeed, the cracks propagate with $v_c \approx 1.5 \cdot 10^{-3}$ m/s for $\varphi = 3\%$ and $v_c > 5 \cdot 10^{-3}$ for $\varphi = 10\%$, while by evaluating the speed of sound with $c = \sqrt{G_0/\rho}$, where ρ is the density of water, we find that $c = 3$ m/s and $c = 14$ m/s for beads prepare at $\varphi = 3, 10\%$ respectively. Thus, the mechanism which rules the cracks propagation needs further investigations.

Moreover, the comparison with shear rheology remains to be understood. Indeed, while in uniaxial compression a brittle-to-ductile transition is observed for samples prepared at different volume fraction, in bulk shear rheology, the stress strain curves perfectly overlap at yielding. We believe that such a difference is given by the localization of the failure in shear rheology. Indeed, in shear the failure most likely develops along the surface of contact between the sample and the plates of the rheometer. Moreover, to make a direct comparison between uniaxial compression and shear, it would be better to perform instead of LAOS shear start up experiments. Indeed, in the latter configuration the sample is deform at constant shear rate as for our uniaxial compression.

Chapter 6

Drying Beads of Colloidal Gels

6.1 Introduction

In this Chapter we present the results on drying beads of colloidal gel. As mentioned in Chapter 1, our goal is to understand how the gel microstructures rearrange when the gel is compressed by the drying stresses. Since it has been proven that sample adhesion with substrate induces delamination and/or cracking [Brinker and Scherer (2013)], to get an smooth isotropic compaction, we dry beads of colloidal gel deposited on top of hydrophobic surfaces.

In Sec. 6.2 we will present a synthesis of main results obtained by the three experimental methods we used: Dynamic Light Scattering, X-ray scattering and uniaxial compression. Then in Sec. 6.3 we will discuss the results, making a comparison with the behavior of other samples investigated in this thesis. Finally in Sec. 6.4 we present additional results and analysis we made to investigate this process.

6.2 Main results

In this section we present the results regarding drying beads of colloidal gel. Firstly we will present the data obtained with DLS measurements: by using the setup presented in detail in Chapter 3 we get information about the microscopic dynamics of the system during drying. Secondly we will show the results regarding the evolution of the structure obtained with X-ray scattering. Finally we show the effects of drying on a macroscopic mechanical property of the gel such as the Young modulus.

6.2.1 Macroscopic behaviour

In Fig. 63a we show a bead of colloidal gel while drying. Thanks to the preparation method and the hydrophobicity of the surface, the bead does not adhere and in the first stage of drying shrinks smoothly with time. At a time $t = 5400$ s the bead stops shrinking and it becomes white, see Fig. 63a vi. The volume of the bead remains constant until the end of the experiment, which has been stopped after ~ 48 h. As mentioned in Sec. 1.2.3,

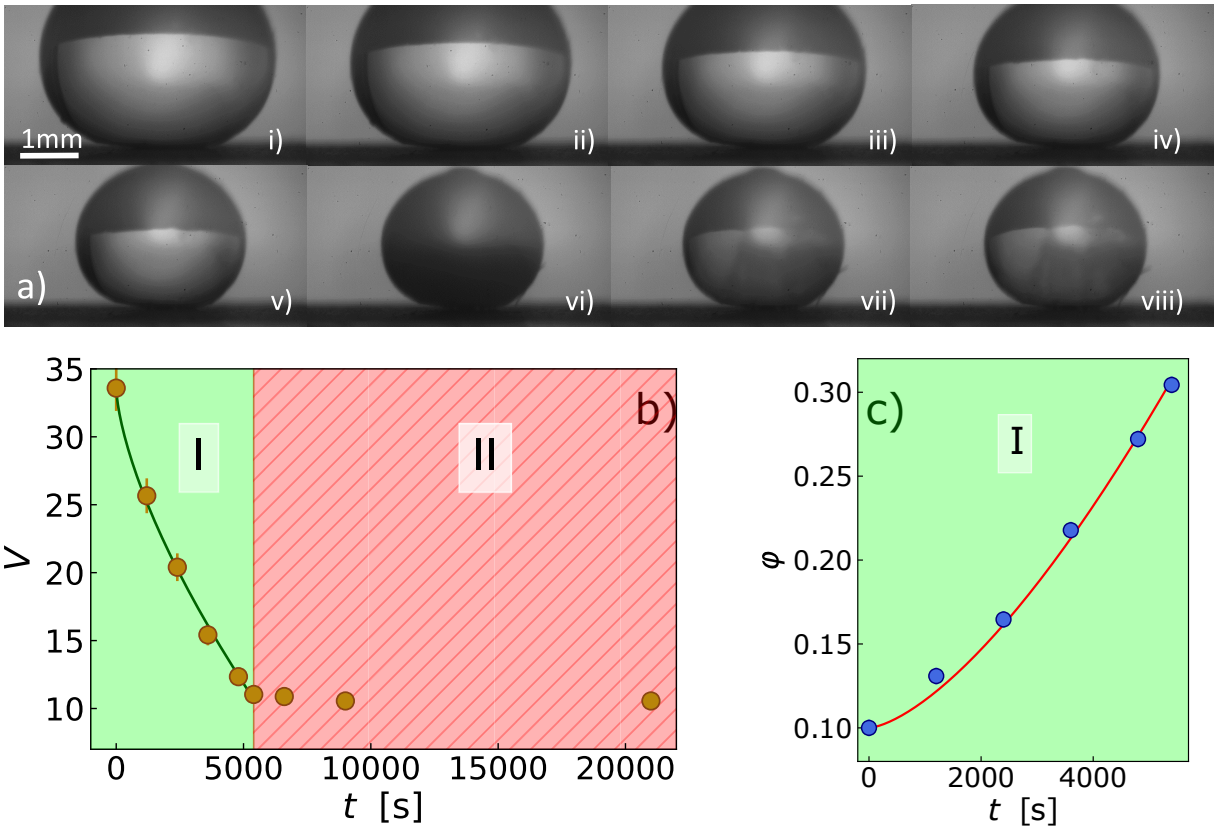

Figure 63: a) Imaging of a bead of colloidal gel prepared at $\varphi_p = 10\%$ while drying (side view). The gel is clean from oil and put onto a hydrophobic surface at the time t=0 s (i) and shrinks at constant rate (i-v). At time t=5400 s (vi) the gel stops shrinking and air invades the solid structure leading the opacity of the sample. The gel keeps drying without reducing its volume and, at time t=9000 s (vii) it becomes translucent and stops drying. b) Normalized volume as a function of time, gold circles represent the data and the red line is a guide line for the eyes. c) Volume fraction as a function of time. the data are plotted until the gel shrink while drying. the blues circles represent the data, the red solid line is a guide line for the eyes.

this change in opacity coincides with the beginning of a second drying regime, in which the water escapes the gel structure flowing through capillary bridges. Even though we did not measure the mass during time, the proof that the bead is still evaporating is given by the second change in the transparency of the gel shown in Fig. 63a vii and viii.

In Fig. 63b we plot the evolution of the volume of the bead as a function of time. The volume has been measured by measuring the area and using the Pappus Guldinus theorem of revolution solids. Knowing the initial volume fraction and the loss of volume we calculate the volume fraction of NPs in the gel while drying. In Fig. 63c we plot the evolution of φ as a function of time. We observe that the maximum volume fraction φ_d reached in the first drying regime, depends on the preparation volume fraction: we find that $\varphi_{d\max} = 18\%$ for a gel prepared at $\varphi_p = 2\%$, while a gel prepared at $\varphi_p = 10\%$ reaches $\varphi_{d\max} = 32\%$. Moreover, for a given φ_p, the maximum volume fraction does not vary in the range of strain rate $\dot{\epsilon} \in [10^{-2} - 10^{-6}]$ s^{-1} at which the beads are dried.

To probe whether the drying is a reversible phenomenon or if it induces irreversible plastic events, we let dry a bead of gel ($\varphi_p = 10\%$) and, when it is still in the first drying regime ($\varphi_d = 20\%$), we immerse the bead in water. We then follow the evolution of the bead appearance with the same imaging setup for about 10h. Interestingly, contrary to what happens for beads of polymer hydrogel, the bead does not swell back and its volume remains unaltered with time. This fact indicates that drying induces permanent structural rearrangements in the gel. So, water evaporation induces a compression which is relaxed by the bead of gel though permanent rearrangements of the solid network.

In the next section we investigate the change on the mechanical properties due to the compaction induced by the drying.

6.2.2 Microscopic Dynamics

First we investigate the microscopic dynamics of the drying beads through DLS experiments with our custom PCI setup capable to resolve microscopic dynamics with time- and space-resolution. With this setup, which has been fully described in Chapter 3, we have succeeded in characterizing the space-dependent dynamics of drying drops of colloidal suspensions and the swelling of a polymeric gels (see respectively Chapter 7 and Chapter 3). Knowing whether the drying is a homogeneous process or not, it is key for the interpretation of the data obtained by X-rays. Indeed, the scattered intensity measured by X-ray scattering is an average quantity, which reflects structural information regarding the whole scattering volume. In this framework, this property might be critical, since one might expect that drying is a spatially heterogeneous phenomena. Indeed, for example, the drying of a drop of colloidal suspension is strongly heterogeneous: while the core of the drop barely does not experience the drying, the periphery is characterized by a dense shell of colloidal particles which structure and dynamics are strongly affected by

the drying Tsapis et al. (2005); Sobac et al. (2019); Basu et al. (2016).

Figure 64a shows the intensity correlation functions for a bead of gel drying at a rate $\dot{\epsilon} = 4.4 \cdot 10^{-5}$ s^{-1}. Data are acquired for different ROIs, centered around different positions x along the bead diameter. The correlation functions are fitted with a stretched exponential decay function (Eq. 2.21). We find that the curves follow a compressed exponential decay, with $\beta \in$ [1,1.5]. Using Eq. 2.22, from the fitting parameters τ_E and β, we obtain the microscopic decay time τ_D. Firstly we notice that the microscopic dynamics during drying are much faster compared to the quiescent one. Indeed, as shown in Chapter 5, the quiescent dynamics of this sample in the order of thousands seconds: the drying fastens the dynamics by two orders of magnitude. We plot in the inset of Fig. 64 the microscopic decay time as a function of the position x along the bead diameter. We see that τ_D is slightly faster on the edge compared to the center. However the difference is quite mild, since the shortest decay is two times faster then the largest one. However from a single experiment it is not possible to evince a clear space dependence. Indeed, due to the low number of speckles in each ROI, the data show large fluctuation.

To have more robust statistics, we run the drying experiment changing the initial volume fraction from $\varphi_p = 2\%$ to $\varphi_p = 15\%$, and changing for each of them the drying rate $\dot{\epsilon}$ by to orders of magnitude ($\dot{\epsilon} \in [10^{-6}, 10^{-4}]$ s^{-1}) by varying the RH. Interestingly, for a given $\dot{\epsilon}$ the decay time does not depend on the volume fraction. However, as we will detail in the following, τ_D strongly depends on $\dot{\epsilon}$. So, to compare the data, we define the adimensional microscopic mobility time: $\tau_M = \left\langle \frac{\tau_D}{<\tau_D>_x} \right\rangle_{exp}$. This quantify is the average over all experiments ($< ... >_{exp}$) of the decay time normalized by its averaged value along the bead diameter ($< ... >_x$). We plot in Fig. 64b the microscopic mobility time: τ_M as a function of the position. Note that by calculating τ_M we average gel at different φ_p and φ_d. Interestingly, we find that τ_M mildly depends on the position along the bead diameter. Indeed, the dynamics on the edges are not even a factor two faster compared to the center of the bead and this dependence is comparable with the fluctuations shown by a quiescent sample, where the dynamics are expected to be completely space independent.

This fact, together with the global fastening of the dynamics, is indicating that, under compression the stress is propagated in the whole gel, which causes a homogeneous speed-up of the dynamics. In other words, the stress applied at the gel/air interface by the solvent loss is propagated, causing rearrangements through the whole volume. This behavior is due to the interconnectivity of the solid structure which leads to very large correlations range of the dynamics, typically of the order of the system size Maccarrone et al. (2010).

Previously we mentioned that the decay time τ_D depends on the compression rate $\dot{\varepsilon}$. To rationalize the dependence we plot in Fig. 65 τ_D as a function of $\dot{\varepsilon}$. Interestingly we find that the microscopic decay time scales with the macroscopic compression rate following the law $\tau_D \sim \dot{\varepsilon}^{-1}$. Such relationship is particularly interesting since it reveals

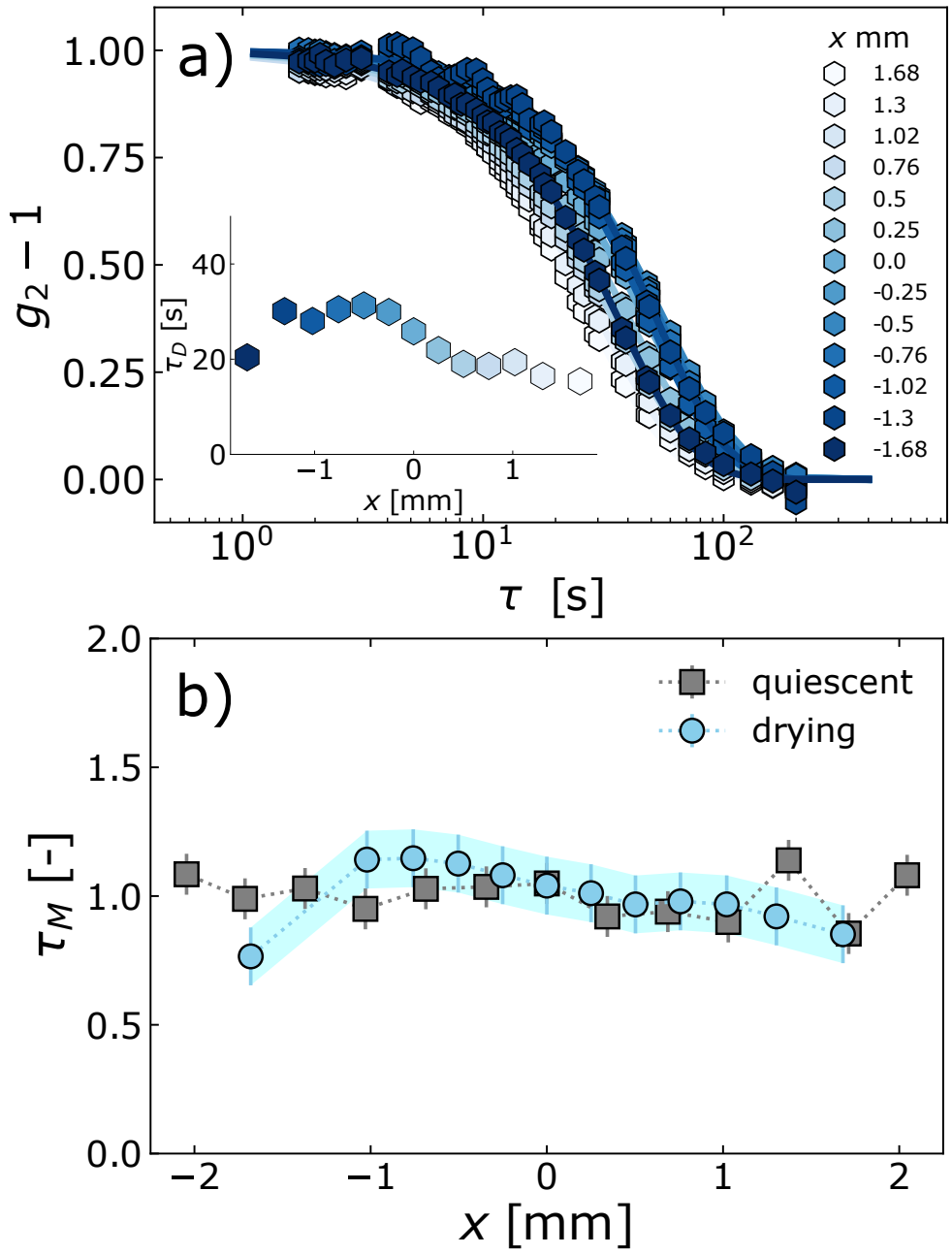

Figure 64: a) Intensity correlation functions for a bead of colloidal gel prepared at $\varphi_p = 14\%$, which is drying at $\dot{\epsilon} = 4.4 \cdot 10^{-5}$. Each correlation function correspond to a position along the bead radius. The solid lines are fits of Eq. 2.21 to the data. (Inset) microscopic decay timeτ_D as a function of the position along the bead diameter. b) Microscopic mobility time τ_M as a function of the position in the bead. Light blue circles represent drying beads, while gray squares represent a quiescent sample (bead immersed in oil) prepared at $\varphi_p = 10\%$.

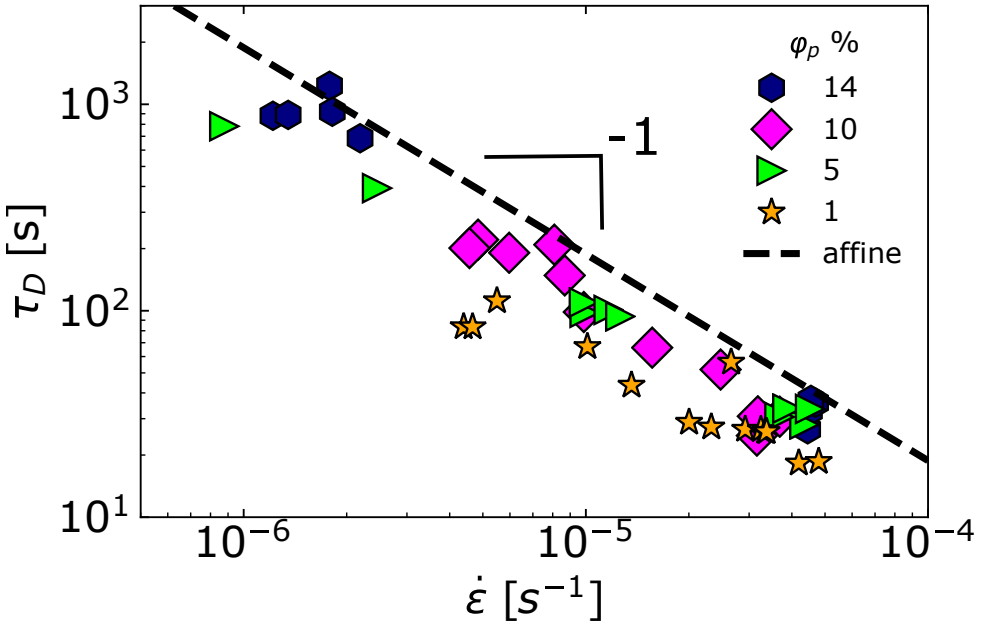

Figure 65: Microscopic decay time as a function of the compression rate $\dot{\varepsilon}$. Different symbols represent data from samples prepared at different volume fraction φ_p. Orange stars $\varphi_p = 1\%$, green triangles $\varphi_p = 5\%$, violet diamonds $\varphi_p = 10\%$, blue hexagons $\varphi_p = 14\%$. The black dotted line is the decay time obtained from the correlation function numerically calculated for the compression of a spherical homogeneous elastic body, see Chapter3

that the microscopic displacements are affine to the macroscopic compression. Indeed, we have shown in Chapter 3, that it is possible to numerically obtain the microscopic decay time given by a compression rate $\dot{\epsilon}$. By definition such a decay time only accounts for the pure affine motion. By plotting the affine decay time together with the experimental data (Fig. 65), we observe that the latter are located slightly below the numerical values. This fact indicates that the microscopic motion is mainly affine to the macroscopic compression.

6.2.3 Microscopic Structure

Since we have probed with DLS the homogeneity of the drying at the micro-scale, we use X-ray scattering to follow the microscopic structural evolution of the bead of colloidal gel during drying. We recall that, to normalize the data of the scattered intensity, we divide the spectra by an arbitrary constant so as to overlap $I(q)$ in the high q regime ($q > 3 \cdot 10^{-1}$ nm^{-1}).

In Figure 66 we plot the evolution of the scattered intensity for a sample prepared at $\varphi_p = 2\%$. The different curves correspond to different volume fractions φ_d reached during the drying by the sample. From the plot we see that the progressive increase of the volume fraction leads the scattered intensity to deviate increasingly from the one of the pristine sample. To be more quantitative, we define the scattered intensity difference $\Delta\tilde{I}$ between the intensity of pristine bead $\tilde{I}_p$ taken just before the evaporation protocol starts,

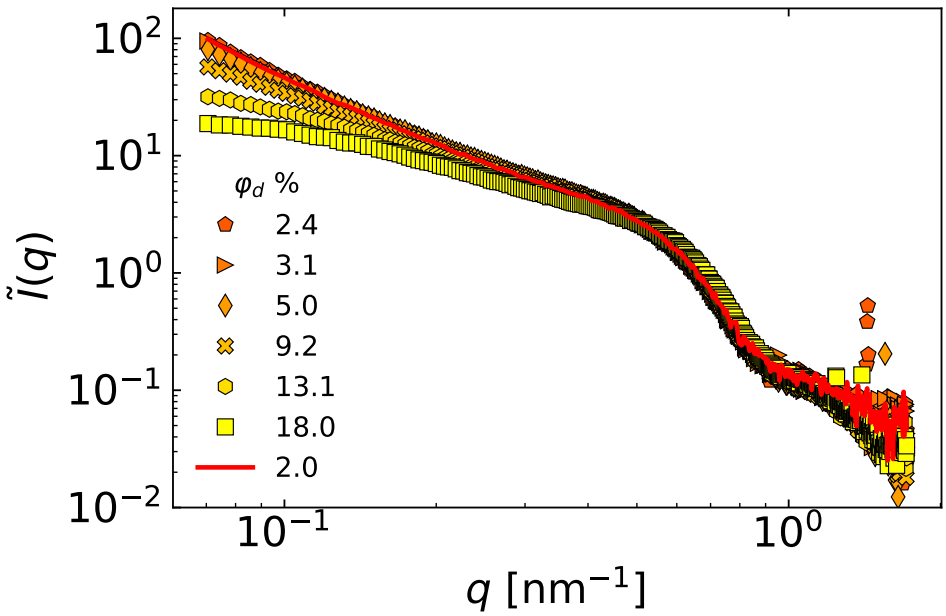

Figure 66: Time evolution of the scattered intensity for a sample prepared at $\varphi_p = 2\%$. Different symbols correspond to different volume fractions φ_d, the red solid line represent the pristine sample prepared at $\varphi_p = 2\%$.

and the intensity $\tilde{I}_d$ corresponding to a volume fraction reached during the compaction: $\Delta\tilde{I} = \tilde{I}_p - \tilde{I}_d$. In Fig. 67a we plot the evolution over time of $\Delta\tilde{I}$ as a function of q for a gel prepared at $\varphi_p = 2\%$. We observe that in the first stages of drying, where the compaction led to volume fraction not higher than $\varphi_d = 2.4\%$, $\Delta\tilde{I}$ fluctuates around 0. This fact indicates that the structural rearrangements are occurring at length scales larger than the largest length scale available with our setup. However, as the compaction keeps increasing, $\Delta\tilde{I}$ start deviating consistently from 0. Moreover, this plot allows to identify precisely two features of the way the bead of gel rearranges while being compacted. Firstly, we observe that $\Delta\tilde{I}$ becomes higher with increasing φ and, secondly, we see that the scattering vector q at which $\Delta\tilde{I}$ deviates from 0 also increases for increasing volume fraction. The first finding is telling that the more the gel is compacted by the drying, the more the microscopic structure rearranges in order to allow for the macroscopic volume loss. The second finding tells how the rearrangements are made by the gel. Indeed, finding that the q at which the $\Delta\tilde{I}$ differs from 0 evolves with φ_d, it indicates that the gel has an hierarchy when accomplishing the macroscopic compression: it starts modifying its structure at lager length scales and later also the smaller ones are modified.

We quantify this feature by defining a characteristic length scale l_c below which the gel does not rearrange. For doing so, as shown in Fig. 67b, we first horizontally shift all the curves $\Delta\tilde{I}$ by a factor S_f such that all the curves overlap with the one relative to the last stage of drying ($\varphi_d = 18\%$). Then we identify the largest q_{max} at which $\Delta\tilde{I} > 0$. In Figure 67b,c,d we plot the shifted data for beads prepared at $\varphi = 2, 5, 10\%$ respectively.

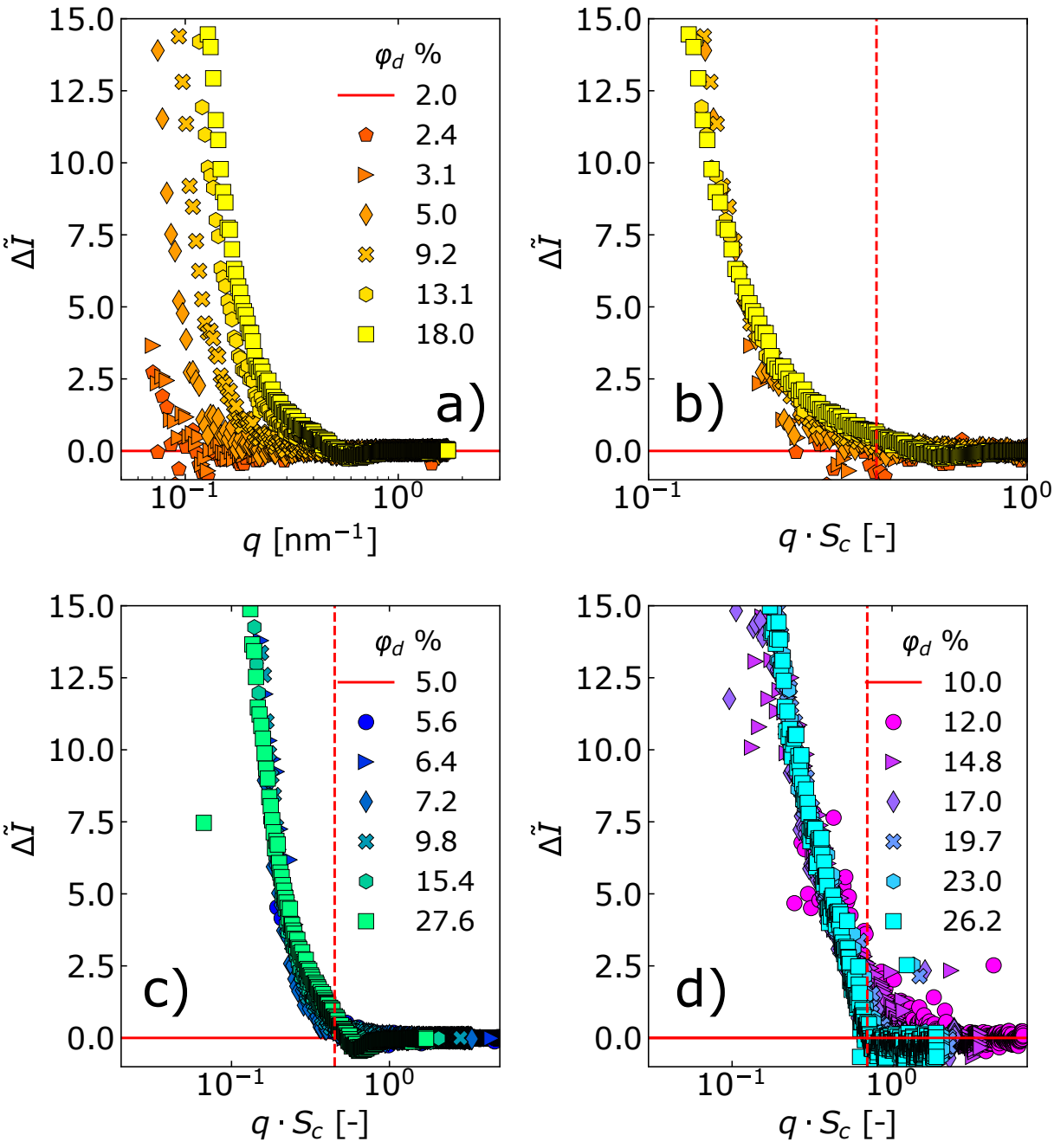

Figure 67: a) Time evolution of the difference between the scattered intensity of the pristine gel and the dried one for a gel prepared at $\varphi_p = 2\%$. The relative intensity are plotted as a function of scattering vector. Each symbol correspond to a different volume fraction reached during the drying. The red dotted line, drawn at $\Delta\tilde{I} = 0$ is a guide for the eyes and stands for the pristine gel. b) Data of panel a) shifted to the curve $\varphi_d = 18\%$. The red vertical line is a guide to the eye to identify q_{max} below which the structure do not rearrange. c) and d) Shifted data

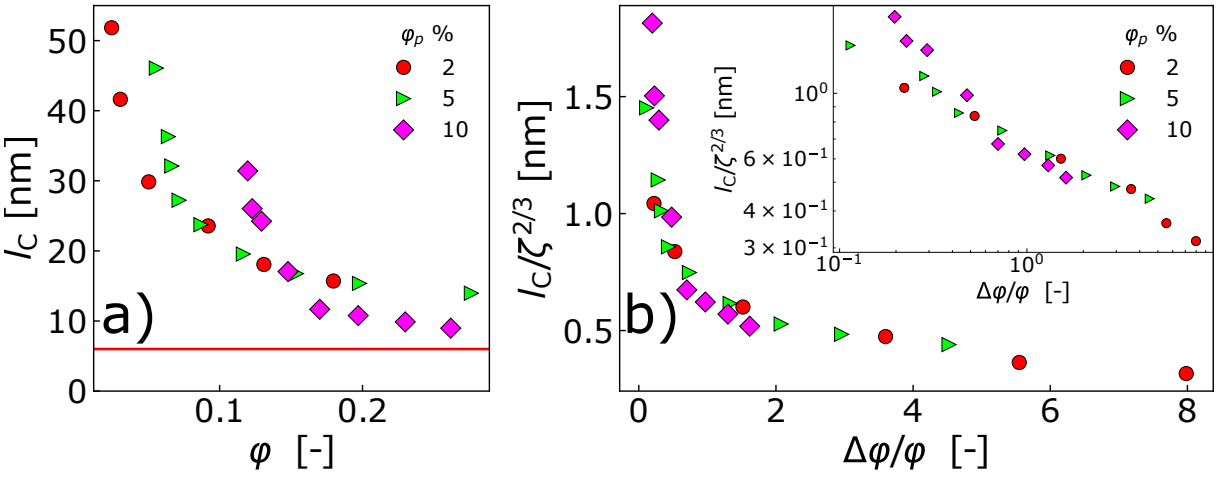

Figure 68: a) Characteristic length scale of drying normalized by the number of particles per unit volume as a function of the relative increase of volume fraction, during the drying process. The red solid line represent the particle size below which the structure do not rearrange. b) Characteristic length scale of drying normalized by the number of particles per unit volume as a function of the relative increase of volume fraction (Inset) Log-log plot of the data of the main panel.

Finally, we define the characteristic length scale $l_c = 2\pi/q_{max} \cdot S_f$. We plot the evolution of the characteristic length scale l_c as a function of the relative increase of the volume fraction $\Delta\varphi/\varphi$ in Fig. 68b.

Interestingly, l_c monotonically decreases with $\Delta\varphi/\varphi$: confirming that the gels have a hierarchy in rearranging their structure. When a macroscopic compression is imposed, colloidal gels firstly rearrange at large length scales, and subsequently the length scale becomes smaller and smaller, until reaching the single particle size. Moreover, we have shown in Chapter 5 that the cluster size ζ for a gel prepared at $\varphi_p = 2\%$ is roughly 500 nm. Since $l_c < 60$ nm, the structural rearrangements might occur within a single cluster. Moreover, we observe that the lower the preparation volume fraction φ_p, the larger the length scales at which the rearrangement occur. Interestingly, as shown in Fig. 68b, the data nicely collapse when plotting l_c divided by $\zeta^{d_f/3}$, where we have used $d_f = 2$ and the cluster sizes ζ measured in Chapter 4. The quantity $\zeta^{d_f/3}$ is directly proportional to the number of particles present in the linear dimension of a cluster. This fact is suggesting that an high number of particles allows the gel to rearrange at large length scale.

Finally, we want to understand if the structure formed by the isotropic compaction is the same of that formed by the Brownian diffusion of clusters during the gel formation. To address this question, we first prepare beads of gel at different volume fraction φ_p =2, 5, 10 % and we let them dry until reaching a target volume fraction $\varphi_d = 10\%$. As shown Fig. 69 the scattering profiles differ from each other. This indicates that the structure of the three gels with volume fraction of 10% are different, suggesting in turn that the different mechanism of bonds formation during gel formation and compaction produces different structure. We will show in the next section that these differences are reflected

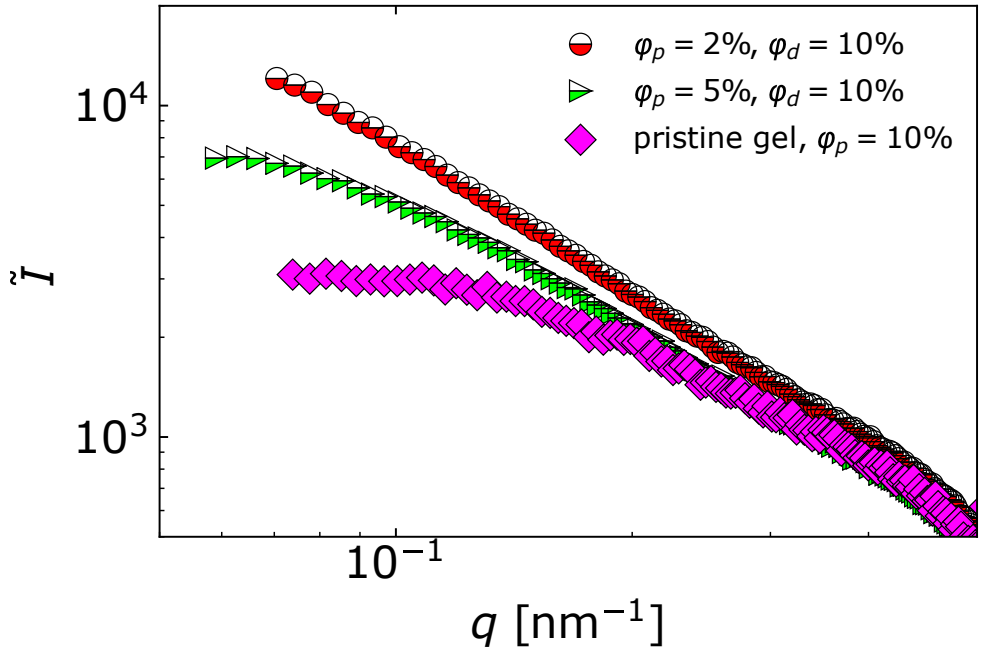

Figure 69: Normalized scattered intensity as a function of scattering vector for gels dried at the same target volume fraction $\varphi = 10_d\%$. Different symbols and colors correspond to the preparation volume fraction: red circles $\varphi_p = 2\%$, green triangles $\varphi_p = 5\%$, violet diamonds $\varphi_p = 10\%$.

at the macroscopic scale in changes of the mechanical properties of the gel.

6.2.4 Mechanical properties

To probe the mechanical properties of beads we perform the compression tests described in Sec. 2.3.2. Figure 70a shows a family of curves of the normal force as a function of the indentation depth for a gel prepared at $\varphi_p = 5\%$. We let the bead of gel dry until it reaches a volume fraction $\varphi_d = 18\%$. For all the curves, as the indentation depth increases, the normal force increases monotonically. By fitting the data at small deformations to Eq. 2.34 , we extract the Young modulus E of the gel. We plot in Fig. 70b E as a function of the volume fraction φ_d reached at different times during the drying process. We find that the compaction induced by the drying leads to an increase of the Young Modulus by almost one order of magnitude, indicating the stiffening of the gel.

The scaling with the volume fraction of the elastic properties is a common feature of pristine colloidal gels. Indeed, as we discussed in Chapter 5, it is know that the shear elastic modulus scales with the volume fraction according to the law: $G_0 \sim \varphi^\alpha$. The scaling exponent, which usually varies between 3 and 8, has been ultimately related to the micro-structural organization of the gel network [Aime et al. (2018a); Grant and Russel (1993); Rueb and Zukoski (1997); Shih et al. (1990); Buscall et al. (1988); Trappe and Weitz (2000)]. Though, recently, it has been shown that the scaling coefficient more intimately depends on the backbone dimension at the inset of rigidity at the percolation

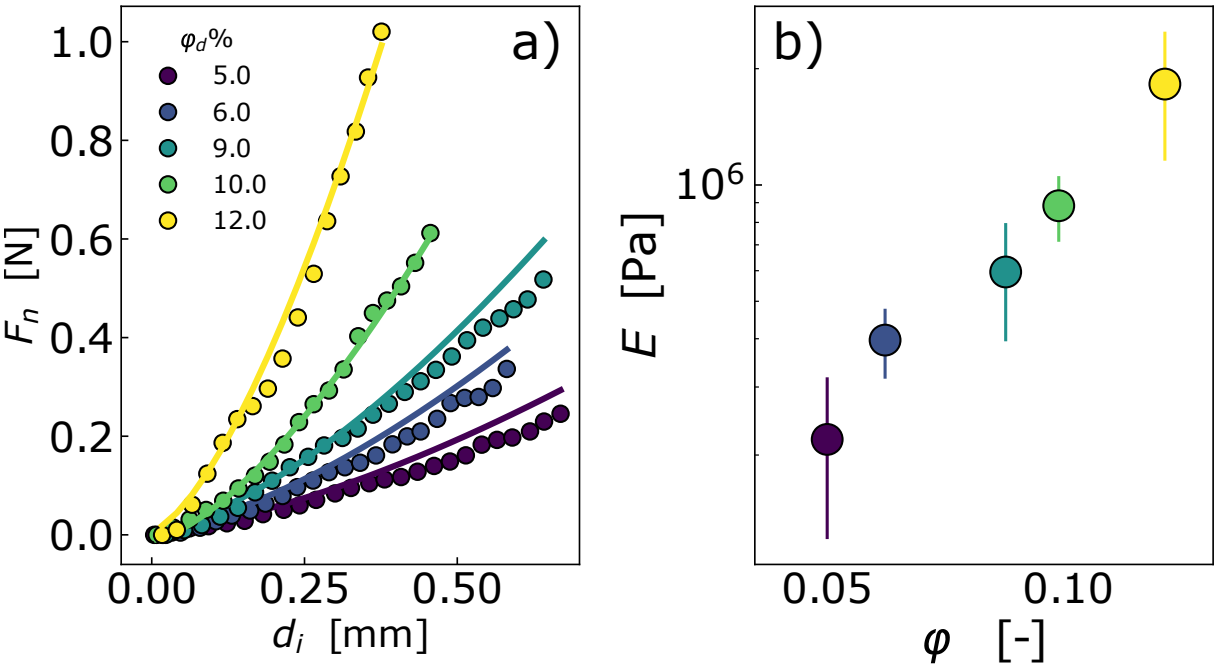

Figure 70: Mechanical test on dried beads of colloidal gel dried at different φ_d. a) Normal force as a function of the indentation depth for a gel prepared at $\varphi_p = 5\%$ that has been dried in a oven at 65° C. Symbols represent the data and solid lines are fits of the data to Eq. 2.34. b) Young modulus obtained from the fit of panel a) as a function of the volume fraction.

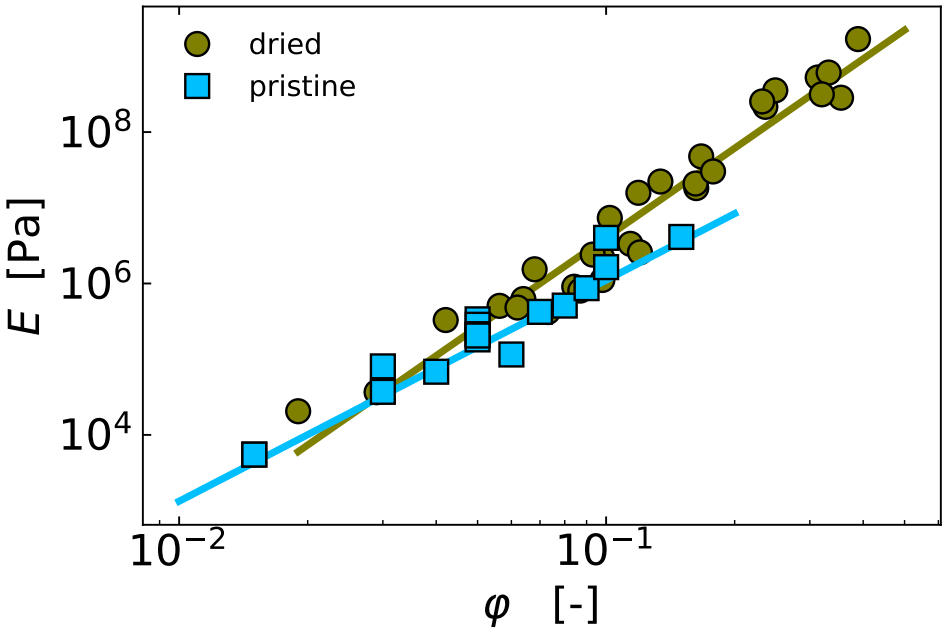

Figure 71: Young modulus as a function of the volume fraction. Blue squares represent the Young modulus of pristine gels prepared in a range of volume fraction $\varphi_p \in [0.015, 0.15]$, Green circles represent the Young modulus of dried beads. Solid lines represent power law fits $\varphi_{p/d} \sim E^{\alpha_{p/d}}$ to the data. For pristine gels we obtain $\alpha_p = 2.8 \pm 0.2$, while for the dried gels $\alpha_d = 3.9 \pm 0.2$.

transition Bantawa et al. (2023).

Since the shear and the Young modulus are linked through $E = 2G_0(1+\nu)$, we expect, for the pristine beads as well, a power law dependence of E on φ. In Fig. 71 we plot the Young modulus as a function of the volume fraction for pristine beads of gel prepared at different initial volume fractions (blue squares). As expected, the data exhibit a power law scaling, and by fitting them to a power law, we obtain an exponent $\alpha_p = 2.8 \pm 0.2$. This value turns out to be slightly lower compared to what has been found for the similar kind of colloidal gels [Aime et al. (2018a); Grant and Russel (1993); Rueb and Zukoski (1997); Shih et al. (1990); Buscall et al. (1988); Trappe and Weitz (2000)]. However, as mentioned in Chapter 5, The reason might be that, as explained before, gels with $\varphi \geq 5\%$ are not composed by cluster with a fractal structure.

Together with pristine gels, we plot in the same graph the data obtained for beads of gel that have been dried (green circles). In this case the volume fraction is the one that the gels have at the moment of compression. The dried beads also show a power law dependence with the volume fraction. However, by fitting the data to a power law we find $\alpha_d = 3.9 \pm 0.2$. These significantly different exponents ($\alpha_p = 2.8 \pm 0.2$ and $\alpha_d = 3.9 \pm 0.2$) are particularly interesting, since they reflect the fact that the compaction alters the microscopic structure as previously shown in Fig. 69.

6.3 Discussion

In this Chapter we have investigated the drying of beads of colloidal gel as a mean to understand the mechanisms of compaction of amorphous materials. Compared to standard geometries, using boundary-free beads allowed us to obtain an isotropic crack-free drying up to very high colloidal volume fractions. The drying has been investigated from a microscopic point of view in order to understand the mechanism of compaction of colloidal gel. Thanks to our multi-technique approach we have discovered unprecedented information regarding the compaction of colloidal gels.

Firstly, thanks to the custom DLS setup, we have discovered that the stress imposed by the macroscopic compression propagated homogeneously though the whole volume, as shown by a global homogeneous fastening of the microscopic dynamics. Moreover, we have found that the plastic rearrangements which characterize the compaction are mainly affine to the macroscopic compression. Such a discovery, despite being surprising given the plastic nature of the rearrangements, is in agreement with previous simulations. Indeed, it has been found that, when a colloidal gel undergoes a bi-axial compression, the resulting microscopic strain field is affine to the macroscopic compression [Islam and Lester (2021)]. Moreover, this result is even more relevant when comparing beads of colloidal gels to other kind of systems. In Fig. 72 we plot, together with the one for beads of colloidal gel, the relationship between τ_D and $\dot{\varepsilon}$ for beads of polyacrylamide gel and drops of colloidal glass.

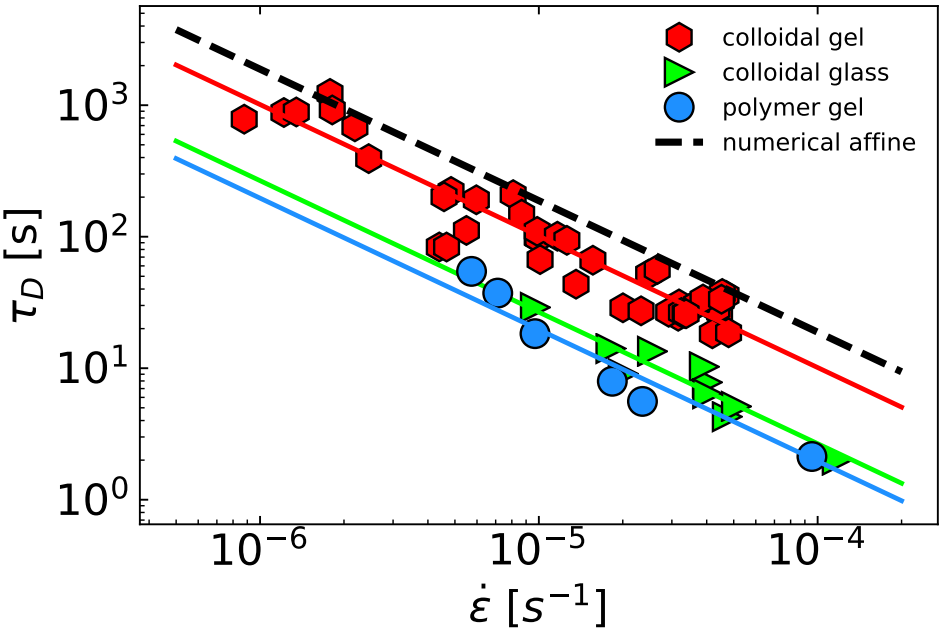

Figure 72: Microscopic decay time as a function of the compression rate $\dot{\varepsilon}$. Different symbols represent data from different sample. Red diamonds represent colloidal gels, green triangles represent a colloidal glass and blue circles a bead of polyacrylamide gel. solid lines represents a fit of $\tau_D = \Lambda\dot{\varepsilon}^{-1}$ to the data. The black dotted line is the decay time obtained from the correlation function numerically calculated for the compression of a spherical homogeneous elastic body, see Chapter3

In the plot we also show fits of the data to the functional form $\tau_D = \Lambda\dot{\varepsilon}^{-1}$, where Λ is a constant which is related to the amount of non affine rearrangements occurring in the sample: the lower Λ the higher is the amount of non affine rearrangements occurring in the sample. As it is possible to see in the figure, the drop of colloidal glass and the bead of polyacrylamide gel are characterized by a Λ value much lower than the colloidal gels: $\Lambda = 1.0 \times 10^{-3}, 2.5 \times 10^{-4}, 1.9 \times 10^{-4}$ respectively for beads of colloidal gel, drops of colloidal glass and beads of polyacrylamide gel. This fact indicates that a nearly affine response to the compression is not universal, but is peculiar to beads of colloidal gel.

Secondly, the X-ray scattering measurements showed that the network restructuring of a colloidal gel occurs following a hierarchical order. Indeed, the gel starts rearranging at large length scales, decreasing progressively with time the length scale of the restructuring. With time, the length scale of the rearrangements becomes smaller than the characteristic cluster size, thus suggesting that the compaction alters not only the inter cluster organization but the internal cluster structure as well. Moreover, we found that the characteristic length scale of the rearrangements scales with the number of particles in the linear dimension of the cluster, which in turn depends on the preparation volume fraction φ_p.

In addition, we have found that the network formation imposed by the compression

during drying differs from the Brownian aggregation through which occurs the cluster aggregation in the standard preparation process. Indeed, the scattered intensity of a pristine bead prepared at $\varphi_p = 10\%$ differs from the structure of a beads prepared at $\varphi_p = 2\%$ or $\varphi_p = 5\%$ that at have dried until reaching $\varphi_d = 10\%$.

Remarkably, we found that this microscopic changes are reflected in the macroscopic mechanical properties of the beads of gel. Indeed, through uniaxial compression, we have found that the compaction induces a stiffening of the gel network, proven by the increase of the Young modulus E of the beads. Moreover, the network stiffening alters the power law scaling between E and the volume fraction φ. Indeed, for pristine beads $E \sim \varphi_p^{2.8}$ while for dried beads $E \sim \varphi_d^{3.9}$. Since the exponent α is directly related to the microstructure of the gel [Aime et al. (2018a); Grant and Russel (1993); Rueb and Zukoski (1997); Shih et al. (1990); Buscall et al. (1988); Trappe and Weitz (2000); Bantawa et al. (2023)], our findings confirm the variation in the scattered intensity observed with X-ray.

6.4 Additional Results

In this section we present additional results obtained performing Dynamic Light scattering experiments on drying beads of colloidal gel. They provide additional support to the general picture described in the previous section. In some cases, the highlight unexpected results, not fully understood yet.

6.4.1 Detection of air invasion with DLS

In Sec. 6.2.1 we have found two different regimes of drying: a first regime in which the gel shrinks homogeneously, and a second regime where the solid network stops reducing its volume and water evaporates through capillary bridges. We have shown that, by imaging the bead, it is possible to identify the onset of the second regime. Indeed, when the gel stops shrinking it is invaded by air which changes the turbidity of the gel. Interestingly, we are even more sensitive to this phenomena when we perform DLS experiments. In Fig. 73 we show a drying bead of colloidal gel which goes from the first drying regime to the second one. Indeed, in between Fig. 73a and b the drying is homogeneous: we see the thin laser beam which crosses the bead, indicating that the gel is transparent. However, the appearance of the gel drastically changes in Fig. 73c: the intensity is much higher at the edges of the bead compared to the center. In Fig. 73d the bead is entirely white and the intensity of the scattered light is much higher. This behavior can be explained in terms of Mie Scattering. Indeed, in Fig. 73a and b, we can see the laser crossing the gel since then sample is in single scattering regime, in this stages the objects which scatter

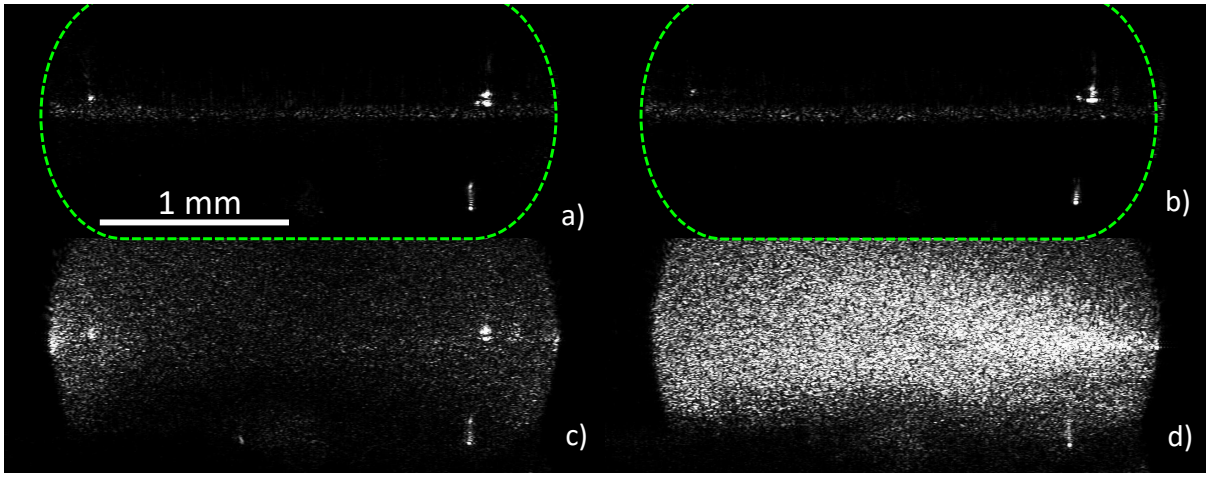

Figure 73: Sequence of a drying bead of colloidal gel illuminated by a thin laser beam. The images are taken with the home-made DLS setup presented in Chapter 3. a) A gel dried for $t_d = 75$ min is crossed by the laser which forms the typical speckle image. b) $t = t_d + 376$ s, the gel dries in the first regime. c) $t = t_d + 572$ s the bead enters the second drying regime: the bead scatters light more on the edges than at the center. d) $t = t_d + 800$ s the bead strongly scatters light in the whole volume due to the strong multiple scattering given by the air which has penetrated the sample. In panels a,b,c the bright spot on the right in correspondence of the laser is stray light given by optical reflections of the spherical geometry of the sample. Scale bar and gray scale are the same of all the images.

light are the cluster of the gel. However, in the second regime, when the air penetrates forms regions of air surrounded by the gel (silica plus water). Presumably this regions are much bigger and with much higher index refraction of mismatch compared to the cluster of the gel, thus leading strong multiple scattering which generates the image in Fig. 73d .

6.4.2 Stopping the evaporation

To elucidated the effects on the microscopic dynamic of a bead of gel which has partially dried we measure the spontaneous decay time before and after drying. To do so, we first measure the dynamics of the bead when it is still immersed in the silicon oil, then we dry it following the same procedure for all the experiment, and finally we immerse it again in oil and we re-measure the dynamics. With this last step we stop the evaporation, which allows us to measure the quiescent dynamics of the same bead but with a higher volume fraction compared to the initial one due to drying. An example of this experiment is shown in Fig. 74a. Interestingly, we see that, when evaporation is stopped the $g_2 - 1$ have a similar decay time: $\tau_d = 5524.2$ s before ($\varphi_p = 10\%$) drying and $\tau_d = 3964.5$ s after drying ($\varphi_d = 17\%$), which is orders of magnitude slower compared to the relaxation time during drying, $\tau_D = 45.8$ s. However, we note that, for a higher volume fraction we found a faster relaxation time. To have more insight we repeated the same experiment by varying the initial volume fraction φ_p. However, as denoted in Fig. 74b, we didn't get

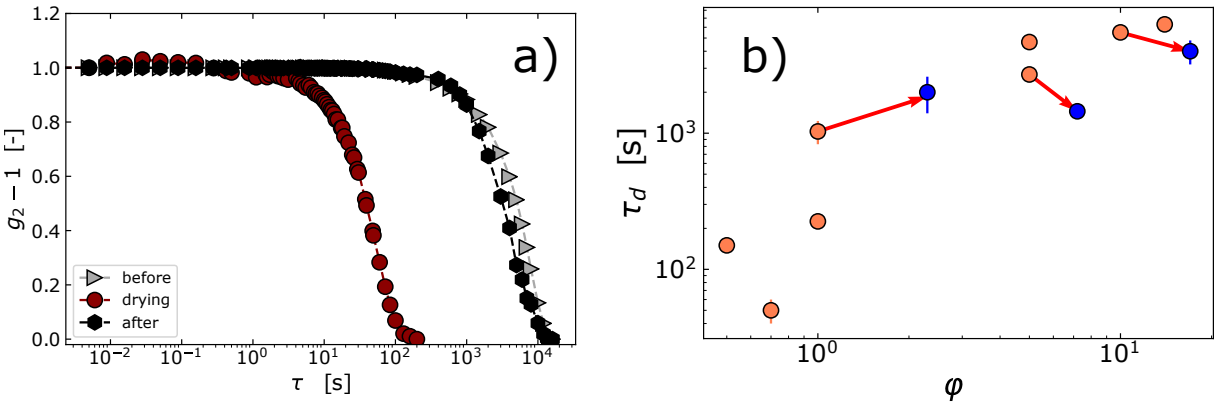

Figure 74: a) Comparison between the $g_2(\tau, x) - 1$ of a colloidal gel at $\varphi = 10\%$ before, during, and after drying. The gel at rest before drying, red curve, has slow dynamics: $\tau_D = 5524.2\ s$. During drying, red curve, the dynamic speeds up to $\tau_D = 45.8\ s$ and once the evaporation is arrested, black curve, the decay time goes to $\tau_D = 3964.5\ s$. b) Decay time as a function of the volume fraction. Blue circles correspond to the quiescent decay time of the gel before evaporation, while the yellow one correspond to the decay time of the sample once the evaporation has been stopped. Red arrows are guidelines for the eye to identify the samples that have been dried.

consistent results. Indeed, a gel prepared at $\varphi_p = 5\%$, as for the previous bead, shows a faster decay when dried at $\varphi_d = 7.2\%$. However, a gel prepared at $\varphi_p = 1\%$ has a slower decay when dried at $\varphi_d = 2.3\%$. Given the results and the long time required by this kind of experiment we did not investigate further this aspect of drying.

6.4.3 Space resolution: additional data

As an example, in Fig. 64a of Sec. 6.2.2 we have plotted $g_2 - 1$ for a bead of gel prepared at $\varphi_p = 14\%$. Here, we plot in Fig. 75 $g_2 - 1$ for all initial volume fraction when drying at RH=20%. As mentioned in Sec. 6.2.2, we used Eq. 2.22 to get the decay time τ_D from the fitting parameters τ_E and β.

To verify the spatial dependence of drying, we calculate the normalized decay time $\tilde{\tau_D} = \frac{\tau_D}{<\tau_D>_x}$, where $< ... >_x$ is an average along the bead diameter. Then, for each volume fraction we calculate the average over different rates of $\tilde{\tau}_D$: $\tau_\varphi =< \tilde{\tau}_D >_{\dot{\varepsilon}}$. In Fig. 76 we plot τ_φ as a function of the position for beads prepared at a different volume fraction φ_p. As one can see, τ_φ mildly depends on position, with dynamics on the edges slightly faster than the center. We note that for $\varphi = 1\%$ and $\varphi = 10\%$ there is a spike in correspondence of the second ROI. This localized slow dynamics are an artifact due to stray light that forms in the bead. For this reason when we calculate the average over all experiment to plot τ_M in Fig. 64b of Sec. 6.2.2 we exclude this point.

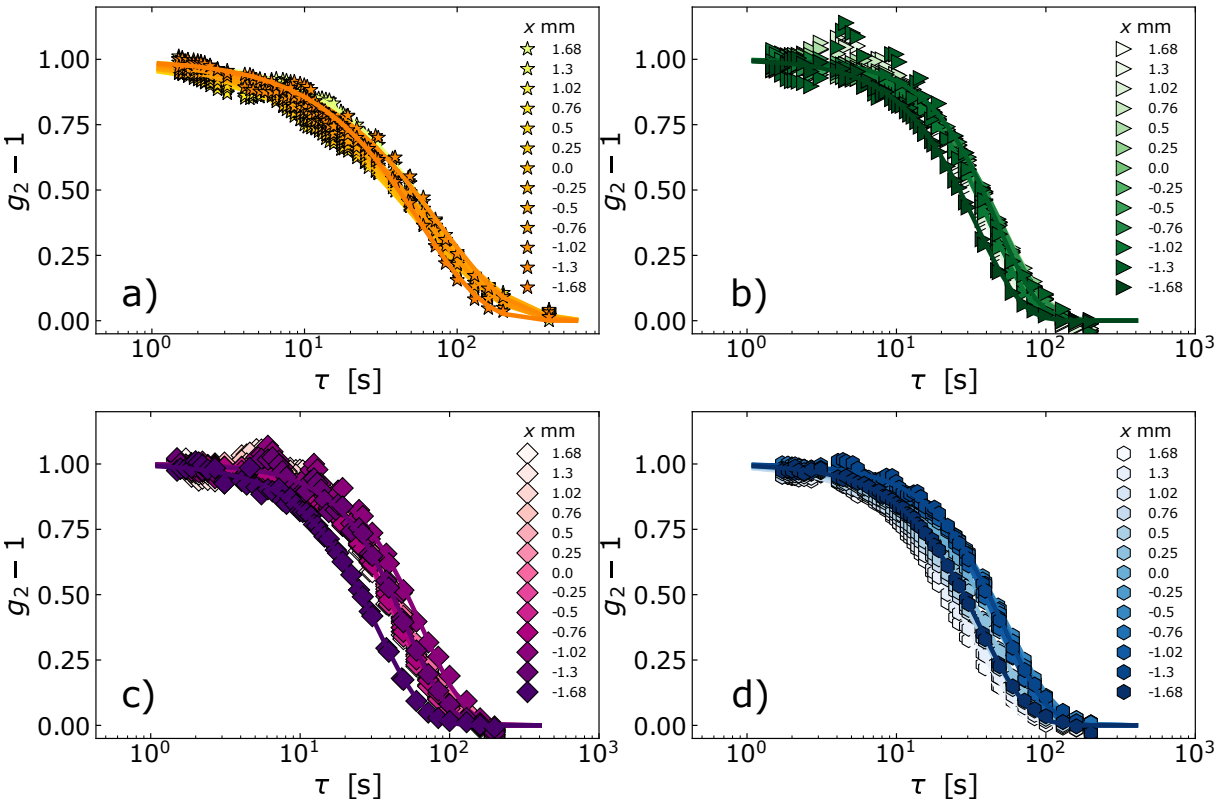

Figure 75: Intensity correlation functions for a beads of colloidal gel, which are drying at the same relative humidity RH=20% (the strain rate is roughly the same $\dot{\varepsilon} \sim 5 \cdot 10^{-5}$). Each correlation function correspond to a position along the bead radius. The solid lines are fits of Eq. 2.21 to the data. Different panels correspond to a different preparation volume fraction φ_p: a) $\varphi_p = 1\%$, b) $\varphi_p = 5\%$, c) $\varphi_p = 10\%$, d) $\varphi_p = 14\%$.

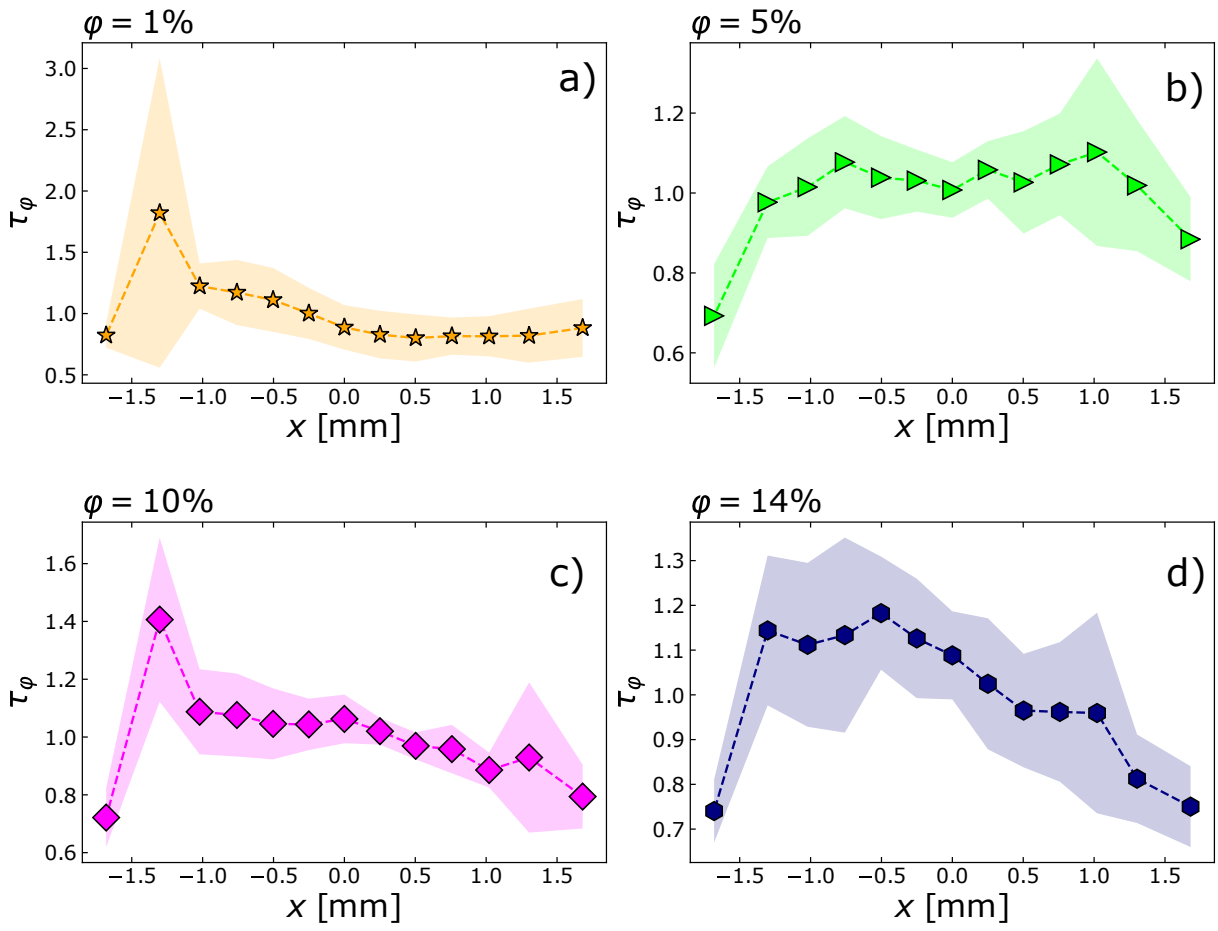

Figure 76: Normalized decay time as a function of the relative position for colloidal gel at various volume fraction. Different panels correspond to a different preparation volume fraction φ_p: a) $\varphi_p = 1\%$, b) $\varphi_p = 5\%$, c) $\varphi_p = 10\%$, d) $\varphi_p = 14\%$.

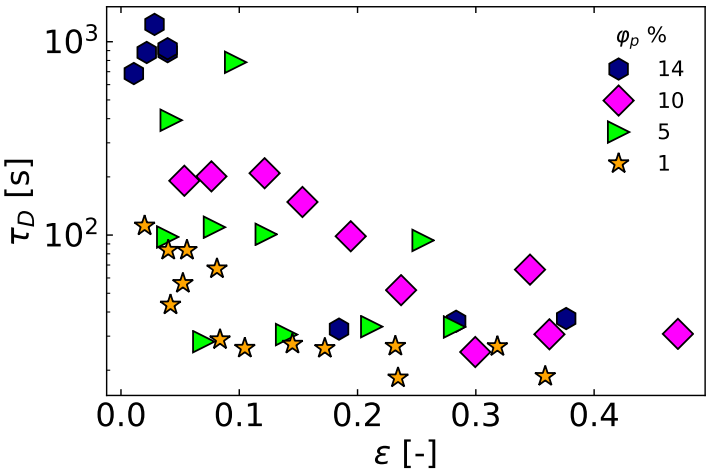

Figure 77: Microscopic decay time as a function of the total compression strain $\varepsilon = \frac{R_0 - R}{R_0}$. Different symbols represent data from samples prepared at different volume fraction φ_p. Orange stars $\varphi_p = 1\%$, green triangles $\varphi_p = 5\%$, violet diamonds $\varphi_p = 10\%$, blue hexagons $\varphi_p = 14\%$.

6.4.4 Exploring other variables

6.4.4.1 Strain dependence

In Sec. 6.2.2 we have shown how the strain rate $\dot{\varepsilon}$ rationalizes the decay time of evaporation. However, one may expect that other quantities may have a meaningful relationship with the microscopic decay time of the bead. Among them, the total strain $\varepsilon = \frac{R_0 - R}{R_0}$ at which the bead has been compressed may play an important role on the microscopic dynamics (in the expression of ε the strain R_0 is the radius at the beginning of drying and R is the radius of the bead when τ_D is measured). For this reason, in Fig. 77 we plot the microscopic decay time τ_D during drying as a function of the total compassion strain ε. Interestingly, we see that τ_D does not have a clear relationship with ϵ as it was for $\dot{\varepsilon}$.

6.4.4.2 Stretching Coefficient

As explained in detail in Sec. 6.2.2, from the $g_2 - 1$ we fit the stretching coefficient β and we use it, together with τ_E, to calculate through Eq. 2.21 the microscopic relaxation time τ_D. However, it has been recently show how the stretching coefficient β may reveal important information regarding the yielding of a material [Aime et al. (2023)]. For this reason, in Fig. 78 we plot β (averaged over all experiments) as a function of volume fraction. We see that β is smaller than the value expected for affine deformations and does not have a clear dependence on the volume fraction.

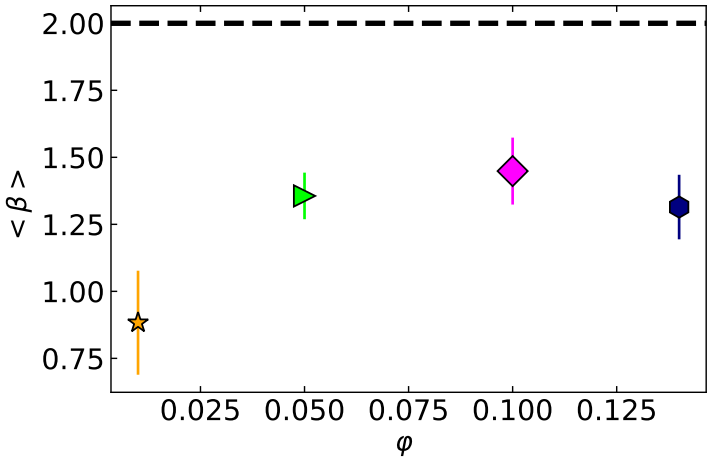

Figure 78: Average stretching coefficient β as a function of the preparation volume fraction φ_p. The black dotted line is the stretching coefficient obtained from the correlation function numerically calculated for the compression of a spherical homogeneous elastic body, see Chapter3

Chapter 7

Drying Drops of Colloidal Suspension

Soft Matter

ARTICLE TYPE

Cite this: DOI: 00.0000/xxxxxxxxxx

A double rigidity transition rules the fate of drying colloidal drops

Matteo Milani[a], Ty Phou[a],Christian Ligoure[a], Luca Cipelletti[a] and Laurence Ramos[a]

Received Date
Accepted Date

DOI: 00.0000/xxxxxxxxxx

The evaporation of drops of colloidal suspensions plays an important role in numerous contexts, such as the production of powdered dairies, the synthesis of functional supraparticles, and virus and bacteria survival in aerosols or drops on surfaces. The presence of colloidal particles in the evaporating drop eventually leads to the formation of a dense shell that may undergo a shape instability. Previous works propose that, for drops evaporating very fast, the instability occurs when the particles form a rigid porous solid, constituted of permanently aggregated particles at random close packing. To date, however, no measurements could directly test this scenario and assess whether it also applies to drops drying at lower evaporation rates, severely limiting our understanding of this phenomenon and the possibility of harnessing it in applications. Here, we combine macroscopic imaging and space- and time-resolved measurements of the microscopic dynamics of colloidal nanoparticles in drying drops sitting on a hydrophobic surface, measuring the evolution of the thickness of the shell and the spatial distribution and mobility of the nanoparticles. We find that, above a threshold evaporation rate, the drop undergoes successively two distinct shape instabilities, invagination and cracking. While permanent aggregation of nanoparticles accompanies the second instability, as hypothesized in previous works on fast-evaporating drops, we show that the first one results from a reversible glass transition of the shell, unreported so far. We rationalize our findings and discuss their implications in the framework of a unified state diagram for the drying of colloidal drops sitting on a hydrophobic surface.

1 Introduction

Drying drops of colloidal suspensions are an extremely intriguing phenomenon, since even a small amount of suspended particles can dramatically alter the fate of a drying drop: rather than shrinking continuously as drops of a simple fluid would do, colloidal drops typically undergo mechanical instabilities, such as buckling[1–3], air invagination[4], and cracking[5,6]. It is widely acknowledged that the fate of the drops is intimately linked to the formation of a dense colloidal shell. To rationalize whether a shell may form or not, one usually introduces a Péclet number, Pe (see Materials and Methods), which compares the efficiency of evaporation-induced advection to that of diffusion of the colloids. At low Pe, the colloids are essentially free to diffuse over the whole volume of the drop and thus are homogeneously distributed. By contrast, at high Pe advection dominates over diffusion and the colloids accumulate at the liquid-air interface as the interface recedes, leading to the formation of a shell.

Processes such as inkjet printing or spray drying involve the evaporation of drops of complex fluids, at very high Pe. In these applications the drops dry in nearly boundary-free conditions, which can be reproduced in the lab by suspending a drop over a hot surface using the Leidenfrost effect[1,2]. In these drying conditions, where $Pe \simeq 10^4$, experiments suggest that shape instability is due to the formation of a colloid-rich, rigid shell. It has been proposed that in the shell capillary forces push the colloidal particles close enough to overcome the repulsive interactions that normally maintain the suspension in a fully dispersed state[1], resulting in the irreversible particle aggregation, due to short-ranged van der Waals interactions. In this scenario, the shell is a rigid porous solid formed by permanently aggregated colloids, and the particle volume fraction in the shell is that of random close packing, e.g. $\phi_{\text{shell}} = \phi_{\text{rcp}} \approx 0.64$ for spherical, monodisperse particles.

However, many drying processes relevant to biology or in industrial applications occur at Pe orders of magnitude lower than those attained using the Leidenfrost effect. Examples include virus survival in aerosols[7] $Pe \sim 10^{-4} - 10^{-3}$, the production of powdered dairies[8] $Pe \sim 70$, or the preparation of func-

[a] *Laboratoire Charles Coulomb (L2C), Université Montpellier, CNRS, Montpellier, France. E-mail: laurence.ramos@umontpellier.fr*

† Electronic Supplementary Information (ESI) available: [details of any supplementary information available should be included here]. See DOI: 10.1039/cXsm00000x/

‡ Additional footnotes to the title and authors can be included *e.g.* 'Present address:' or 'These authors contributed equally to this work' as above using the symbols: ‡, §, and ¶. Please place the appropriate symbol next to the author's name and include a `\footnotetext` entry in the the correct place in the list.

tional supraparticles for catalysis, photonics, or sensing applications[9] $Pe \sim 0.1-1$,[10] $Pe \sim 300$,[11] $Pe \sim 10-300$, [12] $Pe \sim 1-100$,[13] $Pe \sim 10^{-3}-10^{-2}$. Even in these mild drying conditions, drops may show peculiar shape instabilities while drying, which have been mainly investigated in specific geometries (see[14] for a review), with the drops deposited on a surface (sessile drops)[15,16] or acoustically levitated[17], or hanging to a thin filament[14,18]. These works aimed at elucidating the effects on the morphology of the drying drop of several parameters, such as the suspension volume fraction and rheological properties, the substrate type and, most importantly, the Péclet number. Unfortunately, no microscopic insight could be provided; consequently, these works had to rely on the untested assumption that the same physical scenario as the one described for high-*Pe* drying also holds at lower *Pe*, namely that shape instability results from the irreversible aggregation of colloids at the drop periphery. To investigate the existence, evolution, and role of a rigid shell, several approaches have been adopted, including measuring the drop optical density[10], probing its structure with X-ray scattering using a synchrotron micro-focused beam[19–21], and imaging the drop illuminated with a laser-sheet[22], or with confocal[23,24] or electron[1,17,22] microscopy, the latter being limited to the *postmortem* analysis of fully dried drops. Unfortunately, these works could not provide detailed information on the shell thickness and its structural or dynamics properties, although they did confirm the existence of a shell.

Experiments in a quasi-2D geometry allow for an easier characterization of the drying process. A few noticeable works provided quantitative measurements of the spatial distribution of the colloids during the evaporation of drops confined between two closely spaced plates. Using interferometry and a Raman confocal micro-spectrometer, the authors of Refs.[25,26] measured the time evolution of the colloid distribution in the drop: no formation of a solid shell could be unambiguously detected and the colloid volume fraction was found to be smaller than $\phi_{\rm rcp}$ at all times. By contrast, Boulogne *et al.* could detect the formation of a shell and followed the evolution of its thickness[27], but unfortunately the concentration of colloids in the shell could not be determined. Overall, although experiments in 2D are insightful and provide a consistent picture, a direct connection with drying in a 3D geometry remains difficult to be established.

Here, we go beyond previous studies by investigating the evaporation of 3D colloidal drops sitting on a hydrophobic surface, at intermediate Péclet numbers, with a unique combination of macroscopic imaging and space- and time-resolved measurements of the microscopic dynamics of the colloidal suspension within the drop. We find that, quite generally, drying drops undergo two distinct, successive shape instabilities, a result unreported so far. The second instability, a cracking instability, with air penetration in the material is concomitant with the irreversible aggregation of colloidal particles, consistently with previous investigations at high *Pe*. The first instability occurs at a stage where the drying process is still reversible and the colloids can be fully re-dispersed. By measuring the microscopic dynamics in the shell, we demonstrate that this instability is triggered by a colloidal glass transition. Finally, we propose a state diagram that rationalizes our experiments and previous measurements, providing a general framework with implications ranging from the synthesis of supraparticles to the survival of biological entities in drying drops.

2 Materials and Methods

2.1 Setup

We show in Fig. 1a a scheme of the Photon Correlation Imaging (PCI[28]) light scattering apparatus specifically designed to probe, with both spatial and temporal resolutions, the dynamics of colloids confined in a spherical drop of radius R of the order of 1 mm (see[29] for details). A laser beam (*in-vacuo* wavelength $\lambda = 532$ nm, maximum power of 2 W) propagates along the x axis and is mildly focused in the drop center by the lens L_1, such that the scattering volume is approximately a thin cylinder of radius $w = 60$ μm oriented along a drop diameter, with the beam waist $w << R$. An image of the scattering volume is formed on the detector of a CMOS camera, using the lens L_2. A vertical slit and a diaphragm are placed in the focal plane of L_2, such that the image is formed only by light exiting the sample chamber within a thin solid angle centered around the y direction[29]. The setup combines features of imaging and light scattering: each location on the detector corresponds to a well-defined position in the sample, as in conventional imaging, but, contrary to conventional imaging, the image formed on the detector result only from light scattered at a chosen angle and thus at a specific scattering vector q.

As schematically shown in Fig. 1b, the light propagating towards the detector is refracted at the drop-air interface. This has two consequences: first, the position along the x axis of a ray exiting the drop is in general different from the x coordinate of the sample volume from which that scattered light originates. Throughout the paper, refraction effects are corrected: the coordinate x refers to the actual position within the scattering volume, $x = 0$ being the drop center. Second, the scattering angle θ_S associated to optical rays exiting the drop along the y direction depends on x. Using Snell's law, we calculate the x-dependence of θ_S and of the modulus q of the scattering vector, with $q = 4\pi n/\lambda \sin(\theta/2)$, $n = 1.33$ being the refractive index of the solvent (water). We find that the x-dependence of q is mild: typically, q ranges from 18 μm^{-1} to 26 μm^{-1} depending on the position x within the drop, see[29] for a detailed discussion.

2.2 Data Analysis

To quantify the dynamics, we use Camera 1 to take a time series of images of the scattered light. The images have a speckled appearance, as shown in Fig. 1d. Camera 1 collects images of size (512×1088) pixels^2, allowing for the acquisition of videos at rates up to 200 Hz, using the acquisition scheme of Ref.[30]. Each image is divided into Regions of Interest (ROIs), typically rectangles of dimension (30×100) pixels^2, corresponding to about (70×260) μm^2 in the sample. The size of the ROIs is chosen so that each ROI contains around 100 speckles, which provides an acceptable statistical noise[31]. The local dynamics within a given ROI are

quantified by a two-time degree of correlation[31]:

$$c_I(t,\tau,x) = A\frac{\langle I_p(t)I_p(t+\tau)\rangle_x}{\langle I_p(t)\rangle_x\langle I_p(t+\tau)\rangle_x} - 1 \qquad (1)$$

with τ the time delay between images, $I_p(t)$ the intensity of the p-th pixel of the ROI at time t, and $\langle ...\rangle_x$ an average over all pixels of an ROI centred around x. The prefactor A is chosen such that the intensity correlation function $g_2(\tau,x)-1$, obtained by averaging $c_I(t,\tau,x)$ over a suitable time interval, tends to 1 for $\tau \to 0$. For a dilute suspension of Brownian particles, $g_2(\tau)-1$ is a simple exponential decay: $g_2(\tau)-1 = e^{-\tau/\tau_D}$. For systems with more complex dynamics, $g_2(\tau)-1$ deviates from this simple shape. In the general case, the relaxation time of g_2-1 can be conveniently obtained experimentally from $\tau_D = \int_0^{\tau_{max}}[g_2(\tau)-1]\,\mathrm{d}\tau$, where τ_{max} is the shortest delay for which $g_2(\tau)-1$ decays to zero to within experimental uncertainties.

2.3 Samples

We use commercial silica nanoparticles (Ludox TM-50 from Sigma Aldrich) suspended in water. The batch is used as received The nanoparticle diameter is $2a = 25$ nm as measured by dynamic light scattering (DLS). For all experiments, the initial volume fraction of NPs in the drop is $\phi = 0.31$. The suspension is transparent to visible light. Hence, when passing through the drop, the laser light is scattered at most once, thus avoiding multiple scattering. Working in the single scattering regime is essential for measuring the dynamics with space-resolution. The NPs are charge stabilized and thus interact through a soft repulsive Yukawa potential. The Debye length is of the order of 20 nm[32], comparable to the NP radius. The dynamics of the same nanoparticles have been previously measured at the same q vector for bulk quiescent suspensions[32]. In the supercooled regime, from $\phi = 0.32$ to the glass transition $\phi = 0.39$, the relaxation time of the system grows steeply with volume fraction (see also Fig. 11 in[29]).

2.4 Experimental protocol

A drop of volume 30 μL and radius $R_0 = 1.9$ mm is gently deposited on a hydrophobic surface, forming a contact angle of 120 deg. The drop is surrounded by air or by silicon oil (47 V 100, VWR chemicals, refractive index = 1.403). Temperature is controlled at (22 ± 1)°C. To control the relative humidity RH, we fill the bottom of the sample chamber (a cubic glass box of side 4 cm) with different chemicals or saturated salt solutions. We vary RH in the range 20% to 94%, thereby imposing different evaporation rates to the drop. The drop evaporates in an intermediate mode between the constant contact radius mode and the constant contact angle mode. The characteristic evaporation time, τ_{ev}, is defined as the time to fully evaporate the drop, should it not contain nanoparticles. As in previous works[33,34], τ_{ev} is evaluated by extrapolating the small-t behaviour of $R(t)^2$, with $R(t)$ the time-dependent drop radius and $t = 0$ the time at which evaporation starts (see Fig. 4 in[29]).

In our experiments, τ_{ev} varies from (465 ± 10) s to (43960 ± 20) s (see[29] for details). The relevant non-dimensional Péclet number, $Pe = \tau_{mix}/\tau_{ev}$, compares the evaporation time to $\tau_{mix} = R_0^2/D$, the characteristic mixing time due to Brownian diffusion over a distance equal to the drop initial size. We take $D = 4.31\times10^{-12}$ m^{2}s^{-1}, the diffusion coefficient of the NPs for $\phi = 0.31$[32]. In our experiments, Pe varies from 63 to 5754. The reduced time $\tilde{t}$ is defined as $\tilde{t} = t/\tau_{ev}$.

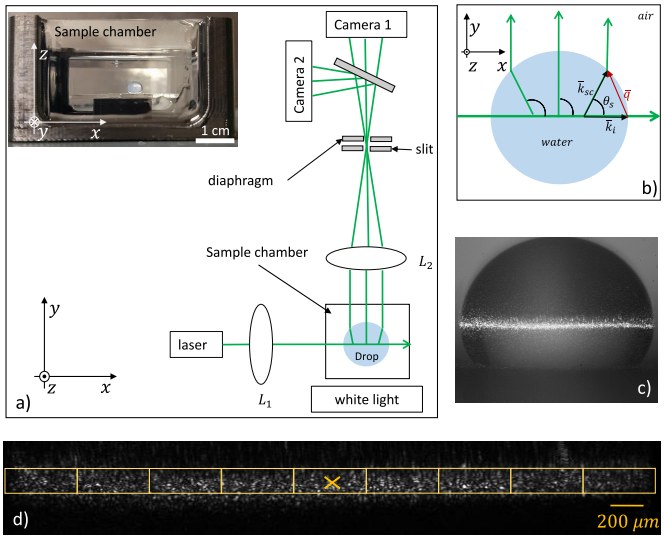

Fig. 1 (a) Scheme of the dynamic light scattering setup used to measure the dynamics of colloids in a drop. The incoming laser beam propagates along the x axis and is mildly focused by the lens L_1 in the middle of the sample. The lens L_2 forms an image of the scattering volume on the sensor of Camera 1. In addition to the laser beam, white light provided by a LED screen illuminates the sample, in order to form on Camera 2 an image of the full drop, to monitor its macroscopic evolution. By combining a vertical slit, parallel to the z direction, and a diaphragm, we ensure that both cameras are illuminated by light exiting the drop along the y direction, to within acceptance angles of 0.55 deg and 1.65 deg in the plane (x,y) and (y,z), respectively. The sample is placed in a cubic glass box of side 4 cm, within which controlled humidity conditions are imposed. The inset shows an image of the sample chamber containing a drop (diameter 3.5 mm) of a colloidal suspension sitting on a hydrophobic surface and surrounded by oil, used to stop evaporation. (b) Schematic top view of the relevant optical rays for a drop surrounded by air. The scattered light is refracted at the drop-air interface such that a somehow different scattering angle θ_s corresponds to each position x. (c) Image formed on Camera 2 of a drop of colloidal suspension illuminated simultaneously by the laser beam and by white light. (d) Cropped speckle image (100×1300 pixels^2), formed on Camera 1 by the light scattered in the drop and collected by the lens L_2. The yellow rectangles indicate the Regions of Interest for the space-resolved data analysis and the cross corresponds to the drop center ($x = 0$).

3 Results

3.1 Shape Instabilities and Nanoparticles Aggregation

To study the macroscopic behavior of drying drops we deposit 30 μL of a silica nanoparticles suspension (NPs, see section Materials and Methods for details) on a hydrophobic surface. The surface and the drop are in a closed chamber with controlled relative humidity. Figure 2 displays a representative sequence of top views of a drop that dries at $Pe = 399$ (see section Materials and Methods for details on the determination of Pe). Right after deposition and up to $t \approx 1420$ s the drop maintains a spherical cap shape

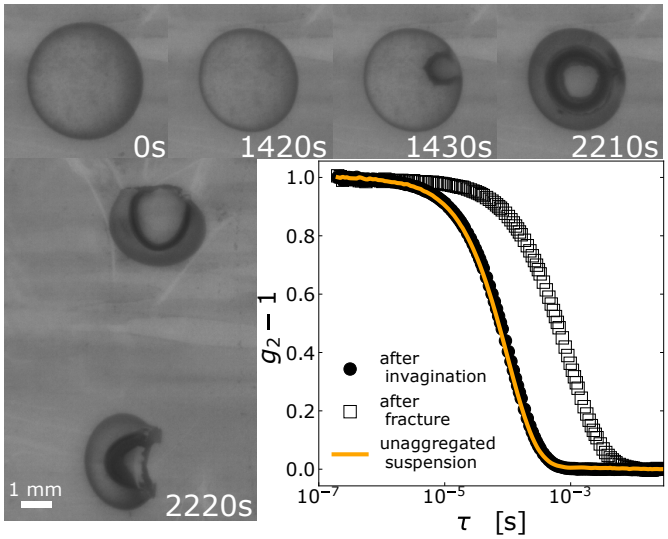

Fig. 2 Shape instabilities and colloidal aggregation. Images: sequence of top views of a drop of colloidal suspension drying at $Pe = 399$. A movie is provided in [29].The scale is the same in all images and the scale bar represents 1 mm. Images are labelled by the time t (in s) since depositing the drop on an hydrophobic substrate. The onset of the shape instability is visible at $t = 1430$ s; subsequently the invaginated region grows until the drop suddenly cracks at $t = 2220$ s. Graph: intensity correlation functions measured by conventional DLS probe the aggregation state of the colloids. Line: batch suspension. Filled circles: drop collected in the invaginated state ($t = 2210$ s) and redissolved in water. Empty circles: fractured drop ($t = 2220$ s) immersed in water and sonicated. All DLS curves are collected at a NPs volume fraction $\phi = 0.014$.

while shrinking. At $t = 1430$ s, a shape instability in the form of air invagination is clearly seen. The shape instability develops with time, see $t = 2210$ s in Fig. 2, until a second shape transition occurs with the sudden macroscopic fracture of the drop, $t = 2220$ s in Fig. 2. By running experiments at Pe in the range $63 - 5754$, we establish that a similar two-state transition always occurs for $Pe > 70$, whereas drops dried at lower rate ($Pe = 63, 70$) do not exhibit the first shape instability but only a macroscopic fracture.

As mentioned above, for drops rapidly dried using the Leidenfrost effect the onset of the shape instability results from colloids aggregating to form a porous solid shell [1]. In our experiments conducted at much lower drying rates, drops that underwent shape instability but did not crack yet (e.g. at $t = 2210$ s in Fig. 2) can be fully re-dispersed in water, as checked by visual inspection, while once the drop has macroscopically fractured ($t = 2220$ s in Fig. 2), the fragments do not dissolve in water even after 48 hours. We confirm these macroscopic observations using conventional dynamic light scattering (DLS [35]) to measure the size of the particles or aggregates after re-dispersing the drop in water. For the invaginated sample, we find that the intensity correlation function $g_2 - 1$ measured by DLS is indistinguishable from that of a freshly prepared suspension of unaggregated NPs. Due to strong Van der Waals attractions, aggregated NPs would not re-disperse spontaneously: we thus conclude that no particle aggregation occurs throughout the development of the shape instability. By contrast, the correlation function for the fractured sample decays on a time scale one order of magnitude larger, even after sonicating the fragments for one hour. In DLS-based particle sizing, the decay time of $g_2 - 1$ is proportional to the particle size; thus, these data demonstrate that the NPs irreversibly aggregate just before the drop fractures, forming strong bonds that are only partially broken by vigorous sonication.

These experiments show that nanoparticles eventually do aggregate during the drying of drops of colloidal suspensions, even for Pe lower than the ones studied in the seminal work of Tsapis and Weitz [1]. However, in the moderate to high $70 < Pe \lesssim 6000$ range, the shape instability sets in before the NPs undergo aggregation, challenging the commonly proposed scenario that attributes quite generally shape instability to colloidal aggregation, including at low Pe [15,27,36]. Our findings thus raise the question of the physical mechanism responsible for the onset of a shape instability for slowly evaporating drops. Previous works suggested that the formation of a shell plays a key role. In the following, we use a custom light scattering setup to measure *in-situ* the shell formation and growth, probing the microscopic dynamics of the NPs within the drying drop. The setup is based on Photon Correlation Imaging (PCI [28]), a space- and time-resolved variant of DLS, see section Materials and Methods and [29] for more details.

3.2 Evolution of the Shell Thickness

Figure 3a displays side views of drops that are simultaneously illuminated by white light, for conventional imaging, and by a thin laser beam, for PCI. (A Side view movie for a drop illuminated only by white light is provided in [29].) Consistently with the top views of Fig. 2, a shape instability is observed for the experiment run at $Pe = 252$, whereas no instability takes place on the time scale of the experiment for a drop drying at $Pe = 70$. As detailed in section Materials and Methods, we compute the $g_2 - 1$ intensity correlation functions from the time fluctuations of the speckle pattern generated by the interference of light scattered by the NPs. Typical $g_2 - 1$ functions are shown in Fig. 3b, for a sample that dries at $Pe = 91$ and for a fixed reduced time $\tilde{t} = 0.23$, defined as $\tilde{t} = t/\tau_{ev}$, with t the actual time since the deposition of the drop on the substrate and τ_{ev} the evaporation time (see section Materials and Methods and Supporting Information [29] for details). The various curves are measured simultaneously for different positions along the drop diameter, identified by the reduced coordinate $\tilde{x} = x/R$, with x the position in the drop ($x = 0$ corresponds to the drop center) and R the drop radius. The decay time of $g_2 - 1$ corresponds to the time it takes to relax particle density fluctuations of wavelength $1/q \approx (40 - 55)$ nm via the microscopic motion of the NPs (q is the magnitude of the scattering vector, see section Materials and Methods).

The intensity correlation functions strongly depend on $\tilde{x}$, with a faster decay in the center of the drop (time scale of the order of 0.1 s for $\tilde{x} = 0$) and a much slower one near the edge (time scale of tens of seconds for $\tilde{x} = 0.83$). Quite generally, the dynamics of a colloidal suspension strongly slow down as the particle concentration increases [37]. Therefore, the spatial variation of the NPs mobility suggests the formation of a colloid-rich shell that surrounds a diluted core. In the whole paper, we define as shell,

the localized region close at the drop periphery where the NP dynamics is at least two orders of magnitude slower than that in the core of the drop.

To quantify the shell thickness h, we average movies of the speckle pattern over a suitable time interval, $\Delta t = 4$ s, intermediate between the decay time of $g_2 - 1$ in the core and that in the shell. Figure 3c shows the results of such processing for a drop drying at an intermediate evaporation rate, $Pe = 91$. The fast-fluctuating core appears as a gray region, while speckles in the shell are clearly visible, because they are essentially frozen on the time scale Δt of the time average. Figure 3c shows that the shell develops with time, thickening progressively. By analyzing the spatial variance of the intensity of the time-averaged images (details in the Supporting Information[29]), we determine the boundary between the shell and the core, yellow lines in Fig. 3c, checking that the value of h thus obtained does not depend significantly on the choice of Δt, see[29]. Here and in the following we show only the results for one half of the drop, for symmetry reasons.

Figure 3d shows the evolution of h normalized by the instantaneous radius of the drop, $R(t)$, as a function of the reduced time $\tilde{t}$. Overall, our findings are in qualitative agreement with the Pe dependence of a shell, as determined through numerical calculations for 3D spherical drops.[36]. For all investigated Pe, we find that the thickness increases with time, at a rate that slightly decreases as Pe increases. The same data displayed in the Supporting Information[29] as plots of h/R versus absolute time t show that the growth rate of the shell in absolute units is approximately the same for all samples, and that shell formation starts after a latency time that decreases with Pe. For the lowest Pe investigated, $Pe \leq 70$, h/R reaches 1, indicating that the shell invades the whole drop volume, and thus the spatial distribution of the nanoparticles becomes homogeneous at long times, in agreement with experimental findings for 2D drops[26]. After reaching such a homogeneous state, the drop shrinks smoothly (see iii)-iv) in Fig. 3a for a sample drying at $Pe = 70$) until it abruptly fractures. By contrast, for drops that evaporate at a faster rate homogeneous shrinking is always stopped by the onset of a shape instability at the bottom of the drop (see i)-ii) in Fig. 3a for a sample drying at $Pe = 252$). Interestingly, as indicated by red circles around the data points in Fig. 3b, for $Pe \geq 175$ the onset of the shape instability occurs approximately at the same $\tilde{t}$ and h/R.

3.3 Space-dependent Microscopic Dynamics and Nanoparticles Concentration

To gain a deeper insight into the NPs microscopic dynamics and their spatial distribution, we calculate τ_D, the space- and time-dependent time scale of the microscopic dynamics, obtained from the decay time of the intensity correlation functions $g_2 - 1$ following the procedure detailed in Materials and Methods. Figure 4a displays τ_D for a representative experiment at $Pe = 91$, as a function of reduced position $\tilde{x}$ and for various reduced times $\tilde{t}$. At early times, the dynamics are spatially homogeneous and slow down with $\tilde{t}$ due to the overall increase of the volume fraction of the nanoparticles as the drop shrinks. At later times, by contrast, the dynamics at the edge of the drop become almost two orders of magnitude slower than those in the center, signaling the formation of a dense shell. Consistently with what seen in the time-averaged speckle images (Fig. 3c), the region with slow dynamics expands with time, until the occurrence of a drop instability at $\tilde{t} = 0.30$. Results for drops drying at $Pe = 63, 70, 175, 252,$ and 399 are shown in Fig. 10 in[29]. At $Pe = 63, 70$ the spatial dependence of the dynamics is initially similar to that shown in Fig. 4a for $Pe = 91$. However, the drops do not display any instability and the nanoparticles eventually recover a homogeneous distribution within the drop, as demonstrated by the weak $\tilde{x}$-dependence of the dynamics at late times, $\tilde{t} \approx 0.3$. The drops then further dry, until abruptly cracking, at $\tilde{t} \approx 0.39$ for $Pe = 70$. By contrast, the samples evaporating more rapidly ($Pe = 175, 252, 399$) form a shell since the early steps of evaporation, $\tilde{t} \approx 0.08$. In these cases, the shell is thinner than that measured at lower Pe, but the contrast between the dynamics of the core and that of the shell, two orders of magnitude in τ_D, is similar for all fast-evaporating samples.

Nanoparticle suspensions in a drying drop are not at thermodynamic equilibrium: we thus expect their dynamics to depend on both the (local) volume fraction, ϕ, and the drying process. To disentangle the effect of ϕ from that of drying, we run an experiment where a drop first evaporates at $Pe = 91$, and then is immersed in oil to stop water evaporation, at $t = t_{\text{stop}} = 5880$ s ($\tilde{t}_{\text{stop}} = 0.16$), before the occurrence of any instability. Figure 4b shows the spatial dependence of the microscopic relaxation time τ_D just before stopping evaporation ($t = t_{\text{stop}} - 600$ s, up triangles and solid line) and for several times $t \geq t_{\text{stop}}$. Remarkably, the relaxation time in the center of the drop, $\tau_D^{\text{core}} \equiv \tau_D(\tilde{x} = 0)$, remains essentially the same as the one during evaporation for at least 500 s after t_{stop}. This indicates that evaporation did not impact significantly the dynamics in the center of the drop. Subsequently, τ_D^{core} progressively increases, because of the re-dispersion of the nanoparticles from the shell to the core, which increases ϕ in the core. Consistently, we find that the dynamics become spatially homogeneous, provided that the drop is let equilibrating under no evaporation conditions for a long enough time. Indeed, for $t > t_{\text{stop}} + 8000$ s, we measure a constant $\tau_D = (949 \pm 17)$ s throughout the drop. (8000 s corresponds roughly to a 1.4-fold the time the drop has evaporated before being immersed in oil). Using the ϕ-dependence of the relaxation time measured for the same sample in quiescent, equilibrium conditions as a calibration curve (Ref.[32] and Fig. 11 in[29]), we find that this value of τ_D corresponds to a spatially homogeneous NPs volume fraction $\phi = 0.385$, in excellent agreement with $\phi = 0.386$ as estimated from mass conservation using the initial nanoparticle concentration and the measured drop volume reduction.

The experiment where drying was stopped proves that the relaxation time in the core is a robust proxy for the nanoparticle concentration and that ϕ_{core} can be reliably calculated from reference data for quiescent suspensions[29,32]. We further confirm this approach by measuring ϕ_{core} at $t = 0$, finding $\phi_{\text{core}} = 0.3014 \pm 0.008$ averaged over all experiments, in excellent agreement with $\phi = 0.312$, the nominal value of the volume fraction of the batch suspension used to prepare the drops.

Knowing the volume fraction in the core and the thickness of

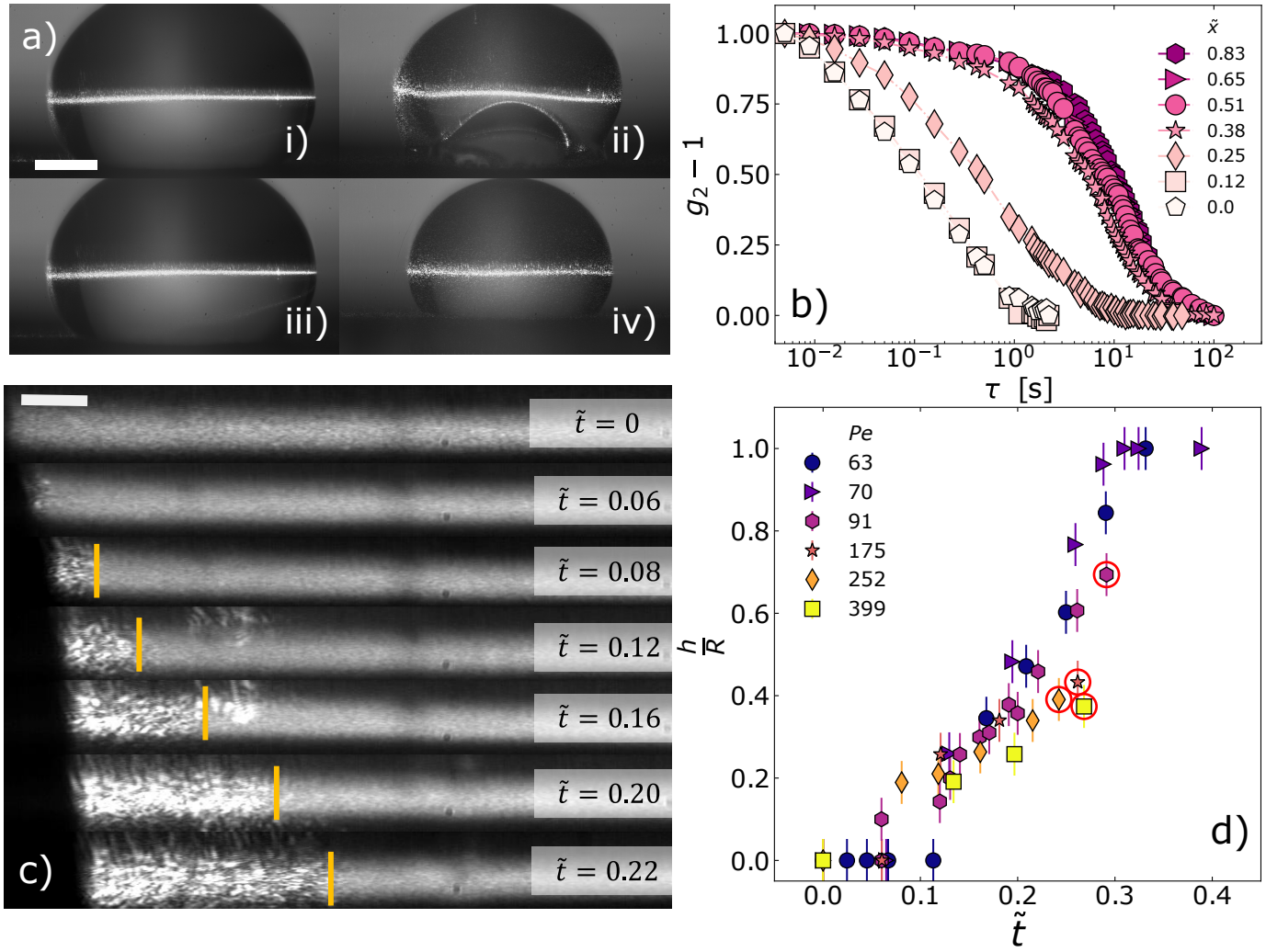

Fig. 3 Shape Instability and Shell Formation (a) Side views of drops drying at $Pe = 252$ (i, ii) and $Pe = 70$ (iii, iv), respectively. The drops are illuminated by both white light and a thin laser beam; the images are taken by Camera 2 as shown in Fig. 1. Images i) and iii) are taken at time $t = 0$; ii) and iv) at reduced times $\tilde{t} = 0.242$ and $\tilde{t} = 0.3$, respectively. In ii), nanoparticles accumulating at the drop-air interface created by the shape instability are visible because they are illuminated by light scattered by the volume directly illuminated by laser beam. Note that no instability occurs for the drop drying at $Pe = 70$ (iii, iv). The scale bar represents 1 mm. (b) Intensity correlation functions taken simultaneously at $\tilde{t} = 0.23$ at different positions, from the drop center ($\tilde{x} = 0$) to near the edge, located at $\tilde{x} = 1$, for a drop drying at $Pe = 91$. (c) Formation and evolution of the shell during drop evaporation for a sample drying at $Pe = 91$. Speckle images averaged over $\Delta t = 4$ s and taken at different reduced times, as indicated by the labels. The vertical yellow lines separate the homogeneous, blurred region corresponding to the core of the drop with fast dynamics, to the shell region where the speckles are still visible after averaging, indicating slow dynamics. For clarity, only the left half of the drop is shown; the center of the drop sits on the right edge of the images. The scale bar represents 0.1 mm. (d) Shell thickness normalized by the drop radius $R(t)$, as a function of the reduced time $\tilde{t}$. Different colors and symbols correspond to different Péclet numbers in the range $63 - 399$, as indicated by the labels. Red circles represent the instant of the invagination, which occurs at $\tilde{t} = 0.27, 0.24, 0.26, 0.29$ for $Pe = 399, 252, 175, 91$ respectively. Error bars results from the uncertainty in the determination of the drop radius and of the shell thickness in the speckle images.

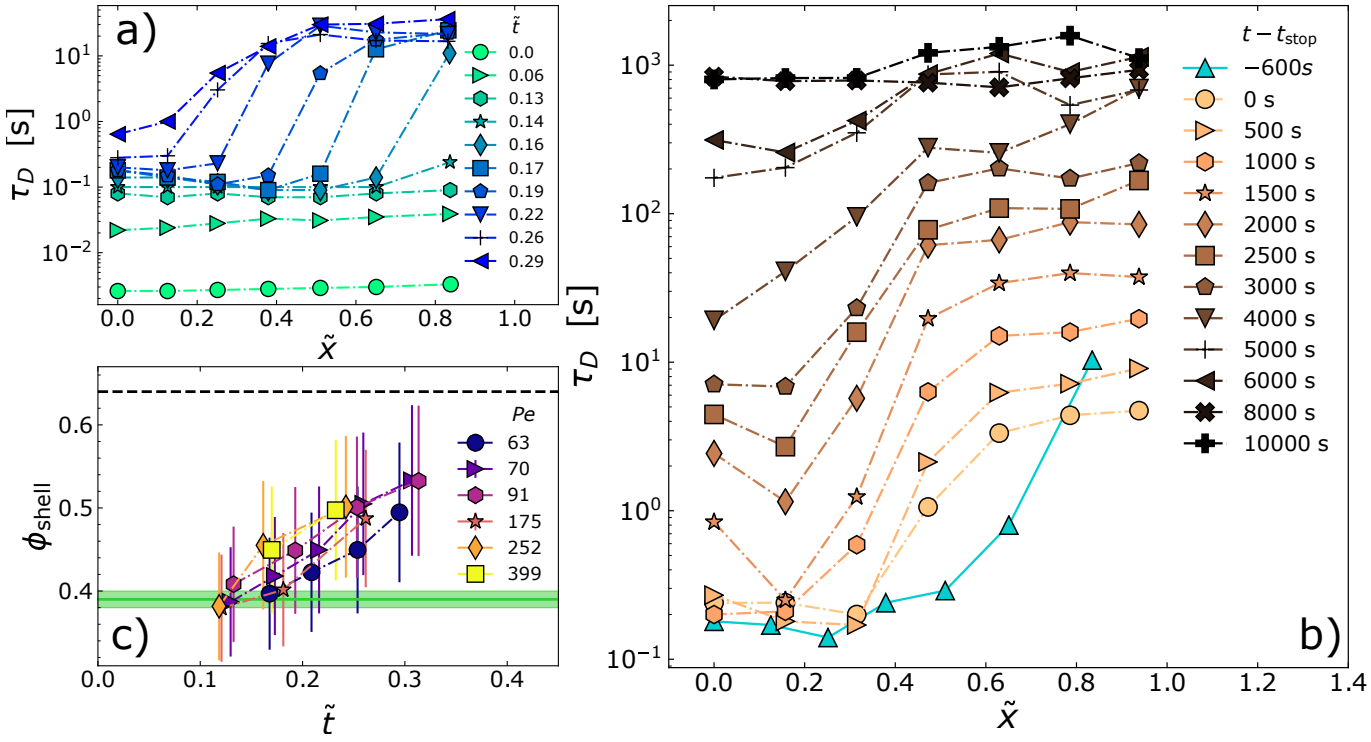

Fig. 4 Microscopic dynamics during drop evaporation (a) Microscopic relaxation time as a function of the normalized position along the drop radius $\tilde{x} = x/R$, for $Pe = 91$. Data are labelled by the reduced time $\tilde{t}$. (b) Decay time of $g_2(\tau) - 1$ as a function of position along the radius for a drop immersed in oil. The drop was previously dried at $Pe = 91$ for $t_{stop} = 5880$ s ($\tilde{t} = 0.16$), leading to a decrease of its radius by 9%, before being immersed in oil to stop evaporation. Curves are labelled by the time since stopping evaporation. The up triangle symbols and solid line correspond to τ_D values 600 s before the drop was immersed in oil. (c) Volume fraction of the shell as a function of reduced time, as obtained from mass conservation and measurements of the shell thickness and core volume fraction. Symbols are data points for drops dried at different Péclet numbers, as indicated by the labels. The error bars are the uncertainty due to approximations on the drop and core shape, which have been considered spherical, see [29]. Horizontal lines: volume fraction of the glass transition for the NPs used here (solid line, $\phi_g = 0.39 \pm 0.01$ [32], the green band shows uncertainties) and the random close packing volume fraction of monodisperse particles (dotted line, $\phi = \phi_{rcp} = 0.64$), a lower bound for the actual volume fraction at rcp for our polydisperse nanoparticles [38,39].

the shell (Fig. 3b), we calculate the time-dependent volume fraction of the shell, ϕ_{shell}, using mass conservation and assuming a step-wise radial concentration profile, with constant ϕ in the core and the shell, respectively. Figure 4c displays the time evolution of ϕ_{shell} for all the Péclet numbers where a shell was observed. We find that ϕ_{shell} steadily increases with time, in a mildly Pe-dependent manner. Surprisingly, we find that the shell is not a very dense medium composed of colloids at random close packing, but rather a concentrated suspension whose volume fraction depends only weakly on the rate at which the drop shrinks, and reaches at most 0.55 when the drop undergoes the shape instability. This value is lower than the reference value for randomly closed packed monodisperse spheres ($\phi_{rcp} \approx 0.64$), a lower bound for the actual volume fraction at rcp for our polydisperse nanoparticles [38,39].

3.4 Glassy Dynamics of the Shell

The values of ϕ_{shell} shown in Fig. 4c confirm the *post mortem* observations of Fig. 2, ruling out the hypothesis that the shape instability is due to the irreversible aggregation of the NPs in the shell. Values of ϕ_{shell} in the range $0.5 - 0.6$, as measured just before the shape instability, are rather suggestive of a colloidal glass transition, upon which the dynamics of a colloidal suspension slow down dramatically and its mechanical behavior approaches that of a solid [32,37], while the sample maintains an unaggregated structure, similar to that of a dense fluid. Indeed, we consistently find that $\phi_{shell} \geq \phi_g = 0.39 \pm 0.01$, the glass transition volume fraction measured for the same system under quiescent conditions [32] (solid horizontal line in Fig. 4c).

To gain insight into the origin of the shape instability, we inspect τ_D^{edge}, the microscopic relaxation time at the drop periphery. Surprisingly, Figure 4a shows that τ_D^{edge} never exceeds a few tens of s, orders of magnitude less than what expected for quiescent glassy suspensions at volume fractions comparable to those estimated for ϕ_{shell} [29,32]. This apparent conundrum is solved by noticing that the dramatic acceleration of the dynamics is due to the strain field imposed by drying: Figure 4b shows that stopping evaporation leads to an increase of τ_D^{edge} by at least two orders of magnitude, compare the data at $\tilde{x} \lesssim 1$ just before t_{stop} (up triangles) and at $t = t_{stop} + 10^4$ s (plus symbols).

We rationalize the relationship between microscopic dynamics and macroscopic shrinkage by displaying in Fig. 5 τ_D^{edge} as a function of the instantaneous drop strain rate $\dot{\varepsilon} = \frac{1}{R}\left|\frac{dR}{dt}\right|$, for various

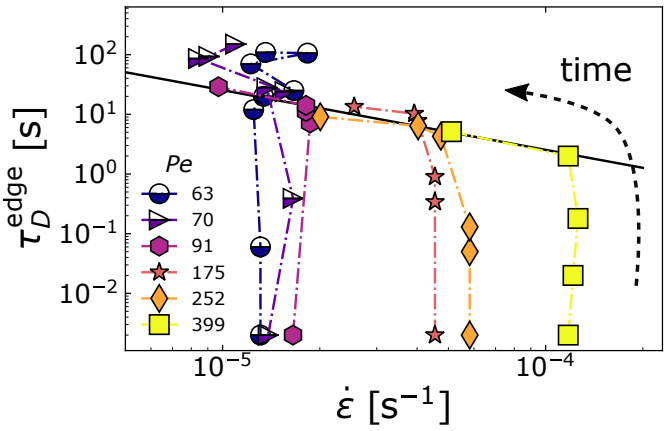

Fig. 5 Shell dynamics driven by macroscopic shrinkage. Microscopic relaxation time, τ_D^{edge}, of the nanoparticles located at the edge of the drop, as a function of the (time-dependent) macroscopic strain rate, $\dot{\varepsilon}$, for various Péclet numbers as indicated in the legend. For all experiments, τ_D^{edge} increases monotonically with time, as shown by the arrow for the sample at $Pe = 399$. Solid (resp., semi-filled) symbols refer to drops that eventually do (resp., do not) exhibit a shape instability. All data shown here are collected before any instability occurs. The black solid line is a fit of $\tau_D^{edge} = \Lambda\dot{\varepsilon}^{-1}$ to the data for $Pe \geq 91$ in the final stages of evaporation, after the formation of a glassy shell, yielding $\Lambda = (2.5 \pm 0.1) \times 10^{-4}$.

Péclet numbers. In all cases, we find that in the early stages of the drying process $\dot{\varepsilon}$ is nearly constant, with a numerical value that strongly depends on Pe. In this regime, the microscopic relaxation time of the NPs smoothly increases over several decades, reflecting the overall increase of their volume fraction in the shell. As drying proceeds, however, we observe two distinct regimes, depending on Pe. At relatively small $Pe \leq 10$, $\dot{\varepsilon}$ remains constant for the entire duration of the experiment, indicating that the NP mobility remains large enough to allow the drop to follow the contraction rate imposed by the drying conditions. In this regime, τ_D^{edge} increases steadily as the overall NP concentration increases. By contrast, at larger Pe, the regime of constant $\dot{\varepsilon}$ abruptly changes to a different regime characterized by a continuous decrease of $\dot{\varepsilon}$ (solid black line in Fig. 5), throughout which the drop retains its nearly spherical shape. This regime lasts until the drop cannot shrink anymore in a uniform manner and the stress imposed by the solvent evaporation is relaxed through the shape instability (see Fig. 2, $t = 1430$ s, and Fig. 3a ii). The shrinking rate therefore displays a cross-over from an evaporation-limited regime at short times to a shell relaxation-limited regime at longer times.

Remarkably, we find that in the relaxation-limited regime and before the onset of the instability the microscopic relaxation time of the nanoparticles in the shell is very well described by a simple inverse proportionality law, $\tau_D^{edge} = \Lambda\dot{\varepsilon}^{-1}$, with a prefactor $\Lambda = (2.5 \pm 0.1) \times 10^{-4}$ independent of Pe. Because dynamic light scattering is sensitive to the relative displacement of scatterers, a possible origin of the $\tau_D^{edge} \sim \dot{\varepsilon}^{-1}$ scaling could be the difference in the displacement velocity of neighbouring portions of the shell associated to the same speckle, due to the radial dependence of the amplitude of the strain field. As detailed in[29], assuming that the local strain field is purely affine, the expected relaxation time would be $\tau_D^{edge} \approx (2wq_y\dot{\varepsilon})^{-1}$, implying $(2wq_y)^{-1} \equiv \Lambda_{aff} = 7.5 \times 10^{-4}$, with w and q_y the waist of the illuminating laser beam and the y component of the scattering vector, respectively. This value is about three times larger than the experimental Λ, indicating that the microscopic dynamics are in fact dominated by non-affine displacements that grow proportionally to and add up to the underlying homogeneous strain field associated with the macroscopic contraction. These non-affine displacements speed up the relaxation dynamics, thereby allowing for efficiently reconfiguring the local structure in the shell, as required for the drop to keep reducing its radius.

The inverse proportionality relationship between τ_D^{edge} and $\dot{\varepsilon}$, together with values of ϕ_{shell} above the glass transition volume fraction but below random close packing (see Fig. 4c) and the lack of aggregation (see Figs. 2 and 4b), strongly supports the notion that the shell is a colloidal glass. Indeed, a similar scaling of the microscopic dynamics with the macroscopic deformation rate has been observed in other glassy and jammed materials[40–44] submitted to an external drive. In all cases, the microscopic dynamics are dictated by the imposed deformation rate when the spontaneous dynamics are too slow to allow for structural relaxation on the time scale associated to the external drive.

4 Discussion and Conclusions

Our experiments on drying drops of colloidal suspensions unveil a richer scenario as compared to that currently accepted, built on experiments at very high $Pe \geq 10^4$ and based only on the notion of permanent aggregation of the NPs. Our findings highlight the crucial role of the shell visco-elasticity through its ability (or not) to relax the stress imposed by the macroscopic shrinking rate on the time scale dictated by the drying conditions. This ability is expected to depend on the drying rate, and thus on the Péclet number, but also on the volume fraction in the shell, which in turn depends on Pe.

We propose an unifying scenario that rationalizes in a single state diagram in the (Pe, $\tilde{t}$) plane the results of all our experiments, as shown in Fig. 6. At relatively low $Pe \leq 70$, a shell is formed since the very early stage of drying ($\tilde{t} = 0.169$ for $Pe = 63$ and $\tilde{t} = 0.129$ for $Pe = 70$) (open circles), but the evaporation rate is slow enough for the NPs to recover a uniform distribution within the drop at larger $\tilde{t}$ (filled symbols). In this regime, the contraction rate $\dot{\varepsilon}$ is constant and imposed by the relative humidity of the environment (see semi-filled symbols in Fig. 5). Eventually, a fracture instability occurs, when the suspension is too dense to allow for further drop contraction. The fracture instability occurs when the system crosses the boundary between a dispersed and an aggregated state, respectively; this boundary is indicated in Fig. 6 by the solid line to the left of the aggregation region.

At larger $Pe > 70$, the drops initially follow the same evaporation-limited evolution as for lower Pe. However, they subsequently enter a driven-glass regime, where the drop contraction slows down and τ_D^{shell}, the microscopic relaxation time of the shell, and $\dot{\varepsilon}$ are mutually slaved, as shown by the solid line in Fig. 5. In this regime, we find that $\Lambda = \tau_D\dot{\varepsilon}$ is essentially inde-

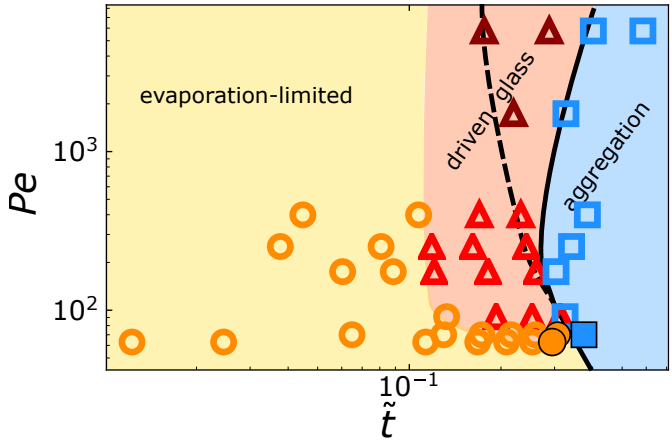

Fig. 6 Unifying state diagram for the evolution of drying drops of colloidal suspensions sitting on a hydrophobic surface.The different regimes through which a drop of colloidal suspension transits while drying are depicted in the (Pe, $\tilde{t}$) plane. The dashed and solid lines indicate the onset of the shape instability and fracture instabilities, respectively. Yellow background and circle symbols: region where the drop shrinkage is ruled by the evaporation rate imposed by the environment relative humidity. Pink background and triangle symbols: driven glass region, where the drop evaporation is limited by the glassy dynamics of the shell. Blue background and square symbols: region where the particles in the shell are permanently aggregated. Open symbols indicate samples with a shell, full symbols at low Pe designate samples with uniform particle distribution within the drop. The three topmost darker triangles correspond to the onset of shape instability for a sample that evaporated too fast for the microscopic dynamics to be measurable.

pendent of Pe and $\tilde{t}$, although both parameters have an impact on ϕ_{shell}. This is consistent with the glassy nature of the shell: once the rearrangement dynamics driven by the macroscopic shrinkage become faster than the spontaneous ones, the structure and quiescent dynamics in the shell become irrelevant, the driving rate $\dot{\varepsilon}$ being the only relevant parameter. As the shell densifies, the drops undergo a first shape instability, by forming an invagination that allows for further water evaporation. This first instability is indicated by the dashed line in the state diagram of Fig. 6 and is well distinct from the fracture instability occurring at later $\tilde{t}$ (solid line). Indeed, we find that no particle aggregation occurs in the driven glass regime and across the shape instability, while in all fractured samples the NPs are permanently aggregated. Intuitively, one would expect that a prerequisite for cracking is particle aggregation and our work clearly indicates that this is indeed the case for our system.

Figures 5 and 6 show that the driven glass regime does not extend to arbitrarily low Pe, since it is not observed for $Pe \leq 70$. Hence, despite similar features of the shell, compare e.g. the shell thickness (Fig. 3d) and volume fraction (Fig. 4c), the drops dried at $Pe = 70$ and $Pe = 91$ behave differently, because the shells are compressed at different rates. At first sight, this is quite puzzling, since one may think that, whatever the drying rate and hence Pe, as ϕ grows beyond ϕ_g the microscopic dynamics would always become too slow for the drop to maintain the initial $\dot{\varepsilon}$. Figure 5 shows that drops that avoid the driven glass regime contract at a rate lower than a threshold $\dot{\varepsilon}_{th} \approx 1.5 \times 10^{-5}$ s^{-1}, suggesting that our NP suspensions can accommodate ultraslow structural relaxations on time scales of the order of $1/\dot{\varepsilon}_{th} \approx 6.7 \times 10^4$ s. This is indeed confirmed by the measurements on quiescent suspensions of Ref.[32]: at large $\phi \gtrsim \phi_g$, the structural relaxation time exhibits a very weak ϕ dependence and plateaus to $\tau_D \approx 2 \times 10^4$ s, a value of the same order of magnitude of $1/\dot{\varepsilon}_{th}$. This peculiar dynamic regime has been observed for a variety of systems interacting through a repulsive interparticle potential softer than the infinitely steep hard sphere potential[32,45,46], as is the case of the screened Yukawa potential of our charge-stabilized NPs.

Note that the shape of the various regions in the state diagram of Fig. 6 changes if one uses the physical time t, rather than the reduced time $\tilde{t}$, as the abscissa, see Fig. 14 in[29]. In particular, the driven glass region becomes increasingly narrower as Pe grows, since the aggregation stage is reached very rapidly. The duration of the glass region lasts about 400 s for $Pe = 91$ and decreases down to 50 s for $Pe = 5754$, see Fig. 15 in[29]. This is likely to explain why the driven glass regime and the occurrence of two distinct instability could not be resolved in previous works on very fast-evaporating drops[1–3,6]. We expect the exact location of the boundaries between the different regions to depend also on other control parameters that are non explicitly included in the state diagram of Fig. 6, such as the nature of the substrate, the interparticle potential, and the initial volume fraction. We confirm this hypothesis by performing additional experiments, changing the contact angle between the drop and the surface, the NP volume initial fraction and the range of the repulsive potential between nanoparticles, see[29]. We find that varying these parameters does indeed shift the boundaries of the state diagram and modifies the detailed morphology of the shape instability, an effect previously reported for the shape instability observed in 2D experiments[15,47]. Crucially, however, the physical picture of a double state transition is not altered, strongly suggesting that the scenario proposed here is robust.

In conclusion, we have shown that drops of colloidal suspensions drying at intermediate to large Pe exhibit a richer-than-expected behavior, generally going through two distinct shape instabilities, which we rationalize in the framework of a unified state diagram. These instabilities are similar in that they both stem from the formation of a dense shell, which eventually becomes too rigid to accommodate the drop retraction imposed by drying. However, rigidity originates from two totally distinct mechanisms: a repulsive glass transition first, and the irreversible aggregation of NPs at larger times. Of note our findings might be reminiscent of the two-state drying identified in directional drying of thin film, with a first state corresponding to a reversible colloidal crystallization and the second state corresponding to irreversible colloidal aggregation[48].

Besides providing a deeper understanding of the drying mechanisms of colloidal drops at the fundamental level, we expect our work to have implications in applications involving relatively slow drying, e.g. in the synthesis of functional supraparticles[9–13,49], or the drying of drops containing biological entities, e.g. viruses or bacteria[7,50,51]. For the former, the finding that shape instabilities and shell formation occur at a stage where the NPs may be fully re-dispersed potentially paves the way to the synthesis of supra-

particles with new morphologies and properties, e.g. by varying the evaporation rate during the processing. For the latter, the formation of a reversible crust that protects against further evaporation while allowing for re-dispersion is likely to may play an important role in the survival, e.g., of cells embedded in drops undergoing cyclic variations between wet and dry conditions[51–53].

Author Contributions

We strongly encourage authors to include author contributions and recommend using CRediT for standardised contribution descriptions. Please refer to our general author guidelines for more information about authorship.

Conflicts of interest

There are no conflicts to declare.

Acknowledgements

We acknowledge financial support from the French Agence Nationale de la Recherche (ANR) (Grant No. ANR-19-CE06-0030-02, BOGUS). LC gratefully acknowledges support from the Institut Universitaire de France. We thank L. Pauchard and F. Giorgiutti-Dauphiné for discussion.

Notes and references

1 N. Tsapis, E. R. Dufresne, S. S. Sinha, C. S. Riera, J. W. Hutchinson, L. Mahadevan and D. A. Weitz, *Physical Review Letters*, 2005, **94**, 018302.

2 E. Lintingre, G. Ducouret, F. Lequeux, L. Olanier, T. Périé and L. Talini, *Soft Matter*, 2015, **11**, 3660–3665.

3 E. Lintingre, F. Lequeux, L. Talini and N. Tsapis, *Soft Matter*, 2016, **12**, 7435–7444.

4 L. Pauchard and Y. Couder, *EPL (Europhysics Letters)*, 2004, **66**, 667.

5 F. Giorgiutti-Dauphiné and L. Pauchard, *The European Physical Journal E*, 2014, **37**, 39.

6 S. Lyu, V. Mathai, Y. Wang, B. Sobac, P. Colinet, D. Lohse and C. Sun, *Science Advances*, 2019, **5**, eaav8081.

7 E. Huynh, A. Olinger, D. Woolley, R. K. Kohli, J. M. Choczynski, J. F. Davies, K. Lin, L. C. Marr and R. D. Davis, *Proceedings of the National Academy of Sciences*, 2022, **119**, e2109750119.

8 C. Sadek, H. Tabuteau, P. Schuck, Y. Fallourd, N. Pradeau, C. Le Floch-Fouere and R. Jeantet, *Langmuir*, 2013, **29**, 15606–15613.

9 W. Liu, M. Kappl and H.-J. Butt, *ACS nano*, 2019, **13**, 13949–13956.

10 D. M. Kuncicky and O. D. Velev, *Langmuir*, 2008, **24**, 1371–1380.

11 A. G. Marin, H. Gelderblom, A. Susarrey-Arce, A. van Houselt, L. Lefferts, J. G. E. Gardeniers, D. Lohse and J. H. Snoeijer, *Proceedings of the National Academy of Sciences*, 2012, **109**, 16455–16458.

12 M. Sperling, O. D. Velev and M. Gradzielski, *Angewandte Chemie International Edition*, 2014, **53**, 586–590.

13 T. Sekido, S. Wooh, R. Fuchs, M. Kappl, Y. Nakamura, H.-J. Butt and S. Fujii, *Langmuir*, 2017, **33**, 1995–2002.

14 C. Sadek, P. Schuck, Y. Fallourd, N. Pradeau, C. Le Floch-Fouéré and R. Jeantet, *Dairy Science & Technology*, 2015, **95**, 771–794.

15 S. Basu, L. Bansal and A. Miglani, *Soft Matter*, 2016, **12**, 4896–4902.

16 E. Both, I. Siemons, R. Boom and M. Schutyser, *Food Hydrocolloids*, 2019, **94**, 510–518.

17 A. Miglani and S. Basu, *Soft Matter*, 2015, **11**, 2268–2278.

18 N. Fu, M. W. Woo and X. D. Chen, *Drying Technology*, 2012, **30**, 1771–1785.

19 D. Sen, O. Spalla, O. Taché, P. Haltebourg and A. Thill, *Langmuir*, 2007, **23**, 4296–4302.

20 D. Sen, J. Bahadur, S. Mazumder, G. Santoro, S. Yu and S. V. Roth, *Soft Matter*, 2014, **10**, 1621–1627.

21 J. Bahadur, D. Sen, S. Mazumder, G. Santoro, S. Yu, S. Roth and Y. Melnichenko, *Langmuir*, 2015, **31**, 4612–4618.

22 L. Bansal, A. Miglani and S. Basu, *Physical Review E*, 2015, **92**, 042304.

23 S. Wooh, H. Huesmann, M. N. Tahir, M. Paven, K. Wichmann, D. Vollmer, W. Tremel, P. Papadopoulos and H.-J. Butt, *Advanced Materials*, 2015, **27**, 7338–7343.

24 M. Sperling, P. Papadopoulos and M. Gradzielski, *Langmuir*, 2016, **32**, 6902–6908.

25 A. Bouchaudy and J.-B. Salmon, *Soft Matter*, 2019, **15**, 2768–2781.

26 B. Sobac, S. Dehaeck, A. Bouchaudy and J.-B. Salmon, *Soft Matter*, 2020, **16**, 8213–8225.

27 F. Boulogne, F. Giorgiutti-Dauphiné and L. Pauchard, *Soft Matter*, 2013, **9**, 750–757.

28 A. Duri, D. A. Sessoms, V. Trappe and L. Cipelletti, *Physical Review Letters*, 2009, **102**, 085702.

29 *See Supplemental Material at [URL will be inserted by publisher].*

30 A. Philippe, S. Aime, V. Roger, R. Jelinek, G. Prevot, L. Berthier and L. Cipelletti, *Journal of Physics: Condensed Matter*, 2016, **28**, 075201.

31 A. Duri, H. Bissig, V. Trappe and L. Cipelletti, *Phys. Rev. E*, 2005, **72**, 051401.

32 A.-M. Philippe, D. Truzzolillo, J. Galvan-Myoshi, P. Dieudonné-George, V. Trappe, L. Berthier and L. Cipelletti, *Physical Review E*, 2018, **97**, 040601.

33 I. Langmuir, *Physical Review*, 1918, **12**, 368–370.

34 B. Sobac, P. Talbot, B. Haut, A. Rednikov and P. Colinet, *Journal of Colloid and Interface Science*, 2015, **438**, 306–317.

35 R. Pecora, *Journal of Nanoparticle Research*, 2000, **2**, 123–131.

36 B. Sobac, Z. Larbi, P. Colinet and B. Haut, *Colloids and Surfaces A: Physicochemical and Engineering Aspects*, 2019, **576**, 110–122.

37 P. N. Pusey and W. Vanmegen, *Phys. Rev. Lett.*, 1987, **59**, 2083–2086.

38 V. Baranau and U. Tallarek, *Soft Matter*, 2014, **10**, 3826–3841.

39 K. Trzaskus, M. Elshof, A. Kemperman and K. Nijmeijer, *Jour-*

nal of Membrane Science, 2016, **516**, 152–161.

40 H.-N. Lee, K. Paeng, S. F. Swallen and M. Ediger, *Science*, 2009, **323**, 231–234.

41 G. Brambilla, S. Buzzaccaro, R. Piazza, L. Berthier and L. Cipelletti, *Physical Review Letters*, 2011, **106**, 118302.

42 R. Besseling, E. R. Weeks, A. Schofield and W. Poon, *Physical Review Letters*, 2007, **99**, 028301.

43 F. Varnik, *The Journal of Chemical Physics*, 2006, **125**, 164514.

44 M. Laurati, K. J. Mutch, N. Koumakis, J. Zausch, C. P. Amann, A. B. Schofield, G. Petekidis, J. F. Brady, J. Horbach, M. Fuchs *et al.*, *Journal of Physics: Condensed Matter*, 2012, **24**, 464104.

45 S. Srivastava, L. A. Archer and S. Narayanan, *Physical Review Letters*, 2013, **110**, 148302.

46 Q. Li, X. Peng and G. B. McKenna, *Soft Matter*, 2017, **13**, 1396–1404.

47 L. Pauchard and Y. Couder, *Europhysics Letters (EPL)*, 2004, **66**, 667–673.

48 L. Goehring, W. J. Clegg and A. F. Routh, *Langmuir*, 2010, **26**, 9269–9275.

49 Z.-M. Kong, H. S. Sandhu, L. Qiu, J. Wu, W.-J. Tian, X.-J. Chi, Z. Tao, C.-F. J. Yang and X.-J. Wang, *Environmental Science & Technology*, 2022.

50 X. Xie, Y. Li, T. Zhang and H. H. P. Fang, *Appl Microbiol Biotechnol*, 2006, **73**, 703–712.

51 M. Grinberg, T. Orevi, S. Steinberg and N. Kashtan, *Elife*, 2019, **8**, e48508.

52 S. Hoefman, K. Van Hoorde, N. Boon, P. Vandamme, P. De Vos and K. Heylen, *PLoS One*, 2012, **7**, e34196.

53 A. M. Wesche, J. B. Gurtler, B. P. Marks and E. T. Ryser, *Journal of Food Protection*, 2009, **72**, 1121–1138.

Chapter 8

Conclusion and Perspectives

8.1 Summary of main results

The aim of this thesis was to investigate three different topics related to jammed colloidal systems with a common feature: being confined in spheres of millimetric size. In this section we briefly recap the main findings obtained in this work.

8.1.1 Dynamic light scattering on spherical samples

Measuring the microscopic dynamics with time- and space-resolution has been a key challenge to directly address the scientific questions faced in this thesis. Indeed, despite some existing Time-Resolved Correlation provide spce- and time resolved data, the millimetric spherical shape of our samples introduce several optical complications. This has required us to develop the ad-hoc setup. As discussed in Chapter 3, two main issues are raised by the macroscopic shape of our sample: light reflection at the sample-environment interface and a space-q entanglement of the light scattered on the detector. Both problems have been solved by a wise design of the optical setup, which we have tested by measuring the microscopic motion of Brownian suspensions and the microscopic dynamics of a polymer bead during swelling. These results, together with the ones presented in Chapters 6 and 7 for the drying of beads of colloidal gel and of drops of colloidal suspensions respectively, demonstrate the versatility of the setup and its efficiency in measuring the microscopic dynamics on spherical samples.

8.1.2 Beads of colloidal gel

A main objective of this thesis was to investigate the behavior of beads of colloidal gel under stress. Two configurations have been studied: beads under uniaxial compression and beads submitted an isotropic compaction induced by drying. Both investigations required the employment of spherical beads of colloidal gel with controlled and tunable structure and elasticity. The development and optimization of a new method to produce spherical beads of colloidal gel is described in Chapter 4. By depositing a small drop

(tens of microliters) of a destabilized colloidal suspension into an oil bath a homogeneous gel forms on a time scale of an hour without evaporating and keeping a spherical shape. Once the bead of gel is formed and aged for about a day, we rinse it from the oil and used it for compaction and drying experiments. Moreover, a large portion of Chapter 4, is dedicated to a detailed characterization of the gelation process of the microscopic properties of the beads. We have used three characterization techniques have been used: DLS was used to measure the gelation time and the microscopic dynamics of the colloids once the gel has formed, small angle X-ray scattering has been employed to measure the pristine structure of the gels, uniaxial compression has been exploited to test the linear mechanical properties of the beads of gel. Overall we find that quiescent properties of the beads do not differ from the ones of bulk samples.

In Chapter 5, beads of colloidal gel have been employed for investigating their yielding behavior under uniaxial compression. We use a standard rheometer to compress one bead of gel between two glass plates and measure the normal force exerted by the bead as a function of the spacing between the plates. From the measurements the stress-strain curves are computed. The setup is coupled with an imaging system to characterize the macroscopic behavior of the bead during compression. Remarkably, by tuning the volume fraction of the beds (thus their stiffness) drastically different behaviors are encountered both in the macroscopic aspect of the beads during yielding and also in the stress-strain curved obtained from the rheological measurements. The mechanical response of a stiff bead of gel is characterized by an abrupt drop of the stress occurring almost in the linear regime. By contrast, for soft beads a much smoother decline of the stress is preceded by a wide non-linear region during which the bead plastically rearranges. Such differences are encountered also in the movies: stiff beads yield by suddenly breaking in several pieces, while soft ones gently deform until expelling water from the solid network of the gel. These yielding behavior are characteristic of the so called brittle-to-ductile transition (BDT). Interestingly, the BDT hardly emerge when the gels yield in shear rheology, while being triggered in uniaxial compression. Thus, our experimental geometry is a good candidate to further investigate the BDT. Moreover, we have shown the robustness of our results, which not strictly dependent on the rate of compression used in the experiments, which we have varied over four orders of magnitude.

In Chapter 6 we investigate the drying of colloidal gels. In this case, the purpose of using beads of gel was to obtain a drying process free from spurious effects given by the interaction with the substrate such as cracking or delamination. As anticipated, the beads undergone a homogeneous isotropic drying, thus allowing us to address several question related to the microscopic compaction of the solid network of the gels. Firstly, by using the DLS described in Chapter 3, we have proven that the stresses imposed by the drying on the surface are propagated into the stress. More precisely, we have found homogeneous dynamics in the whole volume and that the microscopic displacement field, as for a pure

elastic body, is affine to the macroscopic compression. Secondly, by means of X-ray scattering, we have followed the structural evolution of the gel network. Remarkably, we have found that the gels rearrange in a hierarchical manner. Indeed, restructuring events occurs at large length scales at the beginning of drying process, and, as the drying proceeds the network reorganization involves smaller and smaller length scales. Remarkably, the length scale above which the rearrangements occur, scales as a power law with the linear density of particles of the pristine gel. Finally, by imposing an uniaxial compaction on partially dried beads, we found that the microscopic network reorganization leads to a global stiffening of the beads, reflected by an increase of its Young modulus.

8.1.3 Drying drops of colloidal suspension

Our work on drying drops of colloidal suspensions has brought to light several key aspects for the understanding this phenomenology. As detailed in Chapter 7, we have focused our investigation on the drying behavior of millimetric sessile drops deposited on top hydrophobic surfaces, characterized by a high initial volume fraction ($\phi \approx 0.3$). Moreover, in the experiments we vary the Peclet number (Pe) in the range $[63, 399]$, .

The problem has been first approached from a macroscopic point of view: by imaging a drop, we have seen that it undergoes two distinct shape instabilities. The first shape instability, which is encountered by drops evaporating at $Pe \geq 91$, is characterized by air invagination which deforms the drop from underneath. The second shape instability, all drop eventually undergo, is an abrupt event that breaks the drop into several pieces. Interestingly, we have checked that particles aggregation only accompanies the second shape instability, thus opening the question on which microscopic state characterizes the drop at the onset of the first shape instability.

To answer this question, we have performed a microscopic investigation of the phenomenon by means of our new DLS setup. Firstly, thanks to this setup we have obtained unprecedented information regarding the shell formed by the colloids lead by the receding air/water interface. In particular, through the measurements of the shell thickness and the volume fraction of the core, we managed to estimate the volume fraction of the shell, which, remarkably, is higher than the critical ϕ_g of the glass transition of this system at rest. Here, at the onset of the first shape instability, the shell is a colloidal glass, thus characterized by low relaxation dynamics. Moreover, by relating the microscopic dynamics to the rate of compression, we found that the invagination shape instability occurs when the colloids in the shell, due to their slow relaxation time, can not accomplish the macroscopic compression. Finally, based on our discovery, we have proposed a state diagram unifying our and previous works on the drying of colloidal suspensions.

8.2 Perspectives

In this section we detail the three main perspectives that this thesis work has opened and would like to address.

8.2.1 Brittle-to-ductile transition in soft materials

In Chapter 5, we have investigated the yielding behavior of beads of colloidal gel under uniaxial compression. Despite very promising results, to get a clear and exhaustive understanding of the BDT, further experimental data are required. In this aspect we propose some experimental improvements. Firstly, without major modification of the experimental setup, a correct synchronization between the imaging system and the rheometer would be extremely useful to better interpret the connection between the mechanical data and the images. Secondly, we aim to use an additional camera to image the yielding from the side, which would allow us to better depict the beads deformation. Possibly, we would like to use a fast camera in order to be able to follow fast events such as the propagation of the cracks observed in stiff gels. Finally, to get even closer to the experiment described in literature for the observation of the BTD, we think about using colloidal gels with a cylindrical shape. To obtain this shape we think about making the gels into cylindrical vials which walls are made hydrophobic throgh a coating. This geometry would allow us to perform a compression in the same condition of the Universal testing machine geometry (UTM).

8.2.2 Hierarchical restructuring of beads of gel during drying

Among the results described in Chapter 6 on the drying of beads of colloidal gel we have shown that crucial microscopic structural information of the solid network of the gel while it dries can be obtained with small angle X-ray scattering. Despite being really insightful for revealing the general mechanism with which the structures are rearranged, the limited q-range of the laboratory setup did not allowed us to fully detect hoe structures is modified over all the relevant length scale of a colloidal gel. Indeed, the maximum length scale we probe with the home machine is almost one order smaller then the cluster size of the most diluted gel. How the structures rearranges at large length scales is still an open question.

To address this question, we aim to probe the evolution of the microscopic structure by X-ray from synchrotron source. As also shown in Chapter 4, the q-range available with large scale facilities source would allow us to fully characterize the micro structure of the gel. Measuring the scattering intensity over a wide range of q would be the starting point to model the microscopic structure of the gel. Indeed, coupled to X-ray scattering,

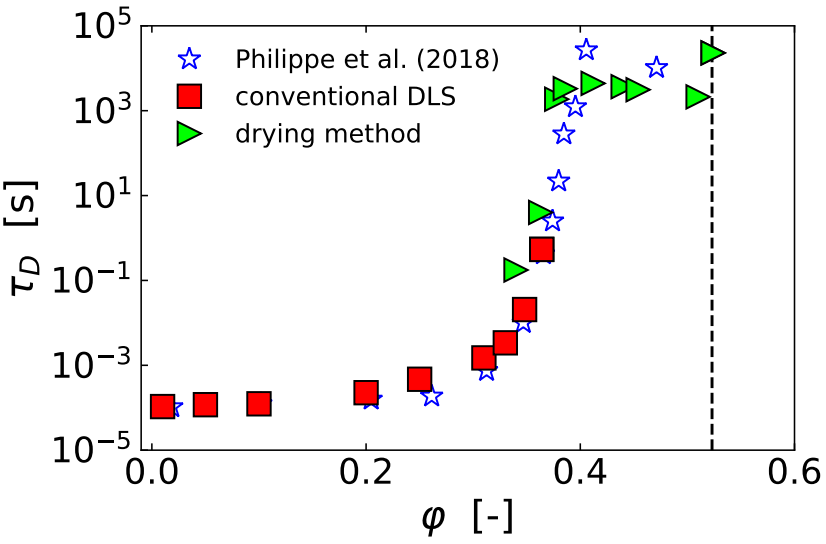

Figure 79: Microscopic relaxation time as function of the volume fraction of the colloidal suspension. The black dotted line is a guide for the eyes indicating the volume fraction of the most concentrated sample $\varphi = 0.523$. The suspensions and glasses are prepared with silica nanoparticles (Ludox TM-50 by Sigma Aldrich) suspended in water, with nominal diameter 25 nm.

we propose to perform inverse Monte Carlo simulations to reconstruct in real space the structure of the gel. For this purpose, we have recently submitted two proposals, one at ESRF of Grenoble (beamline iD2) and a second one at Soleil in Paris (beamline Swing) to obtain beamtime to perform these additional experiments.

8.2.3 Beads of colloidal glass

In this thesis we have largely used the results on the glass transition of Philippe et al. ([Philippe et al. (2018)]) to interpret our results. In particular, we have exploited the curve (Fig. 79) relating the microscopic decay time τ_D with the colloidal volume fraction φ for a quiescent sample. The dynamics weakly slow down as the volume fraction increases, until reaching the critical volume fraction $\varphi \approx 0.39$ after which the decay time sharply increases. However, for $\varphi > 0.40$, the decay time plateaus and the dynamics seems to be volume fraction independent. Despite being extremely interesting, we think that this result required further investigation, since it may raise from the preparation method of the sample. Indeed, due to their extremely slow relaxation dynamics, preparing and handling colloidal glasses with prescribed concentration, e.g. through centrifugation of a less dense suspension, is an extremely challenging task. Firstly, the centrifugation creates internal stresses which persist in the sample without being relaxed. Secondly, due to the high viscosity even transferring the sample to the measurement cell is not trivial and may cause additional internal stresses in the sample that is long reflected in its dynamics.

To overcome the issue, we propose to exploit drying at slow rates to produce beads

of colloidal glasses. Indeed, as shown in Chapter 7, when a drop of colloidal suspension dries at low evaporation rates, the system, before aggregating, does not undergo a shape instability but become instead a dense glass. Moreover, as shown by Sobac et al. in their theoretical studies ([Sobac et al. (2019)], described in the introduction), the lower the evaporation rate, the more homogeneously the colloids are distributed in the drop. Therefore, to reach extremely low evaporation rates, we deposit a small drop (2 mm in diameter) of colloidal suspension on top of a hydrophobic surface immersed in silicon oil. In such a way, we exploit the miscibility of water in oil at small diffusion rates to slowly evaporate the water thus gently increase the volume fraction of the colloids. In order to stop the evaporation, once a target volume fraction is reached, we change the silicon oil with a water-saturated oil. Once a bead of colloidal glass is produced, the microscopic dynamics are measured through DLS by using the setup described in Chapter 3.

The validity of this approach has been tested by preliminary experiments on drops of silica nanoparticles (Ludox TM-50 by Sigma Aldrich) suspended in water (same nanoparticles as the one used in Chapter 7). The results of these tests are represented by the green triangles in Fig. 79. Firstly, we see that, the highest volume fraction we managed to obtain is equal to $\varphi = 0.523$, which is higher than the one obtained with centrifugation methods $\varphi = 0.48$ with standard preparation methods. Secondly, measuring the dynamics with space resolution, we observe that, once the evaporation is stop, the microscopic motion is homogenous and steady all over the sample; suggesting that the system doesn't has embedded stresses. Moreover, the microscopic dynamics of our samples is in good agreement with previous experiments [Philippe et al. (2018)], confirming the soundness of this new experimental approach. Finally, we found that the decay time of a sample prepared at $\varphi = 0.523$ deviates from the plateau and has dynamics 10 times slower, encouraging further exploration for suspension prepared at even higher volume fraction.

Bibliography

Adhikari, B., Howes, T., Shrestha, A. K., and Bhandari, B. R. (2007). Development of stickiness of whey protein isolate and lactose droplets during convective drying. *Chemical Engineering and Processing: Process Intensification*, 46(5):420–428.

Aime, S. (2017). *Dynamic failure precursors in soft matter*. PhD thesis, Université Montpellier.

Aime, S., Cipelletti, L., and Ramos, L. (2018a). Power law viscoelasticity of a fractal colloidal gel. *Journal of Rheology*, 62(6):1429–1441.

Aime, S., Ramos, L., and Cipelletti, L. (2018b). Microscopic dynamics and failure precursors of a gel under mechanical load. *Proceedings of the National Academy of Sciences*, 115(14):3587–3592.

Aime, S., Ramos, L., Fromental, J.-M., Prevot, G., Jelinek, R., and Cipelletti, L. (2016). A stress-controlled shear cell for small-angle light scattering and microscopy. *Review of Scientific Instruments*, 87(12).

Aime, S., Truzzolillo, D., Pine, D. J., Ramos, L., and Cipelletti, L. (2023). A unified state diagram for the yielding transition of soft colloids. *Nature Physics*, pages 1–7.

Akl, M., Huang, L., and Shi, Y. (2023). Brittle to ductile transition during compression of glassy nanoparticles studied in molecular dynamics simulations. *Journal of Applied Physics*, 134(3).

Alexander, K. and Judson King, C. (1985). Factors governing surface morphology of spray-dried amorphous substances. *Drying Technology*, 3(3):321–348.

Augier, F., Coumans, W., Hugget, A., and Kaasschieter, E. (2002). On the risk of cracking in clay drying. *Chemical Engineering Journal*, 86(1-2):133–138.

Baggioli, M., Kriuchevskyi, I., Sirk, T. W., and Zaccone, A. (2021). Plasticity in amorphous solids is mediated by topological defects in the displacement field. *Physical Review Letters*, 127(1):015501.

Bahadur, J., Sen, D., Mazumder, S., Santoro, G., Yu, S., Roth, S., and Melnichenko, Y. (2015). Colloidal nanoparticle interaction transition during solvent evaporation investigated by in-situ small-angle x-ray scattering. *Langmuir*, 31(16):4612–4618.

Bamboriya, O. P. and Tirumkudulu, M. S. (2023). Universality in the buckling behavior of drying suspension drops. *Soft Matter*, 19(14):2605–2611.

Bansal, L., Miglani, A., and Basu, S. (2015). Universal buckling kinetics in drying nanoparticle-laden droplets on a hydrophobic substrate. *Physical Review E*, 92(4):042304.

Bantawa, M., Keshavarz, B., Geri, M., Bouzid, M., Divoux, T., McKinley, G. H., and Del Gado, E. (2023). The hidden hierarchical nature of soft particulate gels. *Nature Physics*, pages 1–7.

Barlow, H. J., Cochran, J. O., and Fielding, S. M. (2020). Ductile and brittle yielding in thermal and athermal amorphous materials. *Physical Review Letters*, 125(16):168003.

Basu, S., Bansal, L., and Miglani, A. (2016). Towards universal buckling dynamics in nanocolloidal sessile droplets: the effect of hydrophilic to superhydrophobic substrates and evaporation modes. *Soft matter*, 12(22):4896–4902.

Berne, B. J. and Pecora, R. (2000). *Dynamic light scattering: with applications to chemistry, biology, and physics*. Courier Corporation.

Bonacci, F., Chateau, X., Furst, E. M., Goyon, J., and Lemaître, A. (2022). Yield stress aging in attractive colloidal suspensions. *Physical Review Letters*, 128(1):018003.

Bouchaudy, A. and Salmon, J.-B. (2019). Drying-induced stresses before solidification in colloidal dispersions: In situ measurements. *Soft Matter*, 15(13):2768–2781.

Boulogne, F., Giorgiutti-Dauphiné, F., and Pauchard, L. (2013). The buckling and invagination process during consolidation of colloidal droplets. *Soft Matter*, 9(3):750–757.

Bouthier, L.-V. and Gibaud, T. (2023). Three length-scales colloidal gels: The clusters of clusters versus the interpenetrating clusters approach. *Journal of Rheology*, 67(3):621–633.

Bouzid, M. and Del Gado, E. (2018). Network topology in soft gels: Hardening and softening materials. *Langmuir*, 34(3):773–781.

Brambilla, G., El Masri, D., Pierno, M., Berthier, L., Cipelletti, L., Petekidis, G., and Schofield, A. B. (2009). Probing the equilibrium dynamics of colloidal hard spheres above the mode-coupling glass transition. *Physical review letters*, 102(8):085703.

Brinker, C. J. and Scherer, G. W. (2013). *Sol-gel science: the physics and chemistry of sol-gel processing*. Academic press.

Brutin, D., Sobac, B., Loquet, B., and Sampol, J. (2011). Pattern formation in drying drops of blood. *Journal of fluid mechanics*, 667:85–95.

Buscall, R., Mills, P. D., Goodwin, J. W., and Lawson, D. (1988). Scaling behaviour of the rheology of aggregate networks formed from colloidal particles. *Journal of the Chemical Society, Faraday Transactions 1: Physical Chemistry in Condensed Phases*, 84(12):4249–4260.

Carpineti, M. and Giglio, M. (1993). Transition from semiorder to disorder in the aggregation of dense colloidal solutions. *Physical review letters*, 70(24):3828.

Channell, G. M., Miller, K. T., and Zukoski, C. F. (2000). Effects of microstructure on the compressive yield stress. *AIChE journal*, 46(1):72–78.

Chen, H., Zhang, Y., Wang, H., Dong, X., and Zang, D. (2022). Evaporation caused invaginations of acoustically levitated colloidal droplets. *Nanomaterials*, 13(1):133.

Chiu, R. C. and Cima, M. J. (1993). Drying of granular ceramic films: Ii, drying stress and saturation uniformity. *Journal of the American Ceramic Society*, 76(11):2769–2777.

Chong, J., Christiansen, E., and Baer, A. (1971). Rheology of concentrated suspensions. *Journal of applied polymer science*, 15(8):2007–2021.

Cipelletti, L., Bissig, H., Trappe, V., Ballesta, P., and Mazoyer, S. (2002). Time-resolved correlation: a new tool for studying temporally heterogeneous dynamics. *Journal of Physics: Condensed Matter*, 15(1):S257.

Cipelletti, L., Manley, S., Ball, R., and Weitz, D. (2000). Universal aging features in the restructuring of fractal colloidal gels. *Physical review letters*, 84(10):2275.

Cipelletti, L., Ramos, L., Manley, S., Pitard, E., Weitz, D. A., Pashkovski, E. E., and Johansson, M. (2003). Universal non-diffusive slow dynamics in aging soft matter. *Faraday discussions*, 123:237–251.

Cipelletti, L., Trappe, V., and Pine, D. J. (2016). Scattering techniques. *Fluids, Colloids and Soft Materials: An Introduction to Soft Matter Physics*, pages 131–148.

Colina, H. and Acker, P. (2000). Drying cracks: kinematics and scale laws. *Materials and Structures*, 33(2):101–107.

Colombo, J. and Del Gado, E. (2014). Stress localization, stiffening, and yielding in a model colloidal gel. *Journal of rheology*, 58(5):1089–1116.

Dagès, N., Bouthier, L. V., Matthews, L., Manneville, S., Divoux, T., Poulesquen, A., and Gibaud, T. (2022). Interpenetration of fractal clusters drives elasticity in colloidal gels formed upon flow cessation. *Soft Matter*, 18(35):6645–6659.

De Gennes, P.-G. (1979). *Scaling concepts in polymer physics*. Cornell university press.

Donley, G. J., Singh, P. K., Shetty, A., and Rogers, S. A. (2020). Elucidating the g overshoot in soft materials with a yield transition via a time-resolved experimental strain decomposition. *Proceedings of the National Academy of Sciences*, 117(36):21945–21952.

Duri, A., Bissig, H., Trappe, V., and Cipelletti, L. (2005). Time-resolved-correlation measurements of temporally heterogeneous dynamics. *Phys. Rev. E*, 72(5):051401.

Duri, A. and Cipelletti, L. (2006). Length scale dependence of dynamical heterogeneity in a colloidal fractal gel. *Europhysics Letters*, 76(5):972.

Duri, A., Sessoms, D. A., Trappe, V., and Cipelletti, L. (2009). Resolving long-range spatial correlations in jammed colloidal systems using photon correlation imaging. *Physical review letters*, 102(8):085702.

Gelderblom, H., Diddens, C., and Marin, A. (2022). Evaporation-driven liquid flow in sessile droplets. *Soft matter*.

Giorgiutti-Dauphiné, F. and Pauchard, L. (2014). Elapsed time for crack formation during drying. *The European Physical Journal E*, 37:1–7.

Gisler, T., Ball, R. C., and Weitz, D. A. (1999). Strain hardening of fractal colloidal gels. *Physical review letters*, 82(5):1064.

Gnan, N. and Zaccarelli, E. (2019). The microscopic role of deformation in the dynamics of soft colloids. *Nature Physics*, 15(7):683–688.

Goehring, L., Conroy, R., Akhter, A., Clegg, W. J., and Routh, A. F. (2010). Evolution of mud-crack patterns during repeated drying cycles. *Soft Matter*, 6(15):3562–3567.

Grant, M. and Russel, W. (1993). Volume-fraction dependence of elastic moduli and transition temperatures for colloidal silica gels. *Physical Review E*, 47(4):2606.

Green, M. D. and Boger, D. V. (1997). Yielding of suspensions in compression. *Industrial & engineering chemistry research*, 36(11):4984–4992.

Guiné, R. (2018). The drying of foods and its effect on the physical-chemical, sensorial and nutritional properties. *International Journal of Food Engineering*, 2(4):93–100.

Guy, B., Hermes, M., and Poon, W. C. (2015). Towards a unified description of the rheology of hard-particle suspensions. *Physical review letters*, 115(8):088304.

Hoekstra, H., Vermant, J., Mewis, J., and Fuller, G. (2003). Flow-induced anisotropy and reversible aggregation in two-dimensional suspensions. *Langmuir*, 19(22):9134–9141.

Huynh, E., Olinger, A., Woolley, D., Kohli, R. K., Choczynski, J. M., Davies, J. F., Lin, K., Marr, L. C., and Davis, R. D. (2022). Evidence for a semisolid phase state of aerosols and droplets relevant to the airborne and surface survival of pathogens. *Proceedings of the National Academy of Sciences*, 119(4):e2109750119.

Iqbal, R., Shen, A. Q., and Sen, A. (2020). Understanding of the role of dilution on evaporative deposition patterns of blood droplets over hydrophilic and hydrophobic substrates. *Journal of Colloid and Interface Science*, 579:541–550.

Iskandar, F., Mikrajuddin, and Okuyama, K. (2002). Controllability of pore size and porosity on self-organized porous silica particles. *Nano Letters*, 2(4):389–392.

Islam, M. M. and Lester, D. R. (2021). Consolidation of strong colloidal gels under arbitrary compressive loadings. *Soft Matter*, 17(8):2242–2255.

Jacob, N. I. and Israelachvili, N. (1992). Intermolecular and surface forces. *San Diego: Academic*.

Jang, B., Uhlmann, D., and Sande, J. V. (1984). Ductile–brittle transition in polymers. *Journal of applied polymer science*, 29(11):3409–3420.

Johnson, K. L. (1982). One hundred years of hertz contact. *Proceedings of the Institution of Mechanical Engineers*, 196(1):363–378.

Johnson, K. L. and Johnson, K. L. (1987). *Contact mechanics*. Cambridge university press.

Koumakis, N., Pamvouxoglou, A., Poulos, A., and Petekidis, G. (2012). Direct comparison of the rheology of model hard and soft particle glasses. *Soft Matter*, 8(15):4271–4284.

Koumakis, N. and Petekidis, G. (2011). Two step yielding in attractive colloids: transition from gels to attractive glasses. *Soft Matter*, 7(6):2456–2470.

Krall, A. and Weitz, D. (1998). Internal dynamics and elasticity of fractal colloidal gels. *Physical review letters*, 80(4):778.

Kuncicky, D. M. and Velev, O. D. (2008). Surface-Guided Templating of Particle Assemblies Inside Drying Sessile Droplets. *Langmuir*, 24(4):1371–1380.

Lakshmikantha, M., Prat, P., and Ledesma, A. (2009). Image analysis for the quantification of a developing crack network on a drying soil. *Geotechnical Testing Journal*, 32(6):505–515.

Langmuir, I. (1918). The evaporation of small spheres. *Physical review*, 12(5):368.

Laurati, M., Egelhaaf, S., and Petekidis, G. (2011). Nonlinear rheology of colloidal gels with intermediate volume fraction. *Journal of Rheology*, 55(3):673–706.

Lintingre, E., Ducouret, G., Lequeux, F., Olanier, L., Périé, T., and Talini, L. (2015). Controlling the buckling instability of drying droplets of suspensions through colloidal interactions. *Soft Matter*, 11(18):3660–3665.

Liu, A. J. and Nagel, S. R. (1998). Jamming is not just cool any more. *Nature*, 396(6706):21–22.

Liu, W., Kappl, M., and Butt, H.-J. (2019). Tuning the porosity of supraparticles. *ACS nano*, 13(12):13949–13956.

Lu, P. J. and Weitz, D. A. (2013). Colloidal particles: Crystals, glasses, and gels. *Annu. Rev. Condens. Matter Phys.*, 4(1):217–233.

Lu, Y., Zhang, Y.-H., Ma, E., and Han, W.-Z. (2021). Relative mobility of screw versus edge dislocations controls the ductile-to-brittle transition in metals. *Proceedings of the National Academy of Sciences*, 118(37):e2110596118.

Lyu, S., Mathai, V., Wang, Y., Sobac, B., Colinet, P., Lohse, D., and Sun, C. (2019). Final fate of a leidenfrost droplet: Explosion or takeoff. *Science advances*, 5(5):eaav8081.

Maccarrone, S., Brambilla, G., Pravaz, O., Duri, A., Ciccotti, M., Fromental, J.-M., Pashkovski, E., Lips, A., Sessoms, D., Trappe, V., et al. (2010). Ultra-long range correlations of the dynamics of jammed soft matter. *Soft Matter*, 6(21):5514–5522.

Macosko, C. W. (1994). Rheology principles. *Measurements and Applications*.

Manley, S., Davidovitch, B., Davies, N. R., Cipelletti, L., Bailey, A., Christianson, R. J., Gasser, U., Prasad, V., Segre, P., Doherty, M., et al. (2005a). Time-dependent strength of colloidal gels. *Physical review letters*, 95(4):048302.

Manley, S., Skotheim, J., Mahadevan, L., and Weitz, D. A. (2005b). Gravitational collapse of colloidal gels. *Physical review letters*, 94(21):218302.

Marin, A. G., Gelderblom, H., Susarrey-Arce, A., van Houselt, A., Lefferts, L., Gardeniers, J. G. E., Lohse, D., and Snoeijer, J. H. (2012). Building microscopic soccer balls with evaporating colloidal fakir drops. *Proceedings of the National Academy of Sciences*, 109(41):16455–16458.

Marty, G. and Tsapis, N. (2008). Monitoring the buckling threshold of drying colloidal droplets using water-ethanol mixtures. *The European Physical Journal E*, 27:213–219.

Mattsson, J., Wyss, H. M., Fernandez-Nieves, A., Miyazaki, K., Hu, Z., Reichman, D. R., and Weitz, D. A. (2009). Soft colloids make strong glasses. *Nature*, 462(7269):83–86.

Meakin, P. (1983). Formation of fractal clusters and networks by irreversible diffusion-limited aggregation. *Physical Review Letters*, 51(13):1119.

Miglani, A. and Basu, S. (2015). Sphere to ring morphological transformation in drying nanofluid droplets in a contact-free environment. *Soft Matter*, 11(11):2268–2278.

Miller, K. T., Melant, R. M., and Zukoski, C. F. (1996). Comparison of the compressive yield response of aggregated suspensions: Pressure filtration, centrifugation, and osmotic consolidation. *Journal of the American Ceramic Society*, 79(10).

Nicolas, A., Ferrero, E. E., Martens, K., and Barrat, J.-L. (2018). Deformation and flow of amorphous solids: Insights from elastoplastic models. *Reviews of Modern Physics*, 90(4):045006.

Ogawa, Y., Nishiyama, Y., and Mazeau, K. (2020). Drying-induced bending deformation of cellulose nanocrystals studied by molecular dynamics simulations. *Cellulose*, 27(17):9779–9786.

Omatete, O. O., Strehlow, R. A., and Walls, C. A. (1991). Drying of gelcast ceramics. Technical report, Oak Ridge National Lab., TN (USA).

Ozawa, M., Berthier, L., Biroli, G., Rosso, A., and Tarjus, G. (2018). Random critical point separates brittle and ductile yielding transitions in amorphous materials. *Proceedings of the National Academy of Sciences*, 115(26):6656–6661.

Pauchard, L., Parisse, F., and Allain, C. (1999). Influence of salt content on crack patterns formed through colloidal suspension desiccation. *Physical Review E*, 59(3):3737.

Philippe, A.-M., Truzzolillo, D., Galvan-Myoshi, J., Dieudonné-George, P., Trappe, V., Berthier, L., and Cipelletti, L. (2018). Glass transition of soft colloids. *Physical Review E*, 97(4):040601.

Pineau, A., Benzerga, A. A., and Pardoen, T. (2016). Failure of metals i: Brittle and ductile fracture. *Acta Materialia*, 107:424–483.

Pusey, P. N. and Van Megen, W. (1986). Phase behaviour of concentrated suspensions of nearly hard colloidal spheres. *Nature*, 320(6060):340–342.

Pusey, P. N. and Van Megen, W. (1989). Dynamic light scattering by non-ergodic media. *Physica A: Statistical Mechanics and its Applications*, 157(2):705–741.

Richard, D., Ozawa, M., Patinet, S., Stanifer, E., Shang, B., Ridout, S., Xu, B., Zhang, G., Morse, P., Barrat, J.-L., et al. (2020). Predicting plasticity in disordered solids from structural indicators. *Physical Review Materials*, 4(11):113609.

Romer, S., Bissig, H., Schurtenberger, P., and Scheffold, F. (2014). Rheology and internal dynamics of colloidal gels from the dilute to the concentrated regime. *Europhysics Letters*, 108(4):48006.

Rueb, C. and Zukoski, C. (1997). Viscoelastic properties of colloidal gels. *Journal of Rheology*, 41(2):197–218.

Sadek, C., Schuck, P., Fallourd, Y., Pradeau, N., Le Floch-Fouéré, C., and Jeantet, R. (2015). Drying of a single droplet to investigate process–structure–function relationships: a review. *Dairy Science & Technology*, 95(6):771–794.

Sadek, C., Tabuteau, H., Schuck, P., Fallourd, Y., Pradeau, N., Le Floch-Fouere, C., and Jeantet, R. (2013). Shape, shell, and vacuole formation during the drying of a single concentrated whey protein droplet. *Langmuir*, 29(50):15606–15613.

Sarkar, A. and Tirumkudulu, M. S. (2011). Delamination of drying nanoparticle suspensions. *Soft Matter*, 7(19):8816–8822.

Savitzky, A. and Golay, M. J. (1964). Smoothing and differentiation of data by simplified least squares procedures. *Analytical chemistry*, 36(8):1627–1639.

Schuck, P., Jeantet, R., Bhandari, B., Chen, X. D., Perrone, I. T., de Carvalho, A. F., Fenelon, M., and Kelly, P. (2016). Recent advances in spray drying relevant to the dairy industry: A comprehensive critical review. *Drying Technology*, 34(15):1773–1790.

Sekido, T., Wooh, S., Fuchs, R., Kappl, M., Nakamura, Y., Butt, H.-J., and Fujii, S. (2017). Controlling the structure of supraballs by ph-responsive particle assembly. *Langmuir*, 33(8):1995–2002.

Sen, D., Bahadur, J., Mazumder, S., and Bhattacharya, S. (2012). Formation of hollow spherical and doughnut microcapsules by evaporation induced self-assembly of nanoparticles: effects of particle size and polydispersity. *Soft Matter*, 8(39):10036–10044.

Sen, D., Bahadur, J., Mazumder, S., Santoro, G., Yu, S., and Roth, S. V. (2014). Probing evaporation induced assembly across a drying colloidal droplet using in situ small-angle x-ray scattering at the synchrotron source. *Soft Matter*, 10(10):1621–1627.

Sessoms, D. A., Bissig, H., Duri, A., Cipelletti, L., and Trappe, V. (2010). Unexpected spatial distribution of bubble rearrangements in coarsening foams. *Soft Matter*, 6(13):3030–3037.

Sherwood, T. (1930). The drying of solids—iii1 mechanism of the drying of pulp and paper. *Industrial & Engineering Chemistry*, 22(2):132–136.

Shih, W.-H., Shih, W. Y., Kim, S.-I., Liu, J., and Aksay, I. A. (1990). Scaling behavior of the elastic properties of colloidal gels. *Physical review A*, 42(8):4772.

Singh, M., Ozawa, M., and Berthier, L. (2020). Brittle yielding of amorphous solids at finite shear rates. *Physical Review Materials*, 4(2):025603.

Sobac, B. and Brutin, D. (2011). Structural and evaporative evolutions in desiccating sessile drops of blood. *Physical Review E*, 84(1):011603.

Sobac, B. and Brutin, D. (2014). Desiccation of a sessile drop of blood: Cracks, folds formation and delamination. *Colloids and Surfaces A: Physicochemical and Engineering Aspects*, 448:34–44.

Sobac, B., Dehaeck, S., Bouchaudy, A., and Salmon, J.-B. (2020). Collective diffusion coefficient of a charged colloidal dispersion: interferometric measurements in a drying drop. *Soft Matter*, 16(35):8213–8225.

Sobac, B., Larbi, Z., Colinet, P., and Haut, B. (2019). Mathematical modeling of the drying of a spherical colloidal drop. *Colloids and Surfaces A: Physicochemical and Engineering Aspects*, 576:110–122.

Sonntag, R. C. and Russel, W. B. (1986). Structure and breakup of flocs subjected to fluid stresses: I. shear experiments. *Journal of colloid and interface science*, 113(2):399–413.

Sperling, M., Papadopoulos, P., and Gradzielski, M. (2016). Understanding the formation of anisometric supraparticles: a mechanistic look inside droplets drying on a superhydrophobic surface. *Langmuir*, 32(27):6902–6908.

Sperling, M., Velev, O. D., and Gradzielski, M. (2014). Controlling the shape of evaporating droplets by ionic strength: formation of highly anisometric silica supraparticles. *Angewandte Chemie International Edition*, 53(2):586–590.

Sugiyama, Y., Larsen, R. J., Kim, J.-W., and Weitz, D. A. (2006). Buckling and crumpling of drying droplets of colloid- polymer suspensions. *Langmuir*, 22(14):6024–6030.

Teixeira, J. (1988). Small-angle scattering by fractal systems. *Journal of Applied Crystallography*, 21(6):781–785.

Thiery, J., Keita, E., Rodts, S., Courtier Murias, D., Kodger, T., Pegoraro, A., and Coussot, P. (2016). Drying kinetics of deformable and cracking nano-porous gels. *The European Physical Journal E*, 39(12):1–14.

Thiery, J., Rodts, S., Keita, E., Chateau, X., Faure, P., Courtier-Murias, D., Kodger, T., and Coussot, P. (2015). Water transfer and crack regimes in nanocolloidal gels. *Physical Review E*, 91(4):042407.

Tirumkudulu, M. S. (2018). Buckling of a drying colloidal drop. *Soft Matter*, 14(36):7455–7461.

Trappe, V., Prasad, V., Cipelletti, L., Segre, P., and Weitz, D. A. (2001). Jamming phase diagram for attractive particles. *Nature*, 411(6839):772–775.

Trappe, V. and Sandkühler, P. (2004). Colloidal gels—low-density disordered solid-like states. *Current opinion in colloid & interface science*, 8(6):494–500.

Trappe, V. and Weitz, D. (2000). Scaling of the viscoelasticity of weakly attractive particles. *Physical review letters*, 85(2):449.

Tsapis, N., Dufresne, E. R., Sinha, S. S., Riera, C. S., Hutchinson, J. W., Mahadevan, L., and Weitz, D. A. (2005). Onset of buckling in drying droplets of colloidal suspensions. *Physical review letters*, 94(1):018302.

Van Der Scheer, P., Van De Laar, T., Van Der Gucht, J., Vlassopoulos, D., and Sprakel, J. (2017). Fragility and strength in nanoparticle glasses. *ACS nano*, 11(7):6755–6763.

van Vliet, T., van Aken, G. A., de Jongh, H. H., and Hamer, R. J. (2009). Colloidal aspects of texture perception. *Advances in Colloid and Interface Science*, 150(1):27–40.

Vlassopoulos, D. and Cloitre, M. (2014). Tunable rheology of dense soft deformable colloids. *Current opinion in colloid & interface science*, 19(6):561–574.

Weitz, D. and Oliveria, M. (1984). Fractal structures formed by kinetic aggregation of aqueous gold colloids. *Physical review letters*, 52(16):1433.

Wilson, S. K. and D'Ambrosio, H.-M. (2023). Evaporation of sessile droplets. *Annual Review of Fluid Mechanics*, 55:481–509.

Witten Jr, T. A. and Sander, L. M. (1981). Diffusion-limited aggregation, a kinetic critical phenomenon. *Physical review letters*, 47(19):1400.

Wong, T.-f. and Baud, P. (2012). The brittle-ductile transition in porous rock: A review. *Journal of Structural Geology*, 44:25–53.

Wyss, H. M., Innerlohinger, J., Meier, L. P., Gauckler, L. J., and Glatter, O. (2004). Small-angle static light scattering of concentrated silica suspensions during in situ destabilization. *Journal of colloid and interface science*, 271(2):388–399.

Xing, Y., Chen, X., Chen, X., and Zhuang, J. (2016). Colloid-mediated transport of pharmaceutical and personal care products through porous media. *Scientific Reports*, 6(1):35407.

Xue, J.-Z., Pine, D., Milner, S. T., Wu, X.-L., and Chaikin, P. (1992). Nonergodicity and light scattering from polymer gels. *Physical Review A*, 46(10):6550.

Yanez, J. A., Shikata, T., Lange, F. F., and Pearson, D. S. (1996). Shear modulus and yield stress measurements of attractive alumina particle networks in aqueous slurries. *Journal of the American Ceramic Society*, 79(11):2917–2917.

Zemb, T. and Lindner, P. (2002). *Neutron, X-rays and light. Scattering methods applied to soft condensed matter*. North Holland.

Appendix A

annex

A double rigidity transition rules the fate of drying colloidal drops Supporting Informations

Matteo Milani[a], Ty Phou[a], Christian Ligoure[a], Luca Cipelletti[a], Laurence Ramos[a*]

August 29, 2023

0.1 Light scattering set-up

We provide here details on the light scattering set-up shown in Fig. 1 of the main text.

0.1.1 Optics

The first lens (L_1 in Fig. 1a of the main text) has a diameter of 65 mm and a focal length of 64 mm. The second lens (L_2) has a diameter of 40 mm and a focal length of 82 mm. The vertical slit has an aperture of 4 mm and the diaphragm has a diameter of 1.2 mm.

0.1.2 Measurement of the beam waist

To determine the beam waist w of the laser light illuminating the sample, we replace the drop with a frosted glass placed perpendicularly to the incoming beam, at $x = 0$, i.e. at the position occupied by the center of the drop during the drying experiments. We record the speckle pattern generated by the light scattered by the frosted glass using a CMOS camera placed in the focal plane of a converging lens with focal length $f = 40$ mm. We calculate the spatial autocorrelation of the intensity pattern, $C_I(\Delta x,\Delta y) = \langle I(x,y)I(x+\Delta x,y+\Delta y)\rangle$. For a scatterer illuminated by a Gaussian beam with beam waist w and wavelength λ, the autocorrelation function reads [1]

$$C_I(\Delta x,\Delta y) = \exp\left[-\frac{\pi^2 w^2}{2f^2\lambda^2}(x^2+y^2)\right]. \tag{1}$$

By fitting Eq. 1 to the measured $C_I(\Delta x,\Delta y)$, we find $w = 59.5 \pm 0.1$ μm.

0.1.3 Camera features

The sample is imaged by either one or two detectors (Camera 1 and Camera 2 in Fig. 1a of the main text). Camera 1 is used in all experiments to collect the speckle images formed by light scattered by the sample. Camera 1 (acA2000 340km by Basler) has a full frame size of 2048 pixels $\times$1088 pixels and a pixel size of 5.5 μm. To allow for faster image acquisition, we typically acquire only a fraction of the full frame, selecting a region of interest of 2048 pixels $\times$512 pixels. In some experiments, we use an additional camera (Camera 2 in Fig. 6a of the main text) to collect conventional images of the drop illuminated by white light. In this configuration, Camera 2 (acA2000 340km by Basler) is run at full frame resolution. At the beginning of drying, the dynamics are too fast to be correctly measured by Camera 1. We thus replace Camera 2 with a fast camera running at 19000 fps, in parallel to Camera 1. The fast camera is a Phantom Miro M310, the size of the acquired images is 896 pixels $\times$184 pixels, and the pixel size is 20 μm.

0.1.4 Refraction effects: corrections to the x coordinate and the modulus of the scattering vector q

As explained in the main text, our setup collects light exiting from the drop along the direction of the y axis. When running a space-resolved scattering experiment, it is important to link the position H of a ray emerging from the sample to the coordinate x of the region inside the drop from which the scattered light originates, see Fig. 1. Indeed, while H is easily read from the position on the detector, the physically relevant position is x. For a drop of radius R and refractive index n_1, embedded in a medium of refractive index n_2, Snell's law reads $n_1 \sin\theta_1 = n_2 \sin\theta_2$. Using simple trigonometry, one can write the following equations:

$$\begin{aligned} H &= R\frac{\sin\theta_1}{\cos(\theta_2-\theta_1)}\frac{1}{(1-\tan(\theta_2-\theta_1))\tan\theta_2} \\ x &= R\frac{\sin\theta_1}{\cos(\theta_2-\theta_1)} \\ \theta_2 &= \arcsin\left(\frac{n_1}{n_2}\sin\theta_1\right) \end{aligned} \tag{2}$$

Equations 2 can be solved to obtain the coordinate x in the scattering volume as a function of the position H on the detector, as shown in Fig. 2a for a water drop in air, oil and water.

A further consequence of refraction at the drop surface is that the scattered light exiting the drop along the y direction at different H corresponds to different scattering angles θ_s. Hence the scattering vector q depends on the coordinate x of the sample region from which it originates. The scattering angle can be obtained from θ_1 using:

$$\frac{R}{\sin(\pi-\theta_s)} = \frac{x}{\sin\theta_1}. \tag{3}$$

We plot θ_s as a function of H in Fig. 2b, for a water drop of radius 1 mm and for three different representative surrounding media. When the external media is water, $n_2 = n_1 = 1.33$, no refraction occurs and the scattering angle for the light collected by the detection optics is 90 deg independently of H. When the sample is surrounded by air, $n_2 = 1$, the light is refracted at the interface: θ_s decreases from 131 deg down to 48 deg as H varies from -1 mm to 1 mm. By contrast, when the external medium has a refractive index higher than that of the sample, e.g. when the drop is immersed in oil, θ_s increases with H. As an example, for the oil used in our experiments for which $n_2 = 1.403$, the scattering angle varies from 77 to 102 deg.

The scattering vector q can be easily calculated from the scattering angle using

$$q = \frac{4\pi n}{\lambda}\sin\left(\frac{\theta_s}{2}\right). \tag{4}$$

As an example, we show in Fig. 3 the variation of q with H for a water drop surrounded by air (solid line). In order to obtain the effective scattering vector probed in each ROI in our experiments, we average $q(H)$ over the range of H corresponding to each ROI, yielding the solid circles shown in Fig. 3. Note that even for a water drop in air, for which the refraction effects are largest, the change in q across the various ROIs remains limited: $q = (22 \pm 5)$ μm^{-1}.

[*a] *Laboratoire Charles Coulomb (L2C), Université Montpellier, CNRS, Montpellier, France. E-mail: laurence.ramos@umontpellier.fr*

0.1.5 Data acquisition and laser alignment

To avoid complications arising when the incident beam is refracted when entering the drop, two conditions should be met: the beam waist w should be much smaller than the drop radius R and the laser beam should propagate along a drop diameter. The first condition is met by using a mildly focused beam, resulting in $w = 59.5\mu m$, much smaller than R, which is of the order of 1 mm.

The second condition is met by adjusting the vertical position of the drop, which sits on a hydrophobic surface positioned on a stage that can be translated in the z (vertical) direction. Since the drop progressively shrinks due to evaporation, the sample is translated upwards in order for the beam to always impinge along a diameter. In practice, we raise the drop by about $100\mu m$ periodically, typically every 15 min for the fastest evaporation experiment ($Pe = 399$), and every 60 min for the slowest one ($Pe = 63$).

0.2 Sample environment

0.2.1 Preparation of the hydrophobic surfaces

To produce the hydrophobic surface onto which the drop sits, a water/ethanol solution ($50\% - 50\%$) of trimethoxy-(octadecyl)-silane (20 mg/mL) is deposited on a glass slide and heated in an oven (1 h ramp from 30°C to 70°C, and then 12 h at 70°C). The contact angle of the drop on the surface, as measured by imaging, is approximately 120 deg. For experiments with a different contact angle, a glass surface is treated with Sigmacote® from Sigma Aldrich. The contact angle of the drop on the surface, as measured by imaging, is approximately 60 deg. Finally, to test a third kind of contact conditions for which the contact with a substrate is reduced as much as possible, we build a support formed by three human hairs that intersect forming a suspended triangle, over which we deposit a drop with a maximum volume of 10 μL.

0.2.2 Humidity control

	RH [%]	Pe	τ_{ev} [min]
H_2O	94	63	732
KCl	85	70	694
NaCl	75	91	476
K_2CO_3	43	175	248
$MgCl_2$	33	252	186
A.S.	20	399	112

Table 1 List of chemicals used to control the relative humidity, the corresponding time for evaporation, τ_{ev}, and Péclet number, Pe. The salts are used as saturated water solutions. A.S. is a commercial silica xerogel.

Table 1 lists the salt solutions and the commercial silica xerogel used to control the relative humidity (RH) of the chamber that contains the sample, together with the corresponding evaporation times τ_{ev} and Péclet numbers Pe. Pe ranges between 63 and 399. The typical amount of humidity-controlling material is 15 mL, and the cell volume is 125 cm^3. RH is measured with a humidity sensor (SENISOR SEK-SensorBridge) and τ_{ev} and Pe are calculated as described below. These experiments are run at room temperature.

0.2.3 Samples at $Pe > 1000$

To achieve faster drying conditions, drops are located in a chamber maintained at a temperature of $T = 75°C$ and $T = 110°C$. While this procedure insures fast evaporation, the evaporation rate is not as well controlled as in all other experiments. Moreover, the microscopic dynamics have not been measured in this configuration, and only aggregation tests have been performed.

0.3 Description of the two movies provided

0.3.1 Side view movie

Side view of a drop of colloidal suspension drying on the top of a hydrophobic surface. The suspension is a suspension of Ludox silica SM-30 ($\phi = 31$ %). The sample is illuminated from behind. The relative humidity is 20% and the Péclet number is 399. The scale bar is 1 mm (384 px) The total duration of the movie is 30 min.

0.3.2 Top view movie

Top view of a drop of colloidal suspension drying on the top of a hydrophobic surface. The suspension is suspension of Ludox silica SM-30 ($\phi = 31$ %). The sample is being illuminated from underneath. The relative humidity is 20% and the Péclet number is 399. The scale bar is 1 mm (42 px) The total duration of the movie is 1 hour.

0.4 Additional results and analysis with the sample described in the main manuscript

0.4.1 Measurement of the evaporation time

The characteristic evaporation time, τ_{ev}, is defined as the time to fully evaporate the drop, should it not contain nanoparticles. As in previous works[2,3], for the experiments performed at room temperature under controlled relative humidity, τ_{ev} is evaluated by extrapolating the short time behaviour of $R(t)^2$, with $R(t)$ the time-dependent drop radius and $t = 0$ the time at which evaporation starts, see Fig. 4. We measure that τ_{ev} ranges between 112 and 732 min (see Table 1). For the experiments run in an oven, the evaporation time, τ_{ev}, is evaluated by measuring directly the time required for a drop of pure water (with the same volume, 30 μL as the drops of colloidal suspension) to completely evaporate. We find $\tau_{ev} = 1545$ s, and $\tau_{ev} = 465$ s, for $T = 75°C$ and $T = 110°C$ respectively, yielding $Pe = 1729$ and $Pe = 5754$, respectively. The relevant non-dimensional Péclet number, $Pe = \tau_{mix}/\tau_{ev}$, compares the evaporation time to $\tau_{mix} = R_0^2/D$, the characteristic mixing time due to Brownian diffusion over a distance equal to the drop initial size, $R_0 = R(t = 0)$, with $D = 4.31 \times 10^{-12}$ $m^2 s^{-1}$, the diffusion coefficient of the NPs for $\phi = 0.31$[4].

Overall, in our experiments, τ_{ev} varies from (465 ± 10) s to (43920 ± 20) s, yielding Pe from 63 to 5754. Most data are analyzed considering a reduced time $\tilde{t}$ defined as $\tilde{t} = t/\tau_{ev}$.

0.4.2 Shell thickness

As explained in the main text, in order to locate the shell and measure its thickness h, we perform a time average of the intensity of the speckle images over a time interval $\Delta t = 4$ s. By plotting the gray intensity, averaged over the z (vertical) direction, as a function of the position along the drop diameter, we obtain plots such as the one shown in Fig. 5. In this figure the regions in blue with high fluctuation (seven times higher than the region in red) correspond to the region of the images which, even after the time average, shows a speckle pattern. In general we define the shell as the region with a variance at least 4 times higher than the one in the center of the drop. The physical origin behind the identification of the shell lies in the fact that when the particles are denser their dynamics is slower. Because of the high sensitivity of the nanoparticle relaxation time with the volume fraction, the characteristic relaxation time of the "core" and the "shell" differ by several orders of

magnitude. One one hand, nanoparticles in the dilute core (whose volume fraction is always smaller than 0.39, see Fig. 25) have fast dynamics, so the time average returns a blurred gray image. On the other hand, nanoparticles in the shell, which is characterized by a high volume fraction (volume fraction > 0.39), has slow dynamics so the speckle pattern evolves slower than time over which the average is performed. As a consequence the time average has still the appearance of a speckle pattern that is characterized by a high spatial variance.

Moreover for a representative sample drying at $Pe = 91$, we check that changing Δt from 2 to 8 s does not change significantly the measured thickness of the shell, as shown in Fig. 6.

Figure 7 shows the shell thickness normalized by the instantaneous radius of the drop as a function of absolute time for experiments performed at different Péclet numbers. These are the same data as those shown in Fig. 3d of the main text, where they are plotted as a function of reduced time $\tilde{t}$.

Figure 8 shows the final value of the shell thickness normalized by the instantaneous radius of the drop as a function of the Péclet number. Data at $Pe = 63, 70$ correspond to measures taken at the end of the experiment, when the particle concentration is uniform throughout the drop (no shell or, equivalently, the shell coincides with the whole drop). For the other Pe data, h is measured at the onset of the drop instability.

0.4.3 Symmetry of the dynamics with respect to the drop center

We plot in Fig. 9 the microscopic relaxation time τ_D as a function of the position x along a drop diameter, for both sides of the drop ($x \leq 0$ and $x \geq 0$), where $x = 0$ corresponds to the center of the drop. The curves measured at different times during the drying are nearly symmetric around $x = 0$ implying that the impact of the slight change of q with x (see Fig. 3) is negligible. This motivated our choice to present only data for one side of the drop in the main text.

0.4.4 Space- and time-dependence of the microscopic relaxation time

Figure 10 displays the variation of the relaxation time with the position in the drop, as measured at different times during the drying process. Plots are shown for experiments run at different Péclet numbers.

0.4.5 Volume fraction in the core and shell

We measure the microscopic decay time in the middle of the drop, τ_D^{core}. By comparing this time to the characteristics decay time for quiescent suspensions of the same nanoparticles, as reported in[4] and also shown in Fig. 11, it is possible to infer the volume fraction of the core of the drop, ϕ_{core}. Having evaluated ϕ_{core} and the shell thickness, we estimate the average volume fraction in the shell, ϕ_{shell}, through mass conservation. To do so, we assume that the interface between the core and the shell is sharp (infinite concentration gradient at the interface), that the thickness of the shell is uniform, and that both the drop and the Brownian core are spherical. In order to make an estimation of the error due to the latter assumption, we also measure the profile area of the drop and measure the volume using Pappus's centroid of revolution theorem, yielding the error bars of Fig. 4c of the main text.

0.4.6 Macroscopic strain rate

We plot in Fig. 12 the strain rate $\dot{\varepsilon} = \frac{1}{R}|\frac{dR}{dt}|$ as a function of time, for drops that dry at different Péclet numbers. Overall, we find that in the initial stages of evaporation $\dot{\varepsilon}$ increases as Pe increases. Conversely, for a fixed Pe, $\dot{\varepsilon}$ is constant with time when the drop is far from an instability threshold and decreases close to the instability, as a glassy shell prevents the drop from smoothly changing its shape.

0.4.7 Contribution of the affine strain field to the decay of the intensity correlation function $g_2 - 1$

We evaluate here the expected relaxation time of $g_2 - 1$ due to a purely affine displacement of the nanoparticles, i.e. if the drop would shrink as an ideal, perfectly homogeneous elastic solid. We focus on the behavior of the microscopic relaxation time at the edge of the drop τ_D^{edge}. The decay of $g_2 - 1$ is due to the temporal fluctuations of the intensity of each speckle. In turn, the intensity of any given speckle changes significantly when the scatterers associated to this speckle move with respect to each over a distance $\Delta\vec{r}$ such that $\vec{q}\cdot\Delta\vec{r} \approx 1$[5]. For the ballistic motion due to the progressive shrinkage of a drying drop, one has $\Delta\vec{r}(\tau) = \Delta\vec{v}\tau$ and thus $\tau_D^{\text{edge}} \approx 1/(\vec{q}\cdot\Delta\vec{v})$, assuming that the relative velocity $\Delta\vec{v}$ of the scatterers does not change over the time scale of the decay of $g_2 - 1$.

In our experiments, the dominant contribution to $\Delta\vec{v}$ stems from the velocity difference between the points A and B shown in Fig. 13, which both contribute to the scattered light associated to the same speckle located at the edge of the drop. For a drop contracting at a radial speed $\dot{R}$, the velocities in A and B read:

$$\vec{v}_A = \dot{R}\left[\cos\left(\frac{w}{R}\right)\widehat{e}_x - \sin\left(\frac{w}{R}\right)\widehat{e}_y\right], \vec{v}_B = \dot{R}\left[\cos\left(\frac{w}{R}\right)\widehat{e}_x + \sin\left(\frac{w}{R}\right)\widehat{e}_y\right], \tag{5}$$

such that $\Delta\vec{v} = \vec{v}_B - \vec{v}_A = 2\sin\left(\frac{w}{R}\right)\widehat{e}_y \approx 2\frac{w}{R}\widehat{e}_y$, where we used $w << R$. We finally obtain

$$\tau_D^{\text{edge}} \approx \frac{1}{\vec{q}\cdot\vec{\Delta v}} \approx \frac{1}{2\frac{\dot{R}}{R}wq_y} = \frac{1}{2\dot{\varepsilon}wq_y}. \tag{6}$$

In our experiments $2w = 120\mu m$ and $q_y \approx 27\mu m^{-1}$, thus

$$\tau_D^{\text{edge}} \times \dot{\varepsilon} \approx \frac{1}{2wq_y} \approx 7.5\cdot 10^{-4}, \tag{7}$$

as reported in the main text. A similar calculation has been done to evaluate the contribution due to the finite size of the speckle along the x direction. Indeed, scatterers corresponding to the edges of a speckle have different velocities, as sketched by the points A and A' in Fig. 13, where the lateral extension of a speckle is exaggerated for the sake of clarity. Taking into account that in our setup the lateral speckle size is $S_s \approx \frac{2w}{10}$ and using simple trigonometry as for deriving Eq. 5, one obtains:

$$\tau_D^{\text{edge}} \times \dot{\varepsilon} \approx \frac{1}{S_s q_x} \approx 7.5\cdot 10^{-3}, \tag{8}$$

which ensures that this contribution is negligible compared to that of Eq. 7, because the decay time of $g_2 - 1$ is ruled by the fastest relaxation mechanism.

0.5 State diagram using physical units for time

In Fig. 14 we plot the state diagram of Fig. 5 of the main text, using, for the x-axis, time in physical units instead of the reduced time $\tilde{t}$. Using time in physical units allows one to clearly appreciate the shortening of the time δt spent by a drop in the driven glass region as Pe increases. The variation of δt with Pe is shown in Fig. 15. We measure that δt decreases from ~ 400 to ~ 50 s as Pe increases from 63 to 5754. This result suggests that, for experiments in which the colloidal drops dry extremely fast $Pe \geq 10^3$, such as in Leidenfrost effect, the time spent in the glassy regime becomes extremely short.

0.6 Evidence of a double double rigidity transition for different experimental conditions

In order to check for the robustness of our findings, we perform additional tests varying several parameters such as (i) the initial nanoparticle volume fraction, (ii) the initial contact angle between the drop and the surface, and (iii) the interaction potential between the nanoparticles. For (i), we test a suspension with an initial volume fraction $\phi = 1-5-20\%$. For (ii), we use different surfaces (see Sample environment above). For (iii), we add salt (KCl) to the suspensions in order to reduce the range of the repulsive potential and reach a potential close to a hard sphere potential. Interestingly, we find that, for all the different conditions, the drops always show two distinct shape instabilities. Moreover, Figure 16 shows that, independently on the volume fraction, contact angle, or length of the repulsion interaction, irreversible aggregation only occurs after the second shape instability, confirming the generality of what has been described in the main text.

0.6.1 Initial volume fraction

We plot in Fig. 17, Fig. 18 and Fig. 19 three examples of the double shape instability faced by samples with different initial particle load. Moreover, in Fig. 20, using the light scattering set-up and the analysis described in the main text, we detect the presence of the shell for a drop with initial volume fraction $\phi = 20\%$ deposited on the same hydrophobic surface as in the main text. Note that, for a given relative humidity, the Péclet number changes with the volume fraction, reflecting the variation of the diffusion coefficient of the nanoparticles with ϕ (see also fig. 11).

0.6.2 Different surfaces

We plot in Fig. 21 an examples of the double shape instability faced by samples with contact angle $\theta_c = 60°$, and in Figure 22 a drop similar to the one investigated in the main text but suspended on a mesh of human hair. For the latter we used the light scattering set-up and the analysis described in the main text to underline the glassy shell.

0.6.3 Reduced interparticle potential

Complementary detailed experiments (at $Pe = 25$ and $Pe = 71$)) are conducted with added salt in the suspension so as to reach a interaction potential close to a hard sphere potential. To do so, we fix the KCl concentration at 15 mM, yielding a Debye length of the order of 3 nm, small compared to the nanoparticle size. The potential is therefore close to a hard sphere potential. To prepare the sample with salt, the batch suspension is first concentrated by centrifugation before adding an appropriate amount of salted water, so that the KCl concentration of the solvent in the final suspension is 15 mM. Experiments are performed at two different relative humidities, RH = 75% and 33%, corresponding to $Pe = 25$ and $Pe = 71$, respectively. Note that, with salt, the diffusion coefficient of the particles D is higher than without salt (for $\phi = 0.31$, $D = 4.31 \times 10^{-12}$ m^{2}s^{-1} with salt, and $D = 1.57 \times 10^{-11}$ m^{2}s^{-1} without salt) (see also fig. 11). We have checked by standard dynamic light scattering on a sample with $\phi = 0.31$ that for KCl concentrations up to 75 mM, the silica NPs do not aggregate and remain perfectly dispersed over a timescale longer than that of the drying experiments. Overall, we find results comparable to those in the experiments performed without added salt, both at the qualitative and quantitative level. Note that we estimated that at the end of the drying process the average salt concentration in the water is 23 mM (resp., 26 mM) for $Pe = 25$ (resp., $Pe = 71$), low enough to rule out aggregation on the time scale of evaporation. We report here the main results obtained for the suspensions with

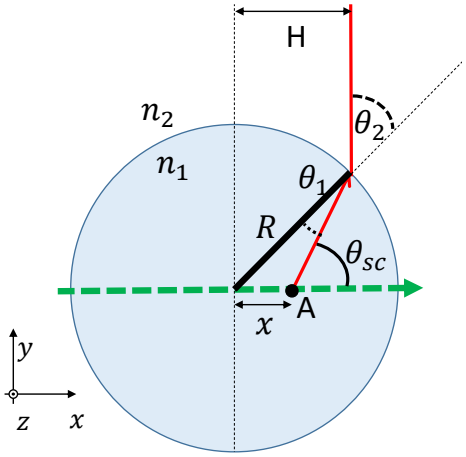

Figure 1 Sketch of a spherical drop with index of refraction n_1 surrounded by a medium of refractive index n_2 (top view). The green dashed line represents the laser beam that illuminates the spherical sample along a diameter in the x direction. The red solid line is the path of light scattered by the portion of the sample located in A and exiting the drop along the y direction. θ_1 and θ_2 are the incidence and refraction angle at the drop-surrounding medium interface and θ_s is the scattering angle.

salt. Figure 23 displays the time evolution of the shell thickness for the two sets of data acquired with added salt, together with all the other data acquired without added salt and described in the main text. Figure 24 shows the time evolution of the NP relaxation time along the drop radius; the time evolution of the volume fraction in the core, ϕ_{core}, is plotted in Fig. 25 together with the data for the suspensions without salt. Note that ϕ_{core} for the suspensions with salt has been computed using a specific calibration curve that we have measured for quiescent suspensions comprising salt, shown in Fig. 26. The time evolution of the volume fraction in the shell for samples with salt is shown in Fig. 27, again together with the data presented in the main text for suspensions without salt. Finally, we plot in Fig. 28 the microscopic decay time at the edge of the drop, τ_D^{edge}, as a function of the macroscopic strain rate $\dot{\varepsilon}$ for all the samples. The overall relationship between τ_D^{edge} and $\dot{\varepsilon}$ is similar for samples prepared with or without added salt.

Overall, the additional measurements suggest that our experiments are robust and that the general picture merging from them does not depend on the details of the interaction potential between the nanoparticles, the initial NP volume fraction or the detailed interaction between the drop and the surface.

Notes and references

[1] J. W. Goodman, *Speckle phenomena in optics: theory and applications*, Roberts and Company Publishers, 2007.

[2] I. Langmuir, *Physical review*, 1918, **12**, 368.

[3] B. Sobac, P. Talbot, B. Haut, A. Rednikov and P. Colinet, *Journal of colloid and interface science*, 2015, **438**, 306–317.

[4] A.-M. Philippe, D. Truzzolillo, J. Galvan-Myoshi, P. Dieudonné-George, V. Trappe, L. Berthier and L. Cipelletti, *Physical Review E*, 2018, **97**, 040601.

[5] B. J. Berne and R. Pecora, *Dynamic Light Scattering: With Applications to Chemistry, Biology, and Physics*, Courier Corporation, 1976.

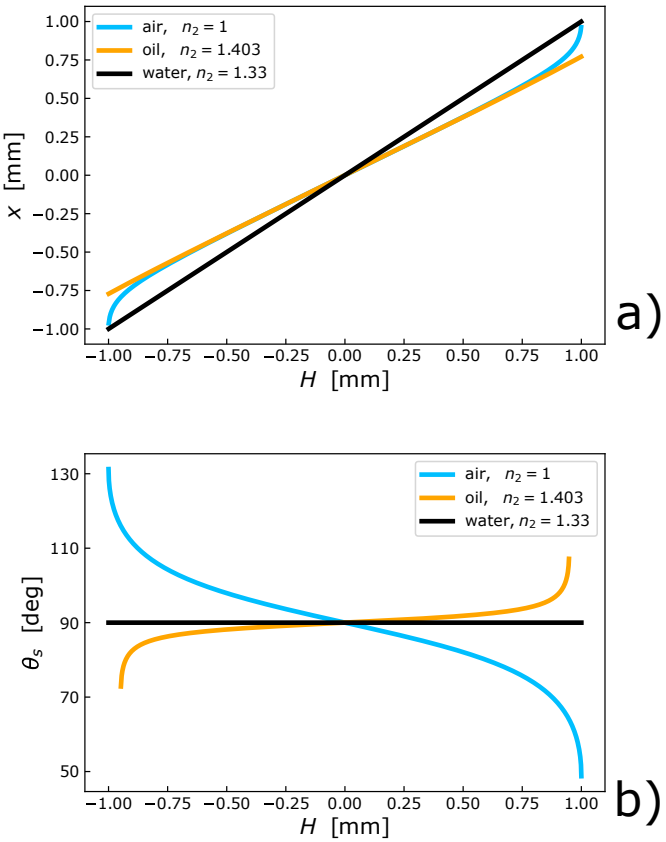

Figure 2 (a) Inner position x of the scatterers as a function of the position H defined in Fig. 1, for a spherical drop of water with $R = 1$ mm immersed in media with different index of refraction (air, water and oil). (b) Scattering angle as a function of H under the same conditions as in (a).

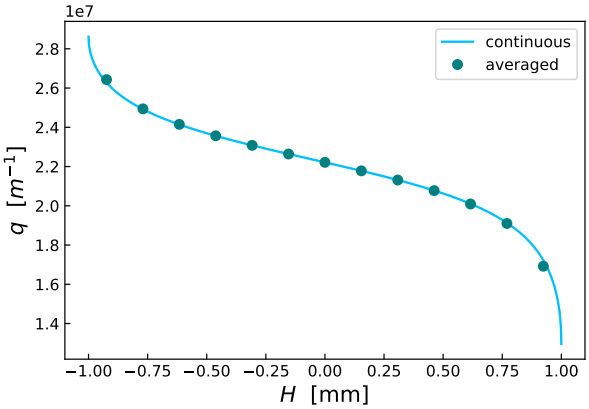

Figure 3 Line: Scattering vector as a function of the position H along the diameter for a water drop of radius 1 mm surrounded by air. Symbols: average q for each ROI, as a function of the position of the ROI center.

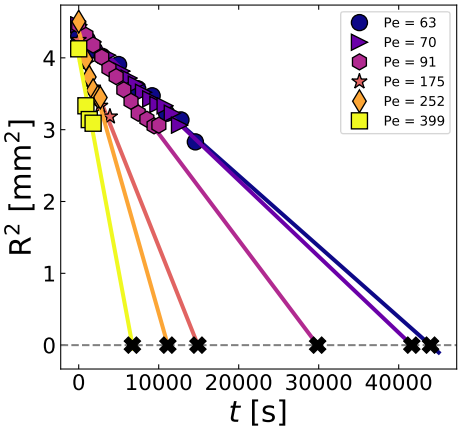

Figure 4 Time evolution of R^2, with R, the radius of the drop, for different Pe. Symbols are data points before the onset of instability and the thin lines are linear fits of the data.

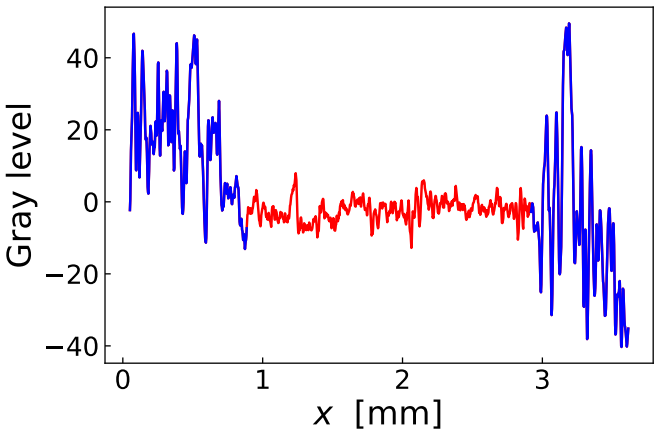

Figure 5 Gray level averaged along the y axis as a function of the position. Blue curve; characterized by a large variance correspond to the shell while the red represent the core.

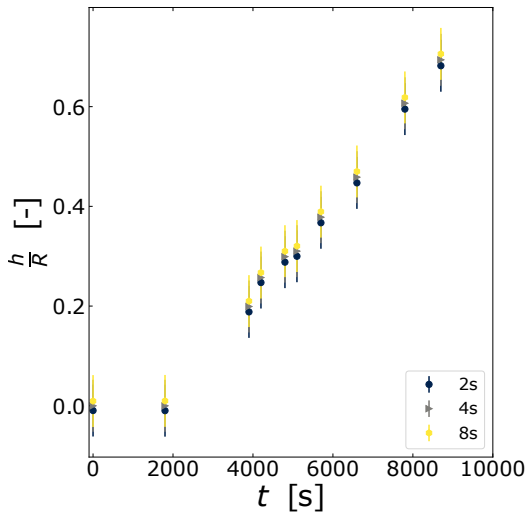

Figure 6 Shell thickness normalized by the radius of the drop as a function of time for a sample that dries at $Pe = 91$. Different colors correspond to different time intervals Δt over which the speckle images are averaged to locate the shell boundary, see Fig. 2c of the main text and the related discussion.

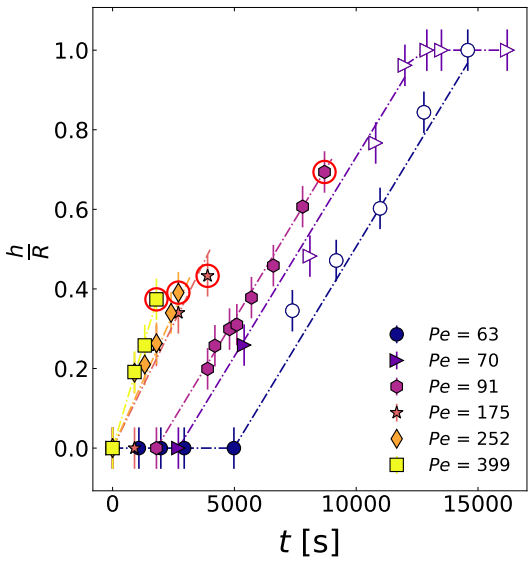

Figure 7 Shell thickness normalized by the radius of the drop as a function of time. Different colors correspond to different Péclet numbers as indicated. The red circles indicate the time for the onset of the shape instability. After the instability we measure that the drop radius does not decrease anymore. Symbols are experimental data points and dotted lines are guides for the eye. Error bars are due to the uncertainty in the determination of the radius and the shell in the speckle images. Empty symbols at low Pe correspond to data above the black line of Fig. 4 of the main text corresponding to $\tau_D^{\text{edge}} = \Lambda \dot{\epsilon}^{-1}$.

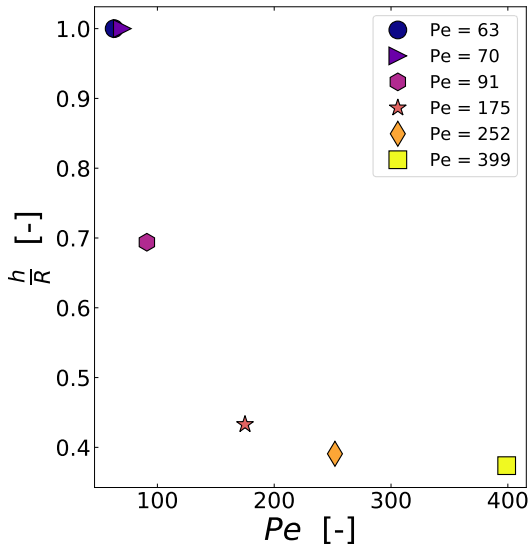

Figure 8 Final value of the shell thickness normalized by the radius of the drop as a function of Pe. Data at $Pe = 63, 70$ correspond to measures taken at the end of the experiment, when the shell has invaded the whole volume of the drop. For larger Pe, h is measured at the onset of instability.

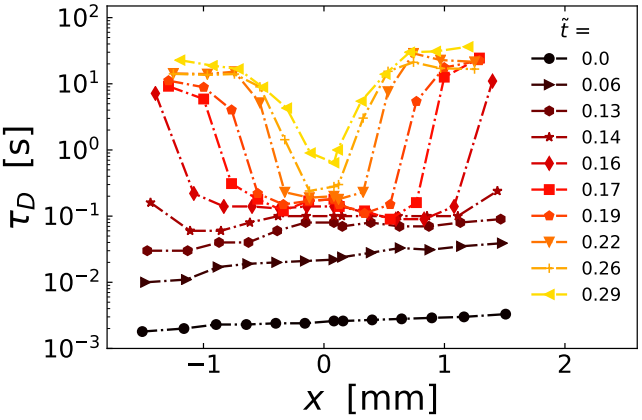

Figure 9 Decay time as a function of the position along a drop diameter, for a drop drying at $Pe = 91$. $x = 0$ correspond to the drop center. Measurements are shown at different reduced times as indicated in the legend.

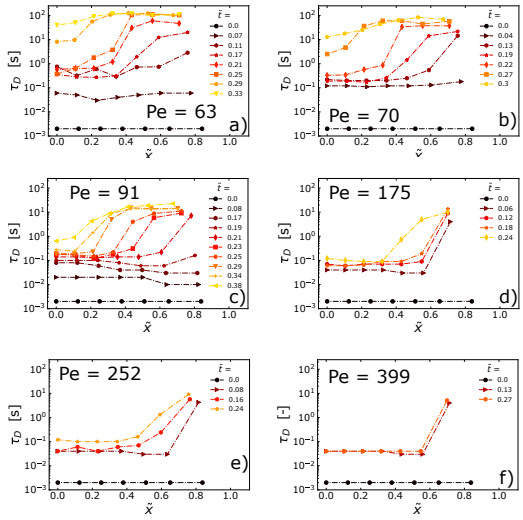

Figure 10 Decay time as a function of the position along the radius of the drop, for different Péclet numbers. Measurements are shown at different reduced times as indicated in the legends.

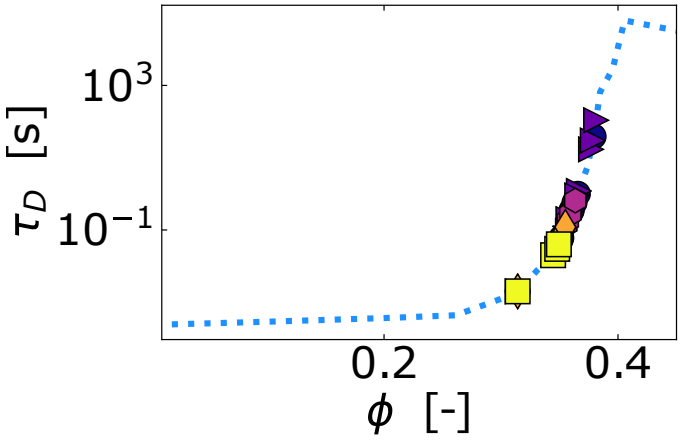

Figure 11 Relaxation time as a function of volume fraction for quiescent homogeneous nanoparticle suspensions. The blue dotted line is the reference curve (from [4]) and symbols correspond to data points for the dynamics of the same nanoparticles located in the core of drying drops.

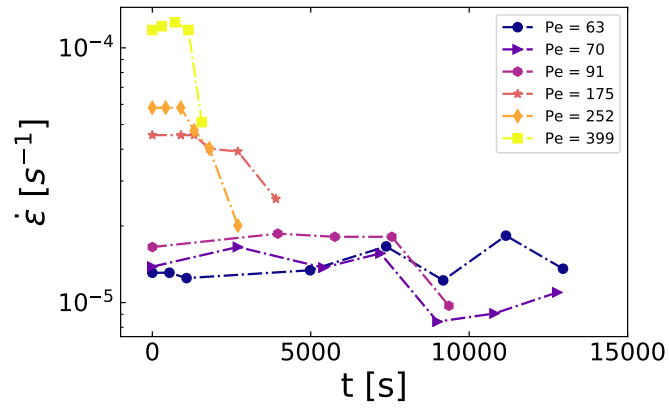

Figure 12 Macroscopic strain rate due to the drop shirking *vs* time. Different colors correspond to different Péclet numbers, as indicated by the legend.

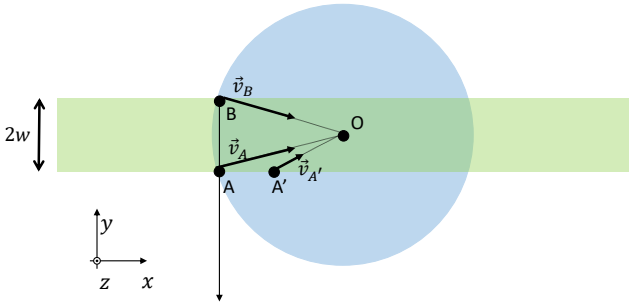

Figure 13 Sketch of the scatterers' displacement in an elastic sphere of radius R undergoing homogeneous compression. The sample is illuminated by a laser beam with beam waist w, whose size is here exaggerated for the sake of clarity. A and B are two points that contribute scattered light to the same speckle, located near the edge of the sample. The points A and A′ correspond to the left and right 'edges' of the same speckle. The distance AA' is exaggerated for the sake of clarity: in the actual setup, $AA' \approx AB/10 = 2w/10$. See text for details.

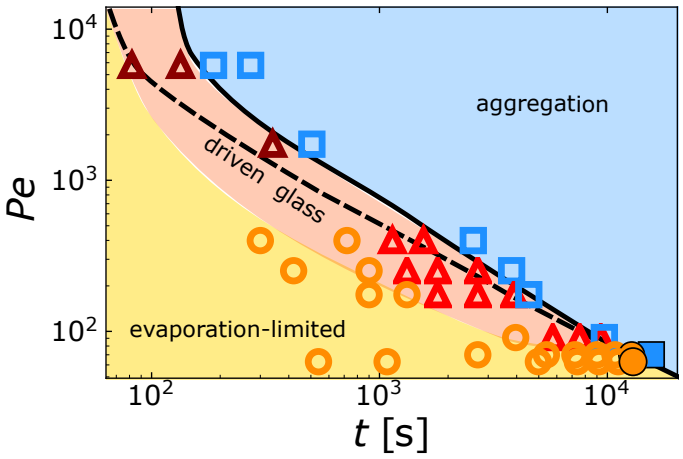

Figure 14 Unifying state diagram for the evolution of drying drops of colloidal suspensions. The different regimes through which a drop of colloidal suspension transits while drying are depicted in the (Pe, t) plane. The dashed and solid lines indicate the onset of the shape instability and fracture instabilities, respectively. Yellow background and circle symbols: region where the drop shrinkage is ruled by the evaporation rate imposed by the environment relative humidity. Pink background and triangles: driven glass region, where the drop evaporation is limited by the glassy dynamics of the shell. Blue background and squares: region where the particles in the shell are permanently aggregated. Open symbols indicate samples with a shell, full symbols at low Pe designate samples with uniform particle distribution within the drop. The three top most darker triangles correspond to the onset of shape instability for sample that evaporated too fast for the microscopic dynamics to be measurable.

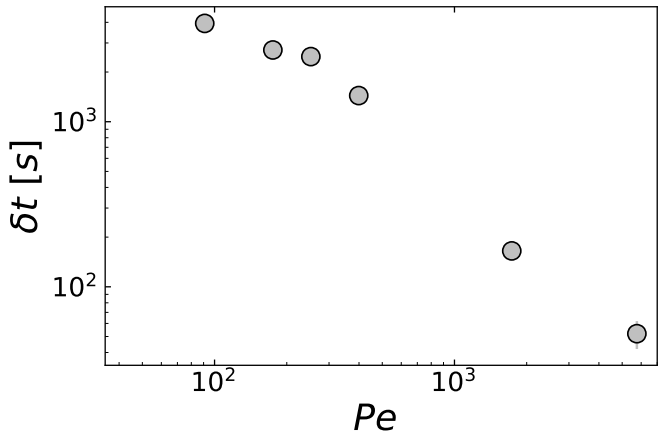

Figure 15 Time interval of the driven-glass regime δt as function of the Péclet number Pe.

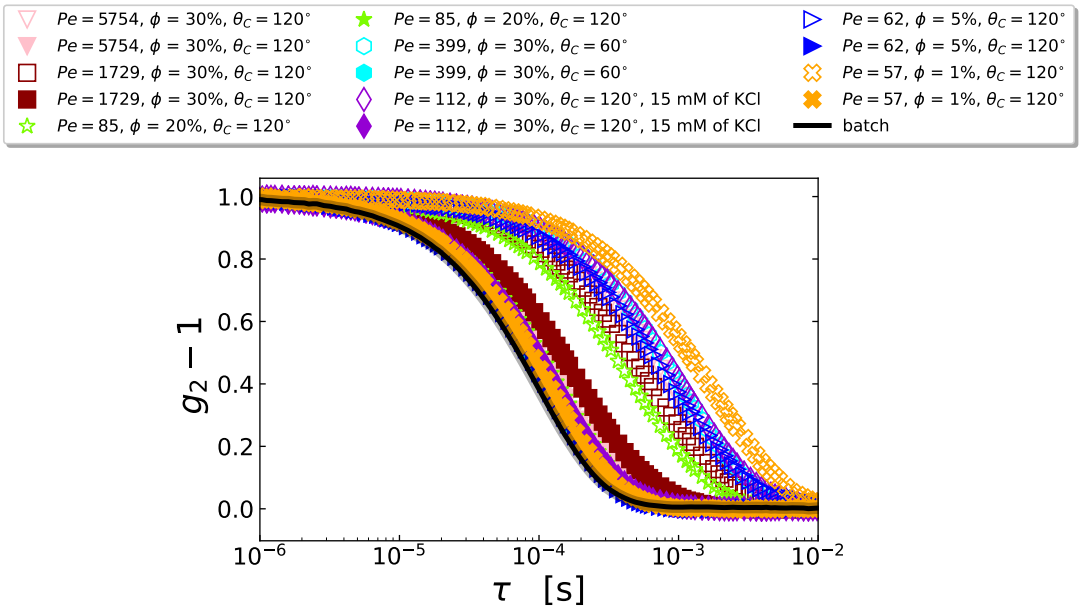

Figure 16 Correlation functions: filled symbols correspond to samples at the first shape instability after having been redissolved in water; empty symbols correspond to samples at the second shape instability after being immersed in water and sonicated. The solid line corresponds to the reference batch suspension of non-aggregated nanoparticles. The three types of samples are prepared at the same nominal volume fraction $\phi = 0.014$. For each sample, the Péclet number at which the drop has dried, the initial volume fraction ϕ, and the contact angle θ_C which depends on the surface on which the drop has been deposited, are indicated.

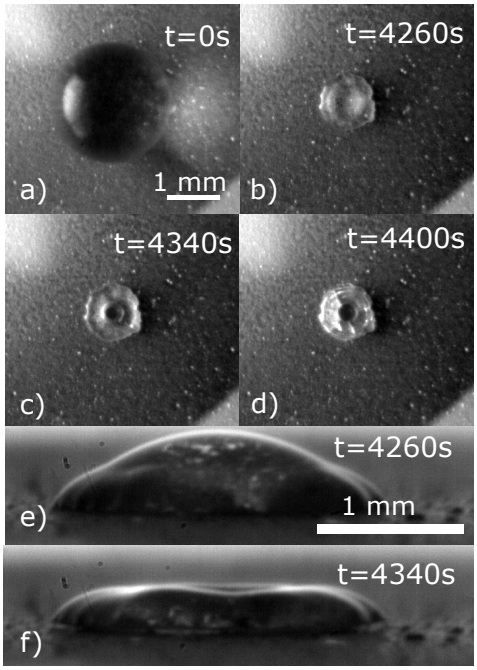

Figure 17 Image sequence of a drop with initial volume fraction $\phi = 1\%$ that dries at $Pe = 57$, as taken by a camera positioned on the top of the drop. At time $t = 0$ the drop is deposited on a hydrophobic surface (contact angle $\theta_C = 120$ deg) (a). The onset of the shape instability occurs at $t = 4260$ s (b), and the instability develops (c, $t = 4340$ s), until the drop fractures into two pieces (d, $t = 4400$ s). The scale bar represents 1 mm and is the same for all images. (e-f) Side views at the onset (e, $t = 4260$ s) and at full development of the instability (f, $t = 4340$ s).

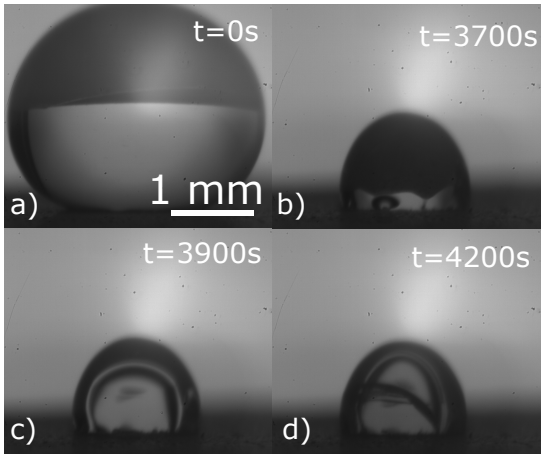

Figure 18 Image sequence of a drop with initial volume fraction $\phi = 5\%$ that dries at $Pe = 62$, taken by a camera positioned on the side of the drop. At time $t = 0$ the drop is deposited on an hydrophobic surface (contact angle $\theta_C = 120$ deg) (a). The onset of the shape instability occurs at $t = 3700$ s (b), and the instability develops (c, $t = 3900$ s), until the drop fractures into two pieces (d, $t = 4200$ s). The scale bar represents 1 mm and is the same for all images.

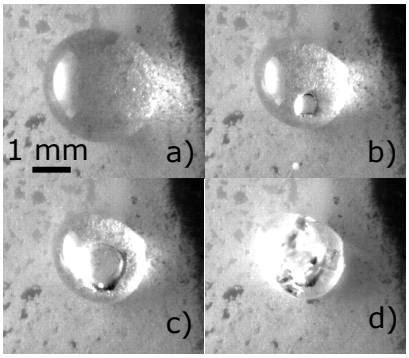

Figure 19 Image sequence of a drop with initial volume fraction $\phi = 20\%$ that dries at $Pe = 85$, taken by a camera positioned on the top of the drop. At time $t = 0$ the drop is deposited on an hydrophobic surface (contact angle $\theta_C = 120$ deg) (a). The onset of the shape instability occurs at $t = 10090$ s (b), and the instability develops (c, $t = 10890$ s), until the drop fractures into two pieces (d, $t = 14350$ s). The scale bar represents 1 mm and is the same for all images.

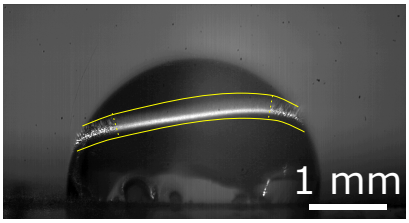

Figure 20 Formation of the shell during evaporation for a drop with initial volume fraction $\phi = 20\%$ that dries at $Pe = 85$. The time average is performed over an interval $\Delta t = 4$ s. Blurred region corresponds to the core of the drop where the nanoparticle dynamics are fast, and the region where the speckles are still visible after averaging, which indicates slow dynamics and corresponds to a shell. Solid yellow lines are guidelines for the reader to identify the region illuminated by the laser. Dashed yellow lines are guidelines for the reader to identify the region with the dense shell.

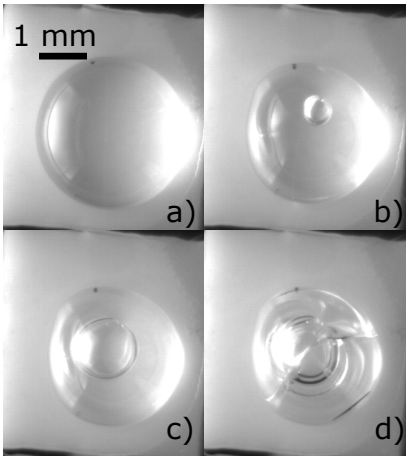

Figure 21 Image sequence of a drop with initial volume fraction $\phi = 30\%$ that dries at $Pe = 399$, taken by a camera positioned on the top of the drop. At time $t = 0$ the drop is deposited on a hydrophobic surface (contact angle $\theta_C = 60^\circ$) (a). The onset of the shape instability occurs at $t = 1415$ s (b), and the instability develops (c, $t = 1982$ s), until the drop fractures into two pieces (d, $t = 2164$ s). The scale bar represents 1 mm and is the same for all images.

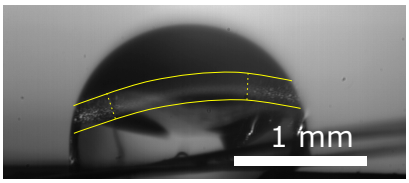

Figure 22 Formation of the shell during evaporation for a drop suspended on a mesh of human hairs and that dries at $Pe = 91$. The time average is performed over an interval $\Delta t = 4$ s. Blurred region corresponds to the core of the drop where the nanoparticle dynamics are fast, and the region where the speckles are still visible after averaging, which indicate slow dynamics and corresponds to a shell. Solid yellow lines are guidelines for the reader to identify the region illuminated by the laser. Dashed yellow line are guidelines for the reader to identify the region with the dense shell.

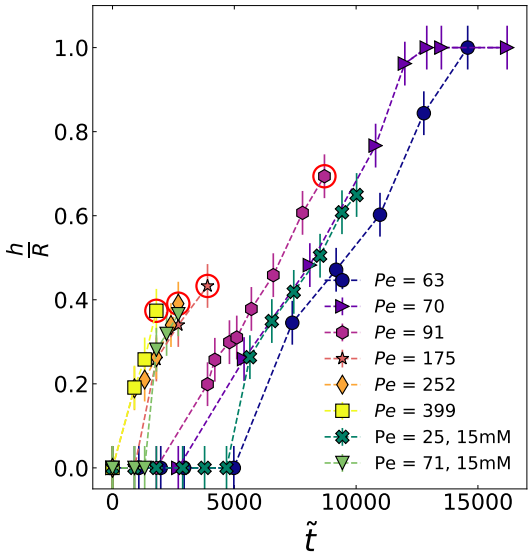

Figure 23 Shell thickness normalized by the radius of the drop as a function of time. Same data as in the main text are shown as well as additional data for suspensions where the repulsive interactions between nanoparticles are screened by adding salt. Different colors correspond to different Péclet numbers as indicated. The red circles indicate the time for the onset of the shape instability. After the instability, the drop stops decreasing. Symbols are experimental data points and dotted lines are guides for the eye. Error bars are due to the uncertainty in the determination of the drop radius and the shell thickness.

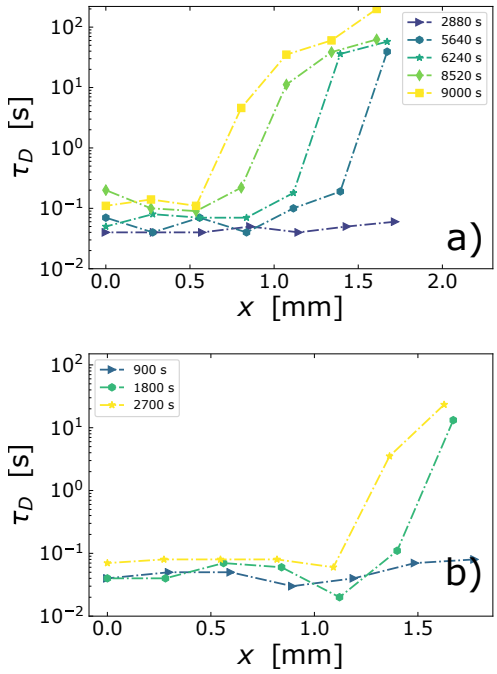

Figure 24 Decay time as a function of the position along the drop radius, for suspensions with added salt (see text for details) and for two different Péclet numbers, (a) $Pe = 25$, (b) $Pe = 71$. Measurements are shown at different times as indicated in the legend.

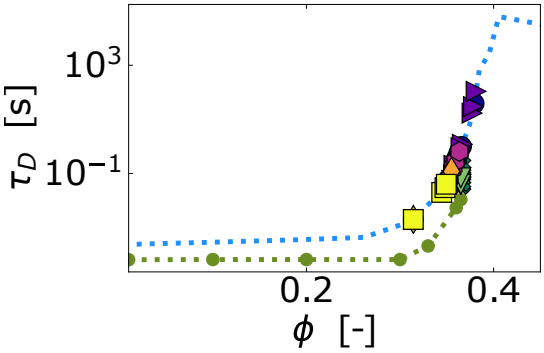

Figure 26 Relaxation time as a function of volume fraction for quiescent homogeneous samples. The blue dotted line is the reference curve (from [4]) and the symbols correspond to data points for the dynamics at the core of drying drops. The green dotted line with circular markers is the reference curve measured for the same colloidal suspension but with added salt (15 mM KCl).

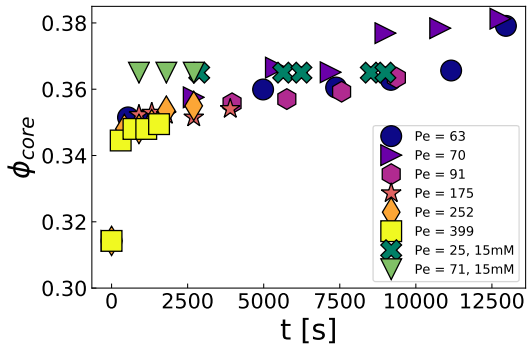

Figure 25 Time evolution of the volume fraction of the core. Symbols are data points for drops dried at different Péclet numbers, as indicated in the legend. Green symbols correspond to data acquired with added salt, thus screening the electrostatic repulsion between nanoparticles.

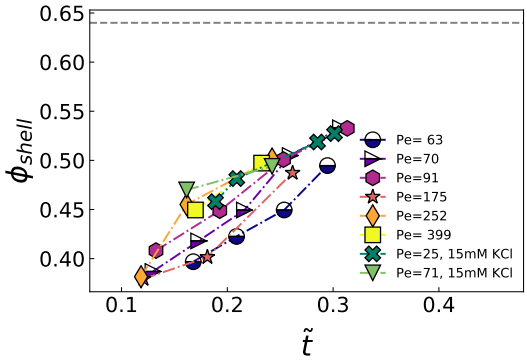

Figure 27 Time evolution of the volume fraction of the shell as a function of time as obtained from mass conservation and measurements of the shell thickness and of the volume fraction of the core. Symbols are data points for drops dried at different Péclet numbers, as indicated in the legend. Data from yellow to purple colors correspond to samples without added salt, and green symbols corresponds to samples with added salt. The dotted line represents the limit of random close packing $\phi = 0.64$ of monodisperse particles.

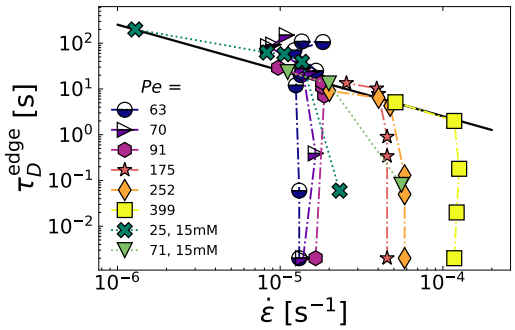

Figure 28 Decay time τ_D^{edge} of the microscopic dynamics measured at the edge of the drop, as a function of the strain rate, $\dot{\epsilon}$, for experiments performed at different Péclet numbers and salt content, as indicated in the legend. When the drop is unstable ($Pe > 70$), τ_D^{edge} is bounded by the functional form $\tau_D^{\text{edge}} = \Lambda \dot{\epsilon}^{-1}$ discussed in the main text (black line). Half-filled symbols correspond to drops evaporating at small Pe, for which no instability is seen on the time scale of the experiment. For all experiments, τ_D^{edge} increases monotonically with time.

Appendix B

annex

For the repeatability of the experiment, I put in table, all the parameters to set in the rheometer and camera program. These data could be change in case of different experimental conditions.
Pay attention that Exp.Time is minor than lag time.

φ [%]	$\dot{\epsilon}_H$ [1/s]	d_i [mm]	Point [ms]	Exp. Time [ms]	lag-time [ms]
15	1	50	12	200	230
	0.1	30	55	300	350
	0.01	10	700	500	800
	0.001	3.6	1500	700	1400
10	1	50	12	200	230
	0.316	30	35	250	300
	0.1	30	55	300	350
	0.0316	10	350	500	600
	0.01	10	700	500	800
	0.00316	4	1100	700	1000
	0.001	3.6	1500	700	1400
	0.0005	3	3000	800	3000
5	1	50	35	200	230
	0.316	30	45	300	330
	0.1	30	60	300	330
	0.0316	10	550	500	600
	0.01	10	800	700	800
	0.00316	4	1300	900	1000
	0.001	3.6	1750	1000	1400
	0.0005	3	3200	1000	3300
3	1	50	65	200	230
	0.316	30	85	250	300
	0.1	30	100	300	350
	0.0316	10	720	400	450
	0.01	10	1100	600	650
	0.00316	4	1600	800	850
	0.001	3.6	2350	1000	1100
	0.0005	3	3700	1000	3000
1.5	1	50	110	200	230
	0.1	30	140	200	230
	0.01	10	1500	500	530
	0.001	3.6	3500	800	3200

Table B.1: Parameters use for experiment, where φ is volume fraction, $\dot{\epsilon}_H$ is the rate compression, d_i is initial entrefer rheometer plates, *Point* is the interval between each point is registered by the rheometer, *Exp.time* is the exposure time of the camera *lagtime* is delay between the camera takes an image.

Acknowledments

In first instance I would like to acknowledge my directors Laurence and Luca and my supervisor Christian. My feeling of profound gratitude is not only due to the vastness of things that you taught me, but is also due to the passion you have shown me with your guidance, each of you with your own way of doing science.

Laurence, I've been immediately conquered by the energy and enthusiasm with which you guided me through this work. I perfectly remember when, after a month from the beginning of the PhD, we were told to work from home due to the Covid pandemic. For a moment I worried about my PhD, projecting myself alone without something to do for several months: few instants after I received from you an email asking to meet the day after to plan properly the following weeks. In that moment I understood that your tenacity would have accompanied me throughout the PhD. Moreover, I would like to thank you for your thirst for knowledge: your question, always so direct, challenge me every time to better understand my research.

Luca, I'm really amazed by your attention to details and generosity. Among many occasions where I've appreciated these qualities, the one that struck me the most has been right before the defense, when, back from one of your trips, you spent three hours to rehearse and giving me advice until 11pm. In that occasion as in many others, looking at you giving your time had been extremely motivating to make extra effort to make a better job all along these three years. Moreover, I would like to thank you for all your time you spent at the very beginning, when speckles, lasers, DLS were an obscure world for me. Nevertheless, I would like to thank both of you for the sincere support you gave me every time I proposed new experiments or ideas: being guided and supported in my creativity was essential to fully enjoy these years.

Christian, I much appreciate the meeting we had together, it has been a pleasure discussing with you. I really appreciate your way of thinking the physics of these systems and your bright ideas have been extremely fruitful for improving my work.

Second, I would like to profoundly thank Kevin Roger, Ludovic Pauchard, Véronique Trappe, Emanuela Del Gado, Cecile Cottin-Bizonne and Wilson Poon to have served on the jury of my defense. I've extremely appreciated the care you put in reading and studying my manuscript. The depth of your question not only helped me to better understand my research but it also opened several intriguing perspectives for the continuation of this work.

I would like to thank all the people that helped me for the realization of this work. To Ty, thank you for the help in all the chemical preparation and your smart ideas that

have been key to solve many practical issues. Thank you also for all the discussion we had about cooking and running, your advice have been extremely helpful. To Philippe, thank you for the X-ray experiments we did together, you've been really kind helping me with these measurements. A special thank goes to my master students: Khaled, Chiara and Emanuele. Teaching to you have been fun and formative at the same time: thank the trust you had in me even we have made nice experiments. Each of you, with your won skill is great, and I wish you all the best for your carrier.

Moreover, I would like to thank all the colleagues I met during these years. To Carole-Ann, I'll never forget the companionship you've made me during these years. Your energy and radiance are really contagious, I've extremely enjoined discussing with you about any subject during our dinners. Now that I'm not in a rush anymore with the writing, I'll find the time to make pizza again for you next time you'll come to see me. To Juliette, thank you for your great generosity. I'm always amazed by the attention you have for the others: I no matter the problem/question I had, I always found you available for helping. Moreover, I'm touched by the fact that every time to step-by Montpellier, you always remember to bring something as a sign of your affection. To Ameur, thanks for all the moment we shared: from soccer matches played and watched together to lunches with spicy (probably too spicy) kebab. Your sympathy makes your company extremely enjoyable. Together with Carole-Ann and Juliette you have been a fantastic company making me feeling at home from the first day I step in in the lab. To Domenico, thank you for all the discussion we had, I really appreciate the patience you have an your genuine enthusiasm you show every time I step into your office with a weird questions on my experiments. To Majid, thank for being a fantastic office mate: it has been really cool to share M&Ms, waffles, and any sort of comfort food from the vending machines. You've done an amazing effort in learning all the Italian expressions I taught you. To Rajam, thanks for all the time we spent together: from all the conferences we attended together (Crete, Athens, Ancona) to beers and restaurants after work. thank you also for your help in making the gnocchi with the highest density I ever made. To Nick, thanks for all the discussion we had, it has been extremely interesting sharing ideas and thoughts with you. To Abdallah, we had started the PhD the same day and finished almost the same week, it has been fun sharing lab life and playing soccer together, Thank you also for all the banana plants with which you decorated my office. To Vincenzo, Numera, Alessandro, new Italian buddies in the lab, I'm really glad you've joined the group and I hope we will share good moments in the next months. Furthermore, thanks also go to all the members of the soft matter team: Julian, Guilhem, Pierre, Cansu, Tom, Nishant, Laura, Alessandro C., Jean-Gab, Aditi, Antonio, William, Vimala, Jabir, Antigoni, Tristan, Martin, Pascale, Mathieu, Christope, Remi, Gladys, Maurizio, Daniel, Amelie and all the other people from the lab that helped me: Jean-Marc, jean-Christophe, Raymond, Remi G. Edouard.

I would like to thank all the friends that I met and, in a way or another accompanied

me during these years. To Stefano, working with you has been vital to do my thesis here Montpellier: you did not simply introduced me to Laurence and Luca, but you ignited the passion for soft matter which has been necessary to start this journey. To Virgilio, Clara and Leonardo, you have been a family for me in Montpellier: thanks for the hospitality you gave me, my stay wouldn't have been the same without you. To Anna, thanks for your friendship and the moment spent together. I really admire the passion you have for the things you do, especially your work: you are the only who managed to bring me several times into a contemporary art museum. To Alice thanks you for all the tennis matches we played, it has been extremely fun. And also thanks to all the people from Communione e Liberazione that have been around in Montpellier: Elisabeth, Camilla, Tommaso, Clara, Mavi, Astrid, Giuditta, Leonardo. To Sam, living with you have been really interesting, I really like your desire of finding always the best way for to do something: from coding when you work to nutrition during trail runs. I'm glad I had the chance to see your way of doing things and I really got inspired by that (even though I still convinced that your theories on how to cut an organ are a bit too much...). To Geoffroy, you are an amazing flatmate too, your calm and patience matches pretty well with my strong character. I really like climbing and racing (even if we arrive a few hours apart) with you. Moreover, I really admire your faith and see how you spent time and energies for it. To Olivier, Kassem and Lena, my climbing friends thanks for all the adventures we lived in the most beautiful place of France: Gorges du Verdon, Mont Blanc, Calanques, Gorges de la Jonte, St. Guilhem and many others. I'm also extremely glad for the friendship between us that have born thanks to our passion. To all the friends from Sitio, in particular to Laetitia, Caroline, Nathan, Myriam and Fr. Max, meeting you last year have been really key for my personal growth.

To all my friends doing their PhD in France Drew and Gaicomo: thanks for keep being my *neighbors* and sharing (at few hundreds kilometers far apart the same adventure). Scott, I still think that you'll be the next big name of soft matter. Thanks for your friendship, even though we do not see each other as often as when we were studying together your friendship is always extremely important for me. To Giovanni and Rachele, the intensity with which you live your live always encourage me to live my life as well. To all the dear friends in Italy and all around the world, in particular to Sabba, Calre, Tappo, Filo, Ste, Luci, Pota.

Finally, I would like to say thank you to my family. To my Uncle Cosimo, my aunt Cristiana and my cousins Edoardo Federico and Cecilia. To my grandparents, Maria Teresa, Filomena and Alfredo for the admiration, sometimes excessive (I'm not gonna win the Nobel as Carlo Rubbia), that you have in my regards. Thanks for having accompanied my parents in my education since I was a child. To my sisters Chiara and Anna, I really admire the things you do and the passion you both have for what you do. The achievements you reached in your studies are incredible but, what is even more incredible

to me is your genuine humbleness, I deeply think that you keep underestimating yourself.

To parents. With time I'm becoming more and more aware of all the sacrifices you made, that most of the time I take for granted. Moreover, from each of your something that I learn from you that turned key to accomplish this work. Mamma, with time I'm noticing how similar we are and how many things we have in common, included our love for teaching. The affection you have for your job for me is the way of being a teacher, you'll always be a model to follow if I'll have a chance to keep teaching. Papa′, you often say: *'Il topolino mangia l'elefante un morso alla volta'*: in its simplicity this statement contains all your calm and strength with which you approach life. Many times during the PhD, especially during the redaction of this manuscript, I faced moments where the amount of work seems to overcome my energies and time. Tough, inspired by your words *'Il topolino* **ha mangiato** *l'elefante un morso alla volta'*, and there we go, the thesis is done.